Università di Pisa

Facoltà di Scienze Matematiche Fisiche e Naturali

SCUOLA DI DOTTORATO GALILEO GALILEI
Corso di Dottorato in Fisica XIX Ciclo

Tesi di Dottorato

Model and simulation of gamma-ray pulsar emission in GLAST

Candidato
Massimiliano Razzano

Relatore
Prof. Ronaldo Bellazzini

Giugno 2007

Contents

Introduction

The Gamma-ray Large Area Space Telescope (GLAST) is an international space mission that will study the Universe in the γ-ray band 10keV-300GeV. A large part of this spectral window, roughly in between 10GeV-300GeV, is rich and partially unexplored.
GLAST is scheduled for launch at the end of 2007 and will carry onboard two main instruments, the *Large Area Telescope* (LAT) and the *GLAST Burst Monitor* (GBM).
The Large Area Telescope (LAT) is the main GLAST instrument and consist in a pair conversion telescope based on advanced detectors for High Energy Physics. The LAT has an effective area and energy and angular resolution better than its predecessor EGRET, a gamma ray telescope aboard the Compton Gamma Ray Observatory (CGRO) during the period 1991-2000.
The LAT will explore the γ-ray sky with an unprecedented detail and will discover thousands of new sources, providing a key contribution in the development of the Astrophysics and Astroparticle Physics.
The GLAST Burst Monitor is mainly devoted to the study of the Gamma Ray Bursts (GRBs), powerful explosions in the cosmos that originate intense flashes of high-energy photons. The GBM is made by a set of scintillation-based detectors that will continously monitor the entire visible sky ready to give alert in case of a new GRB appears.
GLAST will provide a deeper insight into many cosmic sources, studying acceleration mechanisms in sources such as Active Galactic Nuclei, Gamma Ray Bursts and Pulsars. GLAST will also study transient sources, e.g. GRBs and Solar Flares, with a full-sky coverage guaranteed by the GBM. Thanks to its angular resolution GLAST will identify most of the sources that were unidentified in the Third EGRET Catalog, where the poorer angular resolution did not allow an unambigous identification. A more detailed presentation of the science goals of GLAST are presented in Chapter 1.
Among the γ-ray known sources there are pulsars, that are highly-magnetized, rotating neoutron stars. Pulsars are astrophysical sources that have been observed in the whole electromagnetic spectrum and have been discovered as sources in radio 40 years ago. Despite this long interval of time since their discovery, today we have only a rough understanding of these objects.
One of the most powerful tool for studying pulsars is their emission at high energies and GLAST will dramatically contribute to solve some of the basic issues on pulsar science. Basically GLAST will provide high-detail observations of the already known γ-ray pulsars and potentially will discover a huge amount of new pulsars.
In this thesis I will present the results of my Ph.D. project that have been developed within the GLAST LAT collaboration. The main focus of the work is devoted to the development of detailed and efficient simulations of pulsar emission. As it will be shown, simulations can be used for several goals, and mainly 1)Study the LAT response to pul-

sar signal, 2)Test and exercise LAT analysis software 3)Study and develop new analysis techniques and tools, and 4) Estimate rough capabilities of the LAT in observing pulsars.
The Ph.D. project have been also focused with some of these simulations goals and some exmples of simulations use are shown.
In Chapter 2 the GLAST Large Area Telescope is described and its performances are reviewed. In this Chapter the main LAT MonteCarlo software is presented and the LAT data analysis tools of the Science Analysis Environment (SAE) are introduced.
Chapter 3 present pulsars as neutron stars, and show the neutron star properties that can be inferred from observations of pulsars at various energies. A simple model for explaining emission from pulsars is also presented and discussed.
Chapter 4 deal with more detail the observational status of the presently known γ-ray pulsars, showing the summarized properties of γ-ray pulsars in the post-EGRET era. In this Chapter the main models for γ-ray pulsars are presented, with a more detailed discussion of the Polar Cap and Outer Gap model.
Chapter 5 describes *PulsarSpectrum* , an high-detailed pulsar simulator capable of reproduce γ-ray emission from pulsars. *PulsarSpectrum* take into account the main timing effects as motion of GLAST into the solar System, spin period change with time and timing noise. *PulsarSpectrum* has ben developed during the Ph.D. project and it has been upgraded and refined because of the requests of the LAT Collaboration for increasing realism in simulations. In this Chapter a description of *Pulsar Simulation Suite* is given. The *Pulsar Simulation Suite* is a set of programs and macros developed for creating realistic pulsar populations and format their parameters to be simulated.
In Chapter 6 an example of LAT data anaysis is presented, using basic simulated data. The LAT data analysis procedure for γ-ray pulsars is presented with reference to some analysis case. The case of Vela pulsar, PSR B1706-44 and PSR B1951+32 are presented and discussed, together with the descrption of the simulated model used and of the results from a basic analysis performed in that Chapter.
The Chapter 7 contain the detailed description of the pulsar simulations used for Data Challenge 2 (DC2). DC2 has been one important milestone in mission preparation and a full simulation of the sky with thousand of γ-ray sources have been prepared. *PulsarSpectrum* was chose for simulating the whole pulsar component in DC2 and I had the responsability to prepare the whole set of simulation model for pulsars in the DC2 simulated sky.
Chapter 8 show how DC2 pulsar data have been analyzed using an automatic analysis procedure written in Python that used the LAT pulsar tools. A statistics on pulsars that LAT would have been detected in the DC2 sky has been produced and the results have been also extrapolated to 1 year for comparing with estimates presented in other works.
Chapter 9 is devoted to present a study where pulsar simulation are very useful, i.e. in testing LAT capabilities to study a particular issue of pulsar physics. One of the most important observation that are expected by the LAT is the capability to study the high-energy spectrum for distinguishing between Polar Cap and Outer Gap emission scenario.
This study show not only that LAT will be able to easily distinguish and constrain betwen these two emission scenarios, but provide also some estimates on the minimum

time required to have such distintion using LAT data collected in normal survey mode. Simulation tools developed during this Ph.D. project have been used widely by the Collaboration during the last 3 years have been refined in order to satisfy the increasing request for realistic simulations, up to contains detailed timing noise or detailed simulations on binary pulsars.
The *PulsarSpectrum* simulator has become an established tool for preparing pulsar simulation and for testing pulsar tools and validate data analysis flow and new techniques in order to gain pratice with LAT data analysis. In addition these tools are currently used and for much detailed study of the capability of GLAST to study pulsars. This is a very important activity since it study what are the expected results from the LAT and what questions will be solved and addressed in pulsar physics after the launch of GLAST.

Chapter 1

GLAST and the gamma-ray Universe

Gamma-ray astrophysics is presently one of the most exciting fields of research for several reasons.
The emission of γ-rays is related to the most violent and powerful phenomena in the Universe and they provide a unique way to probe extreme physical environments, e.g. the physics of the compact objects.
The γ-ray energy range is the most energetic portion of the electromagnetic spectrum, that extends from about 100 keV up to multi TeV energies. Because Earth's atmosphere absorbs γ-rays it is necessary to put detectors at high altitudes using balloons or satellites such as GLAST (Michelson, 2000). At energies above 100 GeV is is possible to use the atmosphere itself as a detector to study the electromagnetic showers of the Very High Energy (VHE) γ-rays from the ground. This is for example the basic concept of the ground γ-ray *Čerenkov* telescopes like MAGIC, HESS, VERITAS or CANGAROO or large arrays like MILAGRO.
Gamma-rays are extremely useful messengers since they are neutral and so they are not deflected by cosmic magnetic fields (as it happens e.g. for cosmic rays). Each γ-ray points directly back to it source. Thanks to this characteristic γ-rays are optimal candidates to study the high-energy cosmic sources, that act as natural engines accelerating particles up to extremely high energies. In addition the Universe is largely transparent to γ-rays at GLAST energies, and this will permit GLAST to observe sources extremely distant, up to $z \sim 5$.
The study of cosmic γ-rays is extremely important for different research fields, including Cosmology, Particle Physics and the search for Dark Matter. The instruments aboard GLAST will provide big steps further in many of these areas and would possibly provide answers to some of the major questions of the modern Physics.
The main goals in the scientific program of GLAST can be summarized as:(Digel & Myers, 2001):

- Understand the **acceleration mechanisms** responsible for γ-ray emission in Active Galactic Nuclei, pulsars and supernova remnants;
- Study the **transient γ-ray sources**, e.g. Gamma Ray Bursts (GRBs) and solar flares;

- Study the **diffuse γ-ray emission**, both Galactic and extragalactic;
- Search for non baryonic **Dark Matter** candidates;
- Probe the **Early Universe** search for γ-ray emission from decay of exotic particles in the first stages of the Universe.
- Find counterparts to the currently **unidentified γ-ray sources**, that are about 60% of the presently known γ-ray detected point sources.

In this Chapter a review of the status of our knowledge about the γ-ray sky in the energy range of GLAST is presented, with an overview of the principal known classes of objects and the GLAST capabilities to study them.

1.1 Explorers of the gamma-ray sky

The key point about γ-ray Astrophysics is that atmosphere absorbs γ-rays, thus the development of this branch of astronomy have been carried mainly in the last decades, when satellite-based detectors were built and sent out of the atmosphere (Digel & Myers, 2001). At energies of hundreds of GeV it is possible to reconstruct the energy and direction of the γ-rays from the study of they electromagnetic showers in the atmosphere itself. This is the detection strategy of the Air *Čerenkov* Telescopes (ACTs) and of the Extended Array Shower Detectors (EASDs). Recently the number of sources detected at this energies is increased significantly, mainly thanks to experiments like MAGIC or HESS.

The first γ-ray space mission was *Explorer XI* in 1961 and it was able to detect about 20 photons uniformly distributed in the sky. The next important step was the NASA *Orbiting Space Observatory III* (OSO III) mission in 1968, that detected a diffuse γ-ray emission concentrated on the Galactic plane. This emission was promptly related to the γ-ray production in the Milky Way. The main detector used scintillators and Cherenkov detectors and was able to detect photons above 50 MeV.

In 1969 and 1970 a group of military satellites Vela that were able to detect X-ray and gamma-ray were launched by the United States. These satellites were intended to monitor possible of nuclear URSS experiment in the Earth atmosphere or on the Moon but they serendipitously discovered transient flashes of radiation named Gamma-Ray Bursts (GRBs) (Klebesadel et al., 1973).

The first satellite entirely dedicated to γ-ray astrophysics was the second *Small Astronomy Satellite* (SAS-2), launched in the 1972. SAS-2 was able to detect with more accuracy the diffuse emission and was also able to resolve the first point sources.

The pulsed γ-ray emission from the Crab pulsar and the Vela pulsar were detected. A map profile along the Galactic plane obtained by SAS-2 is displayed in Fig. 1.1. In 1975 the *European Space Agency* (ESA) launched COS-B whose discoveries are contained in the first γ-ray catalog of point sources, including the well known extragalactic source 3C 273(Mayer-Hasselwander et al., 1982). A big step forward occurred in 1991 with the launch of the NASA mission *Compton Gamma Ray Observatory* (CGRO).

The *Burst And Transient Source Experiment* (BATSE) and the *Energetic Gamma Ray Experiment Telescope* (EGRET) were the two main instruments more similar to the instruments aboard GLAST and then more interesting for the road to developing GLAST.

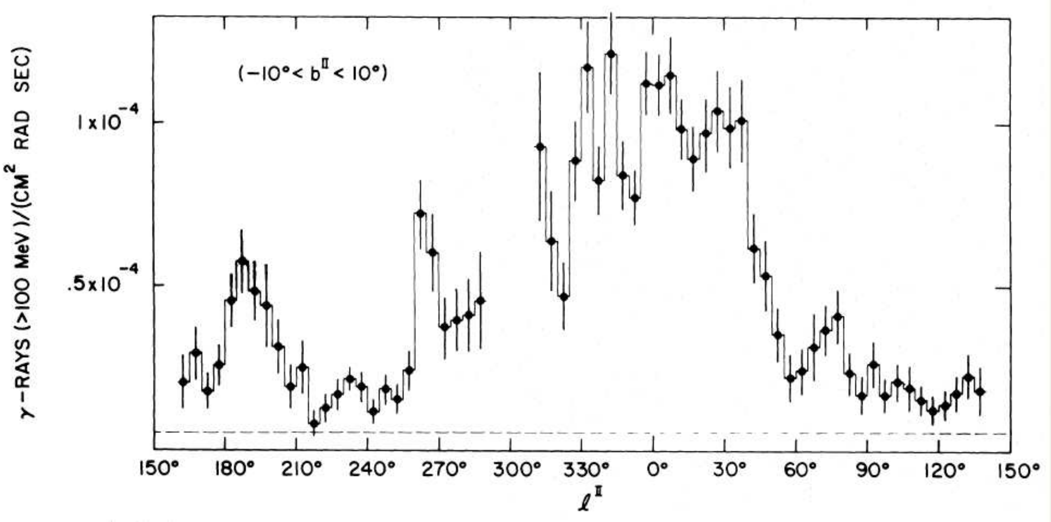

Figure 1.1: Distribution of high-energy (E>100 MeV) γ-rays along the Galactic Plane observed by SAS-2. The SAS-2 data are summed from b=-10° to b=-10°. The diffuse background level is shown by a dashed line. From (Fichtel et al., 1975)

The first was devoted to the science of the transient γ-ray sources, while the second was devoted to the highest energy ever observed from the space, reaching the upper limit of E∼30 GeV. A map of the γ-ray emission above 100 MeV obtained by EGRET is shown in Fig. 1.2.
On April 23, 2007 it has been launched the AGILE mission by the Indian PSLV-C8 rocket from the Satish Dhawan Space Center SHAR, Sriharikota. AGILE (Astrorivelatore Gamma ad Immagini LEggero) is a completely italian γ-ray small satellite that uses new technology and have sensitivity compared to EGRET. AGILE carries a γ-ray pair conversion telescope sensitive form 30 MeV up to 50 GeV and a hard X-ray detector in the range 15-60 keV (Tavani et al., 2006). AGILE can be considered the forerunner of GLAST. The upper part of the γ-ray spectrum is presently investigated from the ground by looking at the electromagnetic showers created when a high-energy γ-ray enters the atmosphere. The main radiation-matter interaction process at these energies is pair production: when a high-energy γ-ray (E>100GeV) enter the atmosphere it produces a pair formed by an electron and a positron, that propagate and initiate an electromagnetic cascade.
The *Extensive Air Shower Detectors* (EASDs) are large arrays that detect the secondary particles created when the γ-rays enter the atmosphere and produce an electron-positron pair and then initiate an electromagnetic shower. Examples of EASDs are CYGNUS, CASA or MILAGRO.
The *Air Čerenkov Telescopes* (ACTs) detect the *Čerenkov* radiation produced by the secondary particles when they cross the atmosphere. Examples of ACTs are MAGIC, VERITAS, HESS or CANGAROO. Recently the strategy is moving toward the use of more telescopes arranged in arrays, working in *stereoscopic mode*, in order to improve imaging capability and background rejection. The *High Energy Stereoscopic System* (HESS), located in Namibia, is already using this strategy, with an array of four Cherenkov telescopes, as well as CANGAROO and VERITAS, while MAGIC collab-

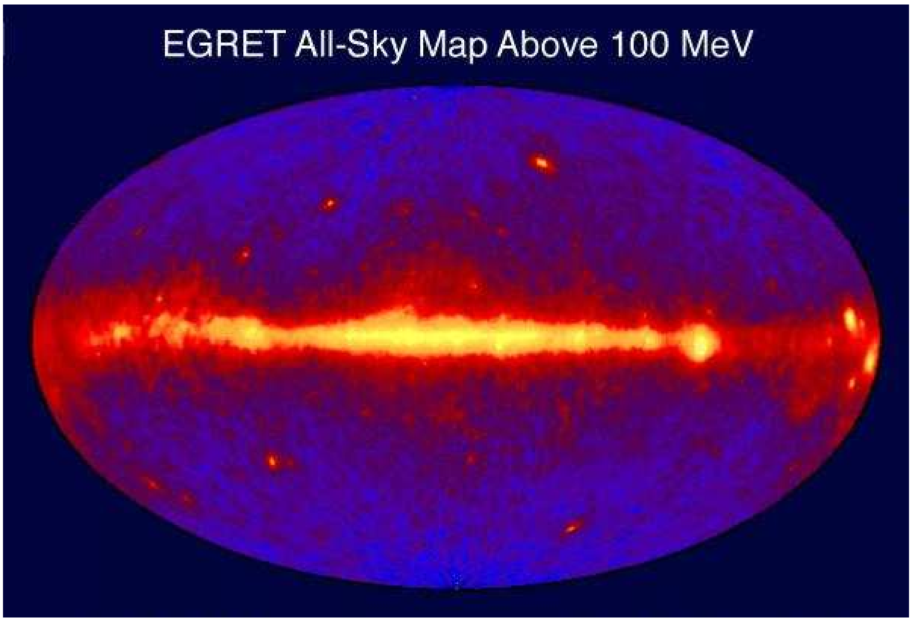

Figure 1.2: Distribution of γ-ray photons above 100 MeV obtained by the EGRET telescope aboard the NASA *Compton Gamma Ray Observatory*.

oration is building MAGIC II, a copy of the first MAGIC telescope that will work in stereoscopic mode.

1.2 Gamma rays from the sky

The GLAST mission has been designed to make fundamental observations of the γ-ray sky. The main GLAST instrument is the *Large Area Telescope* (LAT), a pair conversion telescope with the same detection philosophy of EGRET but based on new generation detectors. LAT will have a higher sensitivity and resolution with respect to its predecessor EGRET. A more detailed description of the LAT and of EGRET will be presented in Chap. 2.
GLAST will carry also the *GLAST Burst Monitor* (GBM), designed mainly for the study of the Gamma Ray Bursts. The GBM is based on scintillator detectors with the same concept of BATSE and will guarantee a total coverage of the whole visible sky. The GBM energy range (10 keV<E<25 MeV) is wider that BATSE energy range in order to have an overlap with the LAT energy range.
The energy interval covered by GLAST will be wider than the EGRET energy range, offering the opportunity to explore the spectral window above 10 GeV and below 100 GeV, that is today still unknown.
The current knowledge of γ-ray sources in the GLAST energy range comes mainly from the experience of the CGRO experiments. The sources of cosmic γ-rays can be divided into galactic sources and extragalactic sources, with a significant contribution due to diffuse Galactic emission.
Galactic γ-ray sources are mainly compact objects, such as neutron stars or accreting black holes(Schoenfelder, 2001). *Supernova remnants* (SNRs) are astrophysical objects

which may contain the secret of cosmic ray acceleration. Structures like shells that interact with the Interstellar Medium (ISM) have been observed with the high resolution telescopes in X-ray wavelengths, and this site have been associated with shocks.
The main sources of extragalactic radiation are the *Active Galactic Nuclei* (AGN), and in particular *blazars*, a particular class of AGN whose jet is aligned with the line of sight. In the extragalactic universe also transient sources, like *Gamma Ray Bursts* (GRBs) are shining flashes of radiation.
The diffuse Galactic component is thought to be related to the interaction of photons with cosmic rays, while the extragalactic component probably results from the contribution of thousands of unresolved point sources. Part of the extragalactic diffuse component could, however, be related with the decay of exotic particles in the primordial Universe.

1.3 Active Galactic Nuclei and blazars

In the Universe there are billions of galaxies, which differ basically from their morphology in the Hubble diagram. In galaxies like the Milky Way the total luminosity is given by the contribution of all the stars in the galaxy (for Milky Way L$\sim 10^{11}L_{\odot}$).
In the 40s, the American astronomer C. Seyfert discovered a new class of galaxies, with star-like nuclei and with broad emission lines, equivalent to motion of 10^3-10^4 km s^{-1}. These objects are now called *Seyfert galaxies.* Later it became clear that Seyfert galaxies, together with some other extragalactic sources such as *Quasars* and *BL Lac objects* (blazars) form a general class of *Active Galactic Nuclei* (AGNs) (Schoenfelder, 2001; Krolik, 1999). The bolometric luminosity of these objects is extremely high (L$\sim 2\times10^{46} erg/s$) which corresponds to more than about 20 galaxies like our Milky Way in an emitting radius of about 100 pc. The first observation at high energy came from COS-B, which observed the brightest quasar, $3C273$ (Swanenburg et al., 1978).
EGRET detected high energy radiation from *blazars* (Lin et al., 1992), very powerful objects characterized by non thermal emission at gamma-rays and a broad multiwavelength emission that extend from radio to TeV gamma-rays.
According to current models, blazars are a class of AGN where the collimated jet is pointing toward the observer. The radiation is boosted by the bulk Lorentz Factor and photons have been observed up to the TeV energies. blazars are also characterized by high degree of polarization, and by variability up to a factor of 100% on the order of a day. The emission above 100 MeV is a significant fraction of the total luminosity, and in flaring state the gamma-ray luminosity can exceed the luminosity in all other bands by a factor of ~ 10 or more.
The Spectral Energy Distribution (SED) show two prominent component: a lower-energy component peaking between radio and X-rays and a high-energy component peaking in γ-rays. In the Fig. 1.3 the SED of the blazar 3C279 contains also the EGRET observation (Hartman et al., 1992).

According to the current *Unified Model* of AGNs, the engine that power the AGN emission is a supermassive black hole (M$\sim 10^8 M_{\odot}$) surrounded by an accretion disk that extends up to about 100 A.U. from the central black hole (see Fig. 1.4)(Padovani, 1997). The sizes of the accretion disk can be also inferred from causality argument by

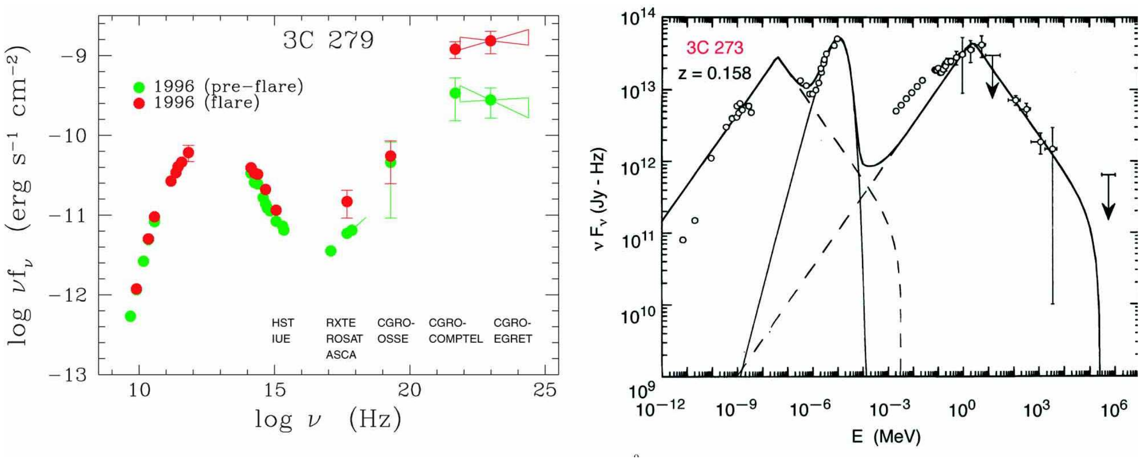

Figure 1.3: Spectral Energy Distribution of the quasar 3C279 (left) and 3C273 (right) (Digel & Myers, 2001)

observing the typical variability timescale Δt of an AGN:

$$R < \frac{c\Delta t}{1+z} \tag{1.1}$$

where z is the redshift of the source. Assuming a Δt of about 1 day, and a redshift $z \simeq 0.1$ this lead to an estimate of R$\simeq 10^{10}$km, about 100 A.U. The accretion is also connected to the presence of large jets where particles are accelerated up to high energies. According to this model at greater distance from the center there is a torus of matter extending from about 1.5 pc to 30 pc.

Between the accretion disk and the torus there should be some fast-moving clouds (v>2000 km/s), that are illuminated by the central engine and originate the emission lines observed in the AGNs spectra, that are widened because of Doppler effect (*Broad Line Regions*) due to their motion around the central black hole.

At greater distance from the black hole this model include some slow moving clouds that emit emission lines with narrower widening due to lower speed (v<2000 km/s). These clouds are the origin of the narrower emission lines (*Narrow Line Regions*) observed in some class of AGN, e.g. the Seyfert of type I.

According to this model the difference between various classes of AGNs is due to the different angle under the AGN is seen, as shown in Fig. 1.4. The current models for the γ-ray emission in blazars are divided in two main classes, the *leptonic models* and the *hadronic models*.

According to the leptonic models the γ-ray emission is created from the interaction of the accelerated electrons and positrons with the environmental soft photons. The origin of these photons depends upon the adopted scenario. Within the *Synchrotron Self Compton* (SSC) scenario the photons are emitted by the same electrons and positrons via synchrotron radiation (Maraschi et al., 1992). In the *External Compton Scattering* (ECS) photons originate in the thermal emission of the accretion disk and are injected into the jet (Dermer et al., 1992).

According to the hadronic models the γ-rays are produced as a consequence of the presence of accelerated protons, that do not radiate synchrotron and can be accelerated up

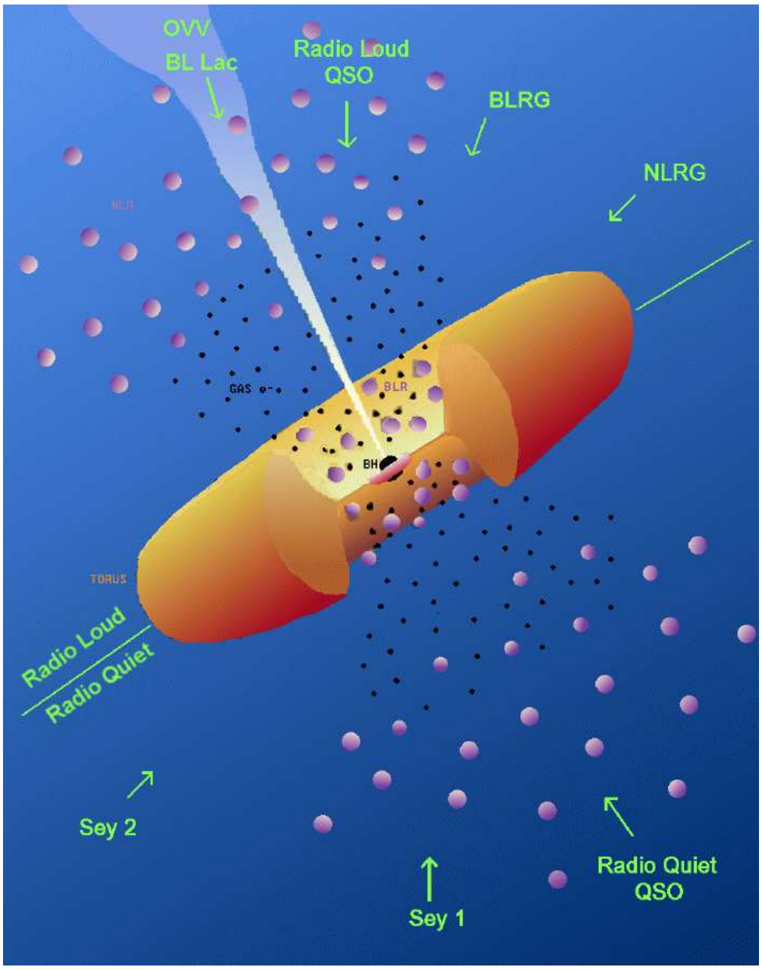

Figure 1.4: Scheme of the Unified Model for AGNs. Detailed explanation can be found in the text.(NASA Archive). The observational difference between classes of AGN is due to a geometric effect.

to E=10^{20} eV. At these extremely high energies processes of photoproduction of pions and electron-positron pairs become possible. The pions can decay into γ-rays and leptons can cool via Inverse Compton and produce γ-rays (Mannheim & Biermann, 1992). A realistic scenario contain both sets of processes and GLAST will help to determine which contribution dominates in each type of source, e.g. by observing the γ-ray emission during flares. Blazar AGNs now compose the largest fraction of identified gamma-ray sources in the EGRET range, with 66 high-confidence and 27 lower confidence identifications according to the criteria adopted using the maximum of likelihood method in the Third EGRET Catalog (Hartman et al., 1999).
Directly comparing the point source sensitivity reached by EGRET in one year of observation for high latitude sources ($|b| > 30$), with that estimated for GLAST, and extrapolating the *LogN-LogS* distribution for blazars shows that the discovery space is enormous (Fig.1.5 shows the *logN-LogS* distribution from (Stecker & Salamon, 1996b,a)). GLAST will increase the number of known AGN gamma-ray sources from about one hundred to many thousands. Moreover, it will effectively be an all-sky monitor for AGN

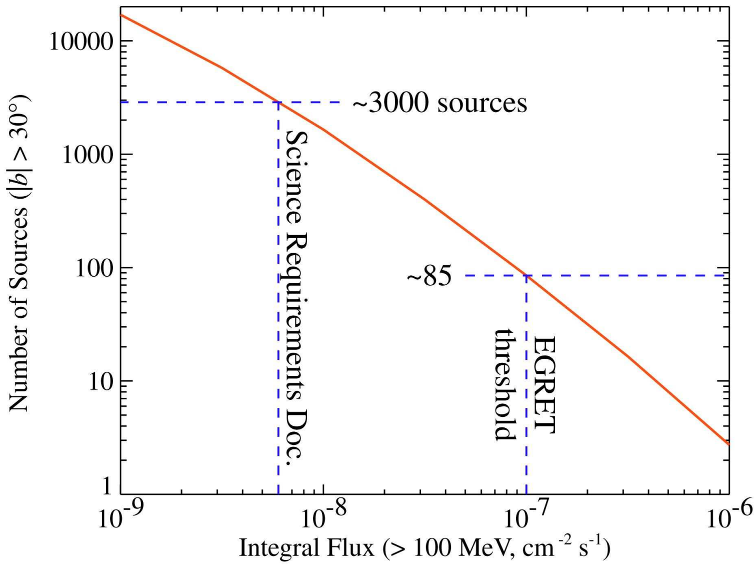

Figure 1.5: Predicted number of observed high latitude Blazars in one year of observation. The comparison is between the EGRET point source sensitivity for sources at high latitude, and the estimated one for GLAST. The *LogN-LogS* distribution is from (Stecker & Salamon, 1996b,a).

flares, scanning the full sky every about three hours. It will greatly decrease the minimum time scale for detection of variability at high energies, and will offer near real-time alerts for spacecraft and ground-based observatories operating at other wavelengths. Using EGRET, AGN flares were measured to vary on the shortest time scales - eight hours - that were able to be determined with statistical significance.
According current models the high energy emission would take place in the inner region of the central engine, then the time resolution of GLAST will permit to study the γ-ray variability of the inner core of the blazars and to probe reaching regions much inner than it can be done using optical or radio observations.
Observation of blazars at high distances will be very important to study the energy range where most of blazar are expected to cutoff. This cutoff could be due either to intrinsic absorption of to interaction with blazar γ-rays to the extragalactic infrared-UV background light (see below). If this is the case, which can be established by regular monitoring blazar spectra and variability to deduce a nonvarying adsorber, the cutoff should vary inversely with redshif in a predictable way (Digel & Myers, 2001).

1.4 Gamma-ray Pulsars

From observations made with gamma ray satellites up to EGRET era, seven high confidence gamma-ray pulsars are known.
Since γ-ray pulsar emission modeling and study of the GLAST capability for pulsar is the main topic of this thesis, a much detailed description about γ-ray pulsars will be presented in Chap. 4.
The discovery and study of new pulsars is one of the main goals for GLAST. The num-

ber of expected number of newly discovered pulsars varies depending on the model, and ranges from some tens up to some hundreds.
The good timing accuracy of the LAT instrument will allow the possibility to study in greater detail the structure of the pulsar lightcurve and to investigate the microstructure, that could reveal some important aspects of the magnetospheric phenomena.
The energy resolution and energy range of the LAT will provide useful data about the high energy cutoff expected in pulsar γ-ray emission. No pulsed TeV component has been observed at the moment then a high energy cut-off is expected at GeV energies. This will provide definitive spectral measurements that will distinguish between the two primary models proposed to explain particle acceleration and gamma-ray generation: the *Outer Gap* models and *Polar Cap* models (Nel & De Jager, 1995).
In some cases the spectral cutoff is steeper than a pure exponential, which is consistent with the magnetic pair production above the polar cap region. On the other hand, there is not enough statistical significance in the EGRET data for comparing the different emission at high energies predicted by the two models (see Fig. 1.6). GLAST will produce the statistics to distinguish between these.
Moreover the high effective area provided by GLAST will permit *blind searches* for Geminga-like pulsars that does not have a radio counterpart, and this is expected to be very exciting field of research for GLAST. High-energy γ-rays have been also observed

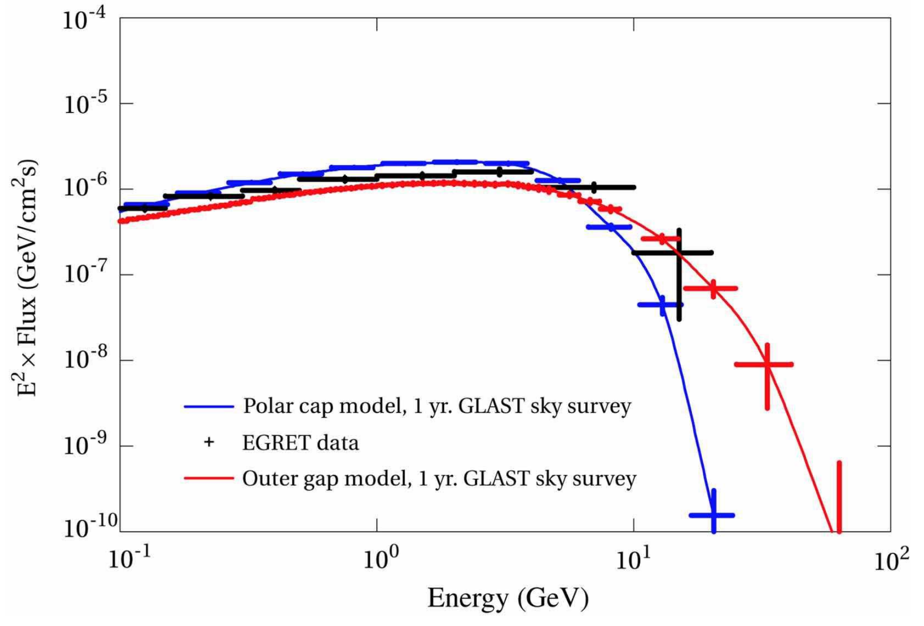

Figure 1.6: Comparison between the two emission models developed for explain the γ-ray emission from pulsars. The error boxes of EGRET do not allow the discrimination between the Polar Cap Model and the Outer Gap Model, while simulations show the GLAST will be the potentiality of distinguish the two models(Digel & Myers, 2001).

from Pulsar Wind Nebulae (PWNe), in particular from the one around the Crab pulsar, Vela pulsar and PSR B1706-44, all of them detected at TeV energies.
In particular EGRET detected the Crab nebula (Nolan et al., 1993; De Jager et al., 1996) as an unpulsed component up to 10-20 GeV and this was the only PWN detected

by EGRET. The spectrum show a synchrotron component with cutoff at around 100 MeV and an Inverse Compton emission above 100 MeV.
PWNe are expected to be also target for GLAST. According to the current models, lower energy emission in γ-rays is due mainly to synchrotron emission from leptons from the pulsar relativistic wind, and the higher energy emission is due to Inverse Compton scattering produced by leptons and lower energy synchrotron photons, Cosmic Microwave Background or infrared photons coming from the pulsar. Leptons are accelerated as a results from interaction between the pulsar wind with the nebula. More recently a more detailed modeling of the observed high-energy emission from the Crab Nebula has been presented (De Jager & Harding, 1992).
It is also possible that γ-rays can be produced by interaction of hadrons in the pulsar wind with the matter can contribute to the observed spectrum, in particular for youger nebulae. From models some other PWN should be detectable by GLAST, in particular the nebula CTB 80, which contain two pulsars: PSR J0205+6449 and the γ-ray pulsar PSR B1951+32 (Bednarek & Bartosik, 2004).

1.5 Supernova Remnants and Interstellar Medium: the physics of Cosmic Rays

Supernova remnants (SNRs) are important not only because they are connected to the study of the late stages of stellar evolution and nucleosynthesis, but also because of their interaction with the surrounding space, that is contaminated and energized by the products of the supernova explosion.
The importance of SNRs in astroparticle physics is related to the origin of the cosmic rays. Cosmic Rays (CR) are relativistic cosmic particles from space and have been extensively studied since early in the $20th$ century. Even so, the question of the origin of cosmic rays nuclei remains only partially answered, with widely accepted theoretical expectations but incomplete observational confirmation.
Theoretical models and indirect observations support the idea that CR are produced in the Galaxy by SNRs. The main mechanism which is believed to be at the base of the CR production is the shock acceleration, taking place when the Supernovae shell shocks with the Interstellar Medium (ISM). The shock mechanism is an efficient particle accelerator up to TeV energies and in the case of SNe on time scales of $10^3 - 10^4$ years. The accelerated CR escape from the SNR and remain trapped in the Galactic magnetic field. Observing charged particles there is no possibility to directly observe the sites of their production because of deviation caused by the large scale chaotic structure of the ambient magnetic fields. CRs interact with the interstellar gas and dust and photons, producing gammas (for examples, via *Bremsstrahlung*, or π^0 decay, or via Compton Scattering). Photons are not deviated by the Galactic magnetic fields and a direct observation of the accelerator sites is then possible, in a similar way of operation of the future neutrino telescopes. GLAST will spatially resolve remnants and precisely measure their spectra, and may determine whether Supernova Remnants are sources of cosmic-ray nuclei. The high resolution radio catalog at 1.4 GHz will be the trace route for detailed searches for Supernovae Remnants (Fig. 1.8).
GLAST will also be able to detect the diffuse emission from a number of Local Group

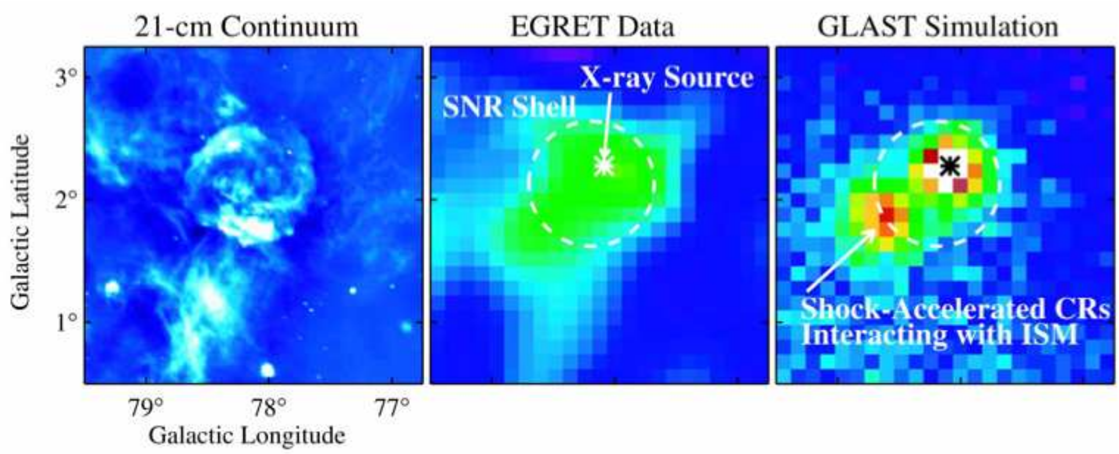

Figure 1.7: Radio continuum emission of the Gamma Cygni SNR at 1.4 GHz from the (Canadian Galactic Plane Survey), compared with EGRET observed and GLAST simulated images at energies > 1 GeV. The dashed circles indicate the location of the shell of the SNR (Higgs et al., 1977). Point X-ray source suspected to be a gamma-ray pulsar (Brazier et al., 1996) is shown as an asterisk. In the GLAST model of data from a 1-year sky survey, the EGRET flux has been partitioned between the pulsar and a region at the perimeter of the shell where the CRs are interacting with an ambient interstellar cloud.

galaxies, e.g. the LMC, and to map the emission within the largest of these for the first time.
The GLAST angular resolution will permit to resolve the SNR structure and the study the different acceleration sites. Moreover the high energy resolution will be decisive in studying and measuring the various spectral components, trying to highlighting leptonic or baryonic contributions.

1.6 The Galactic Center

A very interesting case of gamma-ray observation is the center of our own Galaxy, located about 8.5 kpc far from the Sun. A strong excess of emission was observed by EGRET in the Galactic Center (GC) region (Mayer-Hasselwander et al., 1998), peaking at energies greater than about 500 MeV. The close coincidence of this excess with the GC (within an error box of 0.2°) and the fact that it is the strongest emission maximum within 15° from the GC was taken as evidence for the source's location in the GC region. The emission intensity, observed over 5 years, did not provide evidence of time variability. The angular dependence of the excess appeared only marginally compatible with the signature expected for a single compact object, and it was more likely associated with the contribution of many compact objects with diffuse interactions within 85 pc from the center of the Galaxy. Finally, the spatial distribution of the emission did not correlate with the detailed CO-line surveys. The observed spectrum was peculiar and different from the large scale galactic gamma-ray emission. Recently HESS detected very high energy emission from the Galactic center (Aharonian et al., 2004). They as-

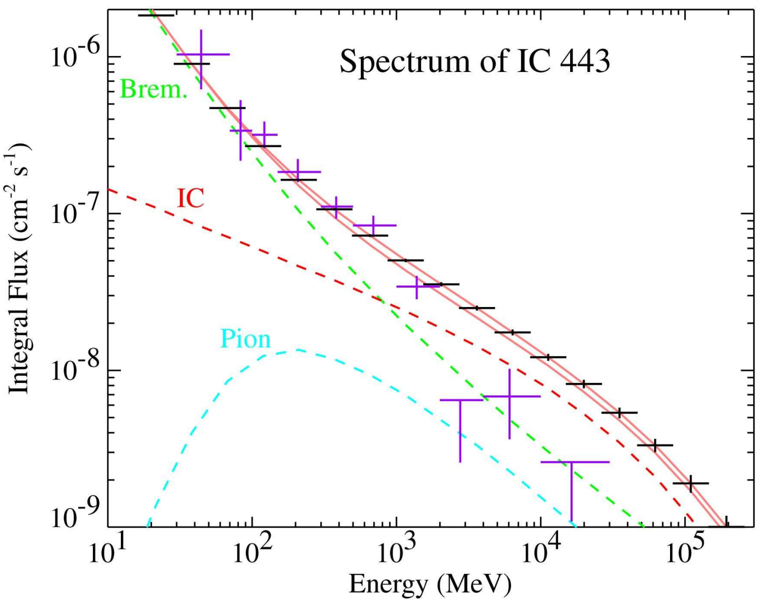

Figure 1.8: Model gamma-ray spectrum for SNR IC 443 illustrating how GLAST can detect even a faint π^0-decay component. The components of the total intensity (upper red curve) are p0-decay, inverse-Compton scattering, and electron bremsstrahlung. The lower red curve is the total intensity without π^0-decay emission. The EGRET data for the source coincident with IC 443 (2EG J0618+2234) are indicated in purple and simulated measurements from a 1-year sky survey with GLAST are plotted in black, with 1-s error bars From (Digel & Myers, 2001).

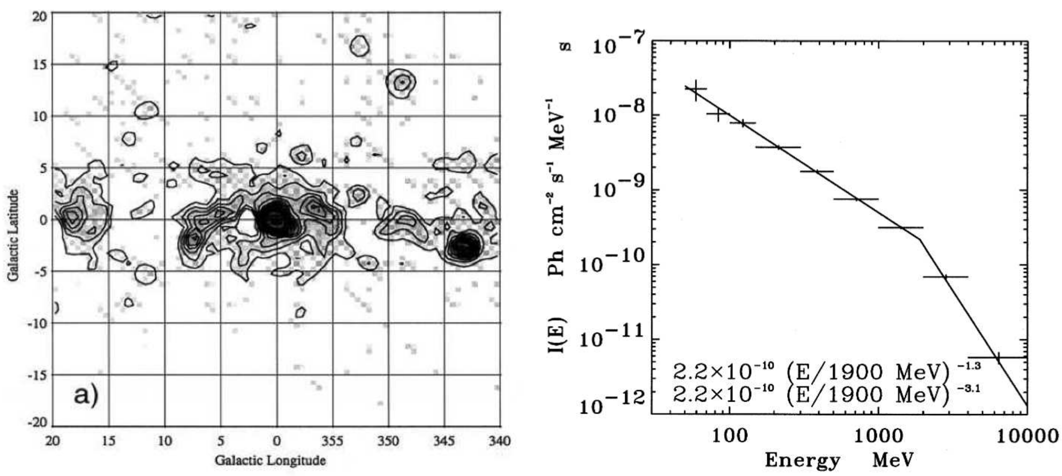

Figure 1.9: High energy emission from the Galactic Center as observed by EGRET. The scale is of 100 pc. Left contour map for energy $> 1GeV$. Right observed differential spectrum (from (Mayer-Hasselwander et al., 1998)).

sociate the excess to a source, coincident within $1'$ of $SgrA*$.
For explaining the excess in the GC different scenarios has been proposed.
An possible candidate for the proton accelerator could be the young (10^4 yr) and un-

usually powerful (total explosion energy $\simeq 4 \times 10^{52}$ erg) supernova remnant Sgr A East (Maeda et al., 2002).
Alternatively, scenarios which the neutralino annihilation is responsible of the excess have also been tested, but no "smoking-gun" was found. Of particular interest for GLAST, the HESS team cannot support the hypothesis that the excess observed by EGRET is the result of a continuum emission resulting from the supersymmetric particle annihilation. In particular, they conclude that, assuming that the observed γ-ray present a continuum annihilation spectrum, the lower limit of 4 TeV on the cut-off implies $M_\chi > 12$ TeV. Above such energy, from particle physics and cosmology arguments (Ellis et al., 2003a,b), the M_χ is disfavored. The possible annihilation channel of supersymmetric particles cannot anyway be excluded. Nevertheless the discovery space for direct evidence of dark matter annihilation is naturally reduced below the HESS energy threshold (~ 100 GeV), falling in the GLAST energy range.

1.7 Gamma Ray Bursts

Gamma Ray Bursts (GRBs) are the most powerful sources of γ-rays. The brightest GRB at GeV energy is 10^4 times brighter than the brightest AGN. GRBs are intense flashes of gamma-ray, lasting from some ms up to hundreds of seconds. They are believed to be the result of a violent explosion in remote galaxies, caused by the collapse of a massive star or by a merging of two compact objects (Schoenfelder, 2001).
GLAST will continue the recent revolution of GRBs understanding by measuring spectra from keV to GeV energies and by tracking afterglows. In this sense the overlap between the GBM and the LAT is very important, as shown also in Fig. 1.10. With its high-energy response and very short dead time, GLAST will offer unique capabilities for the high-energy study of bursts that will not be superseded by any planned mission. GLAST will make definitive measurements of the high-energy behavior of GRBs, a goal that EGRET cannot have pursued. The spectral variation with time is an open question, as well as the spectral shape above 30 MeV.
Time-resolved spectral measurements with GLAST, combining data from LAT and GBM, will permit determination of the minimum Lorentz factors for the acceleration of particles, and the possibility of a Inverse Compton Scattering emission at high energies. Of particular interest for Cosmology is the determination of the distances using the GRB as standard candles (Ghirlanda et al., 2004; Barbiellini et al., 2004). Another interesting use of GRBs as standard candles at cosmological distances has been suggested by (Amelino-Camelia et al., 1998), which suggest that the fine-scale time structure and hard spectra of GRB emissions are very sensitive to the possible dispersion of electromagnetic waves in vacuum with velocity differences $\delta v \sim E/E_{QG}$, as suggested in some approaches to Quantum Gravity. Measurements of the delay between the arrival time of high energy photons and low energy photons might be sensitive to a dispersion scale E_{QG} comparable to the Planck energy scale $E_P \sim 10^{19}$ GeV, sufficient to test some of these theories.
Thanks to the possibility of simultaneous observations of high-energy photons and low-energy photons together with the LAT very short dead time (t$\sim$ $100\mu s$), GLAST is certainly the most suitable observatory for these studies (see, for reference, (Omodei et al., 2004)).

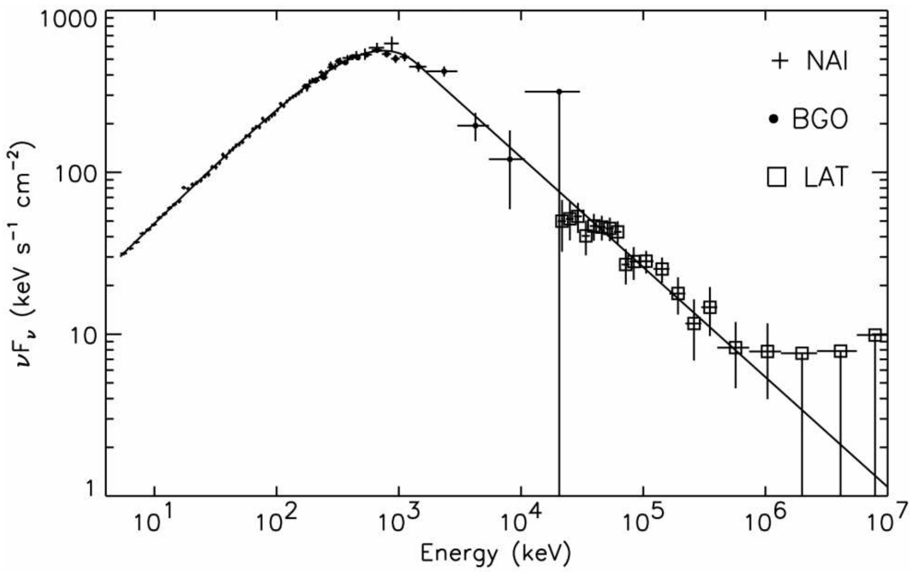

Figure 1.10: Simulation of a GRB joint observation with LAT and GBM. The spectral coverage is of 6 orders of magnitude.

The LAT and the GBM will detect more than 200 bursts per year and provide near-realtime location information to other observatories for afterglow searches. GLAST will have the capability to slew autonomously toward GRBs to monitor for delayed emission with the LAT.
The trigger will be given by the GBM that has a coverage of the whole sky or by the LAT itself, that has been provided with some onboard triggers for GRBs. Altough they are known from about 30 years, GRBs still remain quite mysterious and the new data provided by GLAST at high energies will contribute to understand the nature of the GRBs.

1.8 Solar flares

The Sun has been known to produce γ-rays with energies greater than several MeV during its flaring period. Accelerated charged particles interact with the ambient solar atmosphere, radiating via *Bremsstrahlung* high energy γ-rays (see, e.g.,(Ramaty & Murphy, 1987; Murphy et al., 1987)). Secondary $\pi^{\pm}$ are produced by nuclear interaction and yield to γ-rays with a spectrum that extends to the energies of the primary particles.
Proton and heavy ion interactions also produce gamma rays through π^0 decay, resulting in a spectrum that has a maximum at 68 MeV and is distinctly different from the *Bremsstrahlung* spectrum.
The processes that accelerate the primary particles are not well known, but stochastic acceleration through MagnetoHydroDynamics (MHD) turbulence or shocks ((Forman et al., 1986; Ryan & Lee, 1991)) are though to be the most credible mechanisms. Particle are accelerated in large magnetic loops that are energized by flares, and they get trapped due to magnetic filed, generating gamma rays ((Mandzhavidze & Ramaty, 1992b,a)).

Fig. 1.11 shows the extraordinary flare of June 11, 1991 detected by the EGRET telescope. The contribution from electron bremsstrahlung and from pion decay are separately shown. GLAST will have unique high-energy capability for study of solar flares.

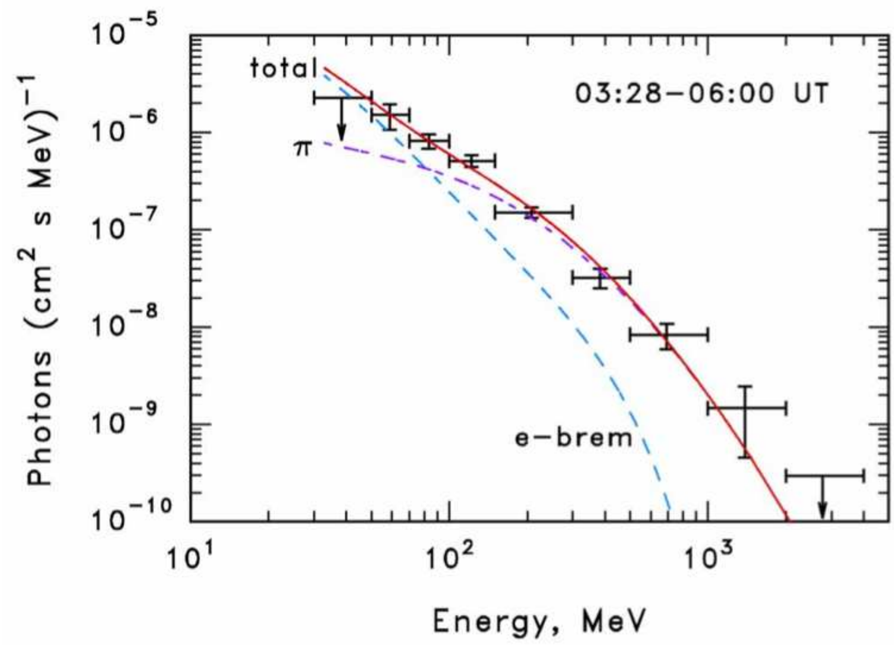

Figure 1.11: The extraordinary flare of June 11, 1991 detected by the EGRET telescope, which produces gamma rays up to GeV energies. The contribution from electron bremsstrahlung and from pion decay are displayed separately.From (Digel & Myers, 2001).

EGRET discovered that the Sun is a source of GeV gamma rays. GLAST will be able to determine where the acceleration takes place, and whether protons are accelerated along with the electrons. The large effective area and small dead time of GLAST will enable the required detailed studies of spectral evolution and localization of flares. Some models are proposed for production of γ-rays from the Sun also in quiescent state, e.g. from nuclear gamma decay of nuclei like the ^{58}Co or from *microflares* already observed in UV and X-rays, but never seen in γ-rays. GLAST will be the only mission observing high-energy photons from solar flares during Cycle 24 and possibly could also study the solar activity far from the flares.

1.9 Gamma-ray background and Extragalactic Background Light

An apparently isotropic, presumably extragalactic, component of the diffuse gamma-ray flux above 30 MeV was discovered by the SAS-2 satellite and confirmed with EGRET. The low sensitivity and the poor angular resolution of EGRET did not allow a identification of this light as the contribution of many point sources.
The hypothesis on the origin of the extragalactic gamma-ray background emission are

various, from the most conservative, such as the summed contribution of thousands of AGN, to more exotic, such as the contribution of the annihilation from exciting particles which came from some unknown process that took place in the primordial Universe, or from some particles deriving from the extension of the standard model to supersymmetric particles (SUSY), which can contribute substantially to the Dark Matter content of the Universe and that can be found in the Galactic halos. The extragalactic gamma-ray background is a spectrum well described by a power law with index 2.1 ± 0.3 over EGRET energies and it is consistent with the average index for blazars that EGRET detected, which lends some support to the hypothesis that the isotropic flux is from unresolved AGN sources (Sreekumar et al., 1998). The improved angular resolution of GLAST will allow the separation and the identification of possible point-like sources to the extragalactiva gamma-ray background.
The sensitivity of GLAST at high energies will also permit the study of the extragalactic background light by measurement of the attenuation of AGN spectra at high energies. This cutoff could be due either to intrinsic absorption or to interactions of blazar γ-rayswith photons of the *Extragalactic Background Light* (EBL) from infrared to UV (Digel & Myers, 2001).
Owing to the large size of the AGN catalog that GLAST will amass, intrinsic spectra of AGNs will be distinguishable from the effects of attenuation. The measured attenuation as a function of AGN redshift will relate directly to the star formation history of the universe.

1.10 New Particle Physics

Thanks to its large effective area the flux limit of GLAST at high galactic latitudes is ~ 30 or more lower than EGRET's. As discussed in previous section about AGNs, whereas EGRET identified about 70 AGNs, GLAST should see thousands of them, resolving a big component of the extragalactic diffuse emission.
Any remaining diffuse emission would be of great interest. It is thought that diffuse extragalactic γ-ray emission could originate from the decay of exotic particles in the primordial universe. The energy spectrum of this component should be different from the AGN contributions.
The left panel of figure 1.12 shows the diffuse contribution of the relics particles, and the measured fluxes for EGRET and GLAST. The large effective area of GLAST, especially at high energies, may allow a statistically significant detection of this spectral difference. This improvement is expected mainly thanks to the much larger energy range and sensitivity of GLAST as compared to EGRET, as well as the ability of GLAST to resolve contributions of point sources to the extragalactic background.
A different contribution is the possible decay of supersymmetric particles. Assuming the existence of the dark matter in the halo of our Galaxy, hypothesis also sustained by the comparison between the rotational curves of the galaxies and the baryonic visible matter, GLAST would be capable to detect the gamma-rays as result from its annihilation.
The lightest supersymmetric particle (LSP) is the *neutralino* (χ) and it is perhaps the most promising candidate for the non barionic Dark Matter in the Universe (Weinberg, 1983; Goldberg, 1983). It is neutral (hence the name neutralino) and stable if R parity

is not violated. Supersymmetry seems to be a necessity in superstring theory (and M-theory) which potentially unifies all the fundamental forces of nature, including gravity. If the scale of supersymmetry breaking is related to that of electroweak breaking, then this density Ω_χ may be the right order of magnitude to explain the nonbaryonic dark matter. Although the highest-energy accelerators have begun to probe regions of SUSY parameter space, the limits set at this time are not very restrictive. The mass of the

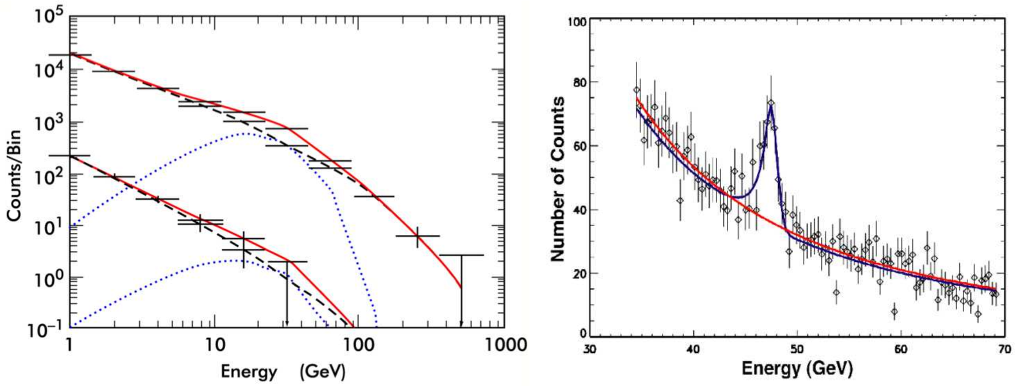

Figure 1.12: Signatures of new particles physics. Left: contribution of the background from the annihilation of relic particles. The plot shows the fluxes for GLAST (upper points) and for EGRET (lower points) in two years of observation. The dashed lines are the contribution from an AGN while the dotted line are the contributions of the particle relic. The large effective area of GLAST will allow to disentangle the two contributions. Right: The signature of a galactic neutralino annihilation into $\gamma\gamma$, in two years of scanning mode observations. The width of the peak is the results of a finite energy resolution.From (Digel & Myers, 2001).

neutralino particle can be constrained, in order to make up the overall Dark Matter in the universe. The required mass is in the range $30GeV < M_\chi < 10TeV$, depending on the model chosen. If neutralinos make up the dark matter of the Milky Way, they have nonrelativistic velocities. Hence, the neutralino annihilation into the $\gamma\gamma$ and γZ final states would give rise to gamma rays with unique energies, that is, gamma-ray lines with:

$$\begin{aligned} E_\gamma &= M_\chi \qquad\qquad or, \\ E_\gamma &= M_\chi(1 - (m_Z/4M2)), \end{aligned} \tag{1.2}$$

depending on the preferred channel. Also an hadronic channel of decay in quarks have been proposed (Digel & Myers, 2001). The signature would be spatially diffuse, narrow line emission peaked toward the Galactic center. Figure 1.12 shows the predicted signal from neutralino annihilation into $\gamma\gamma$, with an assumed mass of $\sim$ 47 GeV:

1.11 Unidentified Sources

More than 60% of the sources observed by EGRET (Hartman et al., 1999) have no counterparts at other wavelengths or there are many couterparts within the EGRET

error boxes so that an unambiguous identification is not possible. The difficulties in the identification is both related to the nature of these sources and due to the experimental limits of the EGRET telescope. Anyway some characteristic of the potential source can be summarized.
These sources should have an high value of the ratio L_γ/L_λ, where L_γ is the luminosity of the source in γ-rays and L_λ is the luminosity of the source at lower energies. This makes them possible powerful accelerators of particles. Nevertheless they are also clus-

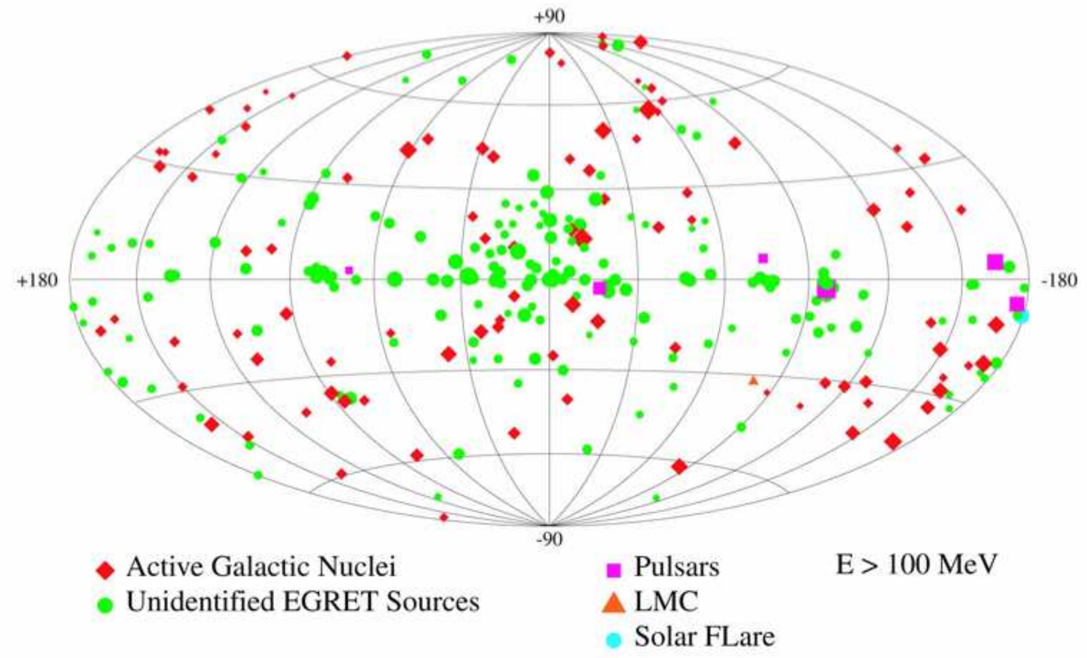

Figure 1.13: The *Third EGRET Catalog* (3EG). The sources, collected by class, are shown in galactic coordinates.From (Digel & Myers, 2001).

tered along the Galactic Plane, making their detection more difficult because of high signal to noise ratio.
Less than one third of these are extragalactic (probably blazar AGNs), with the remaining most likely within the Milky Way. Recent work suggests that many of these unidentified sources are associated with the nearby Gould Belt of star-forming regions that surrounds the solar neighborhood (Gehrels et al., 2000), while apparently-steady sources are likely to be radio-quiet pulsars (Harding et al., 2004a).
The poor angular resolution of the EGRET detector ($\sim 5.8°$) and its relatively small effective area, which can be converted in poor sensitivity to faint sources, represent the main reason of the unidentification of these sources.(see also: (Oezel & Thompson, 1996; Grenier, 2002, 2003))
GLAST will be the first telescope with an appropriate combination of angular resolution ($\sim 3.5°$ at 100 MeV and $\sim 0.15°$ above 10 GeV) and sensitivity to faint object, to enable the identification of the EGRET sources. GLAST will be able to directly search for periods in sources at least down to EGRET's flux limit. Transient sources within the Milky Way are poorly understood, and may represent interactions of indi-

vidual pulsars or neutron star binaries with the ambient interstellar medium. Some of the unidentified EGRET sources may be associated with recently discovered Galactic *microquasars*. Microquasars are a subclass of X-Ray Binaries (XRBs) that show a jet of

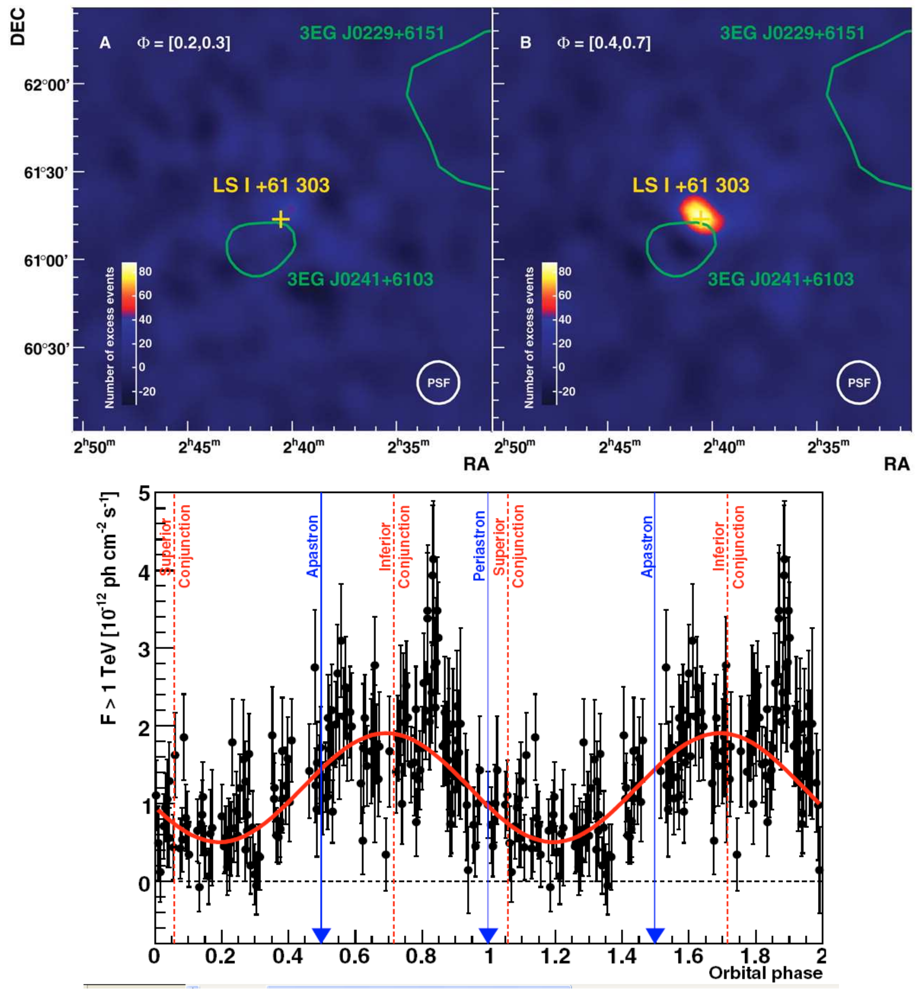

Figure 1.14: Top: The microquasar LS I +61 303 observed by MAGIC (Albert et al., 2006) in two states. Bottom: the orbital modulation of the LS 5039 microquasar observed by HESS (Aharonian et al., 2006).

mild relativistic accelerated particles. They are believed to be a binary system made up of a compact object, perhaps a neutron star or a black hole, orbiting around a massive star. The jet of particle should be the basic of γ-rays emission both in the leptonic or hadronic scenarios. The name *microquasars* have been proposed since they mimic on smaller scales the phenomenology of the quasars, then their investigation is believed to be much important for the understanding of the AGNs physics. Recently two microquasars have been observed, the LS I +61 303 by MAGIC (Albert et al., 2006) and LS 5039 by HESS (Aharonian et al., 2006), both shown in Fig. 1.14. In both cases the orbital modulation of the γ-ray flux have been observed.

1.12 GLAST and Ground-Based Telescopes

GLAST in orbit will complement the capabilities of the next-generation Air Cherenkov Telescopes (ACTs) and Extended Arrays Shower Detectors γ-ray telescopes that are planned or under construction or beginning operation such as HESS, MAGIC, CANGAROO and VERITAS, or MILAGRO, ARGO. Complementarity also with the Italian satellite AGILE recently launched is well recognized.
The ground-based telescopes detect the Cherenkov light or air-shower particles from cascading interactions of very high-energy γ-rays in the upper atmosphere. Since that high energy cosmic rays convert in the atmosphere, they have very large effective collecting areas ($> 10^8$ cm^2), but small fields of view ($\sim 1°$)[1], and limited duty cycles relative to satellites. The next-generation Cherenkov telescopes will have sensitivities extending

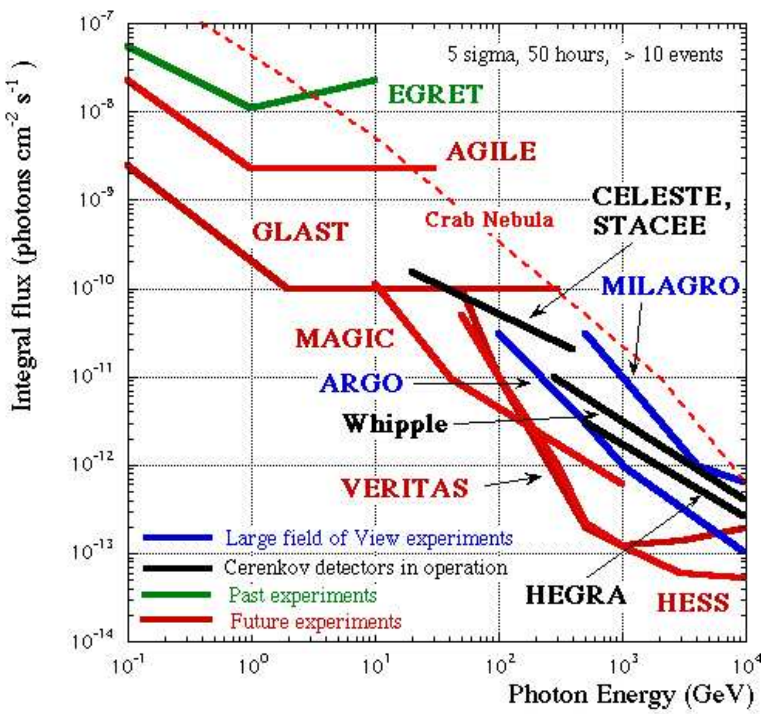

Figure 1.15: Different sensitivity curves and energy range for planned ACT and space telescopes. The sensitivity are computed considering the effective area of the various experiments and the observational time (50 hours), requiring a significance of at least 5 σ above the background level. The crab flux (dashed line) is also represented on the plot for direct comparison (Morselli, 2002a,b).

down to 50 GeV and below, as in the case of MAGIC telescope for which the threshold is supposed to reach 10 GeV, providing a broad useful range of overlap with GLAST. Figure 1.15 shows the predicted sensitivity of a number of operational and proposed ground-based Cherenkov telescopes. The sensitivity for VERITAS and other ACTs is for a 50 hour exposure on a single source. For the EGRET, GLAST, and AGILE satellites, and for MILAGRO and ARGO the computed sensitivity is for one year of all sky survey. The

[1] with the exception of MILAGRO

level of the diffuse background assumed is 2×10^{-5} $ph\ cm^{-2}\ s^{-1}\ sr^{-1}$) $(100\ MeV/E)^{1.1}$, in agreement with the background measured by EGRET at high galactic latitudes. In the figure a Crab-like flux is also shown (with power law index equal 2), requiring that the number of source photons detected is at least 5 σ above the background (Morselli, 2002a).

1.13 Summary

In this Chapter the main issues regarding γ-ray astrophysics at GLAST energies have been reviewed. The development of γ-ray astronomy have been carried mainly from space and the last mission was the CGRO observatory.
The GLAST mission will contribute in a decisive way in several topics of modern understanding of the γ-ray Universe, from the study of galactic and extragalactic cosmic accelerators to the detailed investigation on the nature of diffuse emission and transient sources.
The energy range of GLAST will guarantee the exploration of the energy range between the EGRET upper limit and the lower limit of the ground based telescopes, a spectral window that would contain a lot of new sources. GLAST will also be complementary to the ground based VHE γ-rays instruments like ACTs and EASDs, so that inter calibration is possible and a more complete multiwavelength investigation could be accomplished.

Chapter 2

The GLAST Large Area Telescope

The Gamma-ray Large Area Space Telescope (GLAST)(Gehrels & Michelson, 1999) is an international space mission devoted to the study of the γ-ray Universe. Planned for launch in autumn 2007, GLAST will bring a dramatic improvement in our understanding of the γ-ray emission processes in cosmic environments, probing the most powerful sources in the Universe.
GLAST will be launched from the NASA Kennedy Space Center with a rocket Delta II 2920-10H, the same used for launching the SWIFT mission. GLAST will be placed at 575 km of altitude in an orbit inclined by 28.5°. During its normal operations GLAST will orbit around the Earth with a period of 95 minutes and will scan the sky with a rocking angle of about 30°. Fig. 2.1 shows an artistic view of the GLAST spacecraft in orbit. GLAST will carry two main instruments, the Large Area Telescope (LAT)(Michelson, 2000) and the GLAST Burst Monitor (GBM)(Meegan, 2000).
The LAT, the main GLAST instrument, is a pair-conversion telescope based on high-

Figure 2.1: Artistic view of the GLAST satellite

precision detectors from High Energy Physics technology (Atwood & et al., 2008). The

LAT will cover an energy range from about 30 MeV up to about 300 GeV. The LAT is the successor of the EGRET telescope aboard the *Compton Gamma Ray Observatory* (CGRO), but it has much higher sensitivity and better resolution.
The GLAST Burst Monitor (GBM) is entirely devoted to the study of the transient γ-ray sources, i.e. Gamma Ray Bursts (GRBs) and Solar Flares. It is made up by two kind of detectors based on scintillating materials, which together will cover an energy window from 15 keV up to about 25 MeV. This energy range will guarantee an energy overlap with the LAT.

2.1 Before GLAST: the Compton Gamma Ray Observatory

The *Compton Gamma Ray Observatory* is the predecessor of GLAST and was launched on April 5, 1991 (Fichtel et al., 1994). It was the second NASA Great Observatory (after the *Hubble Space Telescope*) and the first entirely devoted to γ-ray astrophysics. The total weight of CGRO was more than 17 tons, the heaviest payload ever put into orbit at that time. The CGRO was put in orbit during a Space Shuttle mission and an image can be seen in Fig. 2.2.
CGRO carried onboard four experiments (Fig.2.2). The *Burst and Transient Source Experiment* (BATSE)(Fishman et al., 1989) was mainly devoted to the study of the Gamma Ray Bursts and monitored the sky at energies of 20-1000 keV. The *Oriented Scintillation Spectrometer Experiment* (OSSE)(Johnson et al., 1993) worked in an energy range of 0.05-10 MeV. The *Compton Telescope* (Comptel)(Diehl, 1988), whose detecting technique was based on Compton scattering, had an imaging capability of about 1 sr in the energy range 0.8-30 MeV. The *Energetic Gamma Ray Experiment Telescope* (EGRET) (Hartman et al., 1999) was a pair conversion telescope designed to cover an energy band between 30 MeV and about 10 GeV.

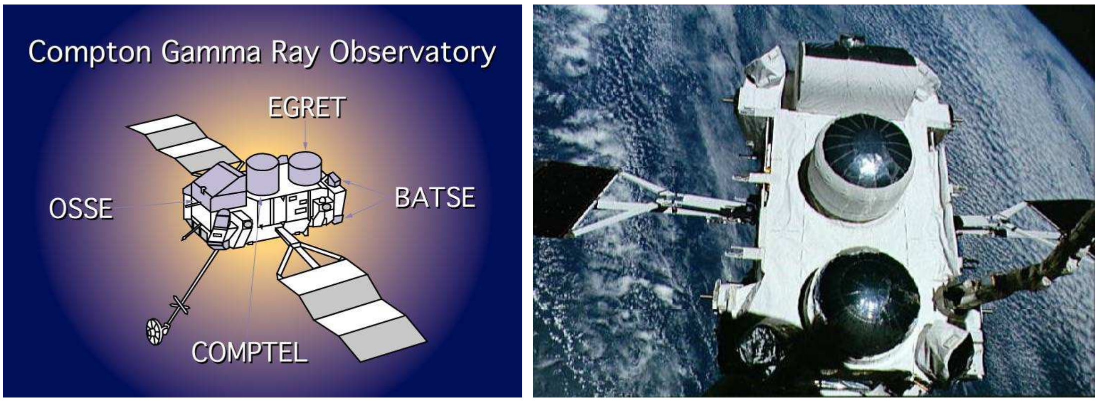

Figure 2.2: Left: Scheme of the CGRO experiments. Right: An image taken during the deployment of the CGRO. The CGRO observatory is clearly visible outside the Space Shuttle bay.

2.1.1 The EGRET telescope

The *Energetic Gamma Ray Experiment Telescope* (EGRET) was the first instrument that performed a complete sky survey in the 30 Mev - 10 GeV energy band. The dominant process of radiation-matter interaction at EGRET energies is pair production, then the EGRET detecting strategy was based on the pair production. This strategy is the same adopted for the LAT, in fact both are *pair conversion telescopes.* A scheme of EGRET is presented in Fig. 2.3. The main detectors of EGRET were a spark chamber tracker, a NaI calorimeter, a *Time Of Flight* (TOF) detector and a monolithic anticoincidence dome for rejecting the charged particles background.

The incoming γ-rays enter the upper detector and converts into an $e^{-}e^{+}$pair in one of

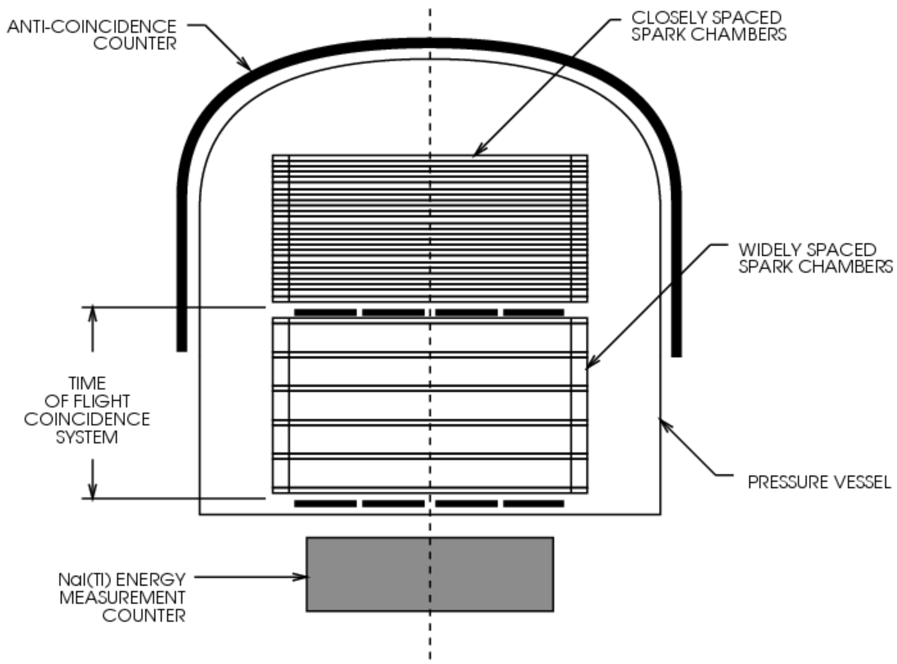

Figure 2.3: Scheme of the EGRET telescope.

the plates between the spark chambers in the tracker. The trigger initiated if at least one of the two pair members was recognized as downward particle by the TOF detectors and there was no signal in the anticoincidence dome. In this case the tracking system provided a digital picture of the event and the measurement of energy started. The energy was obtained with the NaI counters located below the tracker.

The tracker consisted of 28 spark chambers detectors interleaved with 27 plates with a thickness of 0.02 Radiation Lengths (R.L.) for gamma-ray conversion. The upper spark chamber provided the initial direction, while the bottom one provided information about the separation between electron and positron and about the energy balance. The energy measurement was provided by an 8 R.L., 76 cm x 76 cm square NaI(Tl) scintillator crystal located below the lower TOF scintillator plate. The energy resolution in the central region of the EGRET energy range was about 20%. The energy resolution is degraded at higher energies because of incomplete shower containment. At energies below 100 MeV the energy resolution also degraded because ionizaton losses in the spark chambers comprised an appreciable portion of the total photon energy.

2.2 The LAT scientific-driven requirements

The basic instrumental requirements for the GLAST experiment are: a short dead time for transient studies, a good energy resolution over a broad energy band, a large field of view and effective area with excellent angular resolution in order to achieve high sensitivity with great localization power. Below, for each science topic, an estimate of the basic telescope properties that are more relevant to reaching the science goals are listed.

- Blazars and Active Galactic Nuclei (AGN):
  - Broad energy response from 20 MeV to 300 GeV to explore the low energy spectrum where many AGN have peak emission, to measure high energy cutoff and to overlap with ground based telescopes.
  - Energy resolution better than 10% between 100 MeV and 10 GeV to facilitate the study of spectral breaks at both low and high energies.
  - Peak effective area greater than 8000 cm^2 to allow for variability studies of bright sources down in the sub-day timescales.
  - FOV at least 2 sr for significant sky coverage.
  - Flux sensitivity better than 6×10^{-9} $\mathrm{cm}^{-2}\mathrm{s}^{-1}$ for the 1 year sky survey to measure the AGN logN-logS function.
  - Mission life of at least 5 years.
- Unidentified sources:
  - Source localization power to less than 5 arcmin for sources of strength $> 10^{-8}$ $\mathrm{cm}^{-2}\mathrm{s}^{-1}$ and 0.5 arcmin for strong sources ($> 10^{-7}$ $\mathrm{cm}^{-2}\mathrm{s}^{-1}$) to facilitate counterpart searches at other energies.
  - Broad energy range to extrapolate spectra into the hard x-ray and TeV regimes to facilitate studies at other wavelengths.
  - Peak effective area greater than 8000 cm^2 to allow for variability studies of bright sources down in the sub-day timescales.
  - Short dead time for short term variability studies.
  - Wide (> 2 sr) FOV to allow high duty cycle monitoring of unidentified sources for time variability.
  - Mission life of at least 5 years.
- Gamma-ray diffuse background:
  - Background rejection capability such that the contamination of the observed high latitude diffuse flux (assumed to be $1.5 \times 10^{-5} cm^{-2} s^{-1} sr^{-1}$) is less than 10% for $E > 100$ MeV.

  - Broad energy response from 20 MeV to 300 GeV to extend the measurement of the diffuse background to unexplored energy ranges.
  - Broad field of view (more than 2 sr) for sensitive full sky maps.

- Dark matter:
  - Broad energy range with response up to 300 GeV to constrain dark matter candidates.
  - Spectral resolution of 6% above 10 GeV for side-incident events to identify relatively narrow spectral lines.
  - Mission life of at least 5 years, for reaching high statistical significance

- Gamma Ray Bursts (GRBs):
  - Quick (less than 5 s) localization of GRBs.
  - Broad field of view (more than 2 sr) to monitor a substantial fraction of the sky at any time.
  - Energy resolution better than 20% above 1 GeV to allow seraching for breaks in the spectra.
  - Less than 100 μs dead time for identifying correlation between low energy and high energy time structures in the bursts.
  - Single photon angular resolution better than 10 arcmin at high energy for good localization.

- Solar flares:
  - Long mission lifetime (more than 5 years) to provide solar flares observations over a range of solar cycle activity.
  - Broad energy band (20 MeV - 300 GeV) to observe high energy emission.
  - Less than 100 μs dead time to ensure good time resolution during flares.

- Pulsars:
  - Energy resolution better than 10% in the 100 MeV - 10 GeV energy range, where pulsars breaks occur.
  - Absolute timing accuracy better than 100 μs dead time for resolving pulsation in the light curve.
  - Large effective area for improving the statistics.
  - Large FOV to allow high duty cycle monitoring of pulsars.

- Interstellar clouds, SNRs, Galactic Center and Cosmic Rays production:
  - Single photon angular resolution better than $3.5°$ at 100 MeV for normal incidence, improving to better than $0.1°$ at 1 GeV for mapping extended sources.

- Point source localization better than 1 arcmin for identifying Supernovae remnants.
- Energy resolution better than 10% above 100 MeV for studying the spectral shape in proximity of SNR and of the GC.
- Broad energy band (up to 300 GeV) for correlating the observations with ground-base telescopes, especially in the observation of the high energy emission from SNR and GC.

Moreover, the direct detection of gamma-ray implies that the observatory has to be placed in orbit, in order to avoid the atmospheric absorption. This necessity is strictly linked with the Space Craft requirements in terms of mass, dimensions and power consumption. The following table summarize “mission requirements” set by the Space Craft interaction.

Parameter	**Mission requirement**
Mass	3000 kg
Center of gravity	<0.246 m from the LAT/SC interface
Overall dimensions	Maximum x-y dimension <1.8 m Maximum z dimension <3.15 m
Power consumption	Average power (1 orbit) <650 W Peak power <1000 W Peak power duration <10 min

2.3 Overview of the Large Area Telescope

Pair production is the dominant mechanism of interaction between radiation and matter at the energies studied by the GLAST Large Area Telescope (LAT)(Michelson, 2000; Atwood & et al., 2008). For this reason a pair conversion telescope is made basically by a tracking system, a Calorimeter and an Anticoincidence system, as displayed in Fig. 2.4. The EGRET experiment aboard CGRO had this structure and contained these detector substystems, and also the previous instruments aboard SAS-2 and COS B mission share the same detecting strategy.
A γ-ray entering the LAT creates an electron-positron pair, whose energies and directions are reconstructed by the LAT subsystems. From this information is is possible to determine the energy and arrival direction of the incoming photon using the conservation of four-momentum.
The tracking system has the primary goal of measuring the tracks of the electron and of the positron. In order to maximize the conversion probability, detecting planes are interleaved with *conversion foils* of particular thickness. Since the conversion probability increase with the atomic number Z as Z^2, the conversion foild are usually made

by high-Z material. As an example, EGRET used tantalum (Ta) foils and LAT use tungsten (W) foils.
The electron-positron pair create an electromagnetic shower in the calorimeter, and from the measurement of the shower performed by the calorimeter the energy of the pair is determined.
The measurements gathered by the tracking system and by the calorimeter are then used to reconstruct the energy of the incoming γ-ray.
The orbit environment is extremely rich of charged particles that enter the detector with rates that are of the order of 10^5 the rate of γ-rays. In order to reject the charged particles background an anticoincidence detector is used. The Anticoincidence surrounds the telescope and it is usually made by plastic scintillator. Charged particles gave a signal when crossing the sintillators of the anticoincidence, while γ-rays does not. This is an useful way to reduce with high efficiency the charged particles background.
The GLAST Large Area Telescope (LAT) share the same base philosophy but is based on new generation detectors developed for High-Energy Physics. The main LAT subsystems are the *Tracker* (TKR), the *Calorimeter* (CAL), the *AntiCoincidence Detector* (ACD) and the Data Acquisition System (DAQ). The tracker is made up of silicon

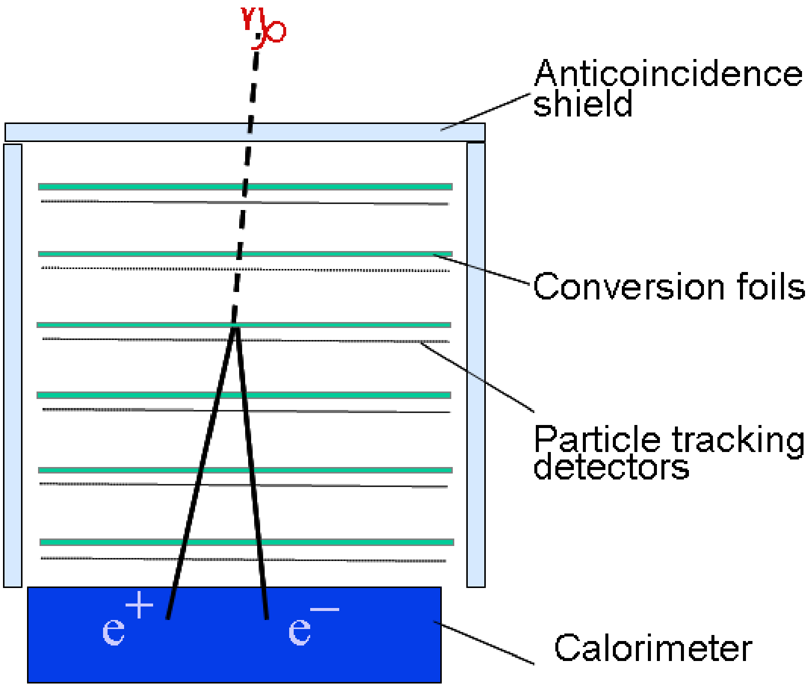

Figure 2.4: Simplified scheme of a pair conversion telescope like the LAT

microstrip detectors and allow the conversion of the γ-rays and the reconstruction of the electron and the positron tracks. The Calorimeter is located below the tracker and determines the energy of the pair. In order to reduce the background due to charged particles, the LAT is covered by an Anticoincidence Detector (ACD), which discriminates the charged particles from γ-rays. The Data Acquisition System (DAQ) will manage the main subsystems functions, e.g. the reading procedures and the trigger control.
An incoming γ-ray pass through the ACD without giving any signal, then enter the Tracker where are converted into an electron-positron pair. The energies and directions

of the pair members are reconstructed by the Tracker itself and by the Calorimeter, as displayed in Fig. 2.4.
Two key concepts of the LAT design are the *modularity*, that simplified the construction and integration phases, and the *redundancy*, that will limit the problems raising from possible malfunctioning during the instrument life. The LAT is made of an array of 4 x 4 *towers*, each made by a Tracker module, a Calorimeter module and a DAQ module (Fig. 2.5). The LAT offer higher performances with respect to its predecessor EGRET thanks to the new design strategy and the new detecting technologies. The main innovation of

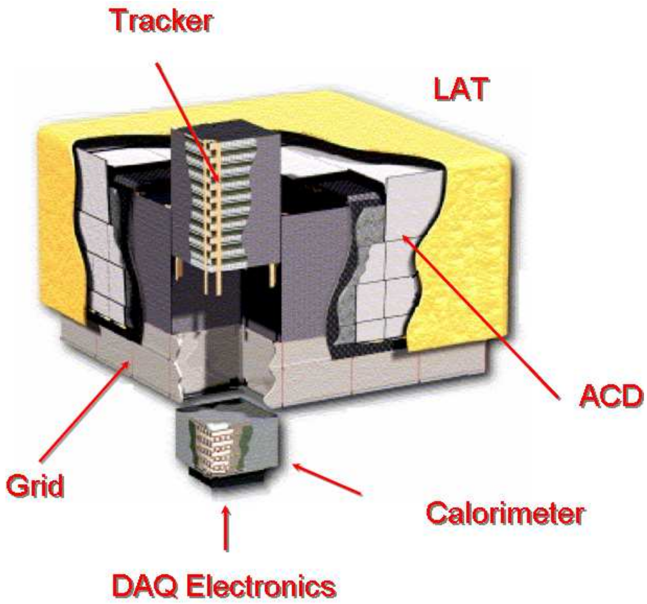

Figure 2.5: The GLAST Large Area Telescope.

the whole LAT is the introduction of the Tracker based on solid-state detectors instead of spark chambers used for the EGRET tracker.
These detectors have many advantages. First of all they provide a spatial resolution about 10 times better than spark chambers without many complications during fabrication. In the silicon trackers of the modern High Energy experiments the distances between the microstrips are of 50-60 μm , while the pitch between LAT Tracker microstrips is of 228 μm . Additionally they offer a lower dead time of about 20 μs, with respect to the dead time of 100 ms of the EGRET spark chambers.
The silicon detectors used for the LAT Tracker are radiation hard and does not contain consumables: this is an enormous advantage for mainly two reasons.
EGRET used spark chambers for the tracking system and the gas deteriorated with time. For this reason it must be substituted many times during the mission using onboard refilling system. In order to maximize the instrument lifetime, the gas must be conserved the most long possible but at each trigger it deteriorates, then EGRET trigger strategy minimized the number of triggers. For this purpose TOF counters were used in order to know if photons were coming from upside or from downside. The use of TOF counters limited the EGRET aspect ratio, since the height of the detector had to be enough to guarantee a measurable time of flight between the top and bottom of the detector. The aspect ratio of the instrument was then constrained to have a Field

Of View (FOV) of about 0.5 sr. Since there are no consumable in the silicon detectors, there are no such limitations in the trigger, then the LAT aspect ratio could be lower, assuring a FOV of about 2.4 sr. A wider FOV will allow a wider sky coverage, allowing a better sky monitoring for the study of transient sources and the observation of a big portion of the sky at the same time. A silicon based Tracker permits to avoid other complications, such the gas refilling of the usage of high potential differences.
Another important aspect is that no consumables aboard GLAST LAT will increase the instrument lifetime, that is currently planned in 5+5 years.
The LAT Calorimeter is made by scintillation bars, in order to better reconstruct the electromagnetic shower development, while the EGRET calorimeter was based on a monolithic scintillating detector.
The segmented ACD detector is also another big LAT innovation, since the EGRET ACD was made by a single scintillator panel. This segmentation will provide an higher detecting efficiency at energies greater than 10 GeV.
At these energies the *self-veto* problem becomes important, because a particle from the electromagnetic shower can backscatter in the ACD producing a spurious signal. In the LAT the ACD is segmented, then is it possible to know roughly which ACD panel gave a signal, in order to determine if the panel has undergone a backsplash or not. In this way it will be possible to avoid efficiency loss at high energies as was for the EGRET telescope.
In order to achieve its scientific goals the LAT must reject most of the background due to various contributions. The main contribution is due to cosmic rays, that enter the detectors producing spurious signals. In order to strongly reduce this background the ACD will be used together with more finer cuts on the reconstructed parameters of the incoming particle. Another contribution comes from the albedo γ-rays from the Earth, that will be removed mainly by considering the position of the spacecraft with respect to our planet. The last contribution to the background is from the radioactive activation of the materials of the satellite, but the simulations have shown that this contribution will be negligible in comparison with the others. Over a sample of 10 million background events, simulations have shown that about 40 events survived the background rejection, confirming the background rejection requirements of 10^5:1.

2.4 The LAT Calorimeter

The LAT Calorimeter(Johnson et al., 2000) measures the energy of the electron-positron pair and gives information about the high-energy photons that have not converted in the Tracker. From the measure of the e^-e^+energy it is possible to determine the energy of the primary photon using the conservations of the energy and momentum. A schematic view of the LAT Calorimeter is in Fig.2.6 The LAT Calorimeter is made up of a set of CsI(Tl) scintillating bars in hodoscopic configuration, in order to obtain more information about the structure and development of the electromagnetic shower. Each scintillating bar is read by PIN photodiodes located at both end of the bar itself.
This strategy provides an high energy resolution, a good signal (roughly 500 $\frac{e^-}{MeV}$) and requires a low working voltage of about 50 Volts. Another relevant characteristic of this system is the compactness, very important for space missions. This calorimeter is similar to the EGRET calorimeter, but it is fine segmented in the longitudinal and traversal

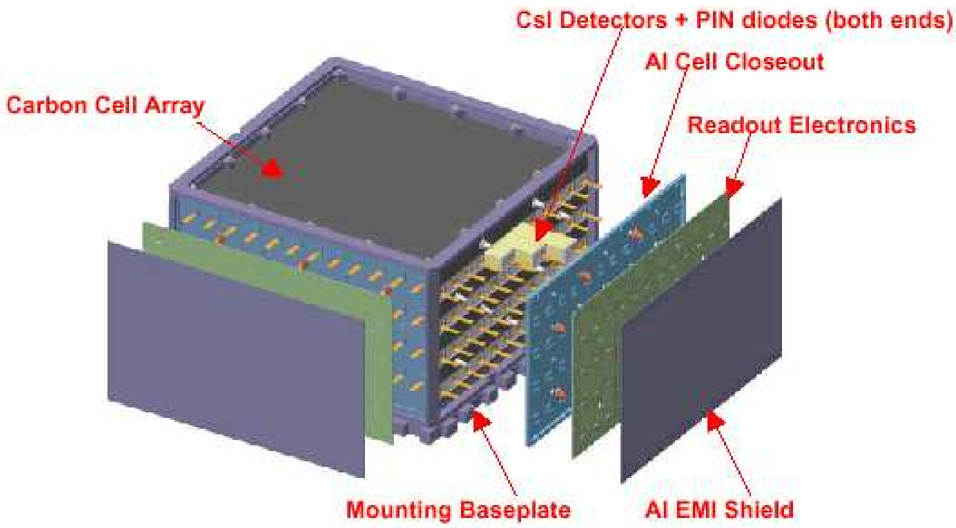

Figure 2.6: Schematic view of the LAT Calorimeter.

direction, while the EGRET calorimeter was a monolithic NaI(Tl) scintillator. This fine segmentation helps to have a good imaging capability in order to better reconstruct the electromagnetic shower. This is important also for estimating the arrival direction of the γ-ray that does not convert in the Tracker and for comparing the direction determined using the shower shape fit with the direction determined by the Tracker.
The total thickness of the calorimeter is 8.5 R.L. The LAT Calorimeter is constituted by an array of 4 x 4 modules, each of them made by 12 scintillating bars of 2 cm x 2.8 cm x 35.2 cm. These dimensions are comparable with the Radiation Length (1.8 cm) and the Moliere Radius (3.8 cm) thus a fine imaging of the shower.
A good shower reconstruction is important for at least two reasons. The longitudinal development helps to determine the energy using fits with analytical models of the longitudinal development. Then the shower shape and symmetry help to determine the arrival direction in case of γ-rays that have passed the Tracker without converting. The information about the shower are also combined with the ones coming from the Tracker and the ACD in order to improve the background rejection.
At both ends of each bar is placed a PIN photo diode used for reading, and the measurement of the relative intensity at both ends helps to determine the position where the energy deposition has taken place. The precision that can be obtained varies from some mm at low energies (about 10 MeV), up to less than a mm for energies above 1 GeV.
In order to obtain information on the position each layer is rotated of 90° with respect to the adjacent layers. This 3D imaging capability helps to determine the direction of the γ-rays that have not converted with a resolution of about 1°.

2.5 The LAT Tracker

The LAT Tracker (Johnson & GLAST LAT Collaboration, 2005; Bellazzini et al., 2003) is used to increase the conversion probability of the incoming photons, to determine its

arrival direction and to start the Level 1 trigger.
First of all the threshold condition for pair production must be satisfied, then the incoming γ-ray must have an energy $E > 2m_{e^-}c^2$, where m_{e^-} is the mass of the electron and c is the speed of light. This process can take place only in the field of a nucleus in order to simultaneously have the energy and momentum conservation (Shapiro & Teukolsky, 1983). In order to understand this we can consider an e^-e^+pair moving with speed v parallel to the original direction of the primary γ-ray, so that the total momentum is $2m_{e^-}v$. We can write the energy conservation equation:

$$h\nu = 2\gamma m_e c^2 \tag{2.1}$$

If both $e^-$and e^+move parallel to the γ-ray direction, the total momentum of the produced pair can be obtained from the Eq. 2.1:

$$P_{in} = 2\gamma m_e v = (\frac{h\nu}{c})(\frac{v}{c}) \tag{2.2}$$

Since v cannot be equal to the speed of light, it is not possible to have simultaneously energy and momentum conservation in vacuum. A third body (in this case a nucleus) is required in order to adsorb part of the energy and momentum of the incoming γ-ray. The pair production cross section is proportional to Z^2, where Z is the atomic number, then is is good to use high-Z conversion foils in order to maximize the conversion probability. The LAT tracker use conversion foils of tungsten (Z=74).
The technology employed in past years in High Energy Physics has been fundamental to choose the tracking detectors, since the alternatives were gas-filled trackers and scintillating fibers detectors. The silicon-based detectors were chosen for the LAT because of their higher sensitivity and angular resolution. A scheme of the LAT Tracker is displayed in Fig. 2.7.

In addition the silicon detectors have been successfully employed as vertex detectors in many High Energy Physics experiments and also in space missions. In particular the cost of these detectors is decreased in the last years, allowing an extensive usage in experiments like the LAT, that requires a wide sensitive area. The total silicon surface of the LAT tracker is of about 82 m^2. Wih respect to previous gas-based detectors the silicon detectors use for the LAT offer many significative advantages:

- Long lifetime;
- High efficiency;
- Stability;
- No consumables
- Operation at relatively low voltages;
- Low dead time;
- Fast readout, which simplify the trigger computation;

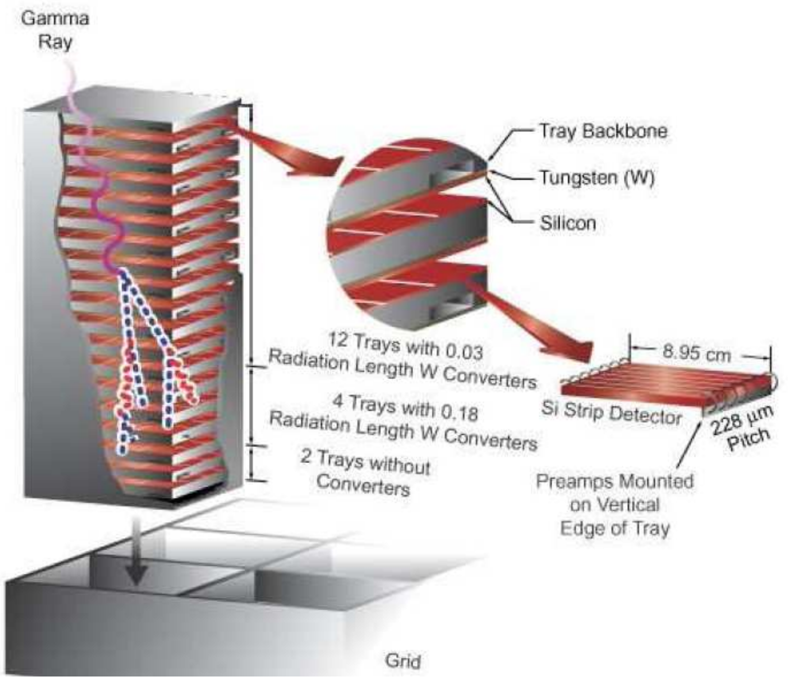

Figure 2.7: Schematic view of the GLAST LAT Tracker.

The LAT Tracker presented some tecnological challenges that have been studied, mainly the number of channels have been extensively studied and optimized.
The solution have been found as a tradeoff between silicon strip length,number of channels and angular resolution and readout noise. The channels number impact directly the readout power budget and the thermal design of the instrument. The mechanical design must also accomodate the transfer of heat dissipated in each module. With careful design 200 μW per channel appeared feasible.
Another aspect that is related to number of channels is the onboard computation power. In order to reduce computation effort on a single processor, each module of the Tracker has an independent readout and trigger system that operate in a semi-autonomous way. As for the other part of the LAT, carefully studies have produced the parameters for the Tracker in order to satisfy all the requirements and mantain the basic constraints as low consumed power, low detector noise and low computation power required.

2.5.1 Structure of the Tracker

The LAT tracker has been designed with the same basic ideas of modularity and redundancy of the whole LAT. The basic unit is a square *Silicon Strip Detector*(SSD) with the size of 8.95 cm x 8.95 cm, where are implanted 384 parallel microstrips spaced by 228 μm .
Four SSDs, each of them is 400 μm thick, are then assembled in a *ladder*. In a ladder the end of each microstrip of a SSD can be connected to the end of the correspondent microstrip on the adjacent SSD in order to form a single longer microstrip. At this point 4 ladders are assembled to form a sensitive silicon microstrip layer, which will be then inserted in a *tray*. The scheme of a tray is displayed in Fig. 2.8. A tray is a

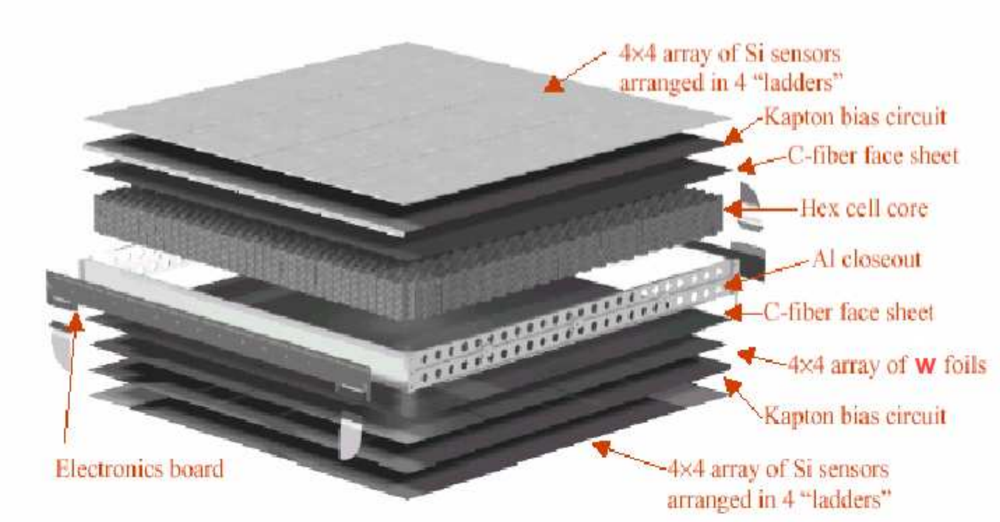

Figure 2.8: Exploded view of a tracker tray.

composite structure with a mechanical structure in carbon fiber that bring at both faces a sensitive silicon plane. The main components of a tray are a detecting silicon layer on the top face, an aluminum core, a tungsten foil for the conversion of the γ-ray and another silicon layer on the bottom face of the tray. The two silicon layers are mounted in a tray with parallel orientation of the microstrips. Each tray is then connected to the reading electronic, with the *GLAST Tracker Front End* (GTFE) chips are directly connected to the end of the microstrips.
Trays are then piled up with a separation of 2 mm and each tray is rotated of 90° with respect to the adjacent tray. In this way the resulting system is made by a conversion foil followed by a couple of silicon layers with perpendicular microstrips in order to have XY detection capability. The resulting module is called *tower* and it is made by 19 trays with 18 XY detection layers. In Fig. 2.9 are diplayed the scheme of a LAT tracker tower compared with a real tower assembled in the INFN laboratory in Pisa. All trays are identical, except for the top and the bottom tray, that have a special mechanical interface for installing in the rest of the LAT.
The first 12 top trays are 0.03 R.L. thick, the following 4 are 0.18 R.L. thick, while the last 3 trays does not have conversion foils.
The different thickness of the conversion foils comes from the design strategy. The conversion foils should be thin in order to reduce the effects of the Multiple Scattering and *Bremsstrahlung* emission, than strongly limit the angular resolution. This will guarantee a better *Point Spread Function* (PSF). On the other side the total thickness should be high in order to increase the conversion probability and then the effective area.
The designers have then decided to divide the tracker in two parts, a *front* section and a *back* section. The front section is made by the first 12 layers with the most thin conversion foils, in order to have a good PSF on the low-energy γ-rays. The back section with the most thick foils should maximize the conversion of the high-energy photons, even with a lower angular resolution. Anyway for these layers in fact the resolution would be lower, because the particles after been tracked, exit the tracker without permitting to measure other points in they trajectory. Last 3 trays does not have conversion foils

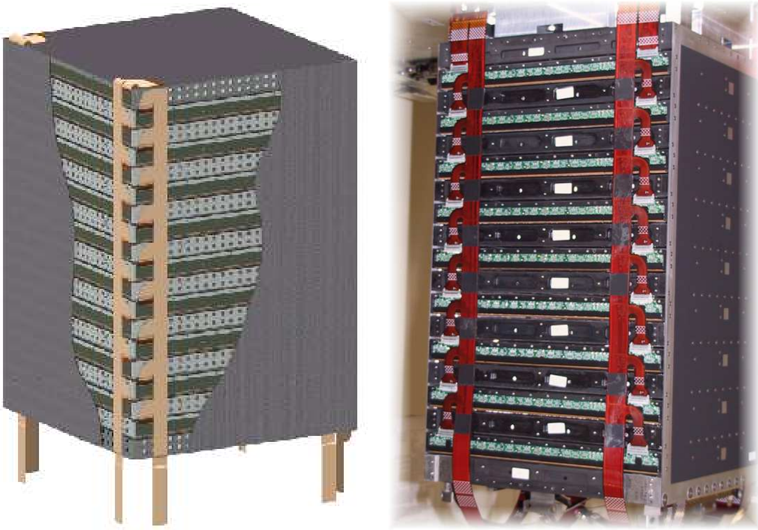

Figure 2.9: Left: Scheme of a LAT Tracker tower. Right: Picture of a completed Tracker tower.

in order to permit the start of a L1 trigger. For the tracker this condition is called *Three-in-a-row*, i.e. 3 planes have triggered.
The total tracker width is 1.3 R.L. because an higher value would make the energy resolution worst.
The total 4 x 4 tower array form the LAT silicon tracker. During the assembly of each tower the single components have been continuously tested electronically. In addition the trays and the towers have undergone thermal and thermovacuum tests and mechanical vibrational tests, in order to test the functionality in space environments and to avoid problems due to the vibrations during launch.
The LAT Tracker have been assembled in Italy under the coordination of the Italian collaboration and has been successfully completed in September 2005.

2.6 The LAT Anticoincidence detector

One of the main problems of the LAT during orbit will be the discrimination of the γ-rays from the background made of charged particles. In γ-ray missions a system often used is the Anticoincidence detector (Moiseev et al., 2007).
When a γ-ray photon enter the LAT, it does not produce any signal in the Anticoincidence detector, but give a signal in the tracker and in the calorimeter due to the produced pair. A charged particle behaves differently, since during the passage a signal also in the Anticoincidence is produced, then it is possible to recognize a γ-ray from a charged particle thanks to the different signature in the subsystems and in particular in the ACD. The events that give signal in the Tracker and in the Calorimeter but not in the ACD can start the trigger, the other are refused as background events.
The LAT *AntiCoincidence Detector* (ACD) is made by a set of plastic scintillators coupled to photomultipliers that uses wavelength shifters (WS) in order to increase the reading efficiency. With respect to the EGRET anticoincidence system, that was made

by a single module, the LAT ACD is fine segmented. A scheme of the ACD assembly is displayed in Fig. 2.10.

The ACD segmentation help to increase the efficiency of background rejection in particular for the high-energy γ-rays. In EGRET it was necessary to reduce the triggers frequency in order to avoid gas consuming in the spark chambers. The EGRET ACD was implemented in the Level 1 trigger. This reduced the working efficiency, mainly at GeV-energies, where the self-veto becomes important. The self-veto happen when a

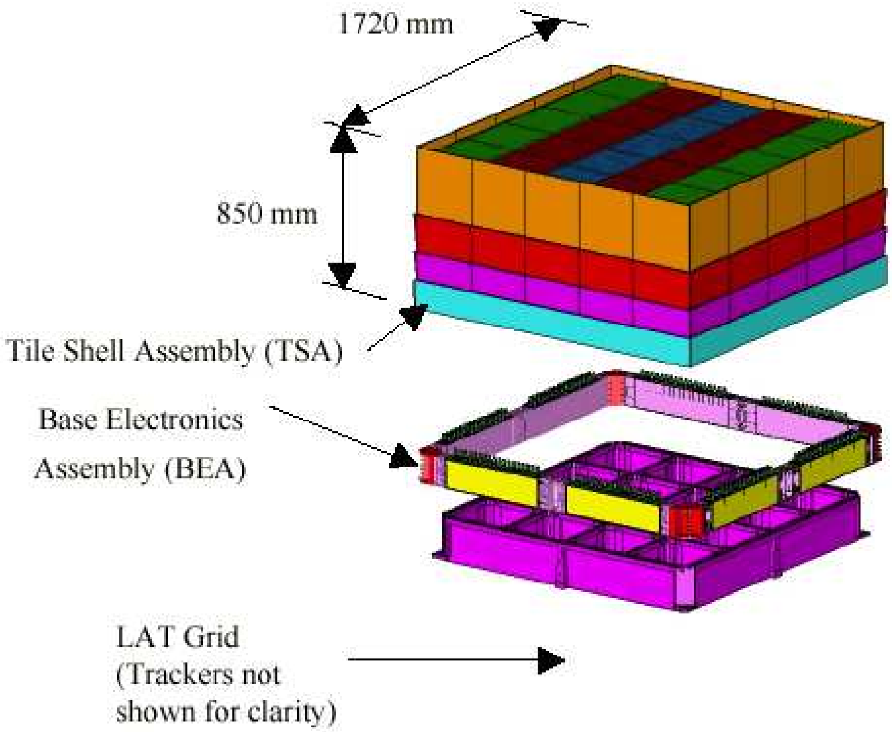

Figure 2.10: Schematic view of the LAT ACD assembly.

member of the electromagnetic shower produced by the e^--e^+pair is deflected and give a signal in the anticoincidence detector (*backsplash*). The event has a signature of a cosmic ray and then it is rejected since it is confused with a background event.

Thanks to the segmentation it is possible to know exactly which scintillator have been hit, and it is then possible to compare the track direction with the position of the hit scintillator. In case of *backsplash* the position of the hit scintillator panel does not correspond exactly with the intersection of the track and the ACD, then a self veto is recognized and avoided.

Thanks to the lower dead time and to the absence of consumables in the Tracker, the LAT can undergo a much higher Level 1 trigger frequency, then the ACD can be inserted in the Level 2 trigger. In this way each event can be analyzed with more care (as will be explained in the following Section) and the self-veto can be avoided in a very efficient way.

A total of 89 panels constitute the ACD, some of them are disposed in a 5 x 5 array on top of the Tracker and the other are at the sides of the LAT.

The assembling scheme of these panels has been designed with overlap in one dimension

and scintillating fibers covering the gaps in the other dimension. Each scintillator is read out by an interleaved set of Wavelength Shifting (WS) fibers, with bundles connected to two phototubes, in order to guarantee redundancy.
The ACD is the first step in the background rejection scheme, and the required rejection factor at this stage is about 3×10^3:1.

2.7 Data Acquisition System and Trigger

The LAT Data Acquisition System (DAQ) have three main functions(Michelson, 2000). First of all it controls the trigger, then it guides the event reading sequence and store it in a temporary memory. The DAQ also manage the data elaboration and transfer to the ground.
This system also is responsible for other functions, among others the control and monitoring and housekeeping of the instrument and the power management of the whole LAT.
The DAQ is made by 16 *Tower Electronic Modules* (TEM) located below each tower and two TEM specific for the ACD. Also two *Spacecraft Interface Unit* TEM are in this system and are located in the spacecraft below the LAT.

2.7.1 The LAT Trigger

The LAT trigger has a multi-level structure, in a similar way of the triggers employed in High Energy Physics experiments.
In particular the hardware trigger is based on special signals, called *primitives*, that originate from from LAT subsystems. Primitives from Tracker, Calorimeter and Anticoincidence Detector are combined to decide if an event is recorded or no.
The trigger of the LAT is very flexible in order to allow change of configuration to optimize trigger efficiency and versatile in order to accomodate various signatures of events. One possible implementation is the one proposed in LAT proposal.
The *Level 1 Trigger* (L1T) is managed by the hardware electronics, while the *Level 2 Trigger* (L2T) is managed by the TEM of each tower. The *Level 3 Trigger* (L3T) filters the results of the L1T and L2T in order to reduce the amount of data to be sent to the ground. The events selected by the L3T are then stored in the *Space Solid State Recorder* (SSSR) before the transmission.
With respect to this original project, there are some chages, for example the ACD signal is used for the L1T. Testing of the trigger are currently done and will be performed also on flight by commands from the ground.
The goal of the L1T is to begin the reading sequence, and it is expected that this trigger will start with a frequency of few kHz. Each tower forms independently a trigger and the global trigger is the logic OR of the single trigger at tower-level. A tower trigger can be initiated by two conditions that can happen in the tracker and in the calorimeter.
The Tracker trigger is made by the logic OR of the signals of every GTFE channel. This asynchronous OR is called *Fast OR* and it is send from each tracker layer to the TEM. The logic system of the TEM search for coincidences in the XY layers and then for the coincidences of 3 consecutive XY planes (*Three-in-a-row* condition). Simulations have shown that this system is very efficient also for the photons misaligned with the axis of

the tower. In order to reduce the noise associated with the electronics it is possible to apply a mask to the read channels in order to avoid the noisy channels.
The trigger in the Calorimeter is based on the counts of the scintillating bars that have given a signal in coincidence. This system is based on two threshold for every crystal face in the Calorimeter. In flight the *Low-Energy Level* trigger threshold (CAL-LOW) will be set to 100 MeV. This will allow the identification of at least 30% of the γ-rays above 1 GeV that does not convert in the Tracker. Another trigger threshold is called *High-Energy Level* (CAL-HIGH) and it is set to 1 GeV. CAL-HIGH trigger plays a role when there are events with an high energy deposit in the calorimeter. In this case the CAL informs the TEM that an high-energy event has occurred. If any crystal goes above threshold, a trigger primitive from the Calorimeter is sent.
The AntiCoincidence detector has also two thresholds for every scintillator tile. One (VETO) is set to 1/2 MIP and is meant to veto charged particles. The other (CNO) is set to several MIPs to trigger on cosmic ray ions for CAL calibration.
Since the timing of the primitives is different for the individual subsystems each trigger line has an input delay which has to be set such that all trigger primitives arrive at the central trigger unit at the same time. In order to be sure that all primitives arrive at the proper time, a calibration on timing is needed.
There are also other trigger sources prepared for different purposes, e.g. external trigger for ground testing, periodic trigger, and software trigger.
The L2T is elaborated in parallel by all TEM modules and serve to combine the information of the L1T with the ACD signal. First of all a simple track reconstruction algorithm is applied and an extrapolation of the track into the ACD is performed by looking for an ACD signal. This strategy allow the recognition of a backsplash event. This check of the track is not performed in case of a CAL-HIGH signal, because it could be due to a secondary particle that could cause a self-veto. It is estimate that the frequency of the L2T is of about 1 kHz.
Finally the software trigger L3T is executed by the SIU modules and give a complete reconstruction using the information of all subsystems. There are no many cuts to the event and the only significant reduction is in the removal of the albedo γ-rays coming from the Earth. The resulting frequency of the events is 15 Hz and the amount of data have been reduced to be trasferred to the ground.

2.8 LAT expected performances

LAT has the typical structure of a pair conversion telescope, i.e. Tracker, a Calorimeter and AntiCoincidence detector and every subsystem is designed with very high requirements (Michelson, 2000; Digel & Myers, 2001). In addition every subsystem of the LAT is based on new High Energy Physics detectors. By comparing LAT performances with EGRET, as done in the Table 2.1, it turns out that LAT will have a superior resolution and sensitivity that will guarantee a big amount of scientific discoveries. One of the main characteristics of LAT is the angular resolution that reach 0.1°at high energies. The angular resolution is not so good at lower energies because the measurement of the tracks is limited by the Multiple Scattering that increases at low energy. At high energy the only factor that limit resolution is the microstrip pitch, while the Multiple Scattering contribution becomes negligible. On the other side it is not possible to have

	EGRET	GLAST LAT (min. req.)	GLAST LAT
Energy range	20 MeV-30GeV	20 MeV-300 GeV	10 MeV-1TeV
Angular Resolution single photon (68% containment)	5.8 (E=100 MeV)	$<$ 3.5 (E=100 MeV) $<$ 0.15 (E>10 GeV)	Front: 3.1 (E=100 MeV) Total: 4.4 (E=100Mev) Front: 0.074 (E=10 GeV) Total: 0.1 (E=10 GeV)
Effective Area peak	1500 cm^2	8000 cm^2	12900 cm^2
Field Of View	0.5 sr	$>$ 2 sr	2.4 sr
Resolution in energy	10%	10% (0.1-100GeV) 50% (20-100MeV)	10% (0.1-100GeV) $<$ 25% (20-100MeV)
Dead Time	100 ms	$<$ 100 μs	20 μs
Sensitivity	2 x 10^{-7} ph cm^{-2} s^{-1}	4×10^{-9} ph cm^{-2} s^{-1}	1.6 x 10^{-9} ph cm^{-2} s^{-1}

Table 2.1: LAT Expected performances compared with EGRET. Quoted sensitivity for the LAT is referred to sources out of the Galactic plane

too many channels mainly because of limitation of total power consumption.
The effective area of the LAT is much higher than EGRET, mainly thanks to the higher geometrical sensitive surface of the LAT Tracker and to the lower dead time of silicon detectors. The effective area decreases at very high energies (E$\simeq$200 GeV). One of the main reasons for this decrease it incomplete shower containement, that makes difficult the reconstruction of photon energy and direction.
One of the main parameters for a telescope is the Field Of View (FOV), that allow the instrument to observe a big portion of the sky. The LAT FOV will be of about 2.3 sr, about five times grater than the FOV of EGRET. This difference is due to the different detectors employed by LAT and EGRET, that constrained the aspect ration of the instrument, as described in Sec. 2.1.1.
The better LAT energy resolution is achieved through the fine segmentation of the calorimeter. In this manner it is possible a better reconstruction of shower development.
LAT will have a much higher sensitivity than EGRET, such that in one day the faintest EGRET source is detectable. This will allow the LAT to discover a lot of new sources and build a very extended catalog of high energy sources in the sky.
A set of plots showing the expected LAT performances is shown in Fig. 2.11.

2.9 MonteCarlo simulations of the LAT

During LAT design and during the study of the LAT capabilities it is very useful to have a complete MonteCarlo simulation of the LAT. This MonteCarlo has been also validated during important milestones in the GLAST mission like the 2006 LAT beamtest at CERN. Presently the GLAST collaboration has provided a detailed MonteCarlo simulation of the LAT called *Gleam*, while a fast observation simulator is also present (*Observation Simulator*, see Sect:2.10).

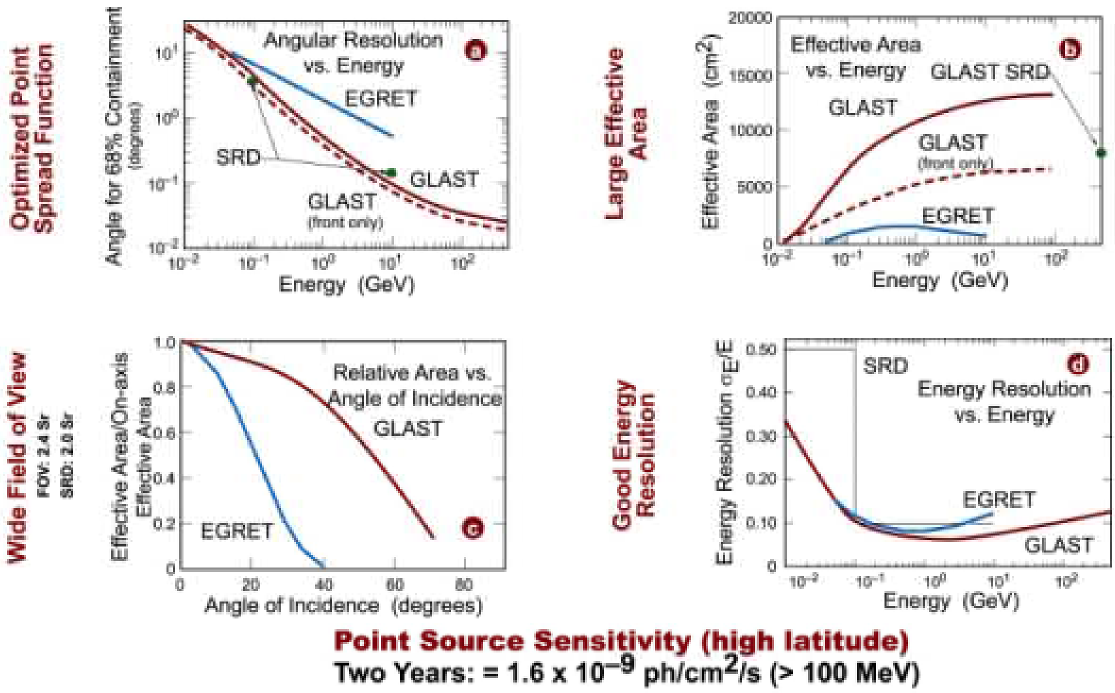

Figure 2.11: *LAT detector performance compared with EGRET for a point source observation.(Michelson, 2000)*

Gleam is based on the *Gaudi*[1] framework often used in High Energy Physics. Gaudi has been designed in order to provide an environment for developing applications and algorithms useful for the generation of events and for the reconstruction and analysis of them. The data that can be manipulated are the event variables, e.g. energy and direction, or the detector characteristics, e.g. geometry of materials.
A first type of algorithms for the generation of events. Different types of particles can be generated, among others γ-rays . For every particle it is possible to specify an energy and direction or give a spectral distribution in order to reproduce emission from a particular source, e.g. a pulsar. The data relative to a source can be inserted in a XML file in a *source model.*
The LAT geometry is managed by *Gleam* through XML files where information about sizes and materials are stored. The simulation of the particle interactions with the detector is managed using the libraries of Geant4[2], the C++-based toolkit used in most of the High Energy Physics experiments simulations today. The simulation can be run in graphical mode or in command-line mode in order to save memory. The Graphical User Interface (GUI) can be switched between the basic one and FRED[3], an advanced Event Display developed mainly in Italy. FRED can be also used for displaying real data, e.g. from the test beam. In Fig. 2.12 an cosmic ray event on 8 LAT towers is displayed with

[1]http://proj-gaudi.web.cern.ch/proj-gaudi/
[2]http://geant4.web.cern.ch/geant4/
[3]http://www-glast.slac.stanford.edu/software/Display/FredDisplay.htm

FRED. Fig. 2.13 show a simulated 5 GeV photon entering the LAT
There is the possibility to simulate the GLAST orbit or to keep the LAT fixed, i.e. for

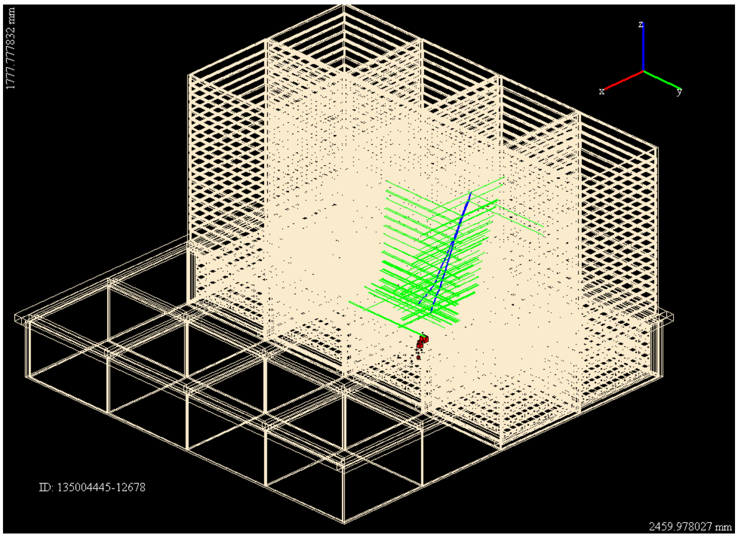

Figure 2.12: An example of an event viewed with the FRED Event Display.

simulating Beamtest setup.
The hit parts of the detectors can be highlighted with different colors and also the recontructed tracks can be visualized in the GUI. A set of Digitization algorithm simu-

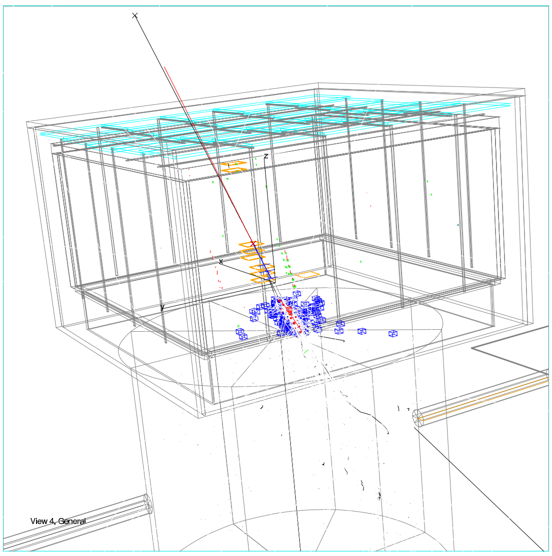

Figure 2.13: An example of a 5 GeV photon entering the LAT viewed by the *Gleam* defaut GUI.

late the conversion from to digital signal in the detectors and then a set of opportune Reconstruction algorithms allow to determine the reconstructed energy and direction of the simulated incoming particle. The data relative to the MonteCarlo events, the

Digitization and the Reconstruction can then be stored into ROOT[4] trees to be used for analysis.

2.10 The GLAST *Science Analysis Environment*

Another major component of the GLAST software is devoted to the Data Analysis. The GLAST Collaboration has developed a suite of analysis tools called *Science Analysis Environment* (SAE). The purpose of the SAE is to collect a set of useful software for managing the data coming from the LAT and GBM.
The concept of the SAE is similar to the suite of analysis tools developed for the CGRO mission and presently available at the NASA *High Energy Astrophysics Software Archive*(HEASARC)[5]. In this site is possible to retrieve not only the data from several High Energy Astrophysics missions, but also a lot of useful software for managing astrophysical data and packages for analyzing mission-specific data.
The SAE is composed by some sections that contain tools for specific purposes. The SAE contains also the definition of the LAT Data Format[6]. A Diagram of the full SAE is displayed in Fig.2.14

2.10.1 Data Format

The communication between tools is guaranted by FITS files, in order to be compliant with this wide-used standard in astrophysics. In this way both the events data and other analysis data are stored under this format with different names that begin. The detailed description of the header content of each FT file can be found at(Band et al., 2005).
The data relative to each event are contained in the $FT1$ files, where the user can find the main high-level information for every photon event, e.g. energy, time, direction. Also some details relative to the reconstruction are stored in the $FT1$ files, e.g. the conversion layer or the cosines of the reconstructed track.
The $FT2$ file contains the data relative to the orbit of the satellite and its position in time. This data files are of particular importance for pulsar analysis, since they are used for barycentric corrections.
The $FT3$,$FT4$ and $FT5$ contain data that can be used for spectral analysis using XSpec software[7], in particular $FT3$ refer to the PHA spectrum files, the $FT4$ to the *Auxiliary Matrix File* (AMF) files and $FT5$ to the *Response Matrix Files* (RMF).
The $FT7$ files contain the data relative to exposure, that for example can be used during the likelihood calculations when studying the stationary sources.
The last data file, called $FT8$, should contain the source definition. This files are important for observation simulations and also for likelihood calculations.
Another set of FITS data file form the *Databases* (D). For pulsar analysis the *Pulsar Database* (D4) and the *LAT Point Source Catalog* (D5) are of particular importance.

[4]http://root.cern.ch
[5]http://heasarc.gsfc.nasa.gov/docs/software.html
[6]A detailed definition of the SAE can be found at:
http://www-glast.slac.stanford.edu/ScienceTools/slwg/SAE/default.htm(Band et al., 2005)
[7]http://heasarc.gsfc.nasa.gov/docs/xanadu/xspec/

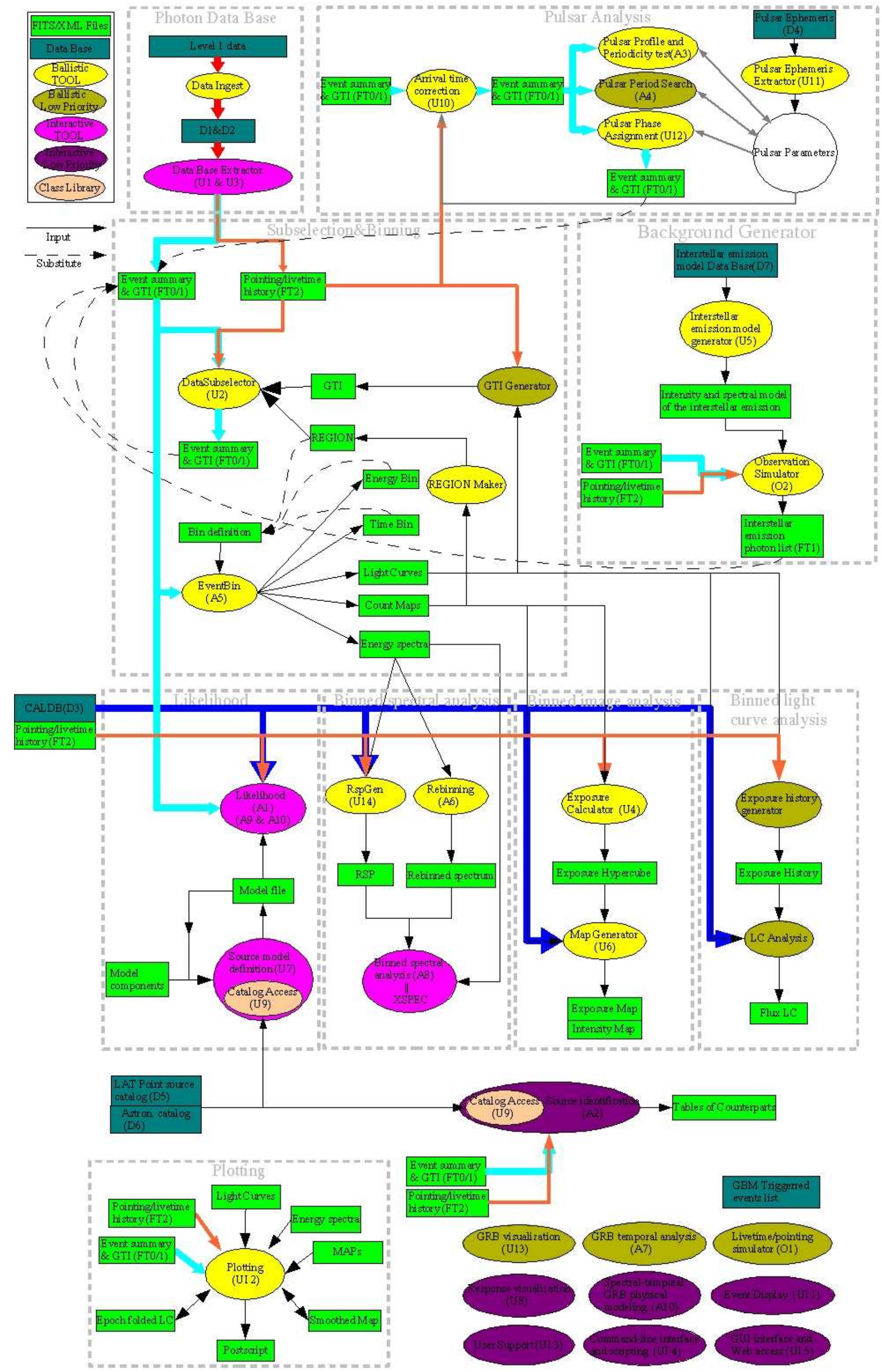

Figure 2.14: The diagram containing all the tools of the Standard Analysis Environment (SAE).

The D4 contains the ephemerides of a set of targeted pulsars that can have a γ-ray counterpart and that can be of interest for GLAST. This database contains also the information about orbits of selected binary pulsars of interest for GLAST. The D5 contains the Catalog of point source that have been detected by spatial analysis through various methods, e.g. maximum of likelihood. The LAT Catalog is important for pulsar analysis since it can give the position of potential γ-ray pulsars that need to be identified through timing analysis.

2.10.2 Science Tools

The GLAST Science Tools are divided in main subclasses depending upon the tool functionality: the main classes are the *Utilities*(U), the *Analysis Tools*(A), the *User Interface*(UI) and the *Observation Simulation Tools*(O).
The Utilities contain several tools that have a wide use, e.g. that can allow the user to select a subset of photons according to some particular selection cuts, or can generate the exposure maps useful for the likelihood analysis. The utilities in the SAE specific for pulsar analysis are the *Photon Arrival Time Converter*($U10$), that perform the barycentric corrections, the *Pulsar Ephemeris Extractor*($U11$) that extract form D4 ephemerides related to a particular pulsar under analysis and the *Pulsar Phase Assignment*($U12$), that assign a phase to each photon according to a particular ephemeris.
The Analysis tools contain the most complex software for data analysis, in particular the Likelihood tool for spatial analysis ($A1$) and several tools for GRB timing and spectral analysis. The Analysis tools useful for pulsar analysis are the *Pulsar Periodicity Testing tool*(A3), that perform basic periodicity test on a set of baricenterized photons (Chi-Squared test, Z_n^2 test and H-test). Another tool currently under development is the Pulsar Period Search tool (A4), that has not yet reached a stable version.
The Observation Simulation part of the SAE is composed by 2 main tools, the Livetime/pointing simulator, that simulate the GLAST position with time given a specific orbit as input, and the *Observation Simulator* ($O2$), that takes a sky model with some sources and simulate a LAT observation according to a specific observational time window. The difference between Observation Simulator and *Gleam* is that the former is much faster since it make a convolution of the input photons with the Instrument Response Functions if the LAT, instead of computing each interaction of each photon in the detector. For the purpose of studying LAT response to some objects, that does not need a very high detailed knowledge of the detector behaviour, the Observation Simulator is pretty good.
The User Interface tools contains some software for plotting data and for event display and are currently still under development and definition.

2.11 LAT status

The construction and assembly of the LAT subsystems have been completed during 2005. The schedule for the 2006 was devoted to the assembly of the LAT, the vibrational and environmental tests and the integration with the GBM. In Fig. 2.15 it is displayed the LAT before the installation of the ACD and the micrometeorites shield. The Termovacuum tests have been performed at the Naval Research Laboratories and have been completed successfully.
Meanwhile during Summer 2006 an italian-french team coordinated the LAT Beamtest at CERN. During this beamtest a *Calibration Unit* (CU) has been exposed to the beam at the CERN PS and SPS. The goal of this beamtest was to study the detectors response

Figure 2.15: A picture of the complete LAT before installing the ACD.

to γ-rays, electrons, positrons, pions, positrons at various energies from 100 MeV up to about 280 GeV. The LAT have been integrated into the spacecraft together with the GBM and will be then transferred to the NASA Kennedy Space Center. The launch is scheduled for winter 2007.

2.12 Summary

In this Chapter an overview of the GLAST Large Area Telescope have been given. The basic detecting strategy of the LAT have been discussed and the comparison between LAT and LAT have been presented.
LAT is the results of careful science driven design that imposed specific Science Requirements In order to design an instrument like the LAT various possible configurations must be considered and all the variables must be taken into account in order to have a trade off among low readout power, low computing power, low noise, high efficiency and resolution and while mantaining cost low. The use of silicon detectors for the LAT Tracker has offered a good solution to these problems a by offering very high performances.
The stucture of the main LAT Subsystems have been discussed with detailed information of the tecnical choices for every detector. At the end the MonteCarlo simulation of the LAT and the Science Analysis Environment containing the LAT data analysis software have been presented since it will be used extensively in this thesis.

Chapter 3

Pulsars as Neutron Stars

Pulsars are among the most exciting sources in the High Energy Astrophysics. They are unique laboratories for testing laws of physics under extreme conditions. Moreover pulsars emit radiation in the whole electromagnetic spectrum, and they can be used to study very different radiation mechanisms acting simultaneously.
A general observed feature of pulsar timing is a steady increase of the period, and by taking that into account pulsars behave as incredibly precise clocks in the Universe. In fact one of the most important features of these sources is the stability of the periodic emission. The deviation from steady increase can be modeled and included in the so-called *timing noise* and some sporadic phenomena known as *glitches*, due probably to abrupt changes in the internal structure of these objects. Indeed most of discoveries related to pulsars have been done using timing information.
The discovery of pulsars had a tremendous impact on our knowledge about the Universe. Today pulsars are used to probe very different fields, as gravitational physics, magnetohydrodynamics, particle physics and stellar evolution.
Soon after their discovery pulsars have been recognized to be rapidly rotating neutron stars with very high magnetic fields. In order to explain most of the emission features observed in pulsars more detailed models were proposed for the surrounding of the neutron star, including the presence of a plasma-filled *magnetosphere*. The magnetospheric model is of fundamental importance for explaining the emission of high-energy radiation from pulsars and in particular of γ-rays.
In order to better understand pulsars is of fundamental importance to know the structure and characteristics of neutron stars. In this Chapter the basic properties of pulsars as neutron stars are reviewed considering also the observational status at radio, optical and X-ray spectral windows. The next Chapter will deal with pulsar γ-ray emission with reference to the theory of neutron stars magnetospheres.

3.1 The discovery of pulsars

Pulsars were discovered serendipitously in 1967 by Jocelyn Bell, a research student in a Cambridge team of astronomers lead by Anthony Hewish (Lyne & Graham-Smith, 1990)(See Fig. 3.1). They had constructed a large array for radio wavelength (3.7 m), sensitive to weak discrete radio sources, for that was especially optimized to study scintillation.

It became clear that the fluctuating radio signal found by Bell were occurring for some minutes each day, as expected for a signal of celestial origin viewed by a transit telescope. In November Hewish and his team using a recorder with a faster response obtained a regular pulse appearing with a period of 1.337 seconds (See Fig. 3.1). What kind of celestial source could this be? A man-made signal, or possibly the first signal from an extraterrestrial civilization? The second possibility was disturbing, then Hewish decided

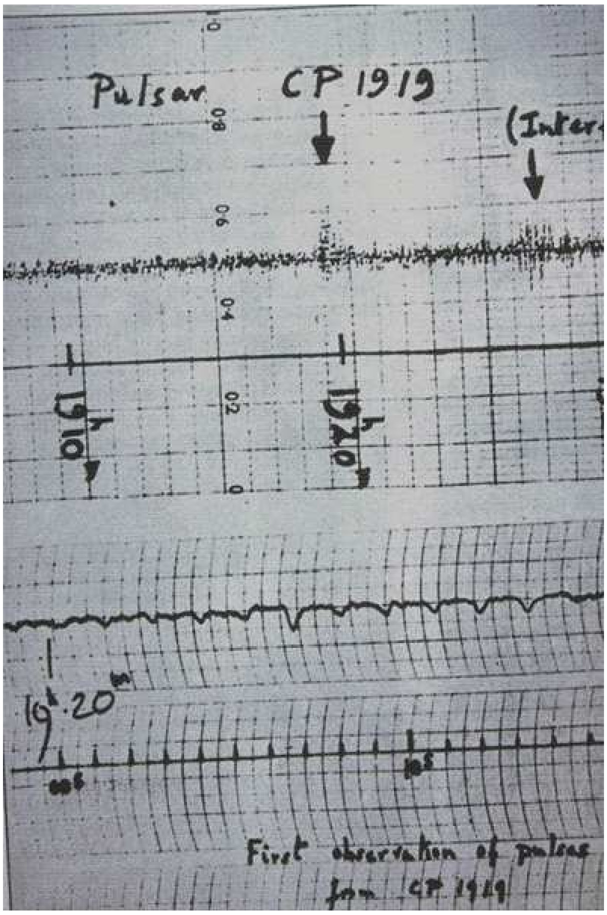

Figure 3.1: Recording of the first discovered pulsar in 1967, PSR 1919+21. At the top of the figure is shown the first recording, where the signal (marked "CP1919") resembled the radio interference also seen on this chart (marked "interference"). Below: the fast chart recording shows individual pulses as downward deflections of the trace.(From (Hewish et al., 1968))

to not provide any official communication in order to avoid hundreds of newspaper reporters coming to the observatory attracted by the *Little Green Men* signal (as Hewish and colleagues named it ironically).
The first official communication was published in a Letter by *Nature* in February 1968 (Hewish et al., 1968). In this letter Hewish presented a first analysis of the pulsating signal and first important conclusions were obtained. Hewish showed that the emitting source was located outside the Solar System, as became evident from the absence of measurable parallax.
The source was then labeled PSR 1919+21, where PSR stands for *Pulsating Radio*

Source, abbreviated in *Pulsar*, a name proposed by a journalist. It is worth to remark that the paper specifically mentions a neutron star as possible origin of signal, while at that time the existence of neutron stars was still hypothetical. The significance of pulsar discovery was highlighted by the award of Nobel prize for Physics to Hewish in 1974.
After the Letter of 1968 to *Nature* many different objects were proposed to explain the observed periodicity of pulsars, among others the radial oscillations of neutron star, as suggested also by Hewish, or white dwarf, orbital modulation in a binary system and rapid rotation of white dwarfs or neutron stars. The discovery of other pulsars with smaller periods ruled out the possibility of binary motion and of radial oscillation of a white dwarf surface. Within the theory of rotation the observed pulsars at that time were not decisive to chose between white dwarfs of neutron stars. In particular the radius could be constrained by imposing the stability against disruption because of rapid rotation. The discovery of pulsars with rotation periods down to ms scale ruled out the possibility of a rotating white dwarf.
Pacini(Pacini, 1967) and then Gold(Gold, 1968) proposed an identification with neutron stars and explained the observed periodicity with the "lighthouse effect".
The first paper of Pacini was based mainly on considerations about the energy that rotating neutron star can supply to the external nebula and proposed as an example the Crab Nebula even before the Crab pulsar was discovered. In this model the radio emission comes from the two magnetic poles and is swept across the observer as in a lighthouse. Since a steady increase of period have been observed in pulsars, Pacini proposed that this loss of rotational energy was converted to particle wind that can eventually energize the Crab Nebula.
The beauty of the model of Pacini resides in the fact that from energetic argument it can constrain the nature of pulsars as highly-magnetized, rapidly rotating neutron stars.Pulsars are then the first type of neutron stars to have been discovered.

3.2 Neutron Stars

The structure of neutron stars were already investigated in 1939 by Oppenheimer and Volkoff, that recognized that the crucial point for understanding these objects is the equation of state of the neutron star matter.
The possibility of such objects made entirely by neutrons was also suggested by Landau in 1932 and Baade and Zwicky in 1934, in two theoretial papers about these kind of new stars not yet discovered (Baade & Zwicky, 1934). From the equation of state it is possible to determine also the mass and radius of a neutron star. Today several equations of state exist for explaining the different components of a neutron star and the poor observational data are not yet decisive to select one of them in an unambiguous way.
However it is possible to give some important parameters that can be estimated from observations and compared with theory. Some basic model of a rotating neutron star can be derived.
According to the current models a neutron star is formed in the core-collapse of a massive star at the end of its evolution.
It is possible to obtain some estimates on the rotational frequency by assuming conser-

vation of angular momentum. Let's assume a star with initial radius R$_{in}\approx 10^9$ m and period of about a couple of week, e.g. P$\approx 10^6$ s. After the collapse in a supernova event, by imposing angular momentum conservation, the final angular velocity of the resulting neutron star will be $\Omega_{fin} = \Omega_{in}(R_{in}/R_{fin})^2$. Assuming a ratio between radii of 10^5 we obtain $\Omega_{fin} \approx 2\pi/10^{-4}$s., corresponding to a period P$\approx 10^{-4}s$. This esimates are in good agreement with the order of magnitude of the observed pulse periods.

3.2.1 Mass and radius

According to current models the mass of a neutron star should be of about 2 $M_\odot$, compatible with the first estimates of Oppenheimer and Volkoff in 1939 (Shapiro & Teukolsky, 1983). A direct and accurate estimate of neutron star mass can be obtained from the observations of binary pulsars (Stairs, 2004). The measurement are in good agreement with an assumed mass of about 1.4 $M_\odot$(in agreement with the Chandrasechkar limit), whereas a long recycling period appears to increase the mass as expected.
The estimate of neutron star radius is somewhat difficult to obtain from observations. a method is to observe thermal emission from neutron star surface in optical and X-rays. This method may yield the best estimates and uses the observed luminosity to infer the size of the emitting region. However the presence of strong gravitational field of the neutron star and of a plasma atmosphere can complicate the calculations.
The gravitational field of the neutron star introduce gravitational redshift that alters the flux distribution and inferred temperature. The corresponding radius R_{obs} inferred is larger than the intrinsic value of radius R as:

$$R_{obs} = \frac{R}{\sqrt{1 - 2GM/Rc^2}} = \frac{R}{\sqrt{1 - R_S/R}} \tag{3.1}$$

where R, M are the radius and mass of the neutron star and G the Newton's gravitational constant, while R_S is the Schwarzschild radius.
The presence of a thin atmosphere surrounding the neutron star alter the spectrum by introducing deviation from a pure black-body spectrum. In particular intense magnetic fields can alter the luminosity distribution by introducing hotter and cooler spots that can be misinterpreted.
Constraints on the radius can be derived from some considerations (Lorimer & Kramer, 2004; Shapiro & Teukolsky, 1983). The minimum radius R_{min} can be for example derived from some equations of state with smooth transition between high-density and low-density regions. In this way an estimate of minimum radius is:

$$R_{min} = 1.5 R_S = 6.2\ km \frac{M}{M_\odot} \tag{3.2}$$

The maximum radius R_{max} can be derived from stability arguments against break-up due to centrifugal forces. In this case it can be estimate that:

$$R_{max} \simeq \left(\frac{GMP^2}{4\pi^2}\right)^{\frac{1}{3}} = 16.8\ km \left(\frac{M}{M_\odot}\right)^{1/3} \left(\frac{P}{ms}\right)^{2/3} \tag{3.3}$$

For the millisecond pulsar PSR1937+21, one of the most rapid pulsars this estimate lead to a radius of 22.6 km assuming a mass of 1.4 $M_\odot$. Most of the theoretical model predict

radius in the range 10-12 km, that can be used in most of the subsequent estimates. These radii are of the order of about 3 times the Schwarzschild radius, demonstrating that these objects are almost black holes, and as such are very dense objects and subject to very intense gravitational effects near the surface (Lorimer & Kramer, 2004).
The moment of inertia I of a neutron star can be written as $I = kMR^2$, where $k = 0.4$ for a sphere of uniform density. For a neutron star the value of k depends on the density profile and hence on the equation of state.
Most of current models predict a values in the range $k = 0.3 - 0.45$ that imply a mass-radius value of about 0.1-0.2 $M_{\odot}\mathrm{km}^{-1}$. In most of cases a value of $I = 10^{45}$ g cm^2 is used considering the conventional values of $k = 0.4$, $M = 1.4M_{\odot}$and R=10 km.

3.2.2 Structure

The structure of a neutron star is strongly dependent on the equation of state. Assuming conventional values now presented it is possible to obtain a mean density $\rho_{mean} \simeq 6.7 \times 10^{14}$ g cm^{-3}. This value is greater than the nuclear density of $\sim 2.7 \times 10^{14}$ g cm^{-3}. In reality a neutron star is not a sphere of uniform density but it is composed by several layers. An example of one of the most common models is presented in Fig 3.2.
Observation of glitches in young pulsars suggest the presence of a solid crust with density $\rho \simeq 10^6$ g cm^{-3} composed mainly by iron nuclei surrounded by a sea of degenerate electrons.
In the inner crust the protons and electrons interact to form neutrons that creates neutron-rich nuclei. Passing the *neutron drip point* at density $\rho \simeq 4 \times 10^{11}$ g cm^{-3} several hundreds of meters below the surface, the number of free neutrons increase rapidly.
The crust dissolve at density $\rho \simeq 2 \times 10^{14}$ g cm^{-3}, where a sea of superfluid neutrons is present with a minor part of superconducting electrons and protons.
The structure of the inner core differs from various theories, in most extreme cases is made up by quarks or exotic matter.

3.3 Spin down in pulsars

Pulse periods are observed to increase with time. The rate of increase $\dot{P} = dP/dt$ can be related to the rate of loss of rotational energy E_{rot}:

$$\dot{E}_{rot} = -\frac{dE_{rot}}{dt} = 4\pi^2 I\dot{P}P^{-3} \simeq 3.95 \times 10^{31} erg\ s^{-1} \left(\frac{\dot{P}}{10^{-15}}\right)\left(\frac{P}{s}\right)^{-3} \tag{3.4}$$

where we have assumed a conventional value of $I = 10^{45}$ g cm^2. Only a tiny part of this energy loss is converted in electromagnetic emission, while most of it is converted to bulk energy of particles of the *pulsar wind*.
Pulsars are neutron stars with very strong magnetic fields and for modeling purposes only the dominant dipole component can be considered. According to classical electrodynamics a rotating magnetic dipole with magnetic moment **m** radiates an electromagnetic wave at its rotation frequency (Jackson, 1962). With this scheme a toy model of dipole emission from pulsars can be built, where the axis of magnetic field is inclined by an

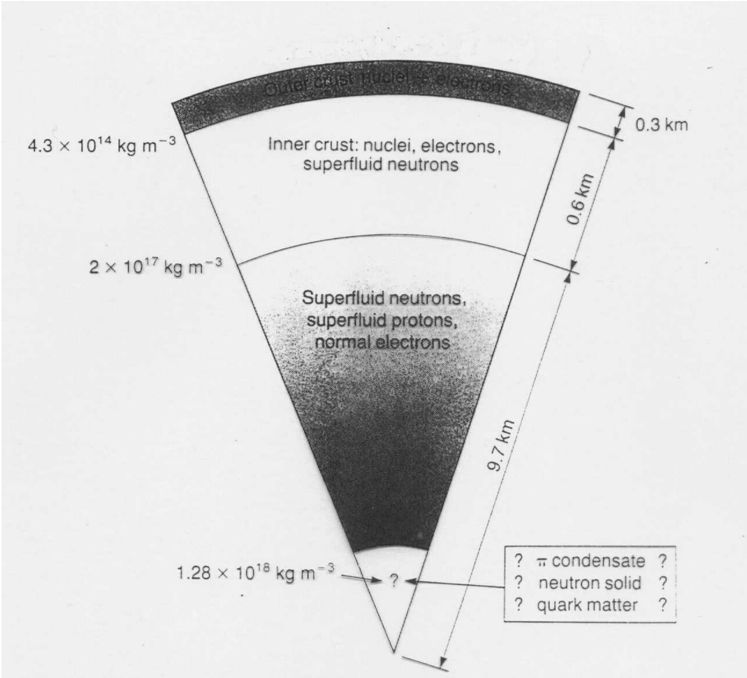

Figure 3.2: A representative model showing the internal structure of a 1.4 $M_{\odot}$neutron star. From (Shapiro & Teukolsky, 1983)

angle α from the rotation axis. A sketch of the model is displayed is Fig. 3.3. Let's consider a neutron star with radius R, magnetic moment **m**, and angular velocity $\mathbf{\Omega}$. The direction of **m** is inclined by an angle α with respect to the rotation axis. Actually the observer's line of sight can be at any angle with respect to the rotation axis. The magnetic dipole varies with time as:

$$\mathbf{m} = \frac{1}{2}BR^3[\mathbf{e}_{\parallel}\cos\alpha + \mathbf{e}_{\perp}\sin\alpha\cos(\Omega t) + \mathbf{e'}_{\perp}\sin\alpha\sin(\Omega t)] \tag{3.5}$$

where $\mathbf{e}_{\parallel}$ is the unitary vector parallel to the rotation axis and $\mathbf{e}_{\perp}$ and $\mathbf{e'}_{\perp}$ are fixed unit vectors mutually orthogonal to $\mathbf{e}_{\parallel}$. The radiation power emitted by by the time-varying magnetic dipole is:

$$\frac{dE}{dt} = -\frac{2}{3c^3}|\ddot{\mathbf{m}}|^2 = -\frac{B^2R^6\Omega^4\sin^2\alpha}{6c^3} \tag{3.6}$$

The radiation is modulated by the rotation velocity Ω and it vanishes when $\alpha = 0$. We assume that the emitted power is supplied by the rotational energy $E_{rot} = \frac{1}{2}I\Omega^2$, then equating the first derivative of E_{rot} with Eq. 3.6 we obtain:

$$\dot{\Omega} = -\left(\frac{B^2R^6\sin^2\alpha}{6c^3I}\right)\Omega^3 \tag{3.7}$$

It is possible to write this equation in a more general way using the frequency $\nu = 1/P$ rather than angular speed we obtain:

$$\dot{\nu} = -K\nu^n \tag{3.8}$$

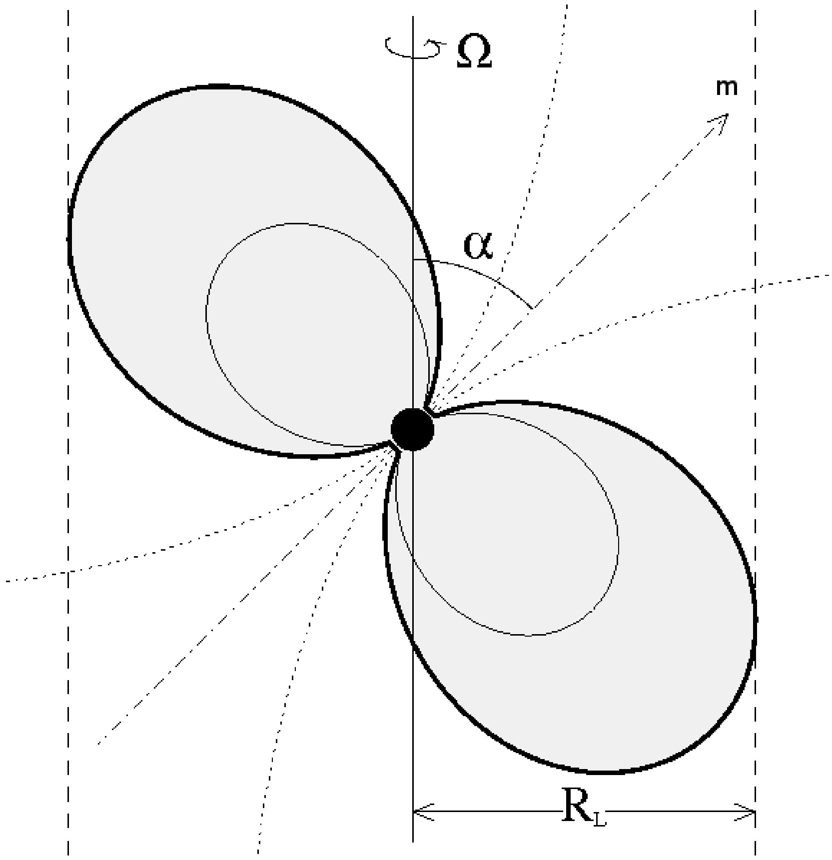

Figure 3.3: A schematic representation of pulsar and its magnetosphere, with the angular velocity Ω, the magnetic moment $\mathbf{m}$. The angle between magnetic axis and rotation axis is indicated by α. R_L indicates the radius of the *light cylinder* (See next Chapter)). Image from (Fierro, 1995).

where n is called *braking index* and K is usually assumed to be constant. From Eq. 3.6 we expect that pure magnetic dipole breaking lead to n=3. However, other dissipation mechanisms may exist (e.g. a wind of outgoing particles) that can also carry out part of the rotational energy. It has been demonstrated that both magnetic dipole braking and wind of outgoing particles lead to the same scaling as given in Eq. 3.8 (Michel & Li, 1999).
If the second derivative of frequency can be measured it is possible to determine the braking index n.

$$n \equiv \frac{\nu\ddot{\nu}}{\dot{\nu}^2} \tag{3.9}$$

In most of cases $\ddot{\nu}$ is affected by *timing noise*, but for few pulsars so far n has been calculated and the results range from n=1.4 to n=2.9 (Lorimer & Kramer, 2004).
These values indicate that the assumption n=3 is actually not correct. Nevertheless, this supposition is useful to *define* some useful quantities that are used to characterize the basic properties of a pulsar. It is important to remember that the resulting quantities are always model-dependent order-of-magnitude estimates.

3.3.1 Age estimates

Equation 3.8 rewritten in function of the period P becomes $\dot{P} = KP^{2-n}$. This equation can be integrated assuming $n \neq 1$ and constant K. The age T of the pulsar is then:

$$T = \frac{P}{(n-1)\dot{P}} \left[1 - \left(\frac{P_0}{P} \right)^{n-1} \right] \tag{3.10}$$

where P_0 is the pulsar spin period at birth. Under the assumption that the pulsar period is much shorter than the period at birth and assuming n=3 the above equation simplifies and it is possible to obtain a *characteristic age* τ_c

$$\tau_c \equiv \frac{P}{2\dot{P}} \simeq 15.8Myr \left(\frac{P}{s} \right) \left(\frac{\dot{P}}{10^{-15}} \right)^{-1} \tag{3.11}$$

This estimate does not always correspond to the real age of a pulsar. In case of the Crab pulsar the value τ_c=1240 yr is compatible with the age of about 950 years obtained from the Supernova explosion of AD 1054. In other cases, as for PSR J0225+6449 born in supernova explosion of AD 1181, this estimates is wrong and leads to τ_c=5370 yr. This example highlights that the characteristic age must be used with care when derived readily from observations.

3.3.2 Birth period

The equation 3.10 can be rewritten for obtaining the spin period P_0 at pulsar birth as:

$$P_0 = P \left[1 - \left(\frac{n-1}{2} \right) \frac{T}{\tau_c} \right]^{\frac{1}{n-1}} \tag{3.12}$$

If T is independently known (e.g. from supernova explosion) and n is measured the birth period can be derived as in case of Crab pulsar, whose birth period was of about 19 ms.
Recent estimates suggest a wide range of birth periods of pulsars ranging from 14 ms to 140 ms. In most cases the estimated birth periods are somewhat larger than the predictions of the core-collapse models, that have still some difficulties explaining birth period as long as a few ms (Lorimer & Kramer, 2004).

3.3.3 Magnetic field strength

Observational estimates of neutron stars surface magnetic fields come mainly from the detection of cyclotron radiation features in the spectra of x-ray binaries (Truemper et al., 1978). The calculated magnetic fields from these data are in a range 10^{11}-10^{12} G. Under the assumption of dominant dipole braking it is possible to obtain an estimate of the surface magnetic field B_S from Eq. 3.6:

$$B_S = \sqrt{\frac{3c^3}{8\pi^2} \frac{I}{R^6 sin^2\alpha} P\dot{P}}. \tag{3.13}$$

Assuming canonical values $I = 10^{45}$ g cm^2, radius R=10 km and an angle $\alpha = 90°$, this equation leads to:

$$B_S = 3.2 \times 10^{19} G \sqrt{P\dot{P}} \tag{3.14}$$

Because of uncertainty on I and R and because α is unknown, this value of B_S should be considered only as an order-of-magnitude estimate.

3.4 Neutron star populations

Most of the information that we have today about pulsars comes from radio observations, but pulsars have been observed in all spectral ranges, from radio to high energy γ-rays. Today more than 1700 pulsars have been detected (Lorimer & Kramer, 2004) and the number is steadily increasing thanks to the better sensitivity achieved in the radio surveys, as for example the Parkes Multibeam Survey (Lorimer & Kramer, 2004). This also mean that pulsars are the largest sample of neutron stars today available. Pulsars appear to be concentrated on the Galactic plane in a layer of about 450 pc of thickness and within a radial distance of about 10 kpc from Galactic Center (Fig. 3.4). Measurements of their velocities show that they are moving at typical speed of 100 km s^{-1} away from the Galactic plane but some are much faster.
Most of pulsars periods P lie in a range $\approx 0.25\ s < P < 2\ s$. The longest observed period is P$\approx$ 10 s. For all pulsars a steady increase of the period is observed with typical value of about 10^{-15} s/s. This slowdown can be interpreted as rotational energy loss due to radiation emission. A powerful tool for looking at pulsars evolution and statistics (as

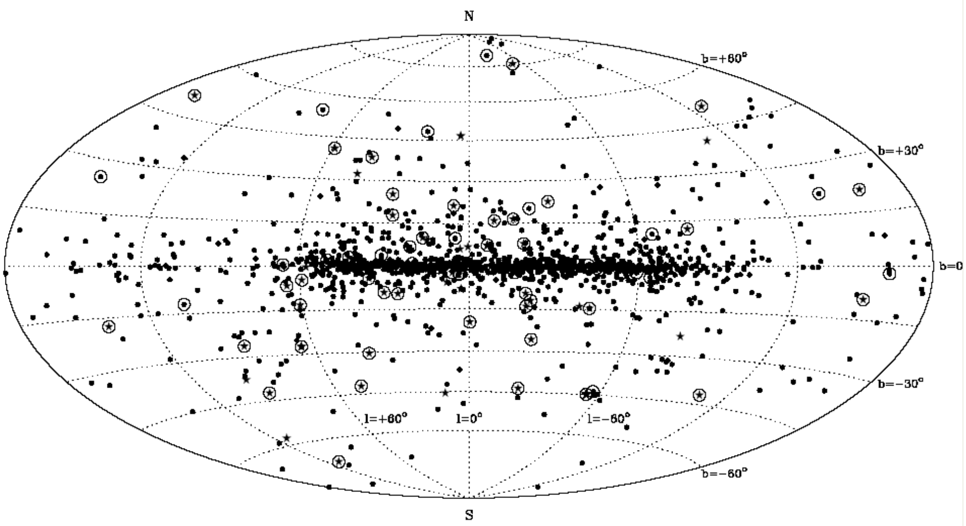

Figure 3.4: Distribution of 1395 pulsars in the Galaxy. Pulsars with period less than 2 s. are marked with a star. From (Seiradakis & Wielebinski, 2004)

the HR diagram for normal stars) is the so-called *P-$\dot{P}$ diagram*, an example of which is shown in Fig. 3.5. In this diagram are represented also lines with equal surface magnetic field B_S and characteristic age τ_c as defined in previous Section.
The distribution of periods and slowdown rates suggests that most of pulsars start their

lives with period below 100 ms, follow similar evolutionary paths and stop emitting after a few million years. This model leads to a birthrate in our Galaxy of about 1 per 50 years, consistent with an origin in a supernova explosion.

A minor group of pulsars have very short periods, less than $\approx$ 20 ms. These so-called

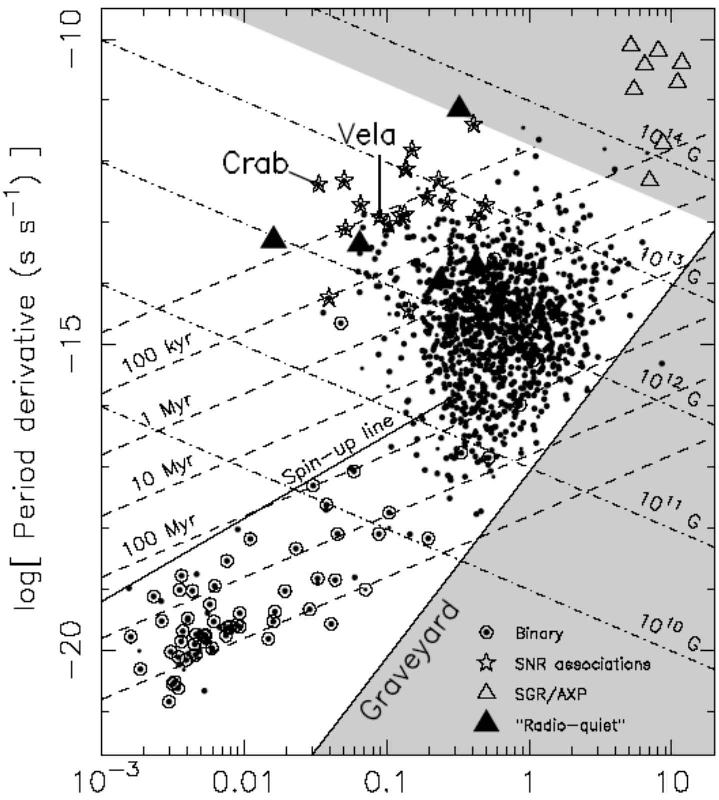

Figure 3.5: The P-$\dot{P}$ Diagram for 1395 pulsars. From (Seiradakis & Wielebinski, 2004)

millisecond pulsars (MSPs) show much smaller slowdown rates, due to much smaller magnetic fields (See Fig. 3.5). They are believed to be "recycled" pulsars, i.e. old pulsars that have been "rejuvenated" by a spin-up process involving a binary partner in accretion on the neutron star.

Another interesting subset of pulsars are those in a binary system. In contrast to what happens for ordinary stars, that are mainly in multiple systems, only 2 % of pulsars have been found in binary systems (Fierro, 1995). This discrepancy can be explained by considering their violent birth in supernova explosion. Even if in origin the star belong to a multiple system, the supernova explosion can disrupt the system leaving in consequence the pulsar alone.

Binary pulsars are a powerful tool for testing several physical laws, in particular for testing gravitational physics.

The first binary pulsar PSR B1913+16 was discovered by Hulse and Taylor at Arecibo in 1974 (Hulse & Taylor, 1975). This pair of neutron stars orbit with a period of 7.75 hours and will coalesce in about 200 Myr due to the emission of gravitational energy the expense of orbital energy. The measurement of orbital shrinkage ($\sim$1 cm/day) due to this effect was the first experimental proof of existence of gravitational waves. Hulse and

Taylor received the 1993 Nobel Prize for Physics in recognizement of this achievement. More recently the discovery of PSR J0737-3039, the first *double pulsar* system opened new possibility to the test of General Relativity. This system is composed by a 22.7 ms pulsar orbiting a 2.77 pulsar and it promise to put more stringent limit on strong-field gravitational theories than PSR B1913+16 (Hulse & Taylor, 1975).
The discovery of pulsars emitting in optical, X-rays and also γ-rays has imposed a slightly change in the definition of the word *pulsar*, no more simply as pulsating *radio source* but as *neutron star that emits radiation that is pulsed due to rotation and powered by rotational energy*(Lorimer & Kramer, 2004). This new definition encompasses also pulsar like Geminga, that emit radiation because of rotation energy loss but it is not yet detected as a radio source.
In contrast to these *rotation-powered* pulsars and *accretion-powered* pulsars, a new classes of rotating neutron stars have been observed as high-energy sources that emit short and sporadic burst of radiation in X-ray and γ-rays.
With inferred spin period of 5-12 s the energy output is too large to be accounted only to the loss of rotational energy. It is believed that emission processes are related to their magnetic fields that are inferred to be very strong, of the order of 10^{15} G. These new objects are called *magnetars* and should include both the so-called *soft-gamma repeaters* (SGRs) and the *Anomalous X-ray pulsars* (AXPs) (Duncan & Thompson, 1992; Kaspi, 2004).

3.5 Radio emission from Pulsars

The radio emission is very high and it is believed that it should be due not to thermal processes but to coherent non thermal processes. The units used to measure the flux density is the *Jansky*(Jy) (1 Jy = $10^{-26} W m^{-2} Hz^{-1}$). For the sample of pulsars in the ATNF catalog [1] the flux densitities measured at 1.4 GHz range from about 20 μJy to about 5 Jy (Lorimer & Kramer, 2004). An important phenomenon that the radioastronomers must deal with is the pulse dispersion of radio waves when they propagated through the ionized InterStellar Medium (ISM). In this situation the pulses observed at higher radio frequencies arrive earlier at the telescope than the lower frequency counterparts. Hewish (Hewish et al., 1968) correctly interpreted this effect as the frequency dependence of the group velocity of radio waves as they traverse the ISM. In this case the delay in pulsar arrival times is inversely proportional to square of the observing frequency. The constant of proportionality is known as the *dispersion measure* (DM), i.e. the integrated columns density of free electrons n_e along the line of sight. As a very crude estimate, the DM can be used to determine the distance as $d \approx DM/n_e$ and using a rough $n_e \approx 0.03 cm^{-3}$. A more sophisticated way is to use the independently known distances to calibrate the electron density in the Galaxy.
The observation of radio pulsar profiles gives a lot of information about pulsars. Most of the intensity is concentrated in a small fraction of the period (the *duty-cycle*) of about 1%-5%. The individual pulses are slightly different one from each other but the integrated profile over hundreds of periods is remarkably stable as shown in Fig 3.6.

[1] http://www.atnf.csiro.au/research/pulsar/psrcat

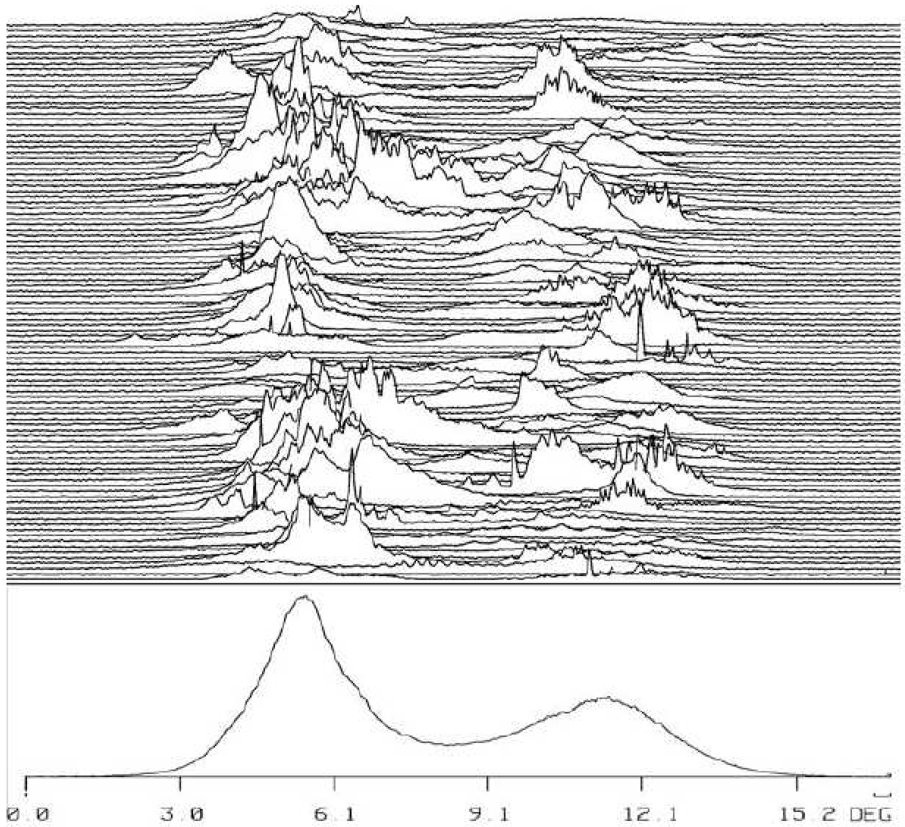

Figure 3.6: An example of the differences between single pulses. Top: The sequence of 100 single pulses from PSR 1133+16 plotted underneath each other. Bottom: By adding the above single pulses, the Integrated profile is obtained. From (Seiradakis & Wielebinski, 2004)

Some pulsars show a single peak and other show two distinct peaks, and there is no simple pattern. An example of integrated radio profiles of several at 1.4 GHz is shown in Fig. 3.7 where the variety of profiles is clearly visible.

3.6 Optical emission

Well before the discovery of pulsars a neutron star was suspected to exist in the center of the Crab Nebula. It should then not surprise that the Crab pulsar PSR B0531+21 was the first to be discovered in optical (Cocke et al., 1969) and after other measurement in optical followed at high time-resolution (Beskin et al., 1983). An example of high-resolution light curve of Crab pulsar obtained in optical using the Hubble Space Telescope is shown in Fig. 3.8. Generally pulsars are very weak in optical, and it took almost a decade to discove the Vela pulsar PSR B0833+45 as the second pulsar in optical(Wallace et al., 1977). Actually, it is worth to note that the discover in optical followed the discovery of γ-ray emission. Here are described the basic characteristics of pulsar emission in a wide range around optical, that span frequency 10^{12} Hz to 10^{16} Hz containing infrared, optical and ultraviolet frequencies. This interval is sometimes

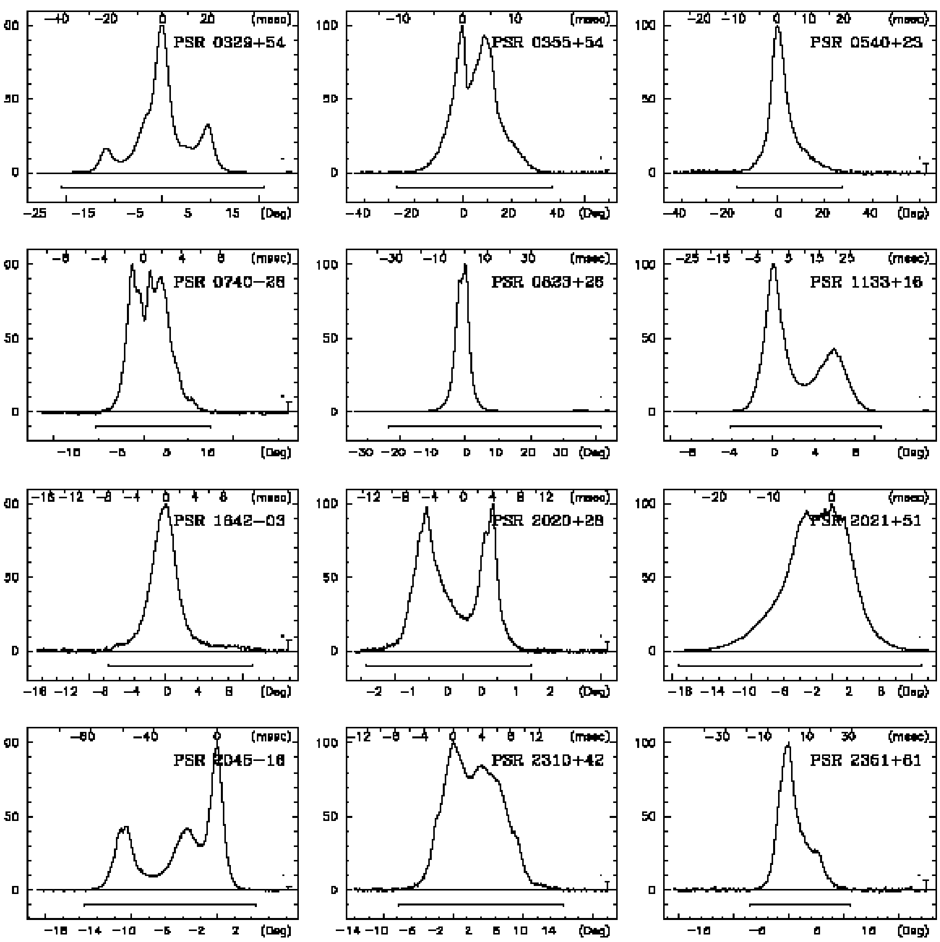

Figure 3.7: An example of the variety of radio profiles. From (Seiradakis & Wielebinski, 2004)

referred as 'optical regime' (Lorimer & Kramer, 2004).
Apart from Crab and Vela, currently two other radio pulsars are known to emit pulsed radiation in these frequencies, PSR B0540-69 and PSR 0656+14. Usually the identification of a pulsar in optical is carried through the periodicity testing of the optical light curves using radio ephemerides and comparing measured proper motion with the proper motion measured in radio. For example PSR 1929+10 has been confirmed to have optical pulsation only with periodicity test since proper motion measurement are not possible yet.
For four additional radio pulsars an optical counterpart has been found but no pulsations have been confirmed yet.
The spectrum at these frequencies range is a combination of a power law and a black body spectrum. Power law spectrum is dominant for pulsars that are very young or very old, while the black body is present mainly in middle age pulsars.
Thanks to its brightness Crab pulsar is the only pulsar with polarization measurements in optical (Lorimer & Kramer, 2004).
There is no apparent correlation between optical spectra and high energy spectra, and

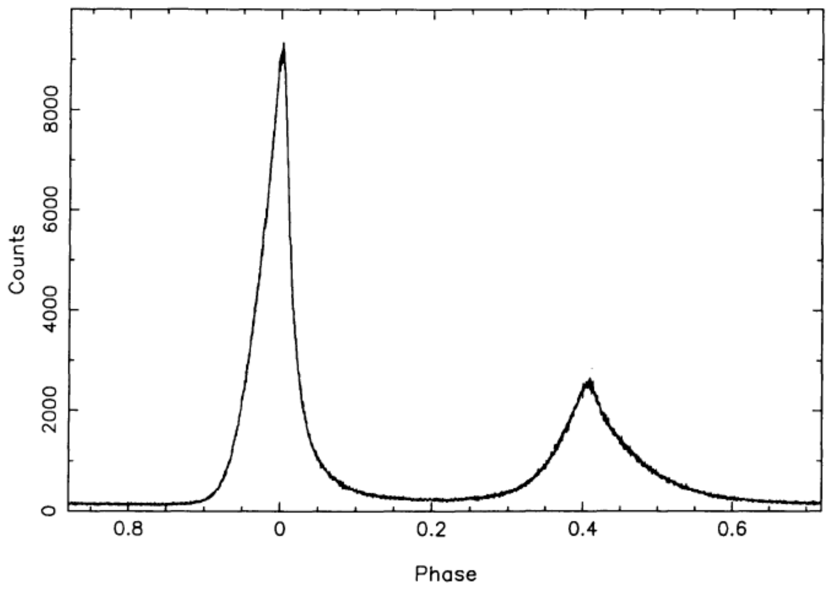

Figure 3.8: Composite pulse profile of the Crab pulsar obtaine with the High speed Photometer of the Hubble Space Telescope in the visible (400-700 nm) with effective time resolution of 22.8 μs. the zero of phase is the peak of the main pulse. From (Percival et al., 1993)

optical spectrum is not always the extrapolation of X-ray spectrum down to lower energies.

Another pulsar that show pulsed emission in optical is Geminga, that is important since it does not show pulsation in radio. This source was first discovered as point source in γ-rays by SAS-2 and later the observation of Einstein satellite find an X-ray counterpart (Bignami et al., 1982). Using the X-ray pulsed emission detected by ROSAT at a period of about 237 ms the γ-ray a periodicity search was performed and γ-ray pulsation form Geminga was discovered.

Today a firm detection in radio is still lacking (Halpern & Holt, 1992). A marginal detection at frequency between 40 Mhz and 102 MHz has been claimed but not confirmed yet (Kuz'min & Losovskii, 1997).

The lack of radio emission, that put Geminga in the so-called *radio-quiet* pulsars, could be due to a extremely low radio flux.

Another possible explanation is related to high-energy emission models. While the narrower radio beam could be not directed toward the Earth the large high-energy can be observed.

3.7 High-energy emission

Pulsars are known to be also X-ray and γ-ray emitters. About three months after detection of optical pulsation from the Crab pulsar two flight rockets found also evidence for X-ray pulsed emission (Fritz et al., 1969).

Thanks to the last-generation space observatories like ROSAT, *Chandra* and *XMM-*

Newton today about 15 isolated pulsars are known to emit pulsed radiation in X-rays and 6 millisecond pulsars (Lorimer & Kramer, 2004).
As in the optical regime the spectrum in X-rays show generally a power-law component and a thermal component. The power law emission is believed to take place in the magnetosphere and extend up to γ-rays (Becker & Truemper, 1997). The black body component should come from surface and may still show a modulation due to rotating hot polar cap. The black body spectrum can be modified by the presence of the thin atmosphere of the neutron star.
The presence of X-ray emission from Pulsar Wind Nebula contributes to make harder the spectrum observation at these energies.
The identification of an X-ray pulsar can be done by folding the X-ray data at the radio ephemerides and testing the periodicity. Another set of about 30 radio pulsars show an X-ray counterpart for which a periodicity is not yet been tested.
According to spectral features the X-ray pulsars can be divided in three main classes. The *young*, or *Crab-like* pulsars show a strong nonthermal emission and a double peak that, if detected, seems to coincide with optical light curve. The *middle-age* pulsars show a spectrum composed by a power law and a black body spectrum and an energy-dependent light curve. The Vela pulsar, that can be included in this group, is particularly interesting since it shows a more complicated light curve and also show an optical counterpart. The class of *millisecond X-ray pulsars* show power law, and/or thermal component that could be mainly due to Polar Cap heating. A particular example is PSR J0437-4715 that appear to show a double blackbody spectrum, probably due to anisotropic PC heating.
The detection of pulsars as gamma-ray emitters came some years later in 1972 thanks to the NASA *Small Astronomy Satellite* (SAS 2), which saw emission from Crab (Kniffen et al., 1974) pulsar and discovered emission from Vela pulsar (Thompson et al., 1975). Gamma-rays from Crab were first discovered by balloon experiments (Browning et al., 1971). Today seven pulsars are known to emit γ-rays. The emission of γ-rays from pulsar is believed to take place in the magnetosphere that surround pulsars and currently two main classes of models are proposed for explaining this emission, the *Polar Cap* and *Outer Gap* model.
A more detailed description of pulsar γ-ray emission characteristics and theoretical models to explain it are presented in next Chapter. In particular the GLAST capabilities for γ-ray pulsar science will be also presented.

3.8 Summary

Soon after their discovery pulsars appeared to be extremely interesting objects and fundamental tools for testing law of physics. Pulsars are believed to be rapidly-rotating neutron stars with an very intense magnetic field. The study of neutron star is of fundamental importance to better understand the physics of pulsars and their emission. Pulsars emit in the whole electromagnetic spectrum, and observations show that several mechanisms are active at different energies. A review of their properties in radio, optical and X-rays has been given, while the γ-ray emission properties will be presented in the next Chapter.

Chapter 4

Gamma-ray emission from pulsars

In the decades since the discovery of pulsars it has become clear that these objects emit across the whole elecromagnetic spectrum. Studies of pulsar emission provided a vast amount of information about physics of neutron stars structure and evolution.
According to first models, pulsars were identified with rotating neutron stars with enourmously strong magnetic fields.
From spectral studies it became evident that most of radiation is emitted at high energies, in particular in the γ-ray range. Unfortunately the γ-ray sources photon flux is very weak, so high-sensitivity instruments are required. Presently only seven pulsars have been detected, but some general features of the γ-ray emission are now clear.
The γ-ray spectrum appears to be non-thermal and the vacuum magnetic dipole model is unable to describe high-energy emission from pulsars. It was recognized that pulsars should be surrounded by a plasma-filled *magnetosphere*, that is responsible of most of the emission processes from radio to γ-rays. According to current models, particles can be accelerated in the magnetosphere up to high energies so that they can emit radiation. This emission is modulated in the observer's frame by the neutron star rotation and beaming is another important parameter in current model development.
In this Chapter the characteristics of γ-ray emission from pulsars are presented based on the most recent observations. The physics of the magnetosphere is then introduced and the main γ-ray emission models are reviewed. The capabilities of GLAST to constrain these γ-ray models are then discussed.

4.1 Gamma-ray pulsars: an observational approach

Our most current knowledge about pulsar γ-ray emission comes from the results of the CGRO instruments, in particular from the EGRET telescope. Thanks to EGRET three new γ-ray pulsars were discovered and those already-known were studied with higher details (Nolan et al., 1996).
Before CGRO pulsed γ-ray emission from only Vela and the Crab were established, both associated to SNR, while Geminga was known only as an isolated γ-ray source. EGRET discovered PSR B1706-44 (Thompson et al., 1992), PSR B1055-52 (Fierro et al., 1993) and PSR B1951+32 (Ramanamurthy et al., 1995).
The modulation with a period of 237 s. from Geminga was first detected in X-rays (Halpern & Holt, 1992) and then confirmed by EGRET in γ-rays (Bertsch et al., 1992).

BATSE and COMPTEL also detected PSR B1509-58 at lower energies (Ulmer et al., 1993).
The weakest of them (PSR B1951+32) has a statistical probability P of occurring by chance of P$\sim 10^{-9}$ using the Chi Squared method for testing periodicity [1]. For this reason this group of pulsars are sometimes referred as *high-confidence* γ-ray pulsars (Thompson, 2003).
Three other pulsars that have been suspected to be γ-ray emitters with a lower confidence level, i.e. with a chance probability using the Chi-Squared Test greater less than P$\sim 10^{-3}$ We will refer here as *low-confidence* pulsars (Thompson, 2003).
Pulsar PSR B1046-58 may be associated with 3EG B1048-5840 and has an associated X-ray source that is not pulsed (Ramanamurthy et al., 1996). The second one, PSR B0656+14, is not coincident with any 3EG sources but shows both optical and X-rays pulsed components (Kaspi et al., 2000). The third pulsar is J0218+4232; it is of particular importance because it is a millisecond pulsar, but the CGRO observation was complicated by the presence of a nearby blazar (Kuiper et al., 2000a).
The present number of known γ-ray pulsars is clearly not large enough to provide good statistics but can allow some simple conclusions from observations and comparison with other wavelengths.

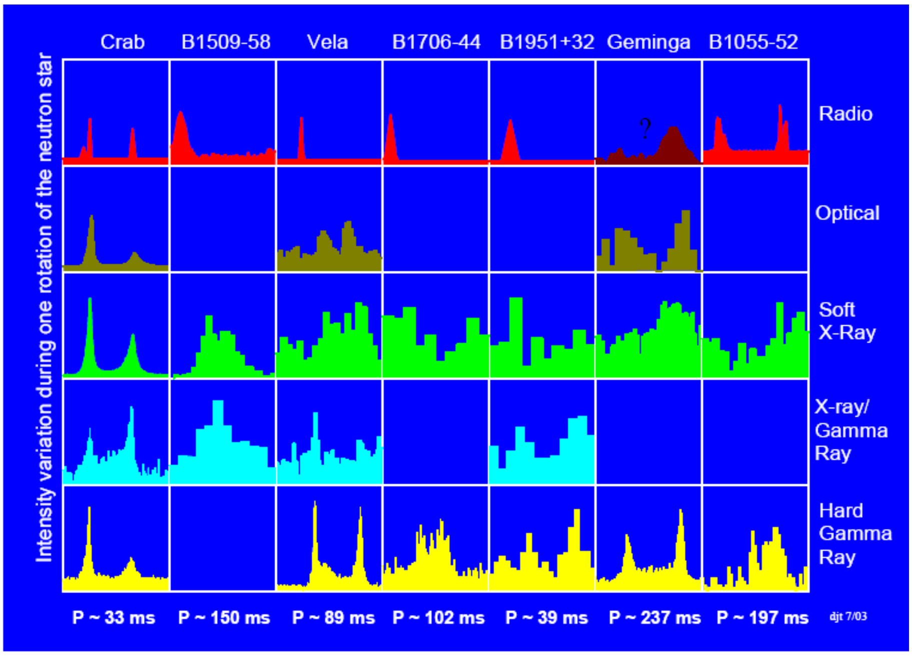

Figure 4.1: The collection of multiwavelength lightcurves from the highest confidence γ-ray pulsars. Lightcurves are in five energy bands: radio, optical, soft X-ray (<1 keV), hard X-ray/soft gamma ray (10 keV - 1 MeV), and hard gamma ray (above 100 MeV). From (Thompson, 2003).

[1]The *chance probability* here reported refer to the χ^2 periodicity test. See Ch. 6 for details.

4.1.1 Pulse profiles

In most cases the γ-ray lightcurve [2] is different from lightcurves from those in other energies, as displayed in Fig. 4.1 (Thompson, 2001, 2003). In some pulsars there is a thermal component in X-rays that suggests emission from the hot polar cap of the neutron star. This is an indication that the geometry and the emission mechanism depends on the energy and for γ-rays the emission is non thermal.
Not all pulsars are visible at high energies, e.g. PSR B1509-58, which was observed by BATSE and COMPTEL up to $\sim$ 10 MeV (Ulmer et al., 1993).
By comparing the lightcurves above 100 MeV it is evident that all γ-ray pulsars show a double peak. The lightcurves above 5 GeV for the four highest-confidence pulsars (Vela,

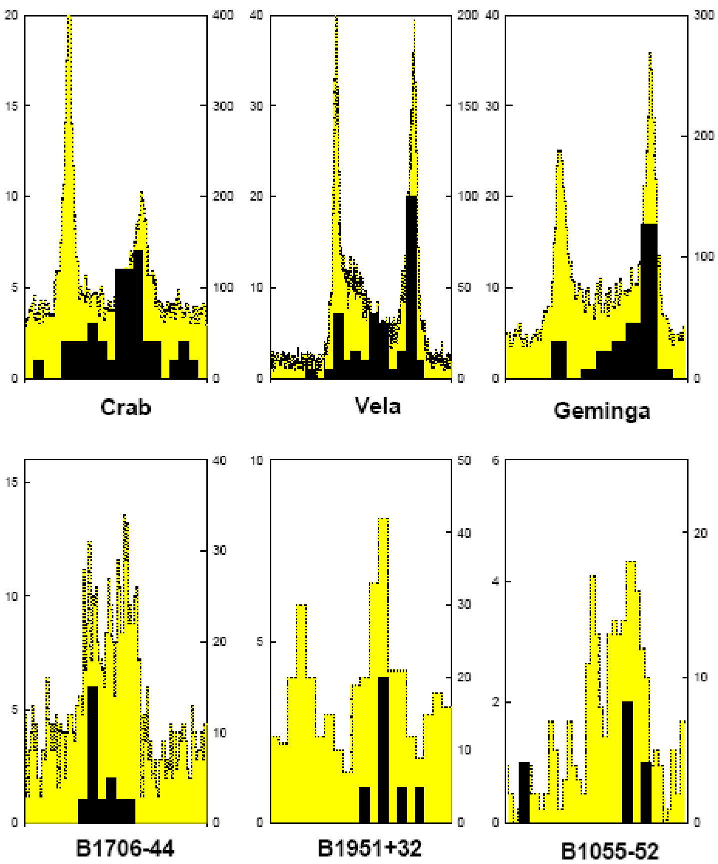

Figure 4.2: Lightcurves of the six highest confidence pulsars above 100 MeV (dotted line, right-hand scale) and above 5 GeV (dark histogram, left-hand scale). From (Thompson, 2003).

Crab, Geminga, PSR B1706-44) show only one peak, usually the trailing one. The one pulse seen for the Crab appears to be displaced from the pulse at lower energies.

[2]Referring to pulsars we will define *lightcurve* the phases curve obtained by phase-folding photon arrival times with the correct pulsar ephemerides obtained from radio observation

4.1.2 Spectral features

A multiwavelength analysis of the known γ-ray pulsars discloses some key observational facts. Most of the power is emitted in the hard X-ray and γ-ray band, as depicted in Figure 4.3, which shows the νF_ν spectrum, that gives an idea of the power emitted per logarithm of energy.
The dominant power goes from 100 keV for Crab up to 10 GeV for PSR B1951+32. For Vela, Geminga and PSR B1055-52 a thermal component in X-rays is clearly visible,

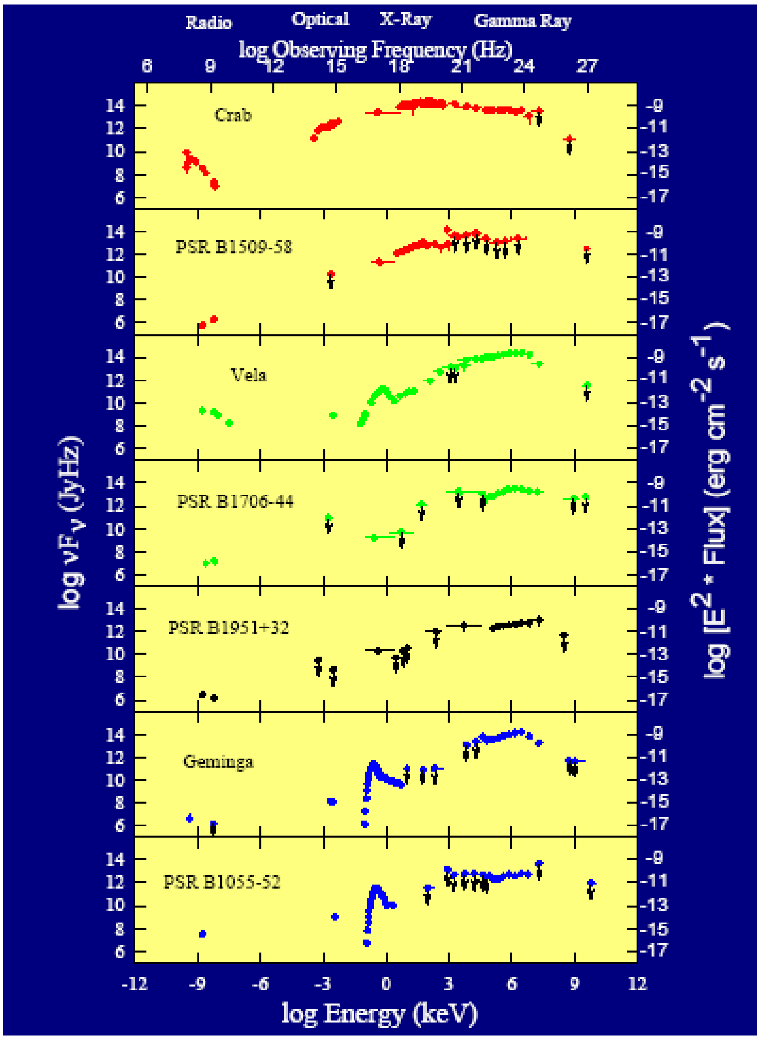

Figure 4.3: The multiwavelength spectra of the highest confidence γ-ray pulsars. From (Thompson, 2003).

suggesting an emission taking place from the hot neutron star surface. In contrast, the high γ-ray emission shows a nonthermal spectrum.
For all pulsars the γ-ray spectrum is a power law with spectral index of ~ 2 (Nolan et al., 1996; Nel & De Jager, 1995) and there is also a spectral break observed at energies 1-4 GeV (Nolan et al., 1996; Fierro, 1995).
The energy at which this break occurr appears to be related with the surface magnetic field of the pulsar, estimated using Eq. 3.3.3. The pulsars with the strongest fields

have lower energy breaks. PSR B1508-58, which has the highest calculated magnetic field, has the lowest break energy and actually was observed only up to the COMPTEL energy band.
The absence of detected pulsed emission detected by Cherenkov Telescopes (e.g. MAGIC or H.E.S.S.) indicates a spectral cutoff. The region above 10 GeV, where EGRET run out of photons, turns out to be a very important band for studying this cutoff and will be observed by GLAST.
A phase-dependent spectral analysis was conducted in the EGRET data on the three brightest γ-ray pulsars (Vela, Crab and Geminga) and no complete phase-dependent pattern was detected (Fierro, 1995). However, a trend in phase-dependent spectra was found, where the peaks are softer than the interpeak and harder than the outer wings of the profile (Fierro, 1995; Nolan et al., 1996). Improving phase-dependent spectral measurements is expected to be a very powerful tools to study the emission processes.

4.1.3 Gamma-ray pulsars compared with radio pulsar population

By plotting the $P - \dot{P}$ *diagram* (See Ch. 3 of the presently known pulsars, as in Fig. 4.4 it is possible to compare the γ-ray pulsars with the general population.
The plot also displays the lines of equal calculated magnetic field (Eq. 3.3.3). The observed γ-ray pulsars show magnetic fields greater than $\sim 10^{12}$ G.
The characteristic age, defined by Eq. 3.11, shows that γ-ray pulsars, except PSR J0218+4232 are young objects, as for example the Crab pulsar.
The open field line voltage, that can be related to the outflow current of charged particle from neutron star, is also recognized to be an important pulsar parameter (Thompson, 2003).

4.2 Basic theory of pulsar magnetospheres

The basic model for pulsar emission based on magnetic dipole emission (Ch. 3) provides order-of-magnitude estimates that are generally in agreement with observations. This model is based on some assumptions that strongly limit its physical applicability:

- Vacuum surrounding pulsar;
- No Relativistic effects at the light cylinder;
- No detailed calculations of electromagnetic fields inside or outside the neutron star;

According to present models the radiation emitted from pulsars has at least two possible origins. The thermal emission is believed to originate from the hot surface of the neutron stars, as observed sometimes in optical and X-rays. The nonthermal component comes from charged particles that are accelerated along the magnetic field lines up to high energies. The emission does not take place in a vacuum, but in the plasma of the *magnetosphere*.
Goldreich and Julian presented (1969) electrodynamical model of a pulsar where for the

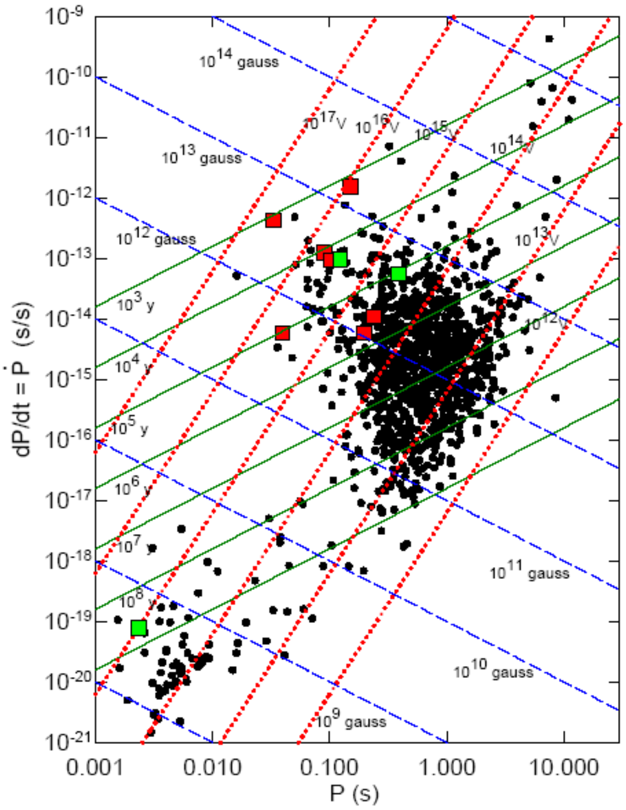

Figure 4.4: The $P - \dot{P}$ diagram for most recently discovered pulsars (black dots), compared to γ-ray pulsars, obtained from the ATNF Catalog of pulsars.The red squares indicate high-confidence γ-ray pulsars, and green squares the low-confidence γ-ray pulsars. At low-right corner it is clearly visible the candidate γ-ray pulsar PSR J2214+0238. From (Thompson, 2003).

first time it was demostrated that pulsars must be surrounded by a trapped, corotating plasma (Goldreich & Julian, 1969).

4.2.1 The need for a magnetosphere

We begin with the first quantitative model: a rotating, magnetized neutron star, the Goldreich-Julian "aligned rotator" model (1969) (Goldreich & Julian, 1969; Lorimer & Kramer, 2004).

They began with a rotating neutron star in a vacuum with a dipole magnetic field aligned with rotation axis. They then showed that electrostatic forces acting at the neutron star surface can extract charged particles that fill the surrounding forming a co-rotating magnetosphere.

The assumption of infinite conductivity is fundamental in the model and is in agreement with the current model of neutrons star interiors. For infinite conductivity the charges arrange themselves in order to balance the Lorenz force acting due to rotation, the unipolar inductor. The resulting electric field in the interior will satisfy:

$$\mathbf{E} + \frac{1}{c}(\mathbf{\Omega} \times \mathbf{r}) \times \mathbf{B} = 0 \tag{4.1}$$

This correspond to a "force-free" condition, so the magnetic lines are also equipotential lines, since $\mathbf{E}\cdot\mathbf{B}$=0. As a first approximation the magnetic field can be modeled as a dipole. In spherical coordinates the magnetic field can be written as:

$$\mathbf{B_{pol}} = \frac{2B_0R^3}{r^3} cos\theta \mathbf{e_r} + \frac{B_0R^3}{r^3} sin\theta \mathbf{e}_\theta \tag{4.2}$$

The last assumption of *aligned rotator* is important to simplify calculations but at the same time contains all the important concepts related to magnetosphere physics. In particular the aligned rotator is useful to show the importance of magnetosphere and of radiation processes taking place in it. However, it is important to remark that the aligned rotator is not a pulsar, because it cannot "pulse" for an observer, since the rotation and magnetic axis are parallel.
Using the Eq. 4.1 and the Laplace equation $\nabla^2\Phi$=0 for the electric potential Φ it is possible to see that the electric charge on the surface induce an external quadrupole field given by:

$$\Phi(r,\theta) = \frac{B_0\Omega R^5}{6cr^3}(3cos^2\theta - 1) \tag{4.3}$$

The electric field tangent to the surface must be continuous while the radial electric field have a discontinuity caused by the surface charge. At the neutron star surface the component of electric field parallel magnetic field is given by

$$E_{||} = \frac{\mathbf{E}\cdot\mathbf{B}}{B} = -\frac{\Omega R}{c} B_0 cos^3\theta \simeq 6 \times 10^{10} B_{12} P^{-1} V cm^{-1} \tag{4.4}$$

where B_{12} is the magnetic field at the surface expressed in units of 10^{12} G and P, the period, is expressed in s. The computed the electrostatic force $eE_{||}$ at the surface exceed the gravitational force by a factor of $5 \times 10^8 B_{12} R_6^3 cos^2\theta/PM$ for protons (M is the neutron star mass) and of $8 \times 10^8 B_{11} R_6^3 cos^2\theta/PM$ for electrons (Goldreich & Julian, 1969).
Goldreich and Julian concluded that the surface charge layer cannot be in dynamical equilibrium. They attempted to obtain an equilibrium solution but they found that it is not possible, thus concluding that *a rotating neutron star cannot be surrounded by vacuum* (Goldreich & Julian, 1969).

4.2.2 The Goldreich-Julian magnetosphere

The Goldreich-Julian model demonstrated that the electrostatic forces at neutron stars surface can overcome gravity and extract charges. These charge fill an external magnetosphere that have been modeled as in Fig. 4.5.
In a plasma-filled magnetosphere, assuming conductivity to be infinite and neglecting particle inertia, the situation is force-free as in Eq. 4.1.
The electric field is determined by the presence of an electric charge in the magnetosphere that is given by:

$$\rho_{GJ} = \frac{1}{4\pi}\nabla\cdot\mathbf{E} = -\frac{1}{2\pi c}\frac{\mathbf{\Omega}\cdot\mathbf{B}}{1-|\mathbf{\Omega}\times\mathbf{r}/c|^2} \simeq 7 \times 10^{-2} B_z P^{-1} cm^{-3} \tag{4.5}$$

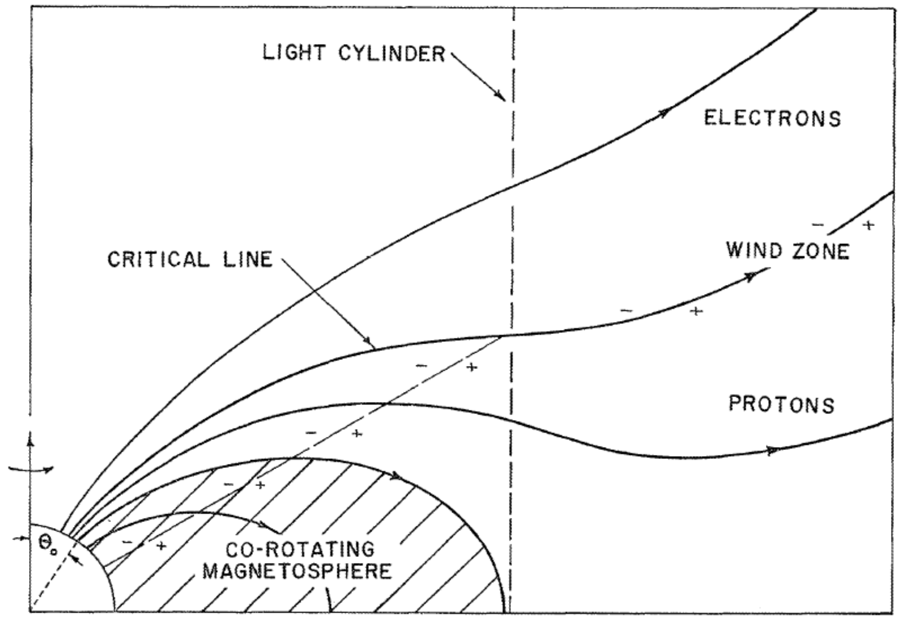

Figure 4.5: A schematic representation of pulsar magnetosphere, from (Goldreich & Julian, 1969). The magnetosphere is charge-separated and the equipotential lines are divided by the critical line, where the potential is equal to the potential of interstellar medium. From (Goldreich & Julian, 1969)

where B_z is the z-component of magnetic field in Gauss. This is called *Goldreich-Julian density* or *corotation density*. The magnetosphere is made up of particles coming from the surface and Eq. 4.1 implies that these charges are in strict corotation with the star. According to Eq. 4.5 is can be seen that there is a surface where $\mathbf{\Omega} \cdot \mathbf{B} = 0$, so that the charge on this surface is zero. This surface is called *null surface*.

However, strict corotation cannot exist beyond a surface where the tangential speed is equal to the speed of light. This cylindrical surface is called the *light cylinder*, its radius being:

$$R_L \equiv \frac{c}{\Omega} = 4.77 \cdot 10^9 cm \left(\frac{P}{1s} \right) \tag{4.6}$$

Strict corotation may exist along field lines that close at distances smaller than the light cylinder, whereas those field lines that, in absence of rotation, would have closed at larger distances penetrate the light cylinder and become open field lines. The region from which these region originates defines two *polar caps*. These field lines close at large radii in the outer interstellar medium.

The edge of the polar cap is defined by the last closed magnetic field line, i.e. the field line that just touch the light cylinder. In spherical coordinates the dipolar field lines obey the equation $\frac{\sin^2\theta}{r}$ = constant. For an aligned rotator the field lines are tangent to the light cylinder at an angle $\theta = 90°$.

In this case the angular radius of the polar cap is given by:

$$\sin\theta_{pc} = (\frac{a}{R_L})^{1/2} = (\frac{\Omega a}{c})^{1/2} \tag{4.7}$$

where a is the radius of the neutron star. Therefore the radius of the polar cap is:

$$r_{pc} \simeq a \sin\theta_{pc} = a(\frac{a}{R_L})^{1/2} = 1.4 \times 10^4 (a/10^6 cm)^{3/2} (P/1s)^{-1/2} cm \quad (4.8)$$

For a magnetic field aligned with the rotation axis as in Fig. 4.5, the potential at the base of field lines near the axis is negative with respect to the exterior environment (e.g. the interstellar medium), so that negative charges stream out. Since there cannot be a net outflux of particles the potential of the lines near the edge of the Polar Cap must be positive with respect to the exterior so that positive charges can stream out from these regions.
Charged particles, that in first approximation can move only along magnetic field lines, escape to infinity only along open field lines generating an outflow current and thus a toroidal component of the magnetic field, which is larger near the critical field line that separate open field lines from the closed ones.

4.2.3 Discussion of the Goldreich-Julian model

The model of the magnetosphere of Goldreich and Julian made some interesting description of the energy loss and of its consequences on pulsar spin down.
Near the light cylinder the poloidal magnetic field and toroidal component become comparable so that the field lines are bent back to penetrate the light cylinder at an angle of about 1 rad. At the light cylinder the magnetic field is an outgoing wave, with an associated electric field **E**∼**B** that carry a Poynting flux S∼ $cB^2/4\pi$. The rate at which the pulsar loses energy can be estimated assuming as an approximation a spherical outflow:

$$\dot{E} = -4\pi R_L^2 S_L \sim -\frac{B_0^2 R^6 \Omega^4}{c^3} \quad (4.9)$$

where S_L is the Poynting flux at R_L. This value agrees in order of magnitude with Eq. 3.6 derived form the simple model of magnetic dipole, but in this case it is obtained for a plasma-filled magnetosphere and an aligned rotator.
The Maxwell stress associated with the wave field also carry angular momentum and extert a torque:

$$T_s \sim \frac{1}{8c^3}(B_0 R^3)^2 \Omega^3 \quad (4.10)$$

This torque agrees in order of magnitude with that is expected from a magnetic dipole of a rotating oblique magnetic dipole in vacuum (Meszaros, 1992).
This model of magnetosphere has some inconsistencies that have been not solved completely. The most important are (Meszaros, 1992)

- Where does the circuit utilizing the potential difference close? (*problem of return current*)
- The model envisages charges of one sign flowing through regions of the opposite charge sign
- The parallel field that is supposed to pull out charges vanish in the magnetosphere of charge ρ_c

- It is not possible to have everywhere the equilibrium charge density ρ_c streaming at velocities close to the light speed.

Nonetheless the important point is that this more sophisticated but still incomplete model give estimates that agree in order-of-magnitude with the ones given by the magnetic dipole moment. The general idea is that many elements present is this model will be conserved in a most complete model.

4.3 Models for gamma-ray emission

Some of the original assumptions of the Goldreich-Julian model have been relaxed, as for example the study of the aligned rotator. After this model several studies attempted to describe the pulsar phenomenon without restricting to the case of the aligned rotator. Currently the theoretical models take into account the emission pattern due to the non alignment of the rotation and magnetic axis, both for Polar Cap (Daugherty & Harding, 1996) and Outer Gap (Cheng et al., 1986a).
The theoretical scenario for γ-ray emission in pulsars envisage the presence of particles accelerated up to high energies that can emit high-energy photons. The capability to accelerate particles require the presence of an electric field parallel to the magnetic field lines, i.e. $\mathbf{E}\cdot\mathbf{B} \neq 0$.
This condition is satisfied in vacuum, then the model for particles acceleration in pulsars are based on the assumption of *vacuum gaps* located around the neutron star in the magnetosphere.
The models for γ-ray emission from pulsars are divided in two main categories: the *Polar Cap* (PC) model and the *Outer Gap* (OG) models, depending on the region where the emission take place. The condition of $\mathbf{E}\cdot\mathbf{B} \neq 0$ can also be satisfied in regions of charge deficit where the density is below the Goldreich-Julian density, as it happens in Polar Cap models. Fig. 4.6 illustrate the case of a pulsar where the magnetic field is not aligned with the rotation axis. The magnetic field lines are included so that the open field lines can easily be seen, as well as the null surface and the light cylinder. The Polar Cap and the Outer Gap regions are clearly indicated.
In the PC models the γ-ray emission comes from vacuum gap at low altitude (comparable with stellar radius) over the magnetic poles, where accelerated particles emit mainly through *curvature radiation* (CR), although a more recent incorporation of the model include Inverse Compton scattering (Harding, 1981; Sturner & Dermer, 1994).
In the OG models the emission comes from regions at larger distance from the star near the light cylinder, and the particles are accelerated in the gap formed above the null charge surface and along the last closed field line as shown in Fig. 4.6. The width of the Outer gaps depend on the age of pulsar. The two classes of models make some different predictions, that GLAST could check as it will be show at the end of this Chapter.

4.3.1 Polar Cap models

Polar Cap models were the first to be developed, and currently there are a lot of variations on the basic theme.
The basic approach was due to Sturrock(Sturrock, 1971).

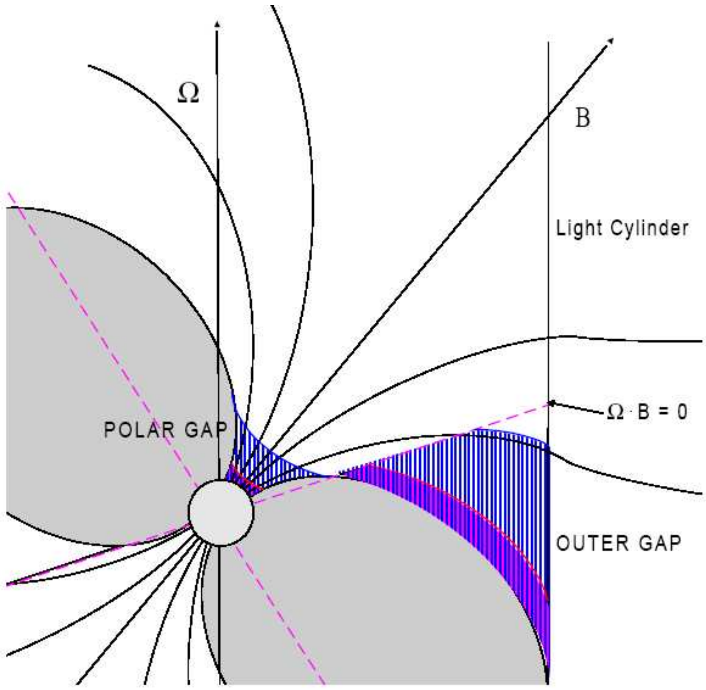

Figure 4.6: A schematic representation of pulsar vacuum gaps where charged particles are supposed to be accelerated and can emit γ-rays. In this example a non-aligned rotator is considered and the null surface and light cylinder are indicated. The Polar Cap and the Outer Gap are highlighted. From (Harding, 2001).

He expanded the model of Goldreich and Julian by considering the effects of charged particle flux above polar caps along open magnetic field lines. The basic line of arguments is that open field lines extending out of the light cylinder should be open since, if it were closed, particles tied to them should move faster than speed of light. The open field lines become twisted into a spiral pattern with a spiral angle of the lines of about 45 degrees. Since the lines are twisted, they cannot be curl-free. The currents associated to the poloidal component of these field lines must flow out of the polar cap region. The charged particles are then accelerated up to reach high energies. Sturrock made the assumption that a radial electric field exists over an height h comparable to the radius of Polar Cap and compute the potential difference ϕ along this height by considering magnetic stresses of the poloidal component of the magnetic field, finding $\phi \approx P^{-1}h^2$. The value found by Sturrock for the polar cap potential was an over-estimate because it was based on the full vacuum potential, which today we know that cannot be sustained. It is limited by pair production, either by breakdown of a vacuum gap (Ruderman & Sutherland, 1975) or at a pair formation front (Arons & Scharlemann, 1979).
The kinetic energy transverse to the magnetic field is rapidly emitted by synchrotron, leaving only the component along the magnetic field lines. Since the field lines are curved, the accelerated charges emit *curvature radiation*. Curvature radiation is emitted when a charged particle is forced to propagate along a curved magnetic line.
Because of the presence of intense magnetic field the γ-rays produces pair through the

process γ + B $\rightarrow$ e^+e^- (*magnetic absorption*). The secondary pairs can also emit synchrotron radiation and this initiates an electromagnetic cascade.
Once the pair production is no longer possible the radiation can escape freely. Since electric potential above polar caps decreases when period increase, pulsars reach eventually a *dead-line* at which electric potential is no more capable of accelerating particles at energies high enough to produce pairs.
Ruderman and Sutherland(Ruderman & Sutherland, 1975) expanded the approach of Sturrock and addressed some concerns associated with the "standard model". They made two basic assumptions. First they assumed that pulsar magnetic moment is antiparallel with their spins (*antipulsar*). Second, they assumed that ions cannot escape the surface because of their large binding energies. Since the positive charges are accelerating out of the surface and eventually no positive charge are supplied by the ions at surface, a vacuum gap forms above the polar caps.
Because the potential difference is increasing as the vacuum gap heights h^2 (smaller that Polar Cap radius), the gap will eventually be discharged by sparks. These sparks will trigger an avalanche process that initiates the cascade of electron-positrons that, in turn, will result in the pair production. The basic difference between two approaches depends on whether the charges are stripped out of the surface or not. It have been remarked that measured temperatures for canonical X-ray pulsars are T $\sim 10^5 - 10^6$K, though higher values are obtained (4 $\times 10^6$-7 $\times 10^6$ K)(Baring, 2004), that are more typical of magnetars. However, both these models need to be considered depending on the source.
More recently new models that explore the the possibility of high-altitude emission from particle accelerated in the Slot Gaps have been explored (Muslimov & Harding, 2003, 2004). A model based on this acceleration will be discussed with more detail in Ch. 7.

4.3.2 Gamma-rays from polar caps

In the Polar Cap model for γ-ray emission (e.g. by Harding (Harding, 1981)) is the curvature radiation that produces γ-rays and initiates the cascade of e^+e^-. At some point the photons have no more energy to produce pairs and escape from the magnetosphere, resulting in a γ-ray beam swept out along the open field line from the magnetic poles. In the initial approach (Harding, 1981) a monoenergetic beam of primary charged particles were injected uniformly above Polar Cap and their interaction were followed with simulations. No details on the initial acceleration were considered, and the simulations were repeated for different values of period and magnetic field. This model was successful in reproducing spectra from the Crab and the Vela pulsars, that were the only γ-ray pulsars known at that time.
A subsequent model developed by Daugherty and Harding (Daugherty & Harding, 1982) assumed some generic acceleration models for initiating the cascade and included also contribution from synchrotron of the secondary pairs. This version of the PC model predicts a sharp cutoff at energies of some GeV, because at low altitude the γ-rays are attenuated by pair production and at higher altitude the weaker field and much lower curvature of magnetic field lines generate less curvature radiation.
The Polar Cap model for γ-ray emission requires high magnetic fields (some 10^{12}G) and explains the double peak emission in terms of geometric effect. The two peaks result from enhanced emission along certain regions of the beam (e.g. the borders of the open field volume, where curvature of field lines is higher) or a sufficiently high inclination

angle so that the Earth's lines of sight can intersect radiation form both polar caps.
Other, more detailed, models (Daugherty & Harding, 1994, 1996; Harding & Muslimov, 1998) find that the acceleration zone extends up to 0.5-1 stellar radii, and that number of subsequent pairs generations in the cascade are 3-4. In order to have a comparison term, let's consider a typical neutron star radius of about 10 km and a period like the Crab: the corresponding light cylinder radius, as computed using Eq.4.6 is of about 150 stellar radii. This also show that the emission region on PC is much smaller that the one in the OG model, which is near the light cylinder. For each primary electron about 10^4 pairs are produced and the synchrotron emission of secondary particles is more important at lower energies(Harding & Muslimov, 1998).
In a more recent the Polar Cap model for γ-ray emission, proposed by Sturner and Dermer (Sturner & Dermer, 1994), has the cascade initiated by Inverse Compton of the charged particles on thermal X-rays emitted by the neutron star surface.
Depending on the process that cools and initiates the cascade of charged particles, i.e. curvature radiation (CR) or Inverse Compton (IC), different values are obtained for γ_e, the maximum Lorentz factor of the charged particles. As reported in (Baring, 2004; Harding, 2001; Harding & Muslimov, 1998; Sturner & Dermer, 1994) for curvature radiation $\gamma_e \sim 10^7$ and for Inverse Compton $\gamma_e \sim 10^5 - 10^6$. A recent variation of the Polar Cap model is the emission for pulsars with high magnetic fields (B $\sim 10^{13}$G), where a third-order mechanism becomes important ,e.g. photon splitting $\gamma \rightarrow \gamma\gamma$ (Meszaros, 1992; Baring, 2004). This process has no threshold and avoids cascade quenching by pair production, so that the synchrotron generation is suppressed.
One of the main difficulties of the Polar Cap models is the inability to explain the wide pulses observed in γ-ray s unless the inclination and viewing angles are both small (less than about 10 degrees), while the energetics and pair cascade spectrum have been successful in reproducing observations.
An alternative acceleration region to the pure Polar Cap, called *Slot Gap*, near the Polar Cap rim has been proposed by Arons (Arons, 1983). The Slot Gap model is based on findings by Arons and Sharlemann that that the pair formation front (PFF), above which the accelerating field is screened, occurr at increasingly higher altitude as the magnetic colatitude approaches the last open field line where the electric field vanishes. The acceleration then takes place up to higher altitudes and the charged particles are accelerated up to Lorenz factor of the order of 10^7.
The Slot Gap is an unavoidable feature in any PC space chargelimited flow mode. The Slot Gap model has been expanded with application to γ-ray emission, e.g. by Harding and Muslimov, which takes into account also effects of general relativity (Harding & Muslimov, 1998). An update of this model has been used for preparing pulsar simulations for GLAST in order to study estimate of how many pulsars will LAT see. The details of this model and the simulations will be presented in Chapter 7 (Muslimov & Harding, 2003).
A recent modification may produce γ-ray emission from millisecond pulsars, based on the fact that low rotation periods could account for high-altitude emission. Millisecond pulsars are located below the curvature radiation pair death line, but above Inverse Compton cascade dead line. A Polar Cap model based on electromagnetic pair cascades could then be a possible scenario for γ-rays emission from millisecond pulsars (Harding et al., 2005).

Such a model has been used for producing a simulated population of γ-ray millisecond pulsars in Chapter 7 for studying LAT capability to detect this particular class of pulsars.

4.4 Outer Gap models

The Outer Gap (OG) model was proposed by Cheng, Ho and Ruderman (Cheng et al., 1986a,b) based on a very different scenario from the Polar Cap models: the γ-ray emission is generated in vacuum gaps in the outer magnetosphere. One basic consequence

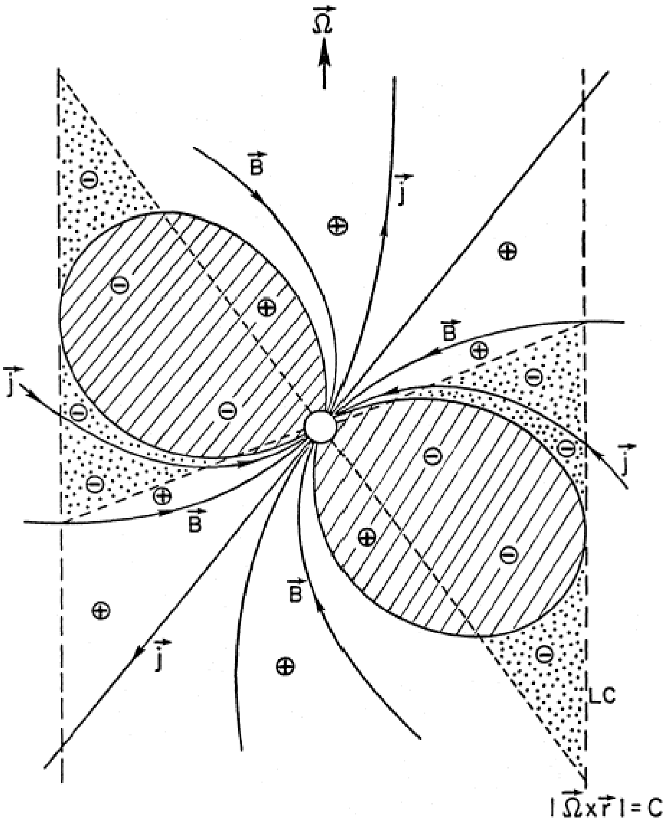

Figure 4.7: Scheme of the Outer Gap model discussed in the text. From (Cheng et al., 1986a)

is that the γ-rays are not as severely attenuated by the magnetic field as thos produced near the surface (as in Polar Cap models).
The model assumes that a vacuum gap *can* exists rather than *should* exist but its success in explaining observational results suggests that it warrants serious consideration.
In this model, the authors consider an oblique rotator with a magnetosphere that at least initially has the same distribution of the standard model, as displayed in Fig. 4.7. The Fig. 4.7 show the situation for $\mathbf{\Omega B}$ <0, and the Goldreich-Julian density greater than zero, but most of the discussion is the same in the opposite case ($\mathbf{\Omega B}$ <0, and the Goldreich-Julian density less than zero) except for a change of sign.
The two basic assumptions made by the basic Outer Gap model are that 1) the return

currents flows through the neutral sheet located on the *null surface* (the layer where $\mathbf{\Omega B}$=0) and 2) the negative charge of the region of open field lines farther from the magnetic axis than the null surface would tend to flow out through the light cylinder surface. The *null surface* exists (i.e. Eq. 4.5), where $\mathbf{\Omega} \cdot \mathbf{B}$=0, along which there is no net charge.
This flows leaves behind a negative charge-depleted region, which act as a positive charge with respect to the positive charges beyond the null surface, repelling them and preventing from flowing outward. This in turn leaves an empty gap which grow until it extend along the field lines between the null surface and the light cylinder.
Pairs formed in the gap just beyond the last closed field line are accelerated and emit γ-rays beam. In the *Crab-like* outer gaps the emitted photons interact with each other further out in the magnetosphere producing pairs via $\gamma + \gamma \rightarrow e^+e^-$, while in the *Vela-like* outer gaps the pair production is sustained by the interaction of the primary γ-rays with the thermal X-rays from the pulsar. Hence, for sufficient pair production rates the pairs will replenish the charge deficiencies, preventing the gap from growing broader.
The Outer Gap will thus be costrained between the last closed field line surface and another surface not too far above it. In thee large outer magnetospheric gaps which for Vela and Crab implies potential drops of ΔV=10^{15}, that envisage the rimary particle acceleration to occurr.
The γ-ray emission from these particles and the subsequent pair generation provides charges for the rest of the region between the null surface and the light cylinder, including the boundary charge layer that screens the electric charge deficit and ensure that $\mathbf{E}\cdot\mathbf{B}$=0 elsewhere.

4.4.1 Gamma-rays from Outer Gaps

Inside the gap, $\mathbf{E}\cdot\mathbf{B}$ is not zero, and the particles can then be accelerated along the curved magnetic field lines. In fact, the electric field component parallel to the magnetic field lines is proportional to $\mathbf{E}\cdot\mathbf{B}$. The presence of this parallel electric field provides acceleration of particles, that radiate γ-rays tangentially to field lines.
Because particles of both signs are accelerated and radiate, the radiation is beames tangentially to the field both in the forward and backward direction, and this can originate to pulses from the back and front regions of the magnetosphere (with respect to the observer).
The model predict four outer gaps, two longer and two shorter, but it can be argued that the short ones are thicker and then harder to see with respect to the other two longer. The outer magnetosphere is divided in three regions according to this models, that are shown in Fig. 4.8. The gap itself, that can be labeled as Region I, is the region were primary particles are accelerated by the electric field up to relativistic energies, until limited by radiation losses to primary γ-rays produced by curvature radiation or Inverse Compton Scattering on infrared photons from the other parts of the magnetosphere. In the original model the Curvature Radiation was the main cooling process argued for Crab and the Inverse Compton scattering was the cooling process for Vela. The emitted γ-rays in part interact one with each other because of the curvature of the field and convert into pairs. There pairs that are created fill the region and thus limit the growing ot the gap. Part of the γ-rays that does not convert goes into a the adjacent region, labeled Region II.

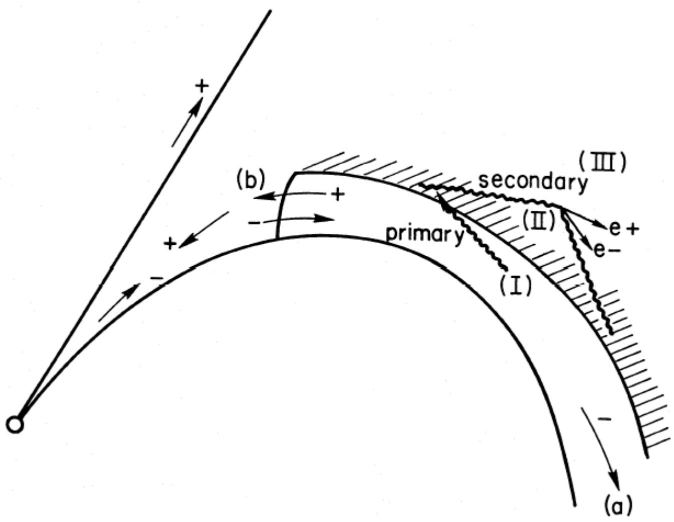

Figure 4.8: Outer Gap structure of the Cheng-Ho-Ruderman model showing the relative position of the primary (I), secondary (II) and tertiary (III) regions associated with an outer gap. The current flow on **B** field lines through an outer gap begins at (b) and extends through (a) for charge density greater than zero above polar cap. For an oppositely spinning pulsar with the same magnetic field but chenrge densiti negative all charge sign would be reversed. From (Cheng et al., 1986b)

In the Region II, there is a small residual **E**·**B**, secondary pairs can be created and accelerated to emit secondary γ-rays and X-rays by synchrotron radiation. Also in the Region II particles of opposite sign are accelerated in both diretions and can give beams tha cross each other and originate tertiary pairs that populate the Region III. In this region these particles have much less energy and can radiate softer photons. For parameters of Vela in the basic Outer Gap models, these soft photons are infrared photons that interact with the particles of Region II cooling them by Inverse Compton Scattering and producing photons of the Region II.
According to (Cheng et al., 1986a), the high-energy spectrum in this model is given mainly by the secondary photons, since the primary photons are mainly used for producing pairs.
Subsequent models introduced modifications to better explain the emission, e.g. Romani and Yadigaroglu (Romani & Yadigaroglu, 1995), who proposed emission coming from one pole. The original model (Cheng et al., 1986a) predicted high γ-ray emission for Vela-type pulsars coming from Inverse Compton scattering by primary particles of Region II on infrared photons, but this prediction violates the observed upper limit at TeV energies (Romani & Yadigaroglu, 1995). Cheng (Cheng, 2004) and Romani (Romani, 1996) revised the model replacing the infrared radiation, which is never observed, with thermal X-ray radiation from the neutron star surface.
As in the Polar Cap models, the age of the pulsar influences the width of the gap. Older pulsars (lower Ω) produce fewer pairs and the gap is more screened than in younger pulsars, as depicted in Fig. 4.6

4.5 GLAST and γ-ray pulsars science

GLAST will enhance our knowledge of γ-ray pulsars thanks to its superior resolution and sensitivity.
It is not, however, an easy task to estimate how many new γ-ray pulsars GLAST will see, because this depends strongly on the assumed model for the emission. There are three main areas where GLAST will contribute to our knowledge of pulsars:

- Distinguish between PC or OG emission models;
- Discover many more γ-ray pulsars, and possibly new sub-populations;
- Discover new radio quiet pulsars like Geminga;

The first two items are related since different emission models also predict different γ-ray fluxes. Beyond these main points, GLAST will be a powerful instrument for probing pulsar physics in much more detail, e.g by finding with high confidence the first γ-ray millisecond pulsars and pulsed γ-ray signals from binary pulsars.

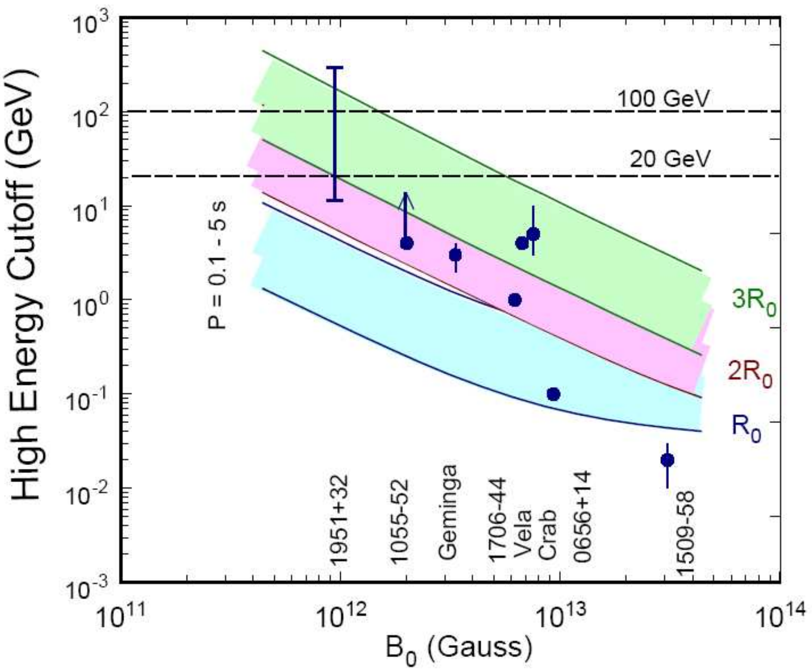

Figure 4.9: Calculated high energy spectral cutoff energies due to magnetic pair production vs. surface field for different periods and different photon emission radii. Also shown the measured turnover energies of detected pulsars(Harding, 2001).

4.5.1 Polar Cap or Outer Gap models?

Observations of pulsars in the energy region above 20 GeV and more sensitive measurements above 1 GeV may finally be able to discriminate between Polar Cap or Outer Gap models or reject both. For Vela pulsar EGRET collected only 4 photons in the

range 10-30 GeV, that are consistent with both the Polar Cap and Outer Gap models. Fortunately the two classes of models make very different predictions on some observational quantities, mainly regarding the spectrum of emission in γ-rays.
The first difference is the behavior of the spectrum at high energies, where Polar Cap models predict a cutoff sharper than an exponential (i.e. a "super-exponential", with exponential index greater than 1), while Outer Gap models predict a slower, simple exponential cutoff.
This is because different mechanisms produce absorption of γ-rays. In Polar Cap the γ-rays are attenuated by *one-photon absorption* in the magnetic field, so the spectrum will exhibit a cutoff at the *pair escape energy*, i.e. the maximum energy of a photon that can escape the magnetosphere without pair-producing (Meszaros, 1992; Harding, 2001). An estimate of this cutoff energy is provided in (Zhang & Harding, 2000)Fig. 4.9 shows a more detailed calculation of the predicted energy cutoff a a function of surface magnetic field strength for differents photon emission radii.
The picture is quite different in the Outer Gap models, since photons are emitted at larger distances, where the magnetic field is much weaker than at the surface. So the one-photon absorption in magnetic field has little effect. Instead the limit comes from

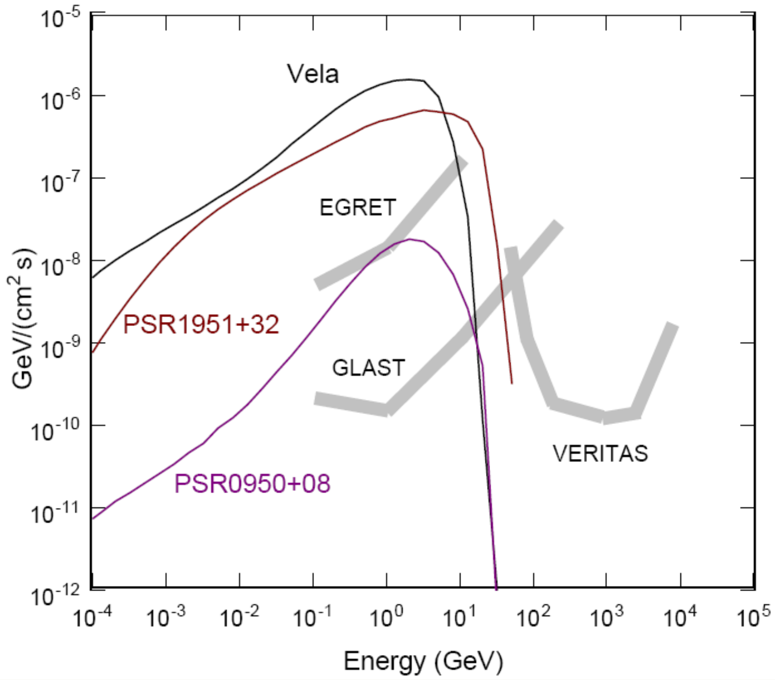

Figure 4.10: Observed optical to VHE spectrum for Vela pulsar with polar cap models for three pulsars, compared with the sensitivities of some instruments. From (Harding, 2001).

the upper limit of the accelerated particle spectrum, that are radiation-reaction limited. Fig. 4.10 shows the spectrum of Vela and other two pulsars (PSR B1951+32 and PSR B0950+08) predicted by Polar Cap compared with sensitivities of GLAST and EGRET and two ACTs as HESS and VERITAS. Also another example of the LAT capability of constraining models is shown in Fig. 4.11, where a simulated observation of the Vela spectrum is presented according to a Polar Cap model (Daugherty & Harding, 1996) and

Outer Gap (Romani, 1996).The large errors in EGRET above 1 GeV cannot discriminate between models. But with the GLAST LAT dynamical range and energy resolution it will be possible to rule out exponential or super-exponential cutoffs, as shown also in Fig. 4.11. Another point where Polar Cap models differ from Outer Gap models is the

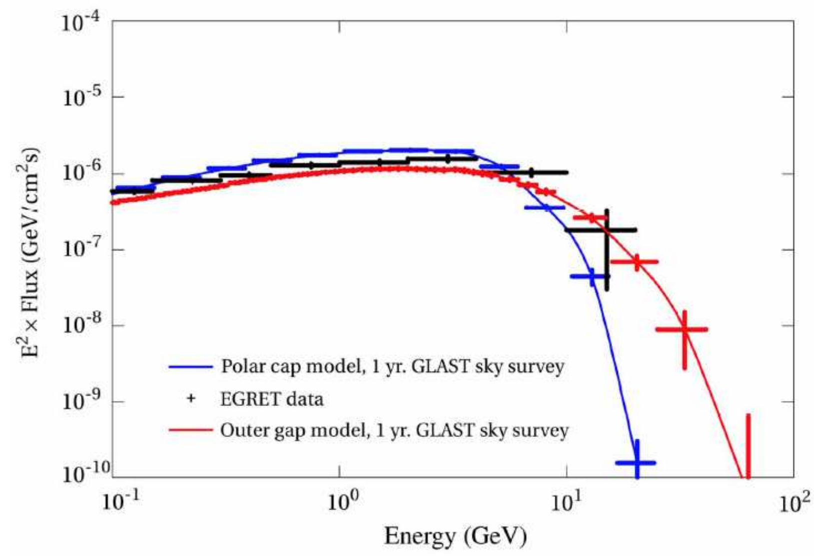

Figure 4.11: Comparison of Polar Cap vs. Outer Gap model spectrum of Vela, compared with EGRET data. From (Thompson, 2003)

predicted γ-ray luminosity. In Polar Cap models the luminosity is proportional to the polar cap current of primary particles, $N_p \propto B_0\Omega^2$. The curvature radiation-initiated cascade model of Zhang and Harding predicts slightly different behavior for young and old pulsars, characterized by two different luminosity dependences on magnetic field and angular velocity (Zhang & Harding, 2000). For the IC-initiated cascade model (Sturner & Dermer, 1994) the luminosity is proportional to $B_0^{-3/2}\Omega^2$.
The Outer Gap models are not strictly related to polar cap currents, but instead depend on the fraction of open field lines spanned by the outer gap accelerator.
For example the model of Romani and Yadigaroglu (Romani & Yadigaroglu, 1995) the luminosity dependence is to $B_0^{0.48}\Omega^{2.48}$.
Polar Cap models predict that all pulsars are capable of γ-ray emission at some level and the number of observable pulsars is matter of sensitivity. The Outer Gap models predict a "death-line" that divides the younger pulsars, capable of sustaining pair production (and thus activity) and older pulsar (which cannot). Thus a critical test of outer gap is the non-detection of pulsars with ages exceeding that of Geminga. Some later Outer Gap models, that not take into account the dependence of the inclination angle, show "death-line" to the right of Geminga.
Another method to possibly discriminate among models is to study the ratio of radio-quiet to radio-loud pulsars. The predictions are very different, mainly because of geometric effects and different γ-rays emission regions relative to the radio emission region, which is in the polar cap regions.
For in Polar Cap models the γ-rays emission is strictly linked to radio emission, while

the Outer Gap models can account for phase offset between radio and γ-rays because the γ-ray emitting region is separated from the one where radio emission originates.
Some studies have been done to estimate this ratio (Harding, 2001), e.g. Yadigaroglu and Romani on Outer Gap, who find that the number of radio-quiet is much greater that the radio-loud γ-ray pulsars (Romani & Yadigaroglu, 1995).
Gonthier,studying the PC models, found a small ratio of radio-quiet to radio-loud detectable by EGRET, $\sim$10 %. He also computed the number of expected detections by GLAST and found that the situation is reversed, with about 180 radio-loud and 302 radio-quiet. This result arises from the fact that GLAST will be sensitive to pulsars at larger distances than the present radio survey (Gonthier et al., 2002). However it is important to recall that all of these studies of the Polar Cap have assumed some beaming for radio and γ-rays and further studies with different geometries are required.

4.5.2 How many γ-ray pulsars?

A typical parameter for pulsar observability is defined the total pulsar spin-down energy output observed at the Earth:

$$F_o = \frac{\dot{E}}{f_\Omega 4\pi d^2} \tag{4.11}$$

where d is the distance and f_Ω is the fraction of solid angle span by the beam of the pulsar (usually assumed to be ≈ 1). This formula give an useful scaling law but it is not a strict predictions, since it has many limitations. By putting the sensitivity limits for GLAST LAT on low-latitude and high-latitude sources it is possible to see that all the EGRET γ-ray pulsars lies above the LAT sensitivity limit and that many more pulsars are above the GLAST LAT limits (Fig. 4.12). It must be remembered that these estimates based on Eq. 4.11 are based on the assumption of a beaming angle of 1 sr, that is probably not true in general. Moreover it is unlikely that the beaming angle is the same for all pulsars. The key point is that GLAST will have much higher possibility to discover new pulsar than EGRET, even if not yet sufficient to discover γ-ray emission from most of the radio pulsars, as it is clear from Fig. 4.12.
The limit on sensitivity is high for low latitude sources because of the background γ-ray emission from the Galactic plane. In order to have a precise prediction we should include the efficiency η_γ of the γ-ray emission, but this is strongly dependent on the models.
Among the known γ-ray pulsars there is only one, Geminga, that has no detectable radio counterpart. GLAST is expected to discover a lot of Geminga-like new pulsars by applying blind searches on data; that was not possible for EGRET data because of its low statistics.
The ratio between the radio-quiet and radio-loud pulsars is probably the best discriminator among models, and in this sense studies on pulsar population statistics are very important to estimate GLAST pulsar capabilities.

4.6 Summary

In this Chapter the theory of γ-ray emission from pulsars have been presented. The emission of γ-rays from pulsars is a consequence of the presence of a plasma magnetosphere

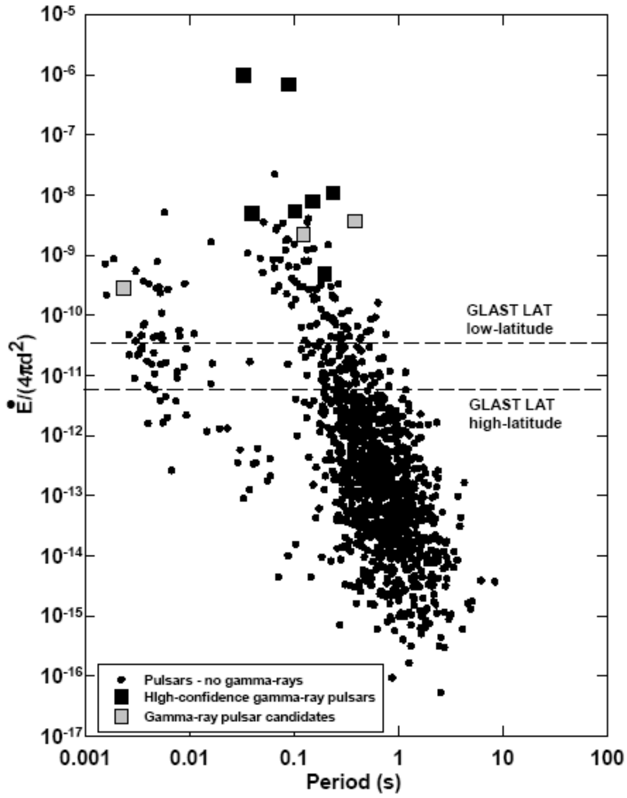

Figure 4.12: Distribution of pulsars according to the observability parameter defined in Eq. 4.11. The sensitivity level of GLAST LAT for high and low galactic latitude are shown. From (Thompson, 2001).

surrounding the neutron star. The basic concepts related to pulsar magnetosphere have been introduced and the two main classes of models have been reviewed. In the Polar Cap models the γ-ray emission take place above the polar caps while in the Outer Gap models the emission is located far from the neutron star.
GLAST will be able to distinguish between those two main scenarios as shown in this Chapter. A large portion of this thesis work is devoted to the sudy of the LAT capability to constrain γ-ray emission scenarios.

Chapter 5

Pulsar Simulation Tools for GLAST

Pulsar are among the most intriguing sources that will be studied with GLAST. As shown in previous chapters they provide an unique source for probing physical laws in extreme environments.
In particular the three brightest persistent sources of the γ-ray sky are pulsars, and these sources are of fundamental importance for calibrating the LAT during the mission.
Simulations are an optimal tool to better study the LAT response and also to prepare to study pulsars and to test the pulsar analysis tools contained in the LAT *Science Analysis Environment*[1].
Within the LAT Collaboration substantial efforts have been made for simulating γ-ray sources. For pulsars specific simulators have been developed. In this Chapter I will present *PulsarSpectrum* , a program that I have developed for simulating γ-ray emission from pulsars as a part of this Ph.D. project.
This simulation software reproduces not only the basic features of the observed γ-ray pulsars, i.e. spectrum and lightcurve, but can also simulate more detailed effects related to pulsar timing. It considers the position of the GLAST satellite and computes the arrival time delays due to its motion in the Solar System Barycenter (SSB). The evolution of the pulsar spin period is taken into account as well as the effect of *Timing Noise* that is simulated in a phenomenological way. *PulsarSpectrum* has been successfully used within the LAT Collaboration for simulating the emission characteristics of a realistic pulsar population during important milestones in the mission preparation, e.g. *Data Challenge 2*, as it will be described in next Chapters. This simulator also fully satisfies the main requirements for testing LAT analysis tools.
Fig. 5.1 shows an example of the comparison between an EGRET observation of the Crab pulsar and Geminga and a 1-week-long LAT observation where Crab and Geminga have been simulated with *PulsarSpectrum* .
The input models and data of pulsars to be simulated with *PulsarSpectrum* can be generated using a set of ancillary tools and macros called the *Pulsar Simulation Suite* , that will be presented at the end of this Chapter.
All the simulations carried out in this thesis for studying LAT capabilities have been made using *PulsarSpectrum* and using the *Pulsar Simulation Suite* as supporting tools, then a detailed presentation will be given here.

[1]See Ch.2

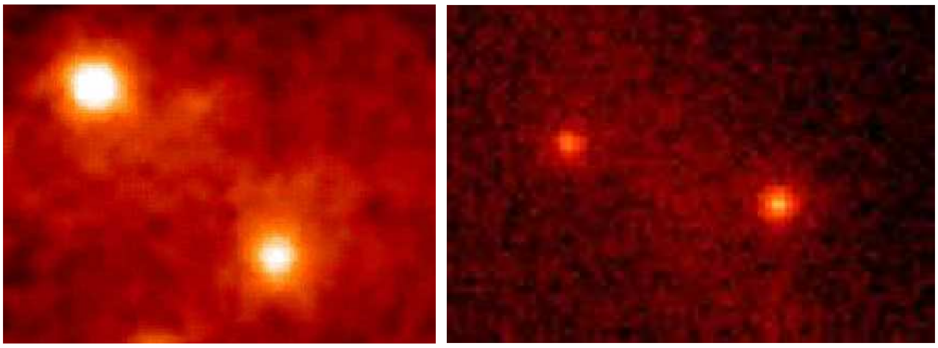

Figure 5.1: Example of pulsar simulation compared with EGRET observation. Left: Crab pulsar and Geminga pulsar observed by EGRET. Right: The same region in a 1-week simulated LAT observation obtained with *PulsarSpectrum* .

5.1 Overview of *PulsarSpectrum*

A schematic diagram of the simulator is displayed in Fig. 5.2. The basic idea of *PulsarSpectrum* is to create a bidimensional histogram N_ν that contains the differential γ-ray flux in function of energy and of time over a time of one period using the ROOT framework [2]. The flux is then expressed in ph $m^{-2}s^{-1}keV^{-1}$. This histogram contains all the basic information about lightcurve and spectrum.
Intervals between photon emissions by the pulsar are computed based on the flux. For each γ-ray an energy is also extracted and the photon event is sent to the MonteCarlo simulation of the LAT. The N_ν histogram is computed using two main *simulation models*

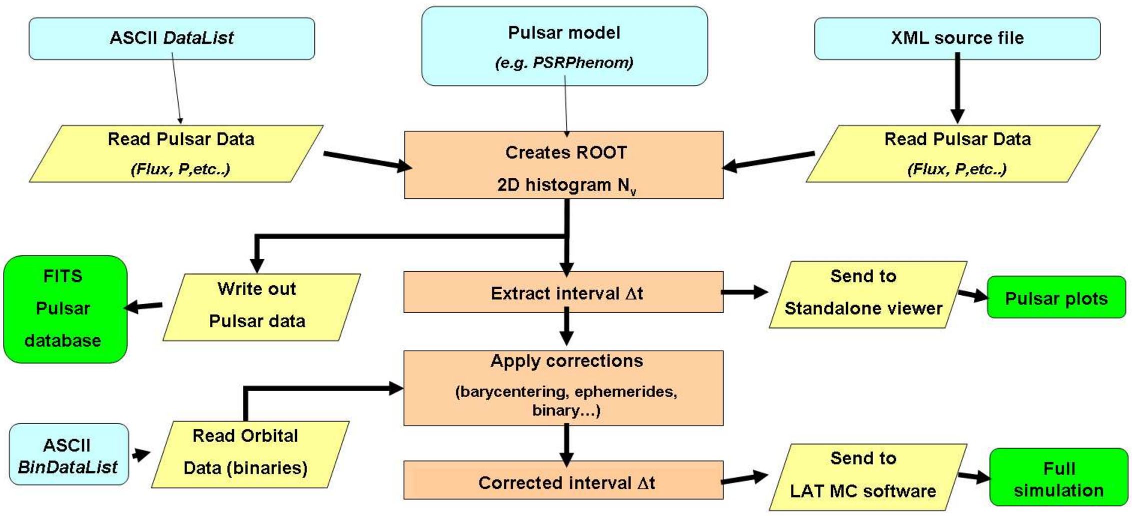

Figure 5.2: Flowchart illustrating the structure of *PulsarSpectrum* .

that will be described in next sections.
One model is called *PSRPhenom* and is based on phenomenological considerations. The

[2] $http://root.cern.ch$

second one is called *PSRShape* and can be used for producing simulations of arbitrary pulsar emission scenarios.

5.1.1 Input Parameters

The input parameters of *PulsarSpectrum* can be divided in two categories:

- *Pulsar Data*;
- *Model-dependent parameters*;

Pulsar Data are all the observable parameters that not depend on the particular model chosen, and are stored in a set of ASCII files that we will call *PulsarDataList*. These parameters are in order:

- *Pulsar Name*;
- *Flux* above 100 MeV (in ph $\mathrm{cm}^{-2}\mathrm{s}^{-1}$);
- *Ephemerides style* (Period and its derivatives or Frequency and its derivatives);
- *Period* P_0 at epoch t_0/*Frequency* f_0 at epoch t_0;
- *Period 1st derivative* P_1 at epoch t_0/*Frequency 1st derivative* f_1 at epoch t_0;
- *Period 2nd derivative* P_2 at epoch t_0/*Frequency 2nd derivative* f_2 at epoch t_0;
- *Start of ephemerides validity range* (in MJD)[3];
- *Epoch* $t0$ of the ephemerides (in MJD);
- *End of ephemerides validity range* (in MJD);
- *Time where rotational phase is conventionally established to be 0* (in MJD);
- *Timing Noise Model* (0=No timing noise,$\neq$0 timing noise included);
- *Binary pulsar flag*, for choosing if the binary demodulation must be applied for simulating pulsars in binary orbits.

The second set of input parameters are dependent upon the simulation model chosen and are located in an XML file called *source definition file*. Some parameters are common to all models:

- *Pulsar Name* used to retrieve pulsar data in *PulsarDataList*;
- *Right Ascension* of the pulsar (in degrees);
- *Declination* of the pulsar (in degrees);
- *Minimum Energy* of the extracted photons (in keV);

[3]MJD indicate Modified Julian Date, defined as an offset from Julian Date JD as MJD = JD-2450000.5

- *Maximum Energy* of the extracted photons (in keV);
- *Simulation model* (1=*PSRPhenom*, 2=*PSRShape*);
- *Random seed*;

Five other parameters are included and are different from the two models, they will be described in next Sections.
From these input parameters *PulsarSpectrum* creates the lightcurve and the spectrum from these parameters and combines them to obtain a two-dimensional histogram that represents the flux in ph m^{-2} s^{-1} keV^{-1} vs. Energy vs. Time.

5.1.2 Simulator Engine and Timing effects

Currently two simulation models are implemented in order to satisfy two different requirements.
The *PSRPhenom* model uses an analytical form for the spectrum, while the *PSRShape* model can also use a numerical model for pulsar emission.
The interval between photons emitted by the sources is computed according to the flux and assuming a Poisson distribution whose mean is related to the flux as it will be described in details later.
The arrival times of the photons must be corrected with some timing effects that are of particular importance for studying pulsar timing with GLAST. These effect include barycentric corrections, period change with time and timing noise. Also the possibility to simulate effects on timing for binary pulsars, whose orbital data can be retrieved from an ASCII *BinDataList* file, is included.

5.1.3 Output products and MonteCarlo simulation of the LAT

All input parameters are used for creating the N_ν histogram that is saved on an external file.
Another set of ASCII files are created with the ephemerids information used for generation of the pulsar. These files can be easily converted into a FITS file compatibile with the standard of the D4 LAT pulsar database, described in Ch. 2.
Each photon extracted with its direction, its arrival time and its energy can be saved in a list and used in a standalone viewing program or can be sent to the MonteCarlo simulation of the LAT in order to have the source spectrum convoluted with the response function of the LAT. As described in Ch.2 there are two main packages that simulate the detector response. The most complete is *Gleam* (Figure 5.3 left), a detailed GEANT4-based simulator that works by using the *Gaudi* framework. *Gleam* is able to compute the MonteCarlo for the propagation of photons and secondary particles in the LAT instrument.
Another program, *Observation Simulator* (described in Ch. 2) uses the approach of the *fast simulation*, i.e. folds the incoming photons with the response function of the instrument instead of make all the detailed calculations for particle propagation.
Gleam is designed to understand the details on the LAT response to better study experimental issues, e.g. *background rejection.* On the other hand *Observation Simulator* provides realistic photons data with which to test and develop analysis programs and

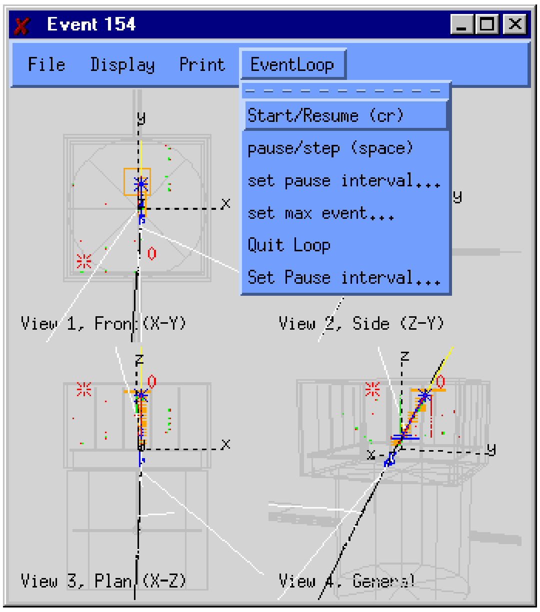

Figure 5.3: A screenshot of *Gleam* with a photon event in the LAT.

techniques. *Observation Simulator* is included in the LAT Science Analysis Environment (SAE).
PulsarSpectrum is very easy to interface with both programs and for now has been intensively used mainly with *Observation Simulator* to study and help the Science Tools Software development.

5.2 *PSRPhenom*, the Phenomenological Model

The first model that has been implemented in *PulsarSpectrum* was called *PSRPhenom* because it is mainly based on phenomenological considerations. In particular the spectrum of the simulated pulsars using this model can be described by an analytical function based on observations (Nel & De Jager, 1995).
Using spectral parameters this model provide some basic data to build reasonable simulations of the EGRET pulsars, as will described in the next Chapter.
The basic idea is to generate a distribution of photons in phase (lightcurve) and in energy (spectrum) and then to combine them to obtain the 2-dimensional ROOT histogram N_ν. The easiest way to combine them is by multiplicating the 1-dimensional lightcurve and the 1-dimensional spectrum to obtain a 2-dimensional histogram. The resulting N_ν is then normalized with the photon flux above 100 MeV given as input parameter in the *DataList* file (See Sect.5.1.1). The lightcurve can be generated with some different methods.
A first method is to generate the curve as a simple or double-peaked Lorentz function whose parameters are extracted from a random generator (See Fig. 5.4. A second opportunity is to use an external ASCII file containing the relative height for every phase bin. We will refer to this file as *TimeProfile*.
The *TimeProfile* used can be for example the pulsar lightcurve measured by EGRET

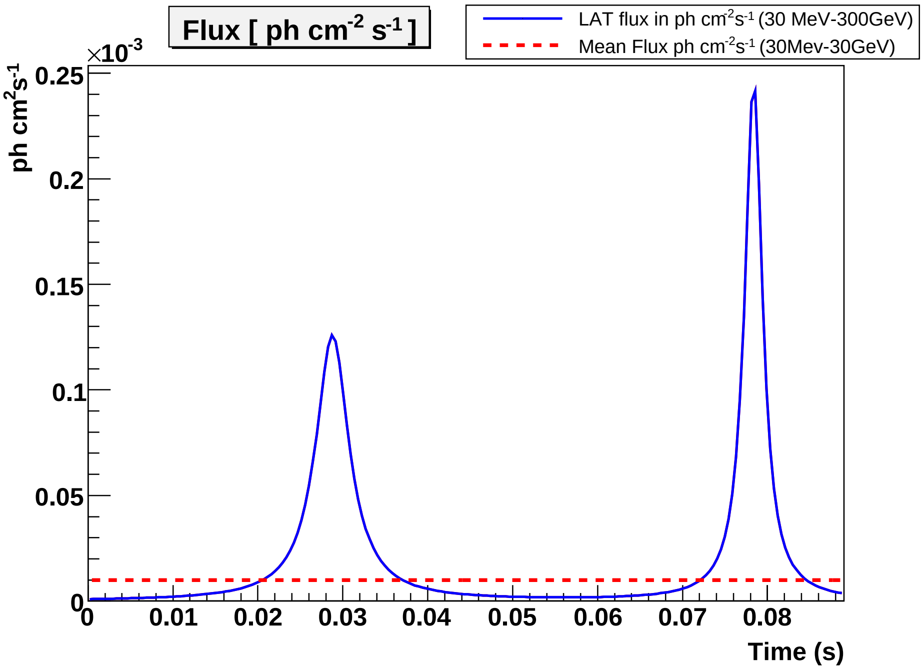

Figure 5.4: A lightcurve model generated with *PulsarSpectrum* using the phenomenological model. This lightcurve is used by *PulsarSpectrum* to extract photons from simulated pulsar. In this case a profile with two Lorentzian peaks has been generated using a random generator.

or synthetic lightcurve obtained from theoretical models.
Examples of lightcurves are shown in Fig. 5.4 and Fig. 5.5.
In some advanced simulations the original EGRET lightcurves have been smoothed to remove the statistical fluctuations due to counting statitics.
The phenomenological spectrum is based on an analytical function composed by a power law with an exponential cutoff whose index can be varied. According to pulsar observation this shape can be usefl to model the spectral cutoff expected at GeV energies as described in Ch.4. This analytical function and some phenomenological motivation can be found in (Nel & De Jager, 1995). The function used in the phenomenological model of *PulsarSpectrum* is:

$$\frac{dN}{dE} = K\left(\frac{E}{E_n}\right)^{\alpha} exp\left(\frac{E}{E_0}\right)^{-b} \tag{5.1}$$

The spectrum modeled with function in Eq. 5.2 can be useful to roughly model a super-exponential cutoff, as predicted by the Polar Cap/Slot Gap models, as described in Ch. 4. Also exponential cutoff can be modeled in order to simulate pulsars according to Outer Gap models,as described in Ch. 4. The value of the normalization constant K is determined from the total flux above 100 MeV.
Fig. 5.6 shows an example of spectra of a *Vela-like* simulated pulsars, i.e. a pulsar with same flux and same observed parameters of Vela pulsar, where the exponential index b has been tuned for a super exponential cutoff or exponential cutoff.
From fitting the observations a value of b$\sim$1.7 is obtained, that lie in between a pure Polar Cap prediction (b>2) and Outer Gap prediction (b=1) as can be seen in Fig.

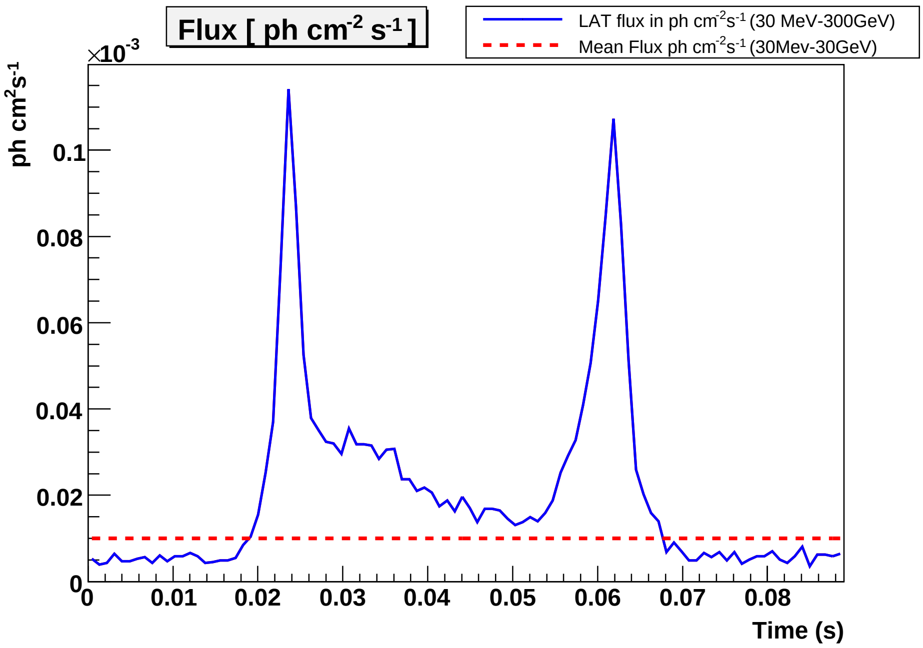

Figure 5.5: A lightcurve model generated with *PulsarSpectrum* using the phenomenological model. This lightcurve is used by *PulsarSpectrum* to extract photons from simulated pulsar. In this case a *TimeProfile* based on EGRET observation of Vela (Kanbach et al., 1994) has been used.

5.6. These spectra can be compared and used for generating the same pulsar with different models predictions. In order to control the different options, a set of five input parameters are taken from the XML file. These parameters have the following meaning, 4 of them related to the spectral function of Eq. 5.2:

- *Lightcurve option*: Random Lorentz peaks or from *TimeProfile*;
- *Energy scale factor* E_n (GeV);
- *Cutoff energy* E_0 (GeV);
- *Spectral Index* α;
- *Exponential index* b;

An example of the final model histogram N_ν is presented in Fig. 5.7.In this example we used the spectral parameters for Vela determined by multiwavelength fit with the spectral shape in Eq. 5.2 in (Nel & De Jager, 1995), so I define it *Vela-like* [4]. The total flux is set to 9×10^{-6} ph cm^{-2}s^{-1}, the cutoff energy E_0 to 8 GeV and the spectral index α=-1.62. The energy scale E_n is always set to 1 GeV.
The main advantage of this model is that a pulsar can be simulated in an easy way using few parameters. For this reason *PSRPhenom* can be used for studies on LAT

[4]Here and in the following in the chapter I define with the *like* suffix a simulated pulsar that has similar spectral parameters to the real pulsar but random lightcurve.

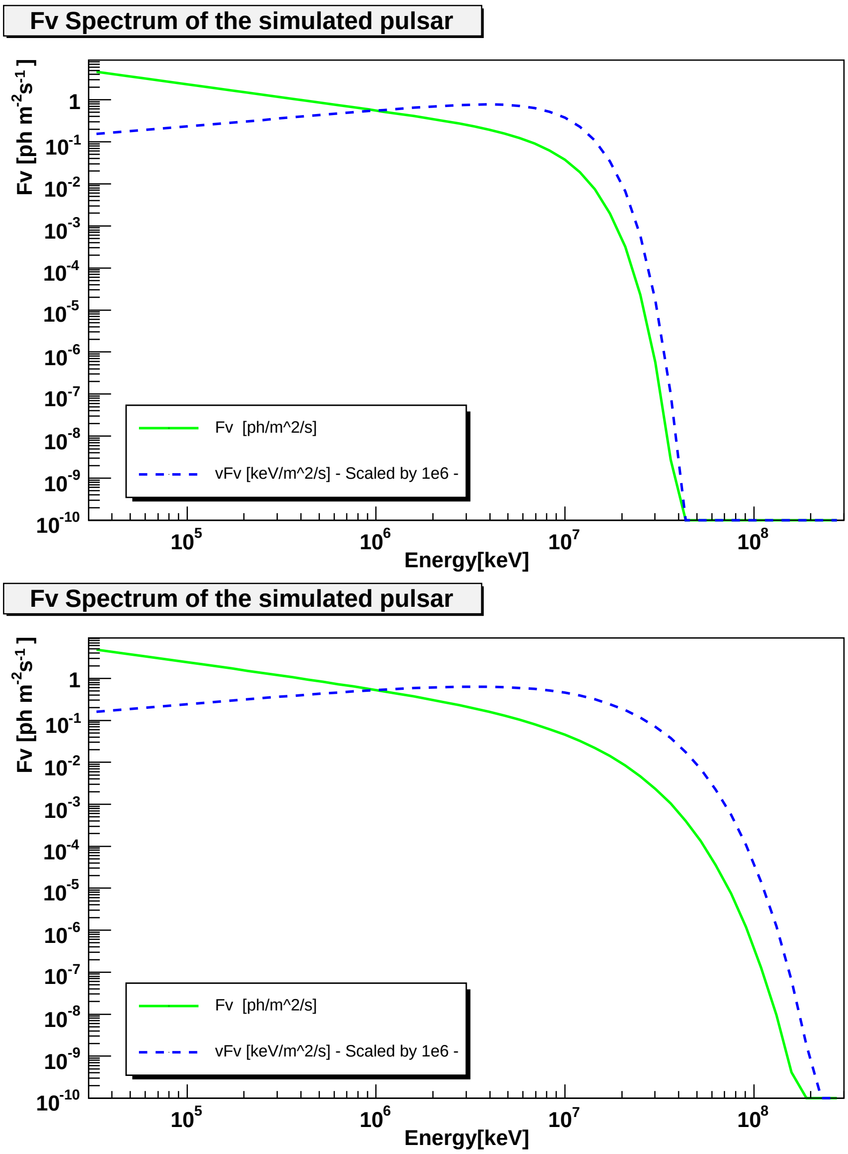

Figure 5.6: Examples of analytical spectra generated with *PulsarSpectrum* using the phenomenological model. Top: An exponential index b=2 is fixed, in agreement with a Polar Cap emission scenario. Bottom: An exponential index b=1 is fixed, in agreement with an Outer Gap emission scenario.

capabilities for pulsar populations as it will be presented in Ch. 8.
Unfortunately this model is not very efficient for studying LAT sensitivity to specific theoretical scenarios or for studying more complex situation, like phase-dependent spectra. For these reasons *PulsarSpectrum* was upgraded by adding another simulator model.

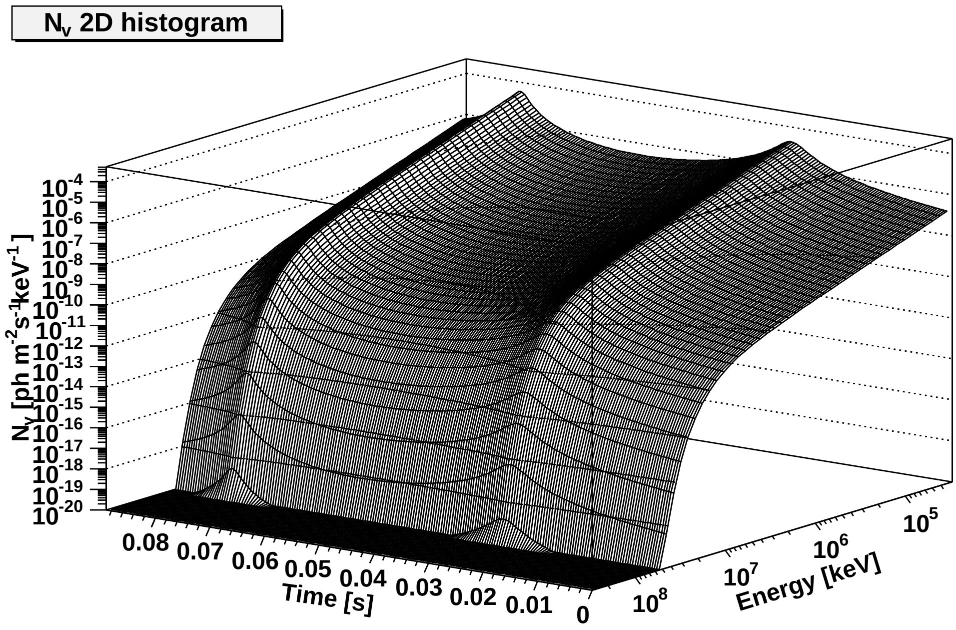

Figure 5.7: An example of final N_ν histogram created by *PulsarSpectrum* using the phenomenological model with a random two Lorentzian peaked lightcurve and spectral parameters as in Fig.5.6 (Left).

5.3 *PSRShape*, simulating complex emission scenarios

To extend the capabilities of *PulsarSpectrum* to simulate more complex emission scenarios and/or phase-dependent spectra, the *PSRShape* model has been formulated.
The basic concept is rather simple. Instead of generating a lightucurve and a spectrum and combining them in analytically, this model takes an external N_ν ROOT histogram and normalizes it according to the flux, to create a final N_ν. This new histogram is used for extracting γ-rays according to its flux.
Currently this model takes input parameters from XML source file, but does not all five parameters, since only two are useful:

- *Pulsar Shape name*, the name of the external N_ν;
- *Normalization flag*, for deciding if the external N_ν must be normalized with the flux or not; A possible application of this model is the capability of the LAT to test some specific emission scenario. In this case an external model is created from the theoretical predictions using a specific tool called *TH2DSpectrum Shaper* included in the *Pulsar Simulation Suite* (See Sect. 5.8) and then it is given as input to *PulsarSpectrum* .

Another example of application of this model is the creation of phase-dependend spectra to test the LAT capabilities for doing phase-resolved spectroscopy, a sample of which is shown in Fig. 5.8, where the phase-dependent spectrum of Vela pulsar has been

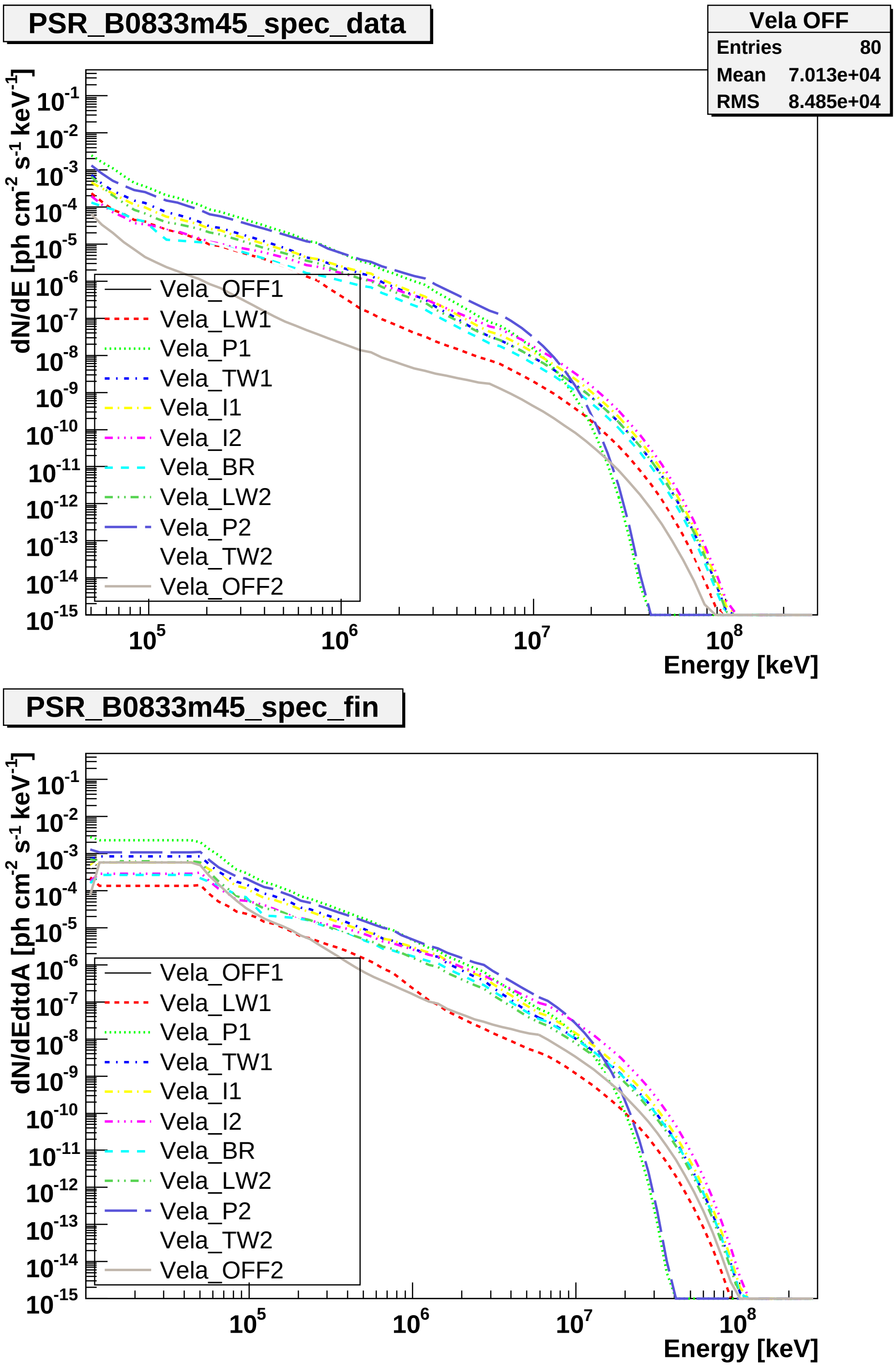

Figure 5.8: The creation of a phase-dependent spectrum using the *PSRShape* model of *PulsarSpectrum* . Top: the Vela phase-resolved spectrum observed by EGRET is considered (Kanbach et al., 1994) for creating the various spectra. Since the high-energy spectrum is not known, we have assumed a super-exponential cutoff within the peaks and an exponential cutoff outside, in agreement with a Polar Cap/Slot Gap scenario. Bottom:The final spectrum after some balances have been done in order to have a smoothed spectrum and to agree with the flux above 100 MeV.

simulated using EGRET data and some elaborations, obtaining the final histogram in Fig. 5.9.

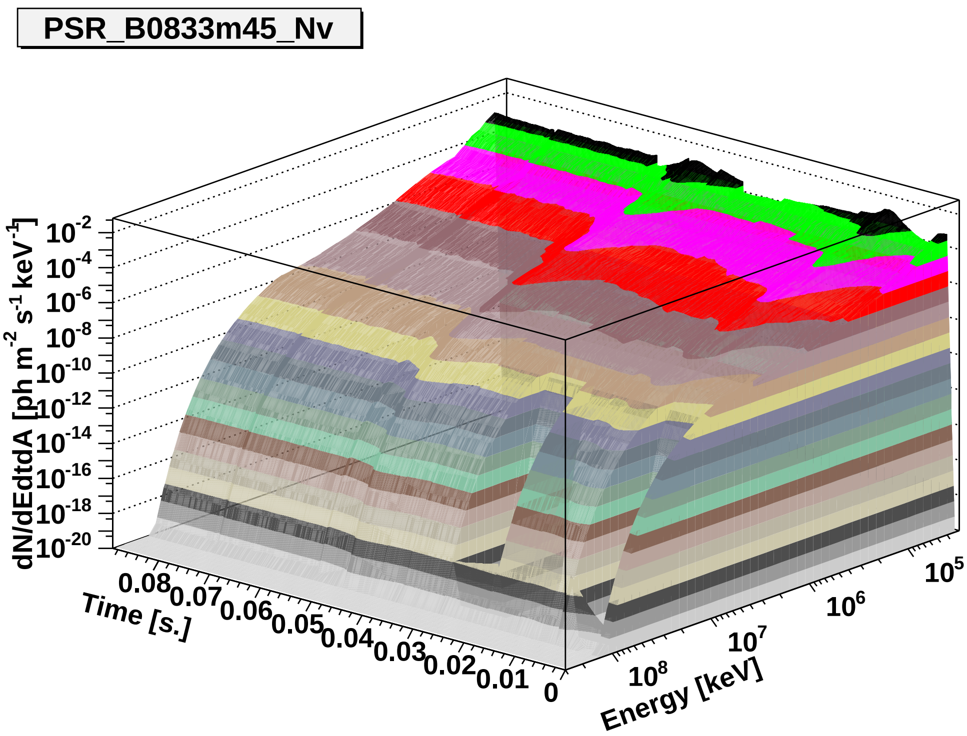

Figure 5.9: the resulting N_ν histogram with phase-dependent spectrum using data from Vela pulsar as in Fig. 5.8.

5.4 Photon extraction from the source

Once the N_ν is created using *PSRPhenom* or *PSRShape*, *PulsarSpectrum* is able to extract photons according to the flux of the pulsar. If these photons must be sent to the MonteCarlo of the LAT some corrections in the photon arrival times must be applied and they will be described in next Section.The energy is randomly extracted using the spectrum as probability distribution.
The extraction of the arrival times, i.e. the calculation of the time interval between successive photons, is a little bit more complicate. Given a simple source the interval between two successive photons extracted from the source is managed by a package called *SpectObj* that is also used by the GRB simulator of the LAT.
For a stationary source, this interval can be calculated from the flux of the source using Poisson statistics. For pulsars the interval between photons should be Poissonian in first approximation and at the same time mantain periodicity, then a shortcut has been adopted.
The interval is composed from two contribution, $\delta\bar{t}_{poiss}$ and δt_{per}. The first represent an interval according to the Poisson statistics and it is evaluated as:

$$\delta t_{poiss} = -log(1.0 - \zeta)/\mu; \tag{5.2}$$

where ζ is a uniform random number between 0 and 1 and μ is the mean rate from the source obtained by integrating the flux over the energy of extraction. From δt_{poiss} the corresponding $\delta\bar{t}_{poiss}$ is derived as the integer number of pulsar periods P smaller than δt_{poiss}:

$$\delta\bar{t}_{poiss} = Int(\frac{\delta t_{poiss}}{P}) \tag{5.3}$$

The second component of the interval is δt_{per} and is a uniform random number from 0 to 1 extracted using as a distribution function the integrated N_{ν} over the energy. The

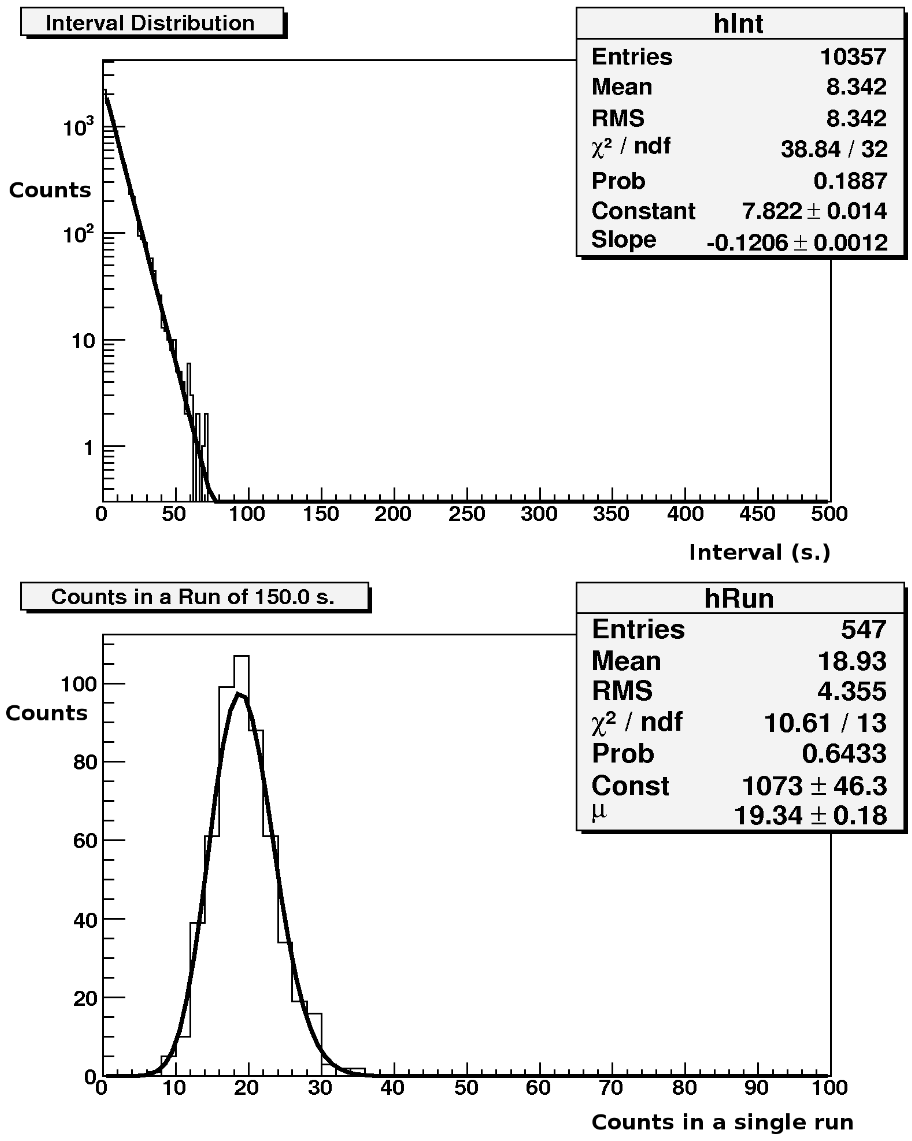

Figure 5.10: Distribution of number of photon extracted form a simulated pulsar with same flux of the Vela pulsar. Top: Distances between events fitted with an exponential distribution as expected form a Poisson source. Bottom: Distribution of counts in interval of 150 seconds, fitted with a Poisson distribution.

resulting interval is the sum of $\delta\bar{t}_{poiss}$ and δt_{per}. The difference between this interval and a pure Poisson interval is very small as can be verified from fits with a pure Poissonian. This is that because of the low fluxes of γ-ray pulsars, the correction δt_{per} is very small

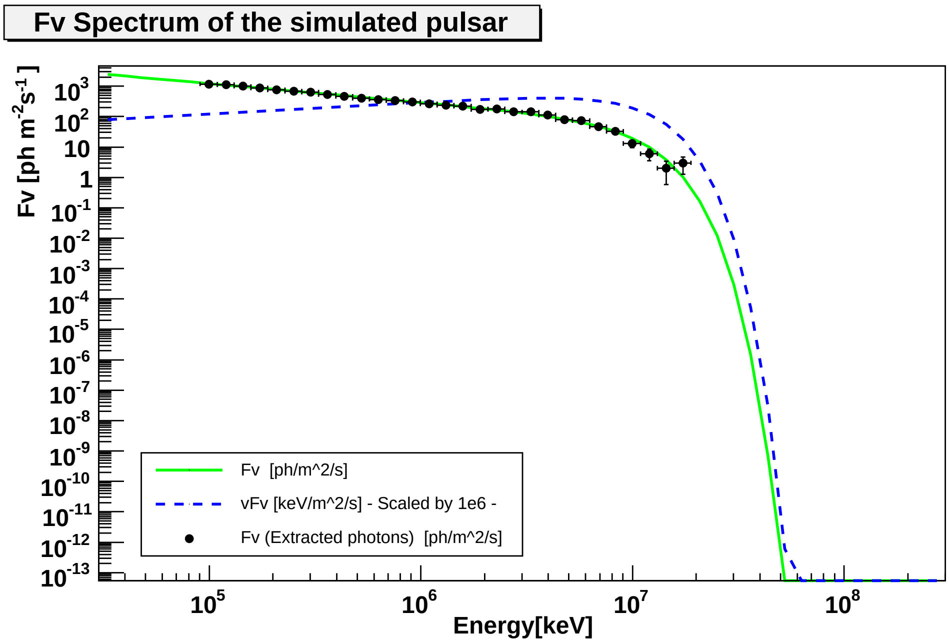

Figure 5.11: Spectrum of extracted photons above 100 MeV in 1 day from a simulated pulsar with same spectrum of Vela of Fig. 5.6(Top) compared with the theoretical spectrum.

compared to the pure Poisson component $\delta \bar{t}_{poiss}$. An example of a Poisson fit for Vela pulsar is shown in Fig. 5.10. With this extraction method the source is periodic and follows closely a Poisson distribution.
Once the photons are extracted they can be sent to a standalone plot program for studying their distribution as in Fig. 5.11. A complete simulation of the photon arrival time from the pulsar requires an additional computation in order to include some timing effects that are fundamental when studying a pulsar signal.

5.5 Timing corrections

The interval between successive photons as described up to now have been calculated under particular assumptions, 1)Pulsar period is constant, 2) LAT is fixed with respect to the source 3) no timing noise and 4) pulsar is not in binary system.
These assumptions are useful when computing interval between successive times but are not realistic. In data analysis of real γ-ray pulsar data, as it will be described in detail in Ch. 6, some timing effects must be considered since 1) pulsar period is not constant but increase with time, 2) the LAT in moving in space, and 3) timing noise is always present. If we want to simulate pulsar in binary orbits, the effects of 4) orbital motion must be considered.
Since a detailed pulsar simulator must consider also these effects that are not considered when photons are extracted from N_ν, each photon is then processed before sending to

the LAT MonteCarlo and opportune *timing corrections* are applied to its arrival time. The main timing corrections computed by *PulsarSpectrum* are:

1. Motion of the spacecraft through the Solar System;
2. General Relativistic effects due to gravitational well of the Sun;
3. Period increase with time;
4. Timing noise;
5. Orbital modulation for pulsars in binary orbit;

These effects must be considered when simulating realistic arrival times, applying some corrections to the extracted interval. In this way the produced photon list by *PulsarSpectrum* are more *realistic*, in the sense that after barycentering and phase-assigment the original simulated lightcurve can be recovered. These timing effects corrections are the core of the *PulsarSpectrum* simulator and its main ability in reproducing photon distribution from γ-ray pulsars. For real pulsars timing is also affected by the proper motion of the pulsar, but at this stage *PulsarSpectrum* neglect this effect.

5.5.1 Barycentric Effects

The first step to analyze pulsar data is the conversion from the arrival times at the spacecraft to arrival times at the Solar System Barycenter (SSB), applying the *barycentric corrections*
Barycentric correction means converting photon arrival times at the spacecraft, usually expressed in Terrestial Dynamical Time (TT or TDT)[5] , to arrival times at the Solar System Barycenter, expressed in Barycentric Dynamical Time (TDB)[6].
The relation between TDB arrival time t_B at Solar System Barycenter and TT arrival time t_G at GLAST spacecraft is:

$$t_B = t_G + f^{TT-TDB}(t_G) + g(t_G) + s(t_G) \tag{5.4}$$

Terms in Eq. 5.4 have the following meaning:

- $f^{TT-TDB}(t_G)$: Conversion from TT to TDB. It takes into account gravitational field of Earth that cause gravitational delays on clocks placed on Earth;
- $\Delta t_{geom}(t_G)$: Geometric delay due to light propagation from the spacecraft to the Solar System Barycenter. It depends on position of the spacecraft;
- $\Delta t_{sh}(t_G)$: "Shapiro delay" caused by gravitational field of the Sun;

[5]According to IAU Standards Terrestrial Time TT is the time reference for apparent geocentric ephemerides and it is related to the *International Atomic Time* (TAI) as as TT = TAI + 32.184 s(Seidelmann, 1992)

[6]According to IAU Standards the Barycentric Dynamical Time is the independent variable of the equations of motion with respect to the barycenter of the Solar System. It is related to TT by a mathematical expression that include position of Solar System bodies (Seidelmann, 1992)

The simulator computes the inverse of Eq 5.4 and returns the corresponding arrival time at the spacecraft, so that the barycentric corrections can be applied during the data analysis.
The accuracy of the computation is hardcoded and currently fixed at 50 μs.
In Fig. 5.12 and Fig. 5.13 an example of the components of the barycentric corrections are shown for a typical GLAST orbit, where the periodic component due to the orbit around Earth is clearly visible. The position of GLAST is computed using the file describing the GLAST orbit, while the position of the Earth and of the Sun are computed using the JLP Ephemerides DE200. These are standard ephemerides used for the Solar System and are used by most astronomers that work on pulsar timing.
The term $f^{TT-TDB}(t_G)$ represent the correction from TT to TDB considering the difference in time of a clock placed at the position of GLAST and a clock if it were positioned at infinite distance from all bodies. This correction then consider the relativistic effects due to the gravitational field of the Earth and it is computed from the JPL tables using the routines AXBARY.C [7].
In order to compute the geometric correction $\Delta t_{geom}(t_G)$ due to lighttravel time from

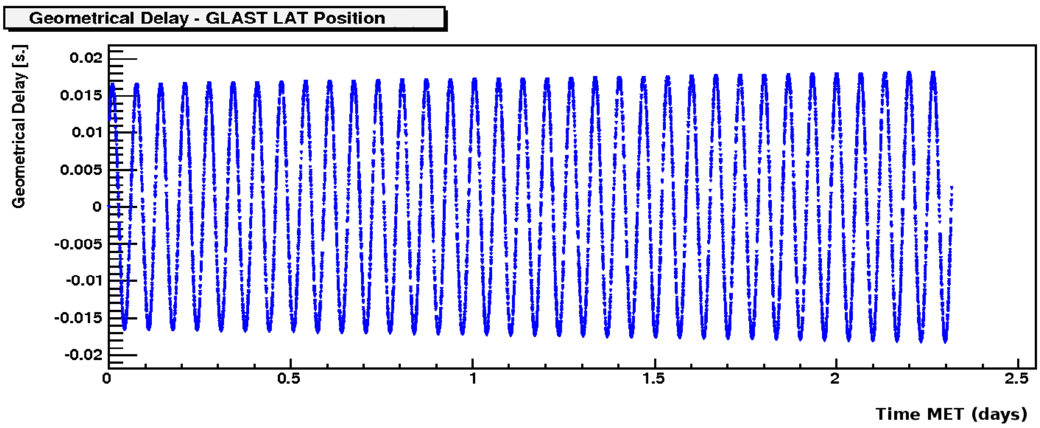

Figure 5.12: The geometrical delay, due to motion of GLAST in the space, used by *PulsarSpectrum* for correcting the photons arrival times. The component due to motion of the GLAST around Earth with an orbital period of about 95 minutes is clearly visible

the position of GLAST to the Solar System Barycenter it is important to know the location of the Earth, of the Sun and of the GLAST satellite in the space. The geometric correction can be written as:

$$\Delta t_{geom}(t_G) = -\frac{1}{c}(\mathbf{r}_{GE}(t_G) + \mathbf{r}_{ES}(t_G) + \mathbf{r}_{SB}(t_G)) \cdot \hat{\mathbf{s}} \tag{5.5}$$

where $\mathbf{r}_{GE}$ is the vector from GLAST to the center of Earth, $\mathbf{r}_{ES}$ from the center of Earth to the center of the Sun and $\mathbf{r}_{SB}$ from the center of the Sun to the Solar System Barycenter. $\hat{s}$ is the unit vector identifying the position of the pulsar in the sky (See Fig. 5.12). The last term is a relativistic correction (See Fig. 5.13 that takes into account

[7]See $http://heasarc.gsfc.nasa.gov/docs/software/lheasoft/RelNotes_504.html$

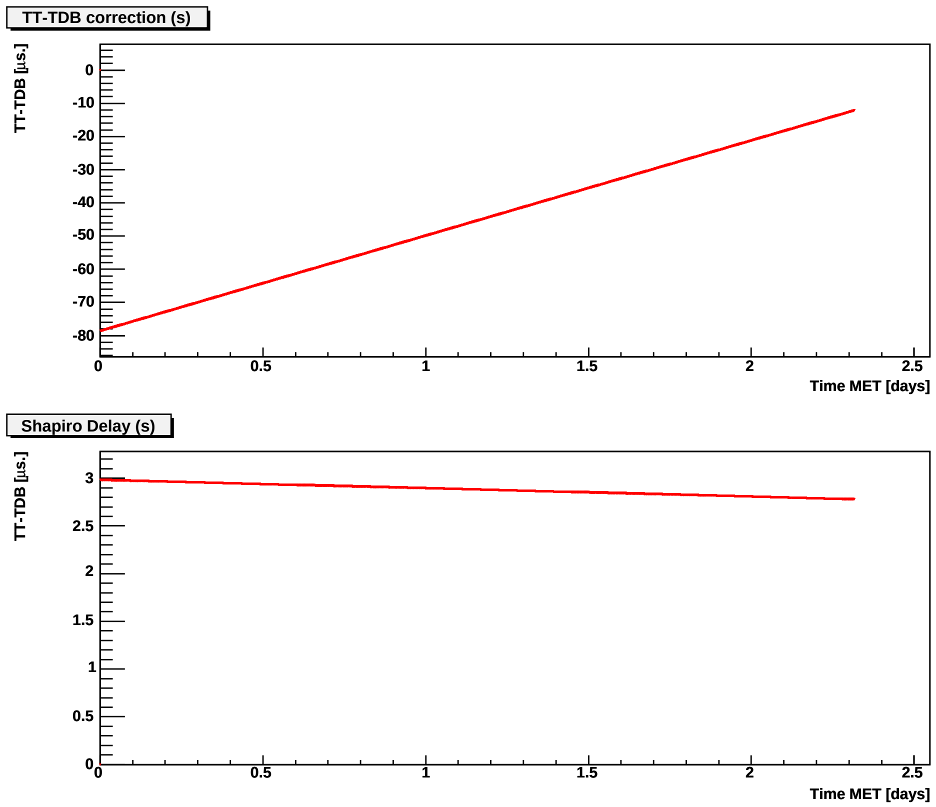

Figure 5.13: The relativistic corrections used by *PulsarSpectrum* for correcting the photons arrival times. Top: The conversion from TT to TDB. Bottom: The Shapiro delay.

the gravitational field of the Sun and it is called *Shapiro Delay* (Shapiro & Teukolsky, 1983). This can be calculated as:

$$\Delta t_{sh}(t_G) = \frac{2G}{c^2} \ln(1 - \hat{\mathbf{s}} \cdot \mathbf{r}_{GS}) \tag{5.6}$$

where $\mathbf{r}_{GS}$ is the vector from GLAST to the Sun. The Shapiro delay become significant only for sources that in the celestial sphere are located close to the Sun.

5.5.2 Period changes and ephemerides

The phase assignment procedure assigns a rotational phase to each photon, taking into account that the period increases with time.
The rotational energy of pulsars decreases with time as describe in Ch. 3 and hence the period increases. For γ-ray pulsar science the radio ephemerides are fundamental for assigning the correct phase to each photon. If we know the frequency *f*(t_0) and its derivatives $\dot{f}(t_0)$ and $\ddot{f}(t_0)$ at a particular time t_0, known as *epoch*, the phase is then:

$$\phi(t) = int[f(t_0)(t-t_0) + \frac{1}{2}\dot{f}(t_0)(t-t_0)^2 + \frac{1}{6}\ddot{f}(t_0)(t-t_0)^3]. \tag{5.7}$$

With *int* we indicate the integer part of a number. The interval between two photons must be "de-corrected" for this effect. In the parameters file the user can specify a set

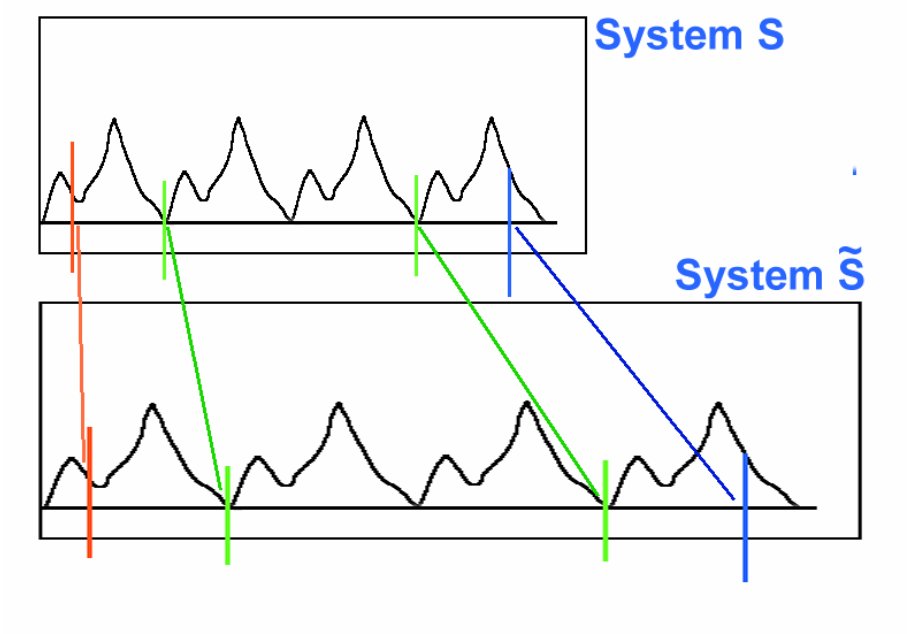

Figure 5.14: The period change correction used in *PulsarSpectrum* . The simulator apply a transformation from a system S where the period is constant to a system $\tilde{S}$ where period varies in time.

of ephemerides with the relative epoch of validity expressed in Modified Julian Date. The simulator then computes the opportune arrival time such that, after applying the barycentric corrections and the Eq. 5.7, the correct phase is obtained.

5.6 Timing Noise

The period variation of pulsars does not follow exactly a steady linear increase since fluctuations in phase occur that are generally called *timing noise*. This is believed to be due to changes in the structure of the neutron star itself and in its magnetosphere and possibly precession.
The effect of timing noise in the observation is to smear the lightcurve of a pulsar and, since this is not predictable, it is a serious limit to all the possible blind searches for γ-rays pulsars. For some pulsars the timing noise in radio has been measured on time scales as small as ms. over time scales of months.
The period evolution can also be subject to abrupt changes in period and its derivative, during phenomena known as *glitches*. Both timing noise and glitches are very important to achieve most detailed simulation of γ-ray pulsars. The implementation of *PulsarSpectrum* is capable of including timing noise but glitches have been not yet included but it will be one of the main next implementations.
In a simplified model of timing noise the rotational phase $\phi(t)$ at an arrival time t can be written as:

$$\phi(t) = \phi_S(t) + \phi_N(t) \tag{5.8}$$

where the first term indicate the phase obtained if pulsar period would evolve in a steady linear regime. The second term is the timing noise contribution. There are other contributions, e.g. due to instrument resolution, but they will be neglected in this modeling. *PulsarSpectrum* has been upgraded to simulate both timing noise using some phenomenological model. Currently there are some proposed models for timing noise is pulsars,e.g.(Arzoumanian et al., 1994; Cordes, 1980) but in *PulsarSpectrum* the followed approach is to obtain a simple phenomenological model for the timing noise in order to have a source of noise to apply to the pulsars.
This contribution is very important since it allow to have noisy pulsars that are much more realistic in case of testing blind search techniques for finding new Radio Quiet pulsars.
The model developed for *PulsarSpectrum* is based on a Random Walk approach to Timing Noise and it will be described in the following.
Since our goal is to include timing noise as a source of limitation of LAT observation, we adopt a very simple approach without going too much into details with the timing noise model.

5.6.1 Random Walk model

Among the many models for Timing Noise the one that has been implemented follow the approach used in the work of Cordes and Downs (Cordes & Downs, 1985) and based on Random Walk modeling.
According to them an *activity parameter* can be defined for estimating the amount of random walk with respect to the timing noise of the Crab pulsar. Using JPL data they studied the phase fluctuations and argued that the phase residuals after fitting data with a second-order polynomial can be modeled with a Random Walk process. For details see (Cordes & Downs, 1985). I will outline here the main modeling conclusions and equations that have been used for introducing timing noise. The priority of developing pulsar simulations were to insert timing noise for blurring data and for studying the LAT response for pulsars that does not follow a pure linear period growth with time. The goal is not yet to study the possibility of studying timing noise in γ-rays. According to this goal the timing noise model adopted is very simple and not too much complicated from physical point of view.
In order to estimate the timing noise to the rms phase residual σ^2_{TN} some fits have been made with a pure linear evolution in order to estimate $\phi_S(t)$ at a time t and then subtracted from the observed phase. An interesting relation arised when studying timing noise in (Cordes & Downs, 1985) between the period first derivative $\dot{P}$ and an *Activity parameter* defined as:

$$A = log_{10}[\sigma_{TN}(m,T)/\sigma_{TN}(m,T)_{Crab}]_{m=2} \tag{5.9}$$

which normalize the rms timing noise in time units with that or the Crab pulsar for the same time span T. the number m indicate that the rms residual is computed from fitting with a polynomial of degreee m. The scaling of the Crab pulsar timing noise at a particular time T is computed using:

$$\sigma_{TN}(2,T)_{Crab} = 12(T/1628days)^{3/2}ms \tag{5.10}$$

A plot of activity A in function of P and $\dot{P}$ as reported in Figure 5.15 has shown a correlation coefficient of 0.63 between A and log$\dot{P}$ using pulsars arrival times derived from (Cordes & Downs, 1985). The relation found is:

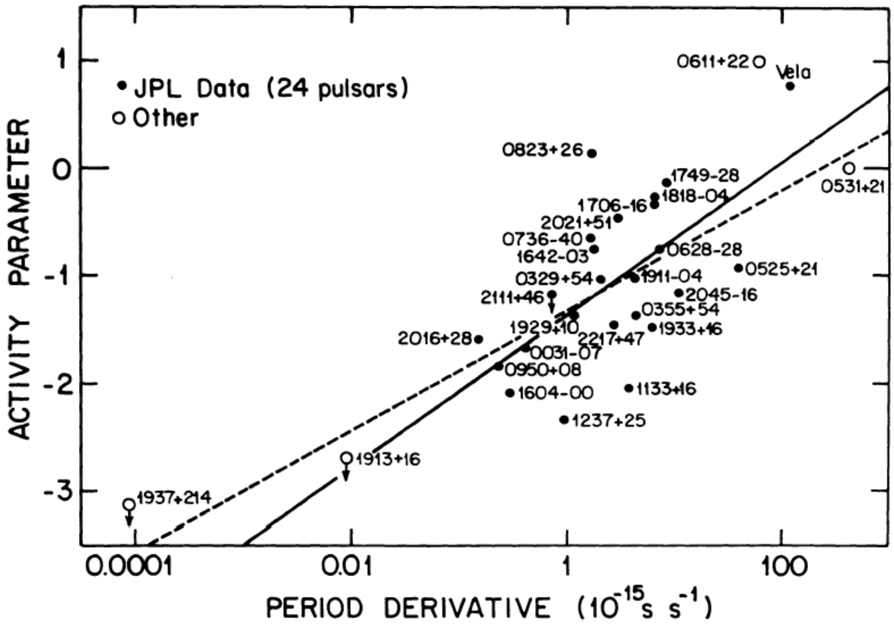

Figure 5.15: Activity parameter of Eq. 5.9 vs. pulsar period derivative $\dot{P}$. The solid line is a fit of all JPL data (except PSR B211+46): th dashed line is a fit which also exclude the poins for the Vela pulsar. From (Cordes & Downs, 1985)

$$A = -1.37 + 0.71 log_{10}\dot{P} \tag{5.11}$$

As a first step the timing noise activity parameter is evaluated (using Eq. 5.9).
From the relation in Eq. 5.11 the corresponding value of σ_{TN} is then derived and used for the Random Walk model.
We assume that at at some particular times t_i during the simulation a *Noise event* occur, i.e. a discontinous change in rotational parameters of the pulsar. The interval between two noise events has ben set to follow a Poisson distribution with mean rate of R=1 day^{-1}.
According to (Cordes & Downs, 1985) I considered that a random walk in the kth derivative of the phase can be modeled as:

$$\frac{d^k\phi(t)}{dt^k} = \sum_i a_i u(t - t_i) \tag{5.12}$$

where a_i is the dispersion with random amplitude with zero mean, u is the unit step function and Noise events occur at times t_i with an average rate R.
Three types of random walk can be defined. The *Phase Noise* Random Walk (PN) correspond to k=0, the *Frequency Noise* Random Walk (FN) correspond to k=1 and

the *Slowing-down Noise* Random Walk (SN) correspond to k=2. I will briefly discuss how *PulsarSpectrum* is able to simulate timing noise according to these three type of Random Walk timing noise.

According to (Cordes & Downs, 1985) the rms of the a_i amplitudes are the rms of

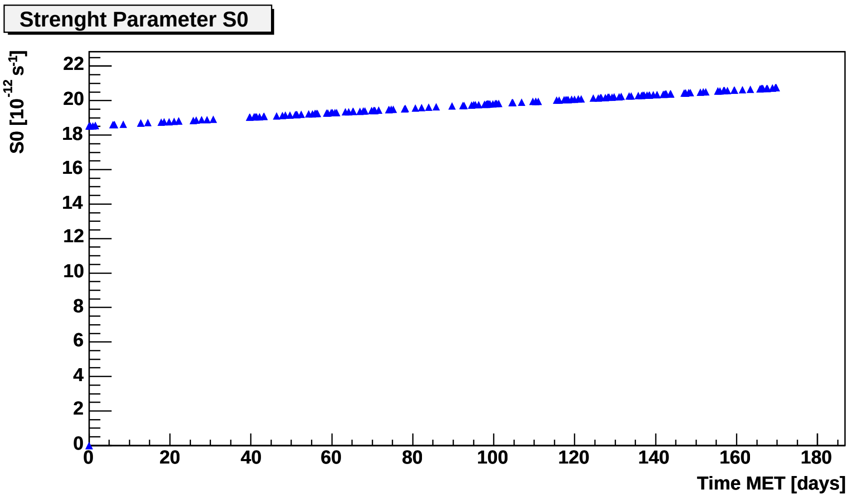

Figure 5.16: Behaviour of the Strength S0 for a PN Timing noise (case of simulated pulsar PSR J0837-3515)

phase ϕ, frequency ν and frequency derivative $\dot{\nu}$, respectively for k=0,1,2.
In case of pure *Phase Noise* (PN) random walk the rms of the phase can be related to a parameter S_0 called *Strength parameter* with the equation:

$$S_0 = R\langle(\delta\phi)^2\rangle \text{ (Phase Noise)} \tag{5.13}$$

where R indicate the function that identify the Random Walk in Phase. The strength can be estimated when RT>1 using the relation:

$$\hat{S}_0 = C^2_{0,2}\sigma^2_{TN}(2,T)(2T^{-1}) \tag{5.14}$$

where the $C_{0,2}$ is a correction factor defined in (Cordes, 1980) evaluated for computing the strength parameters using a second order polynomial fit for period evolution. For PN Random Walk this coefficient has a value of 3.7. The evolution of $\hat{S}_0$ with the observation time T is shown in Fig. 5.16 for the case of the simulated pulsar PSR J0837-3515 [8].
This simulated pulsar has been used to show an example of pure *Phase Noise* (PN) and has a period of about 1 s and a $\dot{P}$=2.78×10^{-14}, with a corresponding activity A≈-0.34. First of all *PulsarSpectrum* compute the activity parameter A from the Eq. 5.11 using the period and period derivative of the pulsar to be simulated. The activity parameter is then used to evaluate the σ_{TN} according to Eq. 5.10. From that value it is possible to have an estimate of the strength parameter $\hat{S}_0$ to substitute in Eq. 5.13 to get the

[8] Despite its name, this is a complete simulated pulsar. Its position has been computed from a population synthesis code by (Gonthier et al., 2002) as it will be described in next Chapter. The name has been given in order to reproduce the standard J2000 naming convention

rms of the phase steps that occurr at times t_i. An example of the resulting PN timing noise phase residual for PSR J0837-3515 is shown in Fig. 5.17.

The second type of Random Walk is where the steps occurr in frequency instead of in

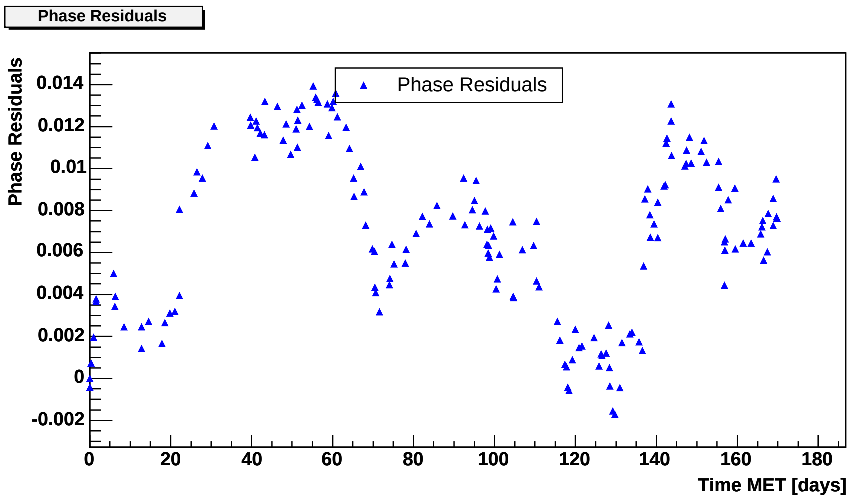

Figure 5.17: Phase residuals for simulated pulsar PSR J0837-3515 with pure PN Random Walk

phase. This is called as in (Cordes & Downs, 1985) *Frequency Noise*(FN).

In case of pure Frequency Noise random walk the rms of the phase can be related to a parameter S_1 called *Strength parameter* with the equation:

$$S_1 = R\langle(\delta\nu)^2\rangle \text{ (Frequency Noise)} \tag{5.15}$$

where R indicate the function that identify the Random Walk in Frequency. The strength can be estimated when RT>1 using the relation:

$$\hat{S}_1 = C^2_{1,2}\sigma^2_{TN}(2,T)(12T^{-3}) \tag{5.16}$$

where the $C_{1,2}$ is a correction factor defined in (Cordes, 1980) evaluated for computing the strength parameters using a second order polynomial fit for period evolution. For FN Random Walk this coefficient has a value of 15.5. The evolution of $\hat{S}_1$ with the observation time T is shown in Fig. 5.18 for the case of the simulated pulsar PSR J1719-7402[9].

This simulated pulsar has been used to show an example of pure *Frequency Noise* (FN) and has a period of about 0.38 s. and a $\dot{P}$=4×10^{-15}, with a corresponding activity A≈-0.93.

The rms of the frequency steps is computed in a similar way than the compuation of PN noise as described before. An example of the resulting FN timing noise phase residual for PSR J1719-7402 is shown in Fig. 5.19.

The last type of Random Walk than can be computed by *PulsarSpectrum* is the one

[9]Despite its name, this is a complete simulated pulsar. Its position has been computed from a population synthesis code by (Gonthier et al., 2002) as it will be described in next Chapter. The name has been given in order to reproduce the standard J2000 naming convention

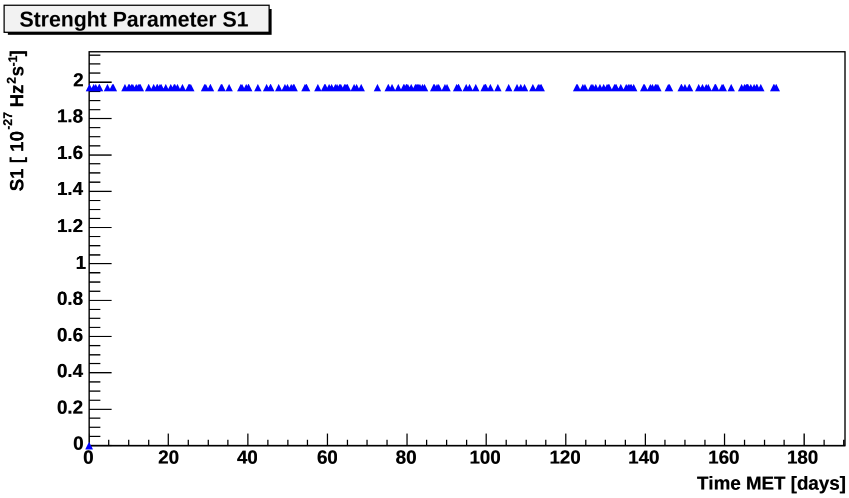

Figure 5.18: Behaviour of the Strength S1 for a FN Timing noise (case of simulated pulsar PSR J1719-7402)

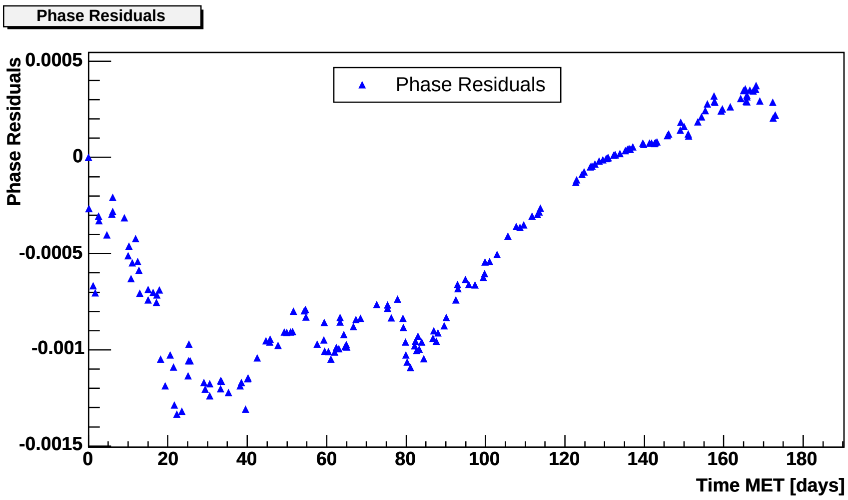

Figure 5.19: Phase residual for simulated pulsar PSR J1719-7402 with pure FN Random Walk

where steps occurr in frequency first derivative instead of in phase or frequency. This is called as in (Cordes & Downs, 1985) *Slow-Down Noise*(SN).
In case of pure Slow Down Noise random walk the rms of the phase can be related to a parameter S_2 called *Strength parameter* with the equation:

$$S_2 = R\langle(\delta\dot{\nu})^2\rangle \text{ (Slow-Down Noise)} \tag{5.17}$$

where R indicate the function that identify the Random Walk in Freqeuncy first derivative. The strength can be estimated when RT>1 using the relation:

$$\hat{S}_2 = C^2_{2,2}\sigma^2_{TN}(2,T)(120T^{-5}) \tag{5.18}$$

where the $C_{2,2}$ is a correction factor defined in (Cordes, 1980) evaluated for computing the strength parameters using a second order polynomial fit for period evolution.

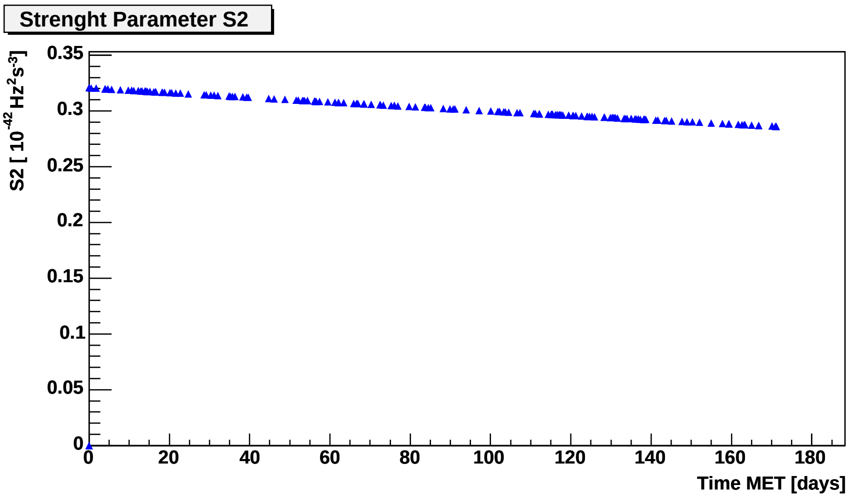

Figure 5.20: Behaviour of the Strength S2 for a SN Timing noise (case of simulated pulsar PSR J1734-3827).

For FN Random Walk this coefficient has a value of 23.7. The evolution of $\hat{S}_2$ with the observation time T is shown in Fig. 5.20 for the case of the simulated pulsar PSR J1734-3827[10].
This simulated pulsar has been used to show an example of pure *Slow-Down Noise* (SN) and has a period of about 0.16 s and a $\dot{P}$=2.27$\times 10^{-15}$, with a corresponding activity A$\approx$-1.11.
The rms of the frequency first derivative steps is computed in a similar way than the computation of PN or FN noise as described before. An example of the resulting SN timing noise phase residual for PSR J1734-3827 is shown in Fig. 5.21.

5.7 Pulsars in binary orbits

As described in Ch. 3, there is a parecentage of pulsars that are located in binary systems. Accretion mechanism is believed to be the responsible of the rejuvenation process that produce millisecond pulsars.
Almost 80 percent of millisecond pulsars are observed in binary systems but less than 1 percent of normal pulsars.
Binary pulsars will be one possible target for GLAST LAT, that is expected to see pulsed emission from pulsars in binary orbit. In particular millisecond pulsars are systems where the companion is a low-mass star, e.g. a white dwarf or a neutron star, then the emission spectrum should be not affected as pulsars around normal or giant stars, as for example PSR B1263-79 recently studied by HESS.
Pulsars in binary orbit show timing effects due to the motion along its orbit and to the gravitational field of its companion. It is possible to correct for these effects in a similar

[10]Despite its name, this is a complete simulated pulsar. Its position has been computed from a population synthesis code by (Gonthier et al., 2002) as it will be described in next Chapter. The name has been given in order to reproduce the standard J2000 naming convention

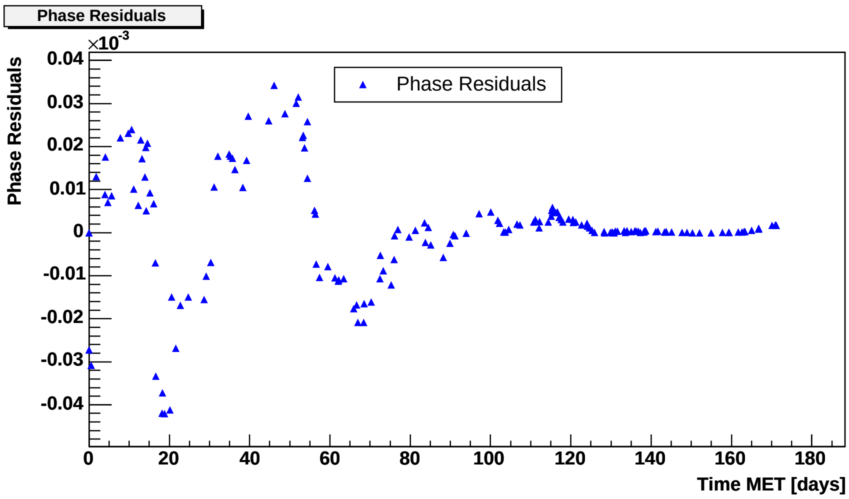

Figure 5.21: Phase residual for simulated pulsar PSR J1734-3827 with pure SN Random Walk

way of the barycentric corrections.
Such *binary demodulations* are currently implemented in the SAE tool called *gtbary* that perform barycentering of photons. In order to test this tool a basic model for binary orbit has been implemented in *PulsarSpectrum* and wil be described here.
When pulsar companion has a very strong gravitational field, the classical description in terms of Keplerian parameters cannot be used. In the implementation of *PulsarSpectrum* , however, I neglect these terms and concentrate only on the basic corrections without considering the post-Newtonian parameterization.
The equation for arrival time corrections described before in Eq. 5.4 must be modified with some terms:

$$t_B = t_G + f^{TT-TDB}(t_G) + g(t_G) + s(t_G) + \Delta_{RB} + \Delta_{EB} + \Delta_{SB} \tag{5.19}$$

where Δ_{RB} is called the *Roemer delay*, Δ_{EB} is the *Einstein delay* and Δ_{SB} is the *Shapiro delay*. These terms can be computed starting from the Kepler Equation and then corrected by some post-keplerian terms. In particular Δ_{SB} and Δ_{EB} need 3 extra parameters that can be given by the user otherwise both are zero and the binary corrections is composed by the Roemer delay only.

5.7.1 Keplerian description

In order to model the motion of a pulsar in a binary orbit Kepler's laws can be used. The description of the system can be performed in terms of the six *Keplerian parameters*, that are shown schematically in Fig. 5.22. The Kepler parameters that are required to refer to arrival time of the photon to the barycented of the binary system are (Lorimer & Kramer, 2004):

- Orbital period P_b;
- Projected major semi-axis $a_p \sin i$, where i is the *orbital inclination*, defined as the angle between the orbital plane and the plane of the sky;

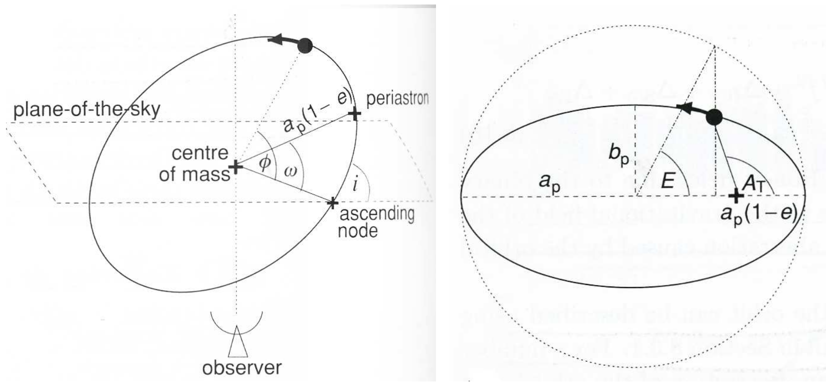

Figure 5.22: Left: Definition of the orbital elements in a Keplerian orbit.The angle i indicate the *orbital inclination*, defined as the angle between the orbital plane and the plane of the sky. Right: Definition of the *Eccentric Anomaly* E and *True Anomaly* A_T. From (Lorimer & Kramer, 2004)

- Orbital eccentricity e;
- Longitude of periastron ω;
- Epoch of periastron passage T_0;
- Position angle of the ascending node Ω_{asc}

These parameters are read by *PulsarSpectrum* in a similar way as the basic pulsar parameters described in Sec. 5.1.1, and are stored in a ASCII file called *BinPulsarDataList.txt*. Since the LAT pulsar database D4 can contain an header with orbital data for binary pulsars, *PulsarSpectrum* is able to save an output ASCII file that can be easily converted into a binary pulsar FITS estension to the D4 database.
In order to find the binary correction the first step is to solve the Kepler equation, that can be written using the *Eccentric Anomaly* E shown in Fig. 5.22(Right).

$$E - e\sin E = \Omega_b \left[(t - T_0) - \frac{1}{2}\frac{\dot{P}_b}{P_b}(t - T_0)^2 \right] \tag{5.20}$$

where Ω_b is the mean angular velocity $\Omega_b = 2\pi/P_b$. The term $\dot{P}_b$ is the change of orbital period and can be computed using the post-keplerian parameters. Since in our description we ignore such terms, the Kepler Equation Eq. 5.20 assumes a simpler form.
For every photon *PulsarSpectrum* solve the Kepler equation Eq. 5.20 numerically and find a corresponding eccentric anomaly E.

5.7.2 Binary corrections

The Kepler Equation provides the basic information for finding the Roemer delay, the Einstein delay and the Shapiro delay.
The Roemer delay is cause by the orbital motion of the pulsar and is similar to the

geometrical delay described for barycentric corrections. If we define the variable $x \equiv a_p \sin i$, the Roemer delay Δ_{RB} can be computed as:

$$\Delta_{RB} = x(\cos E - e)\sin\omega + x\sin E\sqrt{1-e^2}\cos\omega \qquad (5.21)$$

Since E is calculated at any arrival time, *PulsarSpectrum* is able to compute the corresponding Roemer delay. Fig. 5.23 show an example of the Roemer delay computed by *PulsarSpectrum* for a simulated millisecond pulsar called PSRJ1735-5757 placed into a binary orbit with eccentricity e=0.78 and orbital period P_b=5.7 days. The orbital periodicity is clearly visible over the entire simulation time of about 3 months. The

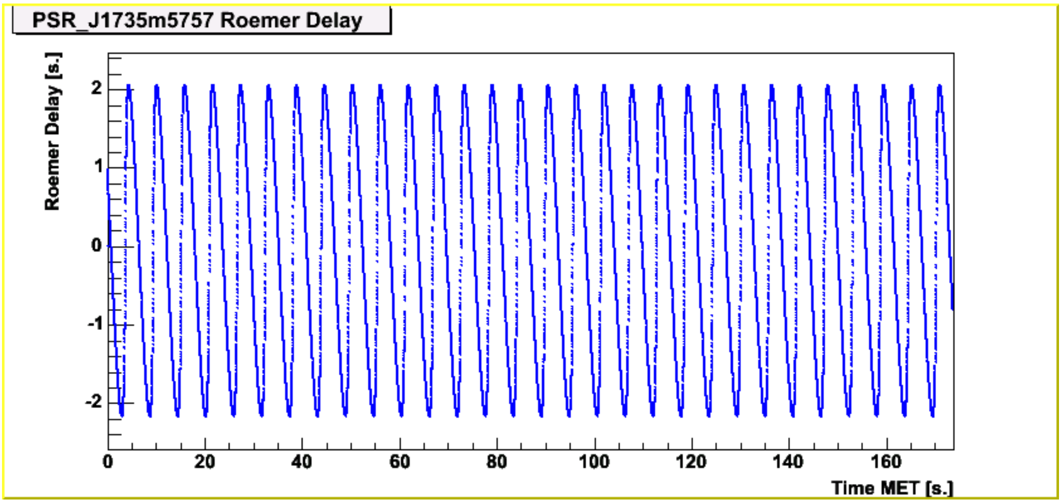

Figure 5.23: Roemer delay calculated by *PulsarSpectrum* for the simulated pulsar PSR J1735-5757 placed in a (hypotetic) binary orbit with 5.7 days orbital period. The time window cover 3 months of simulation.

Einstein delay Δ_{EB} describes the modification in arrival times caused by the varying effect of the gravitational redshift due to pulsar companion and the time dilation as the pulsar moves into the orbits at varying speeds and distances (Lorimer & Kramer, 2004). It can be written as:

$$\Delta_{EB} = \gamma \sin E \qquad (5.22)$$

where γ is a post-keplerian parameter that denotes the amplitude expressed in seconds and that can be computed from the mass function of the binary system as in (Lorimer & Kramer, 2004). *PulsarSpectrum* is able to compute this delay if the parameter γ is given in input, but future developments will compute this from at least the lowest-order post-Newtonian equations.
The Shapiro delay Δ_{SB} for binary pulsars is caused by the gravitational field of the pulsar companion and can be characterized by two post-keplerian parameters *range* r and *shape* s. The Equation for Shapiro delay can be expressed as:

$$\Delta_{SB} = -2r\ln\left[1 - e\cos E - s\left(\sin\omega(\cos E - e) + \sqrt{1-e^2}\cos\omega\sin E\right)\right] \qquad (5.23)$$

This delay can be computed if the parameters r and s are known, in a similar manner than γ.

The terms here described are computed for each arrival times and applied to each photons. Binary corrections have been implemented after the Data Challenge 2 (See Ch. 7) then they are not included in the sample studied in the next Chapters regarding DC2.

5.8 The *Pulsar Simulation Suite*

The *PulsarSpectrum* can simulate in considerable detail γ-ray emission from pulsars but in many cases it is necessary to create large sample of parameters for simulating a large number of pulsars.
During the LAT Data Challenge 2 (See Ch. 7), for example, a population of about 400 pulsars was created.
The *Pulsar Simulation Suite* is a collection of ROOT C macros that are able to per-

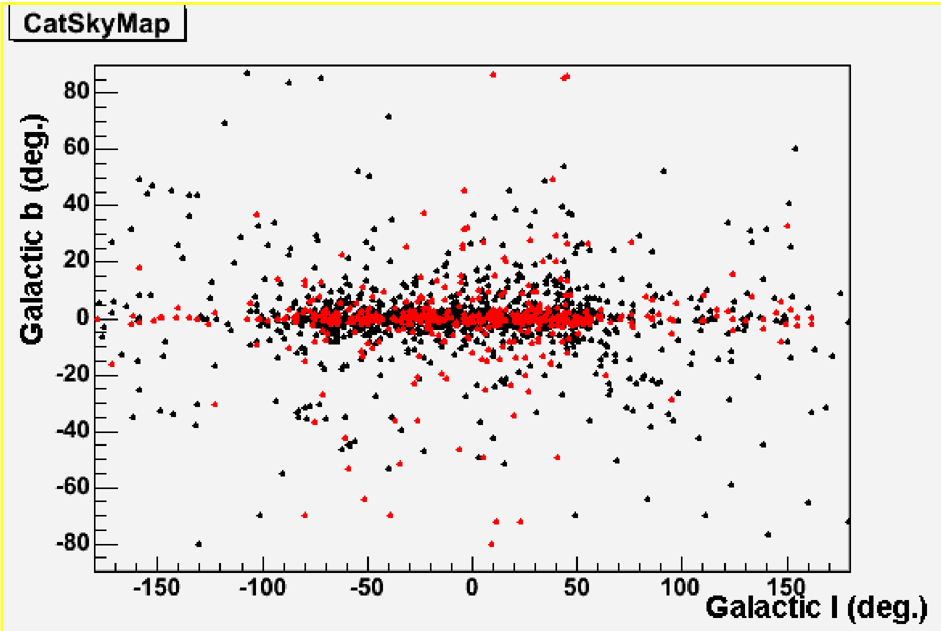

Figure 5.24: Examples of synthetized pulsar population (red) prepared with *Pulsar Simulation Suite* and the comparison with the real population of radio pulsars in the ATNF Catalog (black). Galactic distribution.

form several tasks, from the generation of a realistic population to the formatting of the parameters in appropriate *DataList* files and *XML source* files. The first component is the *PulsarSynthetizer*, that has been designed to create a large population of pulsars with parameters that are in agreement with the observed distribution of radio pulsars. Starting from the ATNF Catalog the distribution of distances, galactic positions and periods are derived. From these distribution a random set of parameters are extracted, considering possible correlations between parameters, e.g. between period and period first derivative. The results are in good agreement with the observed data as can be ssen in Fig. 5.24 and in Fig. 5.25.
It it important to remind that this program is not a full population synthesis code and

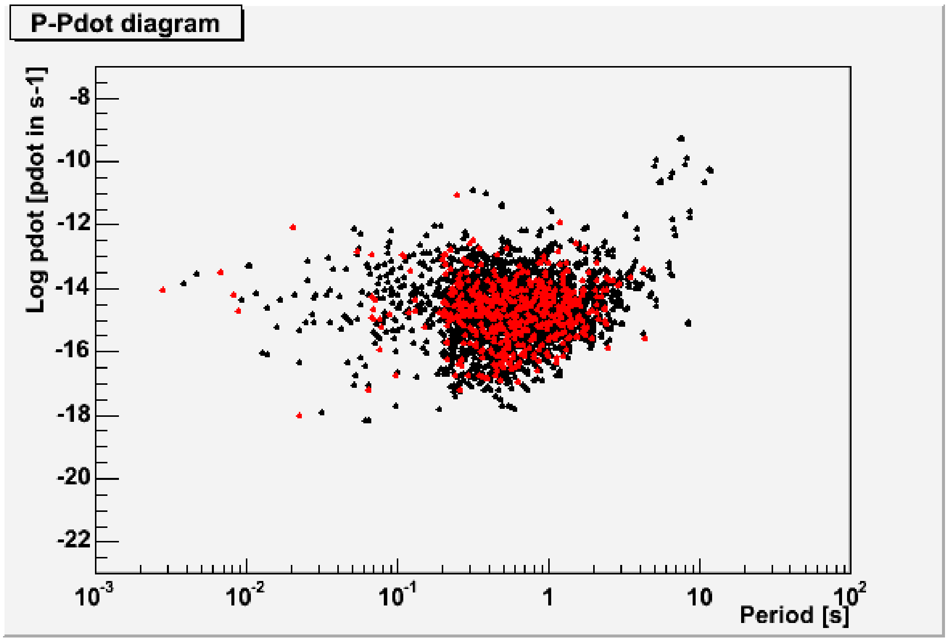

Figure 5.25: Examples of synthetized pulsar population (red) prepared with *Pulsar Simulation Suite* and the comparison with the real population of radio pulsars in the ATNF Catalog (black). $P - \dot{P}$ diagram.

it is not able to reproduce the whole population of pulsars, but only of those with timing available. The so-called *Radio Loud* pulsars, i.e. those without a radio emission and thus a timing solution, cannot be reproduced with the *PulsarSynthetizer* in the *Pulsar Simulation Suite* .
Once these first parameters are computed the flux is determined according to some analytical approximation of a specific emission scenario.In this case some very rough estimates of flux limits for GLAST are possible (Fig. 5.26). This tool is very useful since it permit to have a realistic sampled population without too detailed calculations. On the other hand this model can only produce distributions of Radio-Loud pulsars, while for estimating the fraction of Radio-Quiet some more sophisticated programs are needed, e.g. evolutionary codes as (Gonthier et al., 2002).
Another tool of particular interest is *TH2DSpectrumShaper*, that is able to producee an N_ν histogram starting from numerical data of theoretical emission model. The output files are a *DataList* and an *XML source file* that can be used directly in the *PSRShape* model of *PulsarSpectrum* . If a list of pulsar parameters is already available, e.g. generated from an outside code, it is possible to generate the *PulsarSpectrum* input files using the *PulsarSetsFormatter*. A pulsar set viewer complete the current release development of *Pulsar Simulation Suite* .

5.9 Summary

In this Chapter I have presented the tools developed for pulsar simulations for GLAST. The tools presented in this Chapter are a major part of the larger Ph.D. project and

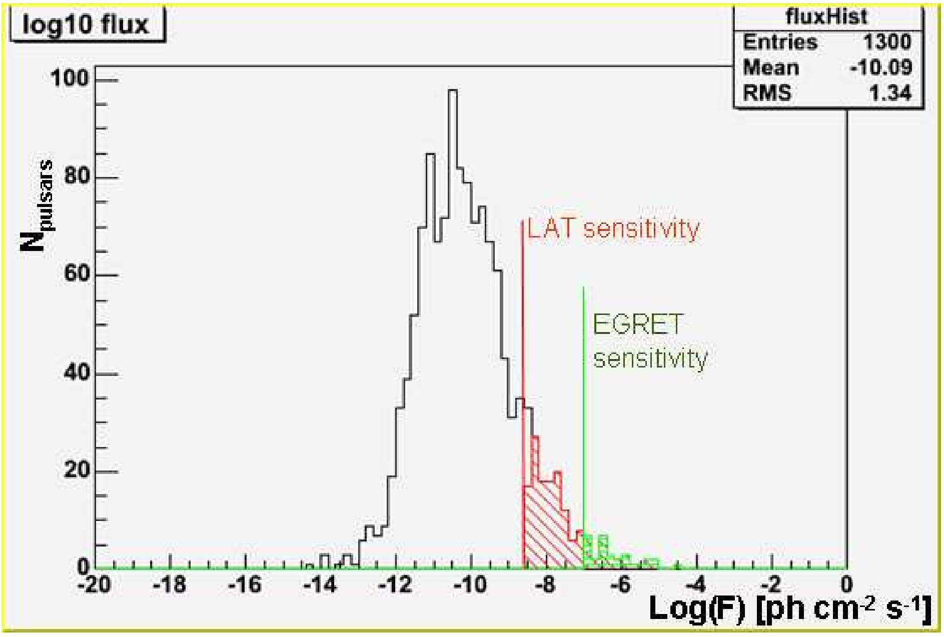

Figure 5.26: Number of synthetized pulsars above EGRET and LAT limits. The model used is the simple Polar Cap (Harding, 1981; Daugherty & Harding, 1996).

are the starting point for all simulations and analysis presented in this thesis.
These tools are continuously used by the LAT Collaboration for testing functionality of the pulsar analysis tools and for making estimates on LAT capabilities for pulsar science.
The main program is the *PulsarSpectrum* simulator, that can reproduce both the emission features from γ-ray pulsars and the detailed computation of the timing effects, including barycentric corrections, period evolution and Timing Noise. This simulator is under continue development in order to satisfy all the incoming requests from the LAT Collaboration for simulating with increasing details γ-ray pulsars.
There are other minor macros and tools specifically designed to prepare realistic population to simulate with *PulsarSpectrum* . We include all these tools in the *PulsarSpectrum* , a collection of programs and macros that have been used during several simulation developments and during important software milestones for GLAST preparation.
One of these important occasion has been the LAT Data Challenge 2, where a complete set of realistic pulsar population has been simulated and analyzed. The application of the pulsar simulation tools presented here to he LAT Data Challenge 2 will be presented in the next Chapter.

Chapter 6

LAT Data Analysis: the case of EGRET pulsars

In this chapter I present a basic analysis of simulated γ-ray pulsars as observed by LAT. This Chapter has two main goals: first of all to show what are the main analysis tools and techniques developed by the LAT collaboration for LAT data analysis. Second, in this Chapter it is shown how the *PulsarSpectrum* simulator can be used to produce simulated dataset that can be useful for testing analysis tools. In this sense some analysis case will be presented, together with examples of how analysis tools can be used and what analysis scripts and techniques I developed as a part of my Ph.D. for managing some simple data analysis of pulsars with the LAT.
The analysis cases presented are based on simulation of 30 days of LAT obsevation in scanning mode.
A typical analysis of a pulsar can be divided in three main categories, *Spatial Analysis*, *Temporal Analysis* and *Spectral Analysis*. These kind of analyses are typical for every sources, but for pulsars temporal analysis has a particular importance, since it can provide a very powerful tool for identifying a γ-ray source with a pulsar using periodic modulation of γ-rays.
The tools available for analyzing LAT data consist of a set of LAT SAE tools specific for basic pulsar analysis. After the basic data reduction a lot of different tools can be used for each kind of analysis. For the analyses carried out in this Chapter I used several analysis packages and tools, in particular the FTOOLS suite [1] for basic manipulation of FITS files, then ROOT Analysis Framework [2] and a set of Python scripts developed for performing automatic analysis of large set of pulsars, as it will be described in next Chapters.
Some specific analysis have been chosen here, in particular a basic temporal analysis of Vela pulsar, in order to show how the periodicity can be easily tested for a bright source. Then the case of PSR B1706-44 is considered, as an example of standard analysis chain consisting of spatial, spectral and temporal analysis. Then an analysis of simulated pulsar PSR B1951+32 show how a fainter pulsar can be analyzed. These analyses are very basic and can be expanded in several ways, as for example the study the phase-resolved spectroscopy in case of pulsars that give enough counts.

[1]See *http://heasarc.gsfc.nasa.gov/ftools/ftoolsmenu.html*
[2]See *http://root.cern.ch/*

6.1 Pulsar Data Analysis

The three basic properties that are of concern by the γ-ray pulsar studies are the spatial, temporal and spectral distribution of photons.
The γ-ray experiments like the LAT are counting telescopes and for each detected photon and energy, an arrival time and a direction are reconstruct. The analysis is done by looking at the distribution of these three variables to derive the characteristics of the source.
Although this is true for all energies, the methods of analysis are as varied as the energy bands in which pulsars are observed. The primary difference between γ-ray astrophysics analysis and analysis at lower energies is the relative sparseness of the data. In order to detect sources in γ-ray observations of the order of days are required.
The better statistics and resolution available by the LAT will permit high-detailed studies on point sources and in particular on pulsars.
In Ch. 2 the LAT *Science Analysis Environment* (SAE) has been presented. It consists of a suite of tools devoted to the data analysis of the LAT data. In particular there are some tools devoted to the data analysis of the LAT data. In particular there are some tools to perform analysis while some other provide analysis for particular source classes. As for previous experiments such as EGRET, the spatial analysis, that is done mainly using the *maximum likelihood* technique, is performed using the tool called *gtlikelihood*. The timing analysis of pulsars in the SAE includes several tools that have been described in Ch. 2.
The spectral analysis can be performed using the maximum likelihood, since this tools provides also fit with the spectrum. A second approach is to build input files that can be used with the *XSpec* package[3].

6.1.1 Spatial Analysis

To perform a sensitive search for point sources it is necessary to do more than look for emission above the predicted diffuse background. If an excess is truly due to a point source, it will be spatially distributed as the energy dependent PSF of the instrument. The technique used in analyzing γ-ray data in COS B and EGRET was the *maximum likelihood method*, fully described in (Mattox et al., 1996). This technique allow the possibility to identify a point source above the background and to estimate the total flux. I briefly review the basic concepts of the method.
Maximum Likelihood method use the Instrument Response Function, that can be written in the most general form as:

$$R(E', \hat{p'}; E, \hat{p}, t) = A(E, \hat{p}, t)P(\hat{p'}; E, \hat{p}, t)D(E'; E, \hat{p}, t) \tag{6.1}$$

where E is the true photon energy, $\hat{p}$ the true photon direction, E' is the measured photon energy and $\hat{p'}$ the measured photon direction. The function $A(E, \hat{p}, t)$ is the instrument *effective area*, $P(\hat{p'}; E, \hat{p}, t)$ is the *Point Spread Function* and $D(E'; E, \hat{p}, t)$ is the *energy dispersion*.

[3] $http://heasarc.gsfc.nasa.gov/docs/xanadu/xspec/$

EGRET used binned Poisson likelihood defined as:

$$L(\mu) = \prod_{ij} \frac{\mu_{ij}^{n_{ij}} e^{-\mu_{ij}}}{n_{ij}!} \tag{6.2}$$

where the sky map under analysis was binned in spatial bins (i,j). In this Equation μ_{ij} is the predicted number of counts in bin (i,j) and n_{ij} the measured number of counts in the bin (i,j). The bin width in sky coordinated, e.g. Right Ascension or Declination, was 0.5°. Count maps for energy above 100 MeV were used for detection, identification and flux extimation. This method was also used for spectral analysis of EGRET data, using 10 standard energy bands from 30 MeV to 10 GeV. A single effective Point Spread Function (for a given measured energy range) was used for convolving the diffuse model and for estimating counts for each of the sources, regardless of intrinsic spectrum.
The nature of the LAT response functions motivated the use of an *Unbinned likelihood* for some reasons. First of all the relatively broad PSF and the high number of expected sources imply that emission from nearby point sources always overlaps. The amount of overlap is less severe for photons above 1 GeV. Second, the Point Spread Function strongly depend on the energy, then the intrinsic spectrum of a source affects the degree of source confusion. Third, the large Field of View and the variation of response in function of incident angle, combined with the scanning mode makes almost impossible to compute a response function valid for all events.
The Unbinned Likelihood is the limiting case of a binned analysis with infinesimally small bins, each containing 0 or 1 count. In this method the data space considered includes an energy axis as well as photon direction. Differently from EGRET, here the spectral fitting is not decoupled from the source flux estimation.
Presently the LAT SAE contain the tool *gtlikelihoof* that is able to perform both *Unbinned Likelihood* and the *Binned Likelihood* analysis. In the analysis of this Chapted I will use the Unbinned Likelihood for spatial analysis of pulsars under consideration. Here then the basic of the Unbinned Likelihood is described, while the Binned Likelihood does not differ significantly from the EGRET likelihood method.
The region of the sky that is under analysis can be modeled including point sources with intensity $s_i(E,t)$, the Galactic diffuse emission $S_G(E,\hat{p})$ and extragalactic diffuse emission $S_{EG}(E,\hat{p})$ and possibly time varying sources S_l (e.g. Moon, SNRs, etc..).
The Source Model can be written as:

$$S(E,\hat{p},t) = \sum_i s_i(E,t)\delta(\hat{p}-\hat{p}_i) + S_G(E,\hat{p}) + S_{EG}(E,\hat{p}) + \sum_l S_l(E,\hat{p},t) \tag{6.3}$$

The Region Of Interest (ROI) is the defined as the extraction region for the data in measured energy, direction and arrival time.
Give the Source Model it is possible to compute the event distribution function M, i.e. the number of expected events gived the model.

$$M(E',\hat{p}',t) = \int_{SR} R(E',\hat{p}';E,\hat{p},t)S(E,\hat{p},t)dEd\hat{p} \tag{6.4}$$

where the Source Region SR is defined as the portion of the sky that contain all sources that contribute significantly to the ROI.

The predicted number of observed events in the ROI is the integral of M over the ROI:

$$N_{pred} = \int_{ROI} M(E', \hat{p'}, t) dE' d\hat{p'} dt \tag{6.5}$$

This calculation can be aided gretaly by defining the quantity $\epsilon(E, \hat{p})$ that is similar to the exposure map computed by EGRET:

$$\epsilon(E, \hat{p}) \equiv \int_{ROI} R(E, E', \hat{p}, \hat{p'}, d) dE' d\hat{p'} \tag{6.6}$$

where primed quantities indicate measured energies,E', and measured directions, $\hat{p'}$. This type of exposure map used by unbinned Likelihood differs significantly from the EGRET exposure maps, which are integrals of effective area over time.
The number of predicted events is then:

$$N_{pred} = \int_{SR} \epsilon(E, \hat{p}) S(E, \hat{p}) dE d\hat{p} \tag{6.7}$$

All these operations are implemented in the SAE tool with specific tools, in particular *gtexpmap*.
Finally, the unibinned likelihood can be computed as:

$$\log(L(\mu)) = \sum_j \log M(E', \hat{p'}, t) - N_{pred} \tag{6.8}$$

where the sum is taken over all the events j . The quantity L(μ) is referred to as the *likelihood function*. Comparing this to the expression for the binned likelihood, the first term can be identified with the factor $\prod_{ij} \mu_{ij}$ and the second term with $\prod_{ij} e^{-\mu_{ij}}$.
We call with $\hat{\mu}$ the optimal model parameters in Eq. 6.2, i.e. the ones that maximize L(μ), or equivalently lnL(μ).
The *Binned Likelihod* start from the Eq. 6.2 and compute the expected counts μ_{ij} in the (i,j)-th bin from the sum of k sources using the response function as:

$$\mu_{ij} = \sum_k \sum_{ij} \int dt \int_{SR} R(E', \hat{p'}; E, \hat{p}, t) S_k(E, \hat{p}, t) dE d\hat{p} \tag{6.9}$$

It is also possible to assume a model μ_0 with no sources, i.e. the *null hypothesis*. In alternative, a model with N source we call μ_N. The *likelihood ratio* λ_N is defined as:

$$\lambda_N = \frac{L(\hat{\mu_0})}{L(\hat{\mu}_N)} \tag{6.10}$$

As the maximum likelihood estimator $\hat{\mu}$ asymptotically approaches the true spatial distribution of the γ-rays, the test statistic, usually called $TS_N \equiv -2ln\lambda_N$ will be distributed as a $\chi^2(N)$ (Fierro, 1995; Mattox et al., 1996).
Thus, the significance S of a detection of a source at a specific position is:

$$S = \int_{TS_N}^{\infty} \frac{1}{2} \chi_1^2(\xi) d\xi = \int_{\sqrt{TS_N}}^{\infty} \frac{e^{-\eta^2/s}}{\sqrt{2\pi}} d\eta \tag{6.11}$$

Where we have used the integrand substitution η=$\xi^{1/2}$. The 1/2 factor at the first integral of Eq. 6.11 takes into account that counts number in a bin is always positive, eliminating one half of the statistical fluctuations. From Eq. 6.11 and adopting the common pratice to indicate the significance as a results of nσ, it turns out that the significance of a source is $\sqrt{T_s}\sigma$.
This method provide the possibility to determine the existence of a source and also gives an estimated of the counts that can be combined with the exposure to obtain the source flux. Additionally this method is very useful to provide also a spectral model of the source, allowing the user to perform a spectral analysis on the data.

6.1.2 Temporal Analysis

The problem with identifying γ-ray sources on the basis of their spatial proximity to the known positions of sources at other wavelength is the possibility of a purely coincidental position alignment. In the case of EGRET a typical likelihood contour had a radius of 0.5° and in many cases of 3EG sources no definitive association can be established(Fierro, 1995). A definite association with a pulsar can be established by finding a γ-ray signal modulated at the period of the known radio pulsars. This method works well for radio-loud pulsars, but for radio-quiet pulsars like Geminga the signal periodicity has to be found with totally different techniques of *blind periodicity search*.
For this reason radio-astronomers teams will coordinate with the GLAST community in order to provide updated ephemerides for a list of candidate γ-ray pulsars.
The low fluxes of γ-ray sources require combining different observations to improve the statistics. For pulsed analyses this requires that each γ-ray detected by the pulsar must be tagged with a corresponding *rotational phase*, i.e. the fraction of revolution at which a γ-ray emitted from the pulsar is detected at the LAT at the measured arrival time. Once the phase assignment, of phase-tagging has ben performed, the pulse analysis (e.g. phase-resolved spectral analysis) can be done.
The temporal analysis procedure for pulsars consists of three steps. The first are the so-called *barycentric corrections* (See also Ch. 5), where the arrival times at the instrument, which are expressed in Terrestrial Time[4], are converted to arrival times at the Solar System Barycenter, and expressed in Barycetric Dynamical Time[5].
This procedure is performed by using the tool *gtbary*, parts of the LAT SAE. It requires the file that describe the position of the LAT during the simulation and the position of the celestial sources.
Once the barycentric corrections have been applied and the arrival times have been referred to Solar System barycenter, it is possible to assign a phase to each photon. The phase is assigned according to ephemerides as following Eq. 5.7.At this point the lightcurve is obtained.
It is also possible to perform some tests for priodicy of the source. The three main tests used in GLAST LAT presently are the χ^2 test (Leahy et al., 1983), the Z_n^2(Buccheri et al., 1983) test and the H-test(De Jager et al., 1989). Here I will use for these examples the χ^2 test for testing periodicity of lightcurve.
The basic periodicy test for photons covering a time range T is to assign phases for

[4]For a definition of Terrestrial Time see Ch. 5

[5]For a definition of Barycentric Dynamical Time see Ch. 5

a range of trial periods from P_{min} = 2T/i_1 up to P_{max} = 2T/i_2, with i = i_2,i_2+1,...i_1. Thus in this case the frequency spacing is 1/2T and the period can be searched is steps of frequency resolution divided by two, but in this analysis also smaller frequency steps are used. The obtained phases are then folded in n bins. In absence of pulsations, or any secular trends, the counts in each bin of a lightcurve obtained by folding at a given period are Poisson distributed, with mean and variance best estimated by the mean number of count per bin $\bar{m}$. If the counts m_i counts in each phase bin i is large enough to assume to be normally distributed, then the statistics S:

$$S = \sum_{j=1}^{n} \frac{(m_j - m_{exp})^2}{m_{exp}} \tag{6.12}$$

is a χ^2 with n-1 degrees of freedom. Then it follows that the probability that the observed signal at any particular period will exceed by chance a level S_0 is given by the integrated χ^2 distribution:

$$Q_{n-1}(\chi_0^2 = S_0) = \int_{s_0}^{\infty} p_{n-1}(\chi^2) d\chi^2 \tag{6.13}$$

where $p_{n-1}(\chi^2)$ is the χ^2 distribution. It is possible to relate this expression with the (percent) confidence level c, such that S_0 has not been exceeded by chance given N_p periods(Leahy et al., 1983),

$$1 - c/100 = N_p Q_{n-1}(\chi_0^2 = S_0) \tag{6.14}$$

Another periodicity test is the Z_n^2-Test(Buccheri et al., 1983), that is based on the variable Z_n^2 defined as:

$$Z_n^2 = 2\sum_{k=0}^{n} (\alpha_k^2 + \beta_k^2) \tag{6.15}$$

where n is the number of harmonics to be considered and the α_k^2 and β_k^2 are defined as:

$$\alpha_k = (1/N) \sum_{i=1}^{N} \cos k\phi_i \tag{6.16}$$

$$\beta_k = (1/N) \sum_{i=1}^{N} \sin k\phi_i \tag{6.17}$$

where N is the number of photons and the ϕ_i's indicate the phases of each photon. It have been shown that in the limit of infinite m the Z_n^2 follows a χ^2 distribution with 2n degrees of fredom.
This method is an improvement with respect to the χ^2 test, but it has a big limitation, as well as the Chi squared test. Both these tests depend upon a smoothing parameter (the number of bins for χ^2 and the number of harmonics for Z_n^2). The power of these tests depend critically on the lightcurve shape (De Jager et al., 2002). For example, in order to detectd a broad peak one should use small values of m or number of bins, but narrow peaks in the lightcurve are best identified when using large values of number of bins.

A great improvement is given by the H-Test, that uses the Z_n^2 as a basis but present a solution to the choice of the number of harmonics. The H variable is defined as:

$$H \equiv \max_{1<m<\inf}(Z_n^2 - 4m + 4) = Z_M^2 - 4M + 4 \qquad (6.18)$$

A detailed discussion of this test and of its power can be found in (De Jager et al., 2002). When the period is not exactly know, because of a lack of radio observation in the time range of the data, it is possible to estimate the central frequency and then check for the periodicity in order to find the value of frequency with the highest confidence level. Once this frequency is found, it is possible to assign the phases to obtain the lightcurve. In this thesis mainly the χ^2-Test and H-Test will be used, and in this Chapter examples of both will be reviewed.

6.1.3 Spectral Analysis

In addition to the total flux determined by the Likelihood analysis and the pulse profile from temporal analysis it is important to measure the energy distribution of the photons coming from the source.
Since energy dispersion and effective area vary with the incidence angle, the distribution of the measured energies do not match the true energy spectrum. It is then important to de-convolve the measured spectrum with the response function of the instrument.
For spectral analysis several standard tools already exist and in this thesis I will use two different approaches that I will discuss briefly here.
The first approach uses the maximum likelihood method for estimating spectral parameters as discussed about the spatial analysis. With this tools it is possible to give as input a source model with a parameterized differential spectrum and the likelihood tools of the SAE return the values of spectral parameters that maximize the likelihood. Additionally the energy distribution of the counts from the model are also provided, usually divided in contribution of the source and of the component of the diffuse background.
The second approach followed in this thesis use the standard package XSpec widely used in X-ray astronomy [6]. The approach of XSpec is based on the fact that a source spectrum $f(E)$ will give an observed count $C(I)$ in a specific energy bin or energy channel I is given by:

$$C(I) = \int_0^\infty f(E)R(I,E)dE \qquad (6.19)$$

where $R(I,E)$ is the Instrument Response Function and it is proportional to the probablity that an incoming photon of energy E will be detected in energy channel I. Since LAT is a counting telescope and data can be binned in energy channels, this approach can also be used, with the caution that in general the counts are smaller than counts in a typical X-ray telescope.
Ideally we would like to determine the actual spectrum of a source, $f(E)$, by inverting this equation, thus deriving $f(E)$ for a given set of $C(I)$. Unfortunately this is not possible in general, as such inversions tend to be non-unique and unstable to small changes in $C(I)$.
The alternative used by XSpec is to choose a trial model spectrum $f_m(E)$ that can be

[6]See $http://heasarc.gsfc.nasa.gov/docs/xanadu/xspec/$

described in terms of parameters p_i and match to the data obtained by the instrument. For each $f_m(E)$ a predicted count spectrum $C_p(I)$ us computed in order to judge how well it fit the observed counts.
The model parameters then are varied to find the parameter values that give the most desirable fit statistic. These values are referred to as the *best-fit parameters*. The model spectrum, $f_b(E)$, made up of the best-fit parameters is considered to be the *best-fit model*.
XSpec uses the most common fit statistic for determining the best-fit model, i.e. the χ^2 statistics, where the χ^2 is defined is the same formula as Eq. 6.12, where now the m_j and m_{exp} refer to observed and expected counts in the j-th energy bin instead of phase bin.
An example of analysis using XSpec will be presented here and in Ch. 9. In order to analyze data with XSpec the LAT data must be converted in spectrum files (.PHA) and *Response Matrix* files (.RMF). The PHA files are files where the observed counts are binned in energy bins defined by the user and the RMF represent the response function of the instrument and are computed considering the LAT orbit and IRF. Both files can be created from the LAT SAE using the *gtbin* tool for creating PHA spectra and *gtrspgen* for creating response matrix RMF files.

6.2 Description of the EGRET pulsar Dataset

For these analysis I simulated one month of GLAST LAT observations in normal rocking mode. The orbital period is set 95 to minutes, with a rocking angle of 35 °.
For the simulation I used the program *Observation Simulator*, described in Ch. 2 and I have used part of the LAT SAE for the spatial and timing analysis, and some other scripts developed in Python, ROOT and IDL for plotting and doing simple analysis. The starting date of the observation has been fixed to Jan 1, 2009, corresponding to MJD 54832 [7].
The launch will take place in the second part of 2007, but for our purposes the total simulation time is more important than its start date.
The main component of the simulations have been all the γ-ray pulsars presently known, i.e Vela pulsar, Crab pulsar, Geminga, PSR B1706-44, PSR 1055-52 and PSR B1951+32. with parameters that will be described below, all of them simulated using lightcurve from EGRET data and spectra simulated using a power law with super-exponential cutoff.
To these point sources I have added a simulated diffuse Galactic and extragalactic emission γ-ray emission. The Galactic emission distribution has been derived by the EGRET γ-ray diffuse map (Figure 6.1)and the simulated spectrum is a power law with spectral index equal to 2.1 and a total flux from 10 MeV to above 655 GeV of F_{gal}=18.58 $ph\ m^{-2}s^{-1}$ in this energy range.
The extragalactic diffuse emission has been modeled as a power-law with spectral index of 2.1 and a total flux of F_{extr}=10.7 $ph\ m^{-2}s^{-1}$ between 20 MeV and 200 GeV.

[7] MJD indicates the Modified Julian Date and it is related by the Julian Date by MJD = JD-24000000.5

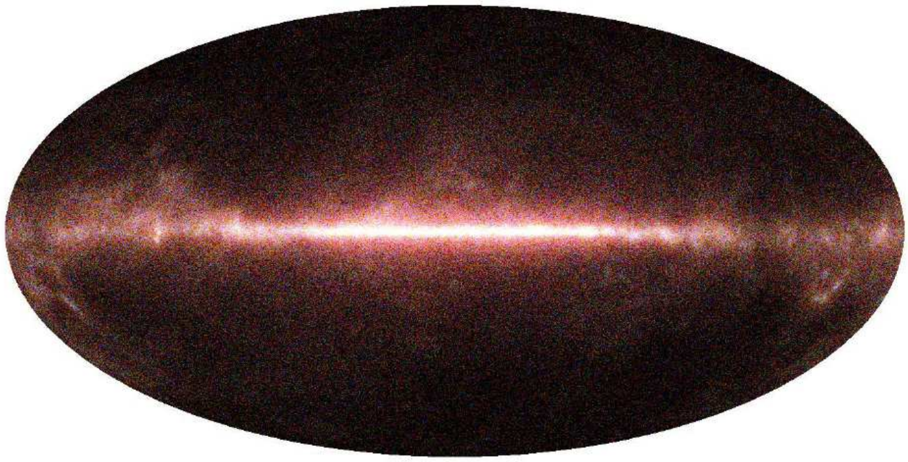

Figure 6.1: Intensity map for the Galactic diffuse γ-ray emission used in the simulations of this Chapter. The map has been determined using GALPROP. Courtesy of Seth W. Digel, LAT Collaboration.

6.3 Testing the periodicity of a bright pulsar: the case of Vela

Vela pulsar (PSR B0833-45) is the brightest γ-ray pulsar. The individual pulses at about 89 ms can be easily distinguished in radio observations. The age of about 11000 year has helped to identify it with the product of the supernova explosion that creates the Vela Supernova Remnant.
Gamma-ray emission from Vela were found in SAS-2 data and one of the first remarkably surprises was that the γ-ray lightcurve shows two peaks separated by about 0.4 in phase, while the radio lightcurve shows a single peak. EGRET has given the opportunity to study in more detail this pulsar and two complete reports can be found in (Fierro, 1995; Kanbach et al., 1994).
In this section I will outline a basic temporal analysis on Vela pulsar, describing how LAT tools can be used to test periodicity of a pulsar. The case of Vela is particularly interesting since the periodicity of the γ-rays is clearly visible.

6.3.1 Simulated Dataset

The simulation model used for Vela pulsar has been created using *PulsarSpectrum* and PSRPhenom model described in Ch. 5. The source has been placed at the position of the radio pulsar retrieved from the ATNF catalog at equatorial coordinates α_{2000}=128.83588 and δ_{2000}=-45.17635. The lightcurve is based on EGRET observation and have been smoothed using a boxcar smoothing algorithm with window of 2 phase bins of width 0.01 in phase, in order to remove statistical fluctuations in the original lightcurve. Such a value is a compromise between a small smoothing window, that can introduce artifacts, and a larger one, that can remove also real structures in the lightcurve of the pulsar. The number of time bin in the smoothed lightcurve has been increased to 8000 by

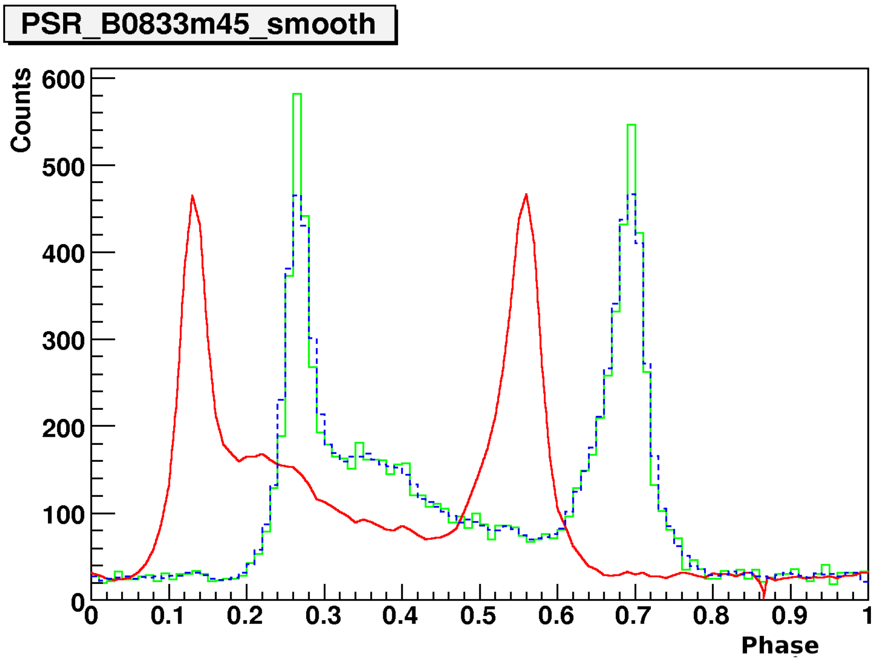

Figure 6.2: Simulated lightcurve for PSR B0833-45. The histogram represent the original EGRET data from (Fierro, 1995) where the lightcurve is binned in 100 phase bins. The dotted blue histogram is the smoothed lightcurve using boxcar algorithm, and the solid line is the resulting lightcurve of 8000 bins using after interpolating the dotted histogram.

interpolation, in order to obtain a bin width of about 11 μs. The resulting lightcurve is displayed in Fig. 6.2. This lightcurve has been taken from (Fierro, 1995) and has been assigned phase 0 the first bin for pratical reasons, then it appear shifted with respect to the original EGRET lightcurve, where phase zero was taken to be the phase of the radio pulse.

The ephemerides have been obtained by radio ephemerides used for EGRET (Fierro, 1995) and the reference epoch was MJD 49605. The simulated dataset start at MJD 54832, then I have decided to mantain the same ephemerides and shift the reference epoch to MJD 54851. The ephemerides used for this pulsar are reported in Tab. 6.3.1:

Vela Ephemerides (Fierro, 1995)	
Epoch (MJD)	54851
$f(t_0)$ (s^{-1})	11.197226013404
$\dot{f}(t_0)$ (s^{-2})	-1.536636$\times10^{-11}$
$\ddot{f}(t_0)$ (s^{-3})	6.26$\times10^{-22}$

The spectrum is modeled in the basis of a power law with super exponential cutoff, with parameters retrevied from (Nel & De Jager, 1995; De Jager et al., 2002). The spectral index for the power law is g=1.62 and the cutoff energy E_0 is set to 8 GeV. The cutoff is super exponential, with a value of b=1.7. The resulting spectrum is shown in Fig. 6.3. According to the value reported by EGRET, the total flux of the pulsar has been set to (9×10^{-6} ph cm^{-2}s^{-1}).

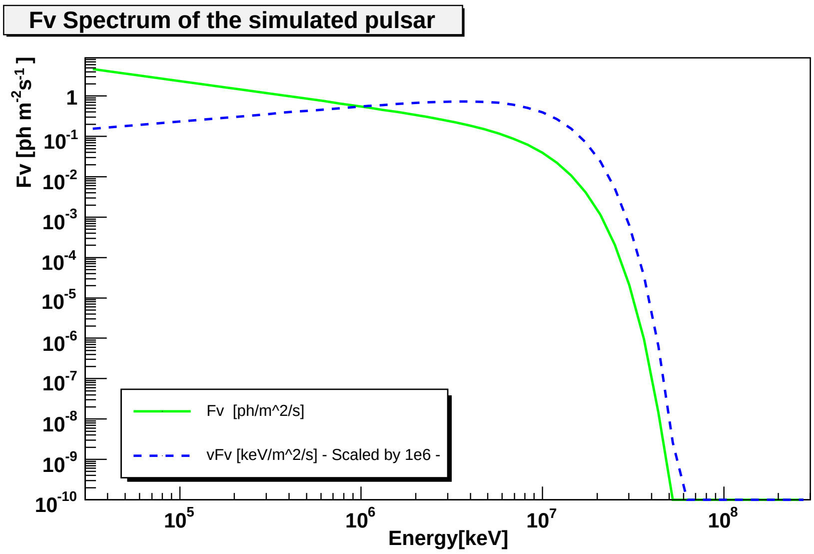

Figure 6.3: Simulated spectrum of PSR B0833-45 using a power law with exponential cutoff. The flux and νF_ν distributions are showed

.

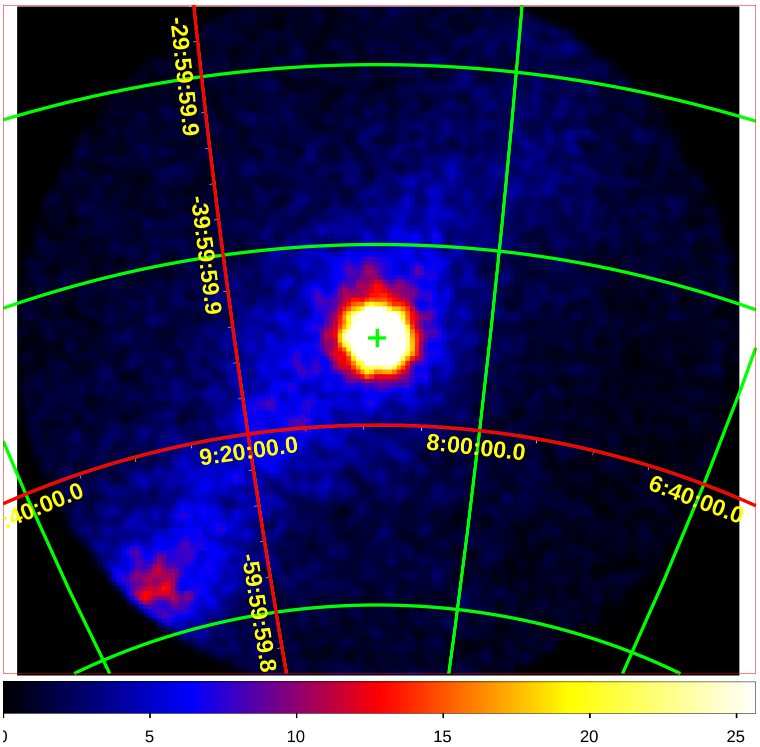

Figure 6.4: Count map of the region within 20° around position of Vela pulsar in equatorial coordinates obtained using the LAT SAE tool *gtbin*. The position of the radio source is indicated by a cross.

6.3.2 Periodicity testing

The count map of Vela pulsar is displayed in Fig. 6.4 in equatorial coordinates, that comprises a region of 20° around the position of the source. This count map has been

obtained using a SAE tool called *gtbin*, and photon counts have been binned with a bin width of 0.25°.
This pulsar corresponds to the source 3EG J0834-4511 in the Third EGRET Catalog (Hartman et al., 1999). From the skymap it is visible that Vela is a very bright source, that overwhelm the diffuse γ-ray emission.
The position used in the barycentric corrections for Vela pulsar is α_{2000}=128.83588°, $\delta_{2000} = -45.17635°$. First a region of radius of 3° has been selected.This radius is compatible with the Point Spread Function of the LAT. A more refined analysis should take into account that PSF radius varies with energy and thus implements an energy-dependent cut.
The periodicity test is a critical step in order to confirm that γ-rays are modulated at the same periodicity of the radio pulsar. This is a powerful tools for identifying a γ-ray source with a pulsar.
In order to do that, I use the LAT SAE tool called *gtpseach*, that can apply the χ^2, Z_n^2 and H-Test to the data file. I used the barycentered file obtained by *gtbary*. Since the total observation time is of 1 month, i.e. T=2.592×10^6 s., the correspondent Independent Frequency spacing (IFS) is $1/T\simeq4\times10^{-7}$ Hz. Since in the periodicity test the trial frequencies are spanned at fixed frequency steps expressed as fraction of IFS, then then I will assume as error on the frequency one half of the frequency step of the scan. The

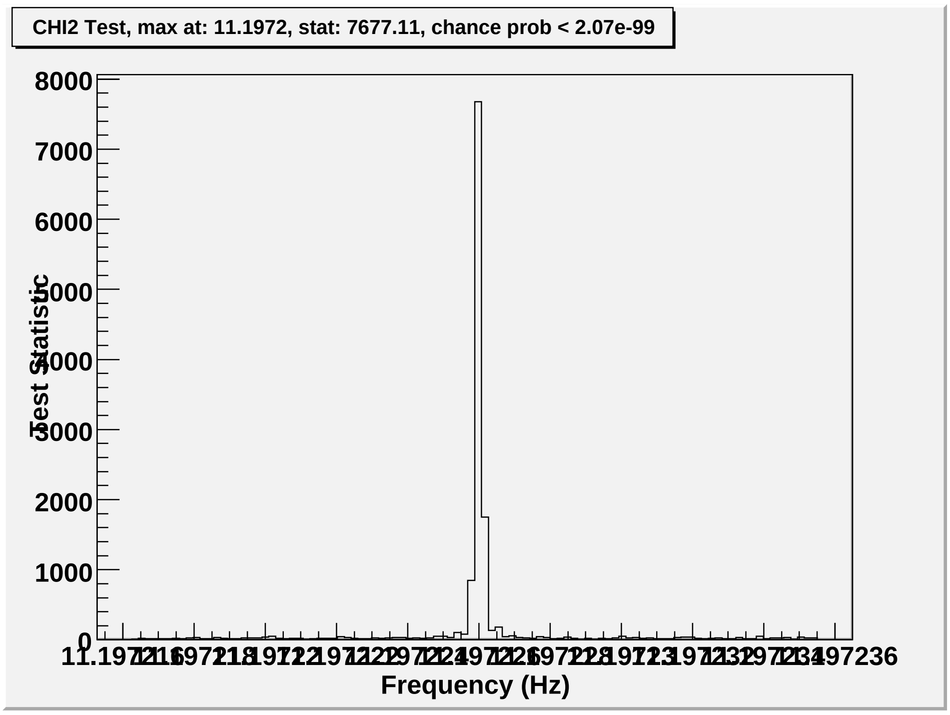

Figure 6.5: $\chi 2$ applied to Vela pulsar by taking into account the frequency first derivative.

starting value for the central frequency is 11.19722 Hz. This value has been chosen by approximating the radio frequency, in order to check if the periodicity search leads to the correct frequency of the signal. In order to better apply the χ^2-Test for periodicity I considered also the frequency derivatives. The frequencies are scanned at intervals

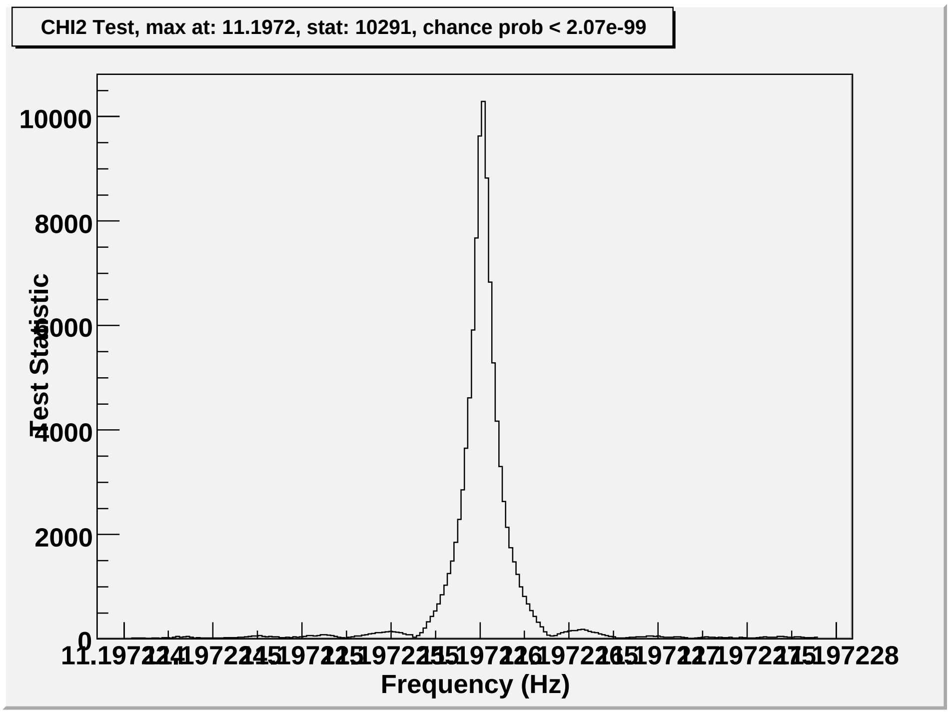

Figure 6.6: $\chi 2$ applied to Vela pulsar by taking into account the frequency first derivative and "zooming" on the central frequency

of 0.5 IFS, i.e. $2{\times}10^{-7}$ Hz, I assumed as error on the frequency estimate a value of 10^{-7} Hz. The results are very good and the peak corresponding to the frequency of the pulsar is clearly visible in Fig. 6.5. A value of $11.1972259{\pm}(1{\times}10^{-7})$ Hz is obtained. This test has been performed with 200 trial frequencies centered at the approximated frequency 11.19722. The used bin number is 20. The statistics S is higher , S=7667.11, corresponding to a chance probability $p{<}2{\times}10^{-99}$, meaning that periodicity is very clear.

I then refined this value by a "zoom" in frequency around the central peak, by choosing steps of 0.05 the frequency resolution centered on the previous value. The frequencies are scanned at intervals of 0.5 IFS, i.e. $2{\times}10^{-8}$ Hz, I assumed as error on the frequency estimate a value of 10^{-8} Hz.The result is remarkably better and the obtained frequency is displayed in Fig. 6.6. A value of $11.19722601{\pm}(2{\times}10^{-8})$ Hz is obtained. This test has been performed with 200 trial frequencies centered at the frequency found with the previous test. The used bin number is 20. The statistics S is higher , S=10290.2, corresponding to a chance probability $p< 2\times10^{-99}$. This means that the periodicy have been found with very high confidence level. In particular the found frequency agree within the error with the simulated frequency at epoch. At this point the identification with the Vela Pulsar could be confirmed.

Once the periodicity has been confirmed, to each photon a rotational phase can be assigned using the Eq. 5.7 in Ch. 5 in order to obtain the reconstructed lightcurve. The photons arrival times have been phase-assigned in order to obtain the lightcurve, displayed in Fig. 6.7.

The *TimeProfile* used for this simulated has been obtained from EGRET observation (Fierro, 1995), then by comparing the reconstructed lightcurve with the Vela pulsar seen

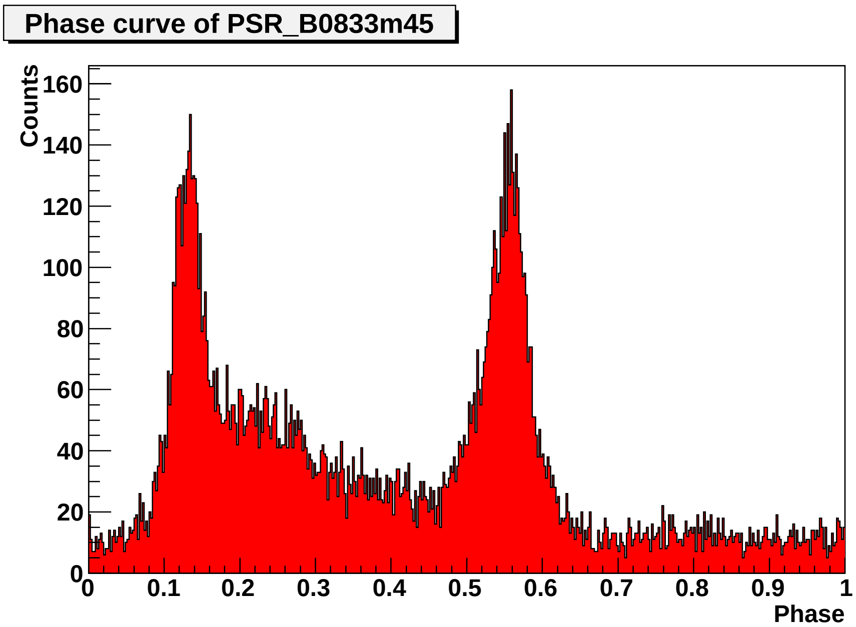

Figure 6.7: Reconstructed lightcurve using 450 bins of Vela Pulsar after the steps described in text for periodicity test.

by EGRET, e.g. in (Kanbach et al., 1994) (Fig. 6.8), it is possible to see that they are very similar.
This is the expected result and confirms that all calculations and timing corrections in the simulation have been performed correctly by *PulsarSpectrum*.

6.4 The analysis of PSR B1706-44

The γ-ray emission from PSR B1706-44 was discovered by EGRET (Thompson et al., 1992). The 102 ms radio pulsar was discovered during a radio survey of the southern Galactic plane and this pulsar was coincident with the COS B source 2CG 342-02 (Fierro, 1995).
The unpulsed X-ray emission has ben discovered in 1995 by ROSAT and then the pulsations have been detected using *Chandra* telescope in 2002 (Gotthelf et al., 2002).
The low statistics of COS B did not allow the discovery of this γ-ray pulsar, but the EGRET observations revealed pulsed γ-ray emission from this source.
Unlike the first three pulsar detected (Vela, Crab and Geminga), PSR B1706-44 shows a different pulse profile, consisting in a single broad peak spanning about 35% of the total period. Since this pulsar is much more weak than Vela, it is more difficult to resolve the lightcurve in detail. PSR B1706 shows a young age $\tau_c \sim 1.7 \times 10^4$years and a there are some Supernova Remnants candidates for association with this pulsar (Fierro, 1995).
Using radio data and a distance of 2.4 kpc the total rotational energy loss is about $\dot{E} = 3.4 \times 10^{36}$erg s^{-1}. The γ-ray luminosity measured by EGRET is of about $L \approx 5 \times 10^{34} \times 4\pi f$ erg s^{-1}, where f is the beaming fraction in steradian. Unless the beaming fraction is extremely small, the γ-ray radiation represent about the 1% of the total

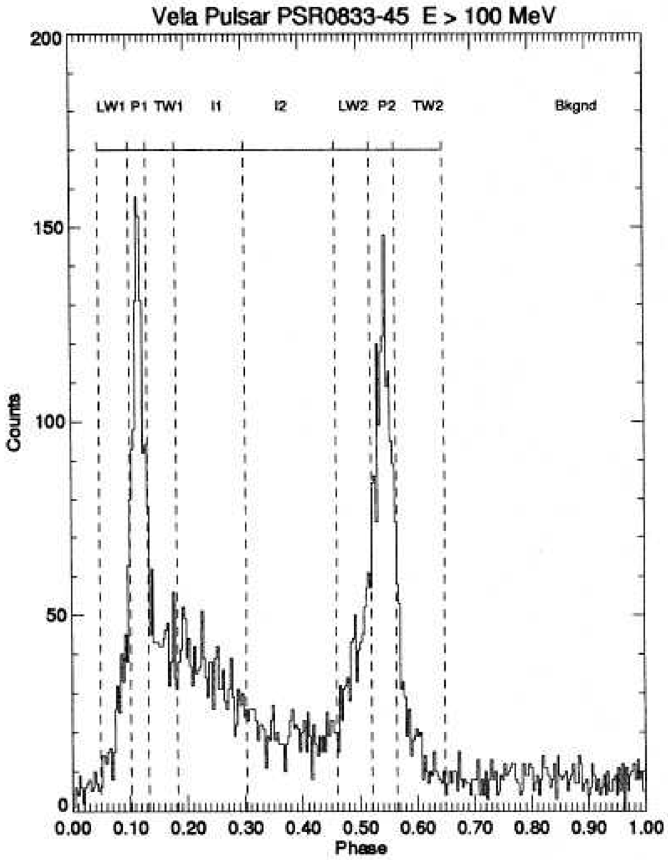

Figure 6.8: The EGRET lightcurve of Vela pulsar obtained by Kanbach et al. in (Kanbach et al., 1994)

rotational energy loss.

6.4.1 Simulation of PSR B1706-44

The simulation model used for PSR B1706-44 has been created with *PulsarSpectrum* and PSRPhenom model described in Ch. 5. The source has been placed at the position of the radio pulsar retrieved from the ATNF catalog at equatorial coordinates α_{2000}=257.42403° and δ_{2000}=-44.48562°. The lightcurve is based on EGRET observation and have been smoothed using a boxcar smoothing algorithm with window of 2 phase bins, in order to remove statistical fluctuations in the original lightcurve. As the case of Vela pulsar, this appear to be a good compromise to reduce statistical fluctuations and mantain lightcurve structure. The period of 102 ms and the goal to have a small bin width ($\sim 10\mu$s, smaller than LAT dead time), lead to a large number of 10000 bins, obtained by interpolating the smoothed lightcurve. This results in a bin width of about 10 μs. The resulting lightcurve is displayed in Fig. 6.9. The original epoch for the epherides was MJD 49447 (Fierro, 1995), but it has been shifted to MJD 54847, because it is nearer the start date of the simulation, MJD 54832. The radio ephemerides used for the phase assignment are the following:

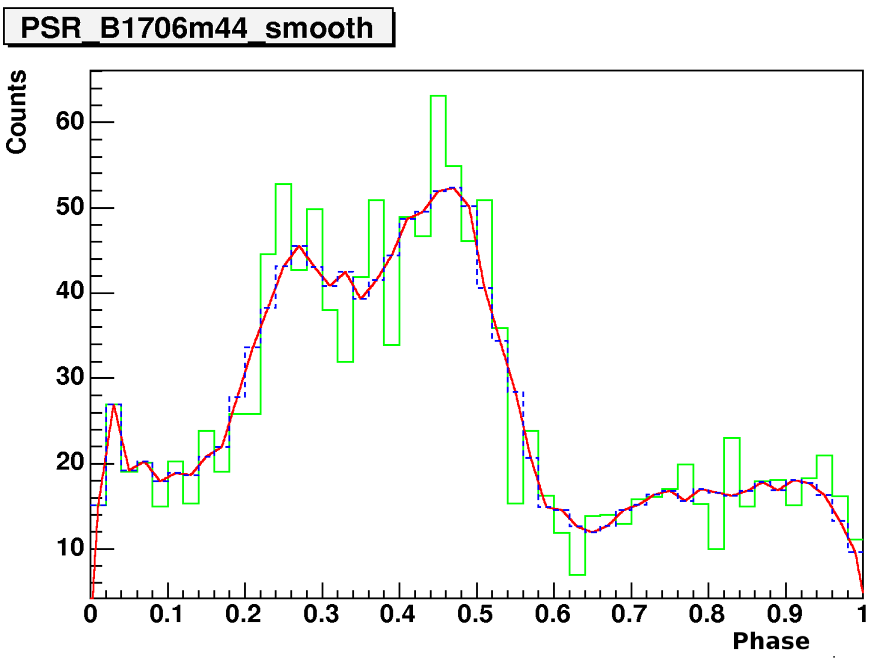

Figure 6.9: Simulated lightcurve for PSR B1706-44. The histogram represent the original EGRET data from (Fierro, 1995) where the lightcurve is binned in 50 phase bins. The dotted blue histogram is the smoothed lightcurve using boxcar algorithm, and the solid line is the resulting lightcurve of 10000 bins using after interpolating the dotted histogram.

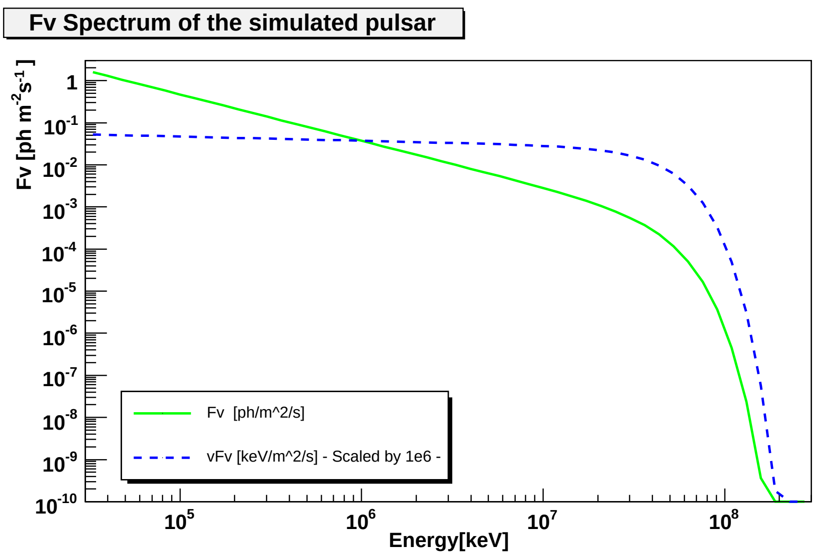

Figure 6.10: Simulated spectrum of PSR B1706-44 using a power law with exponential cutoff. The flux and νF_ν distributions are showed

.

PSR B1706-44 Ephemerides (Fierro, 1995)	
Epoch (MJD)	54847
$f(t_0)$ (s^{-1})	9.7601985856255
$\dot{f}(t_0)$ (s^{-2})	-8.86669$\times 10^{-12}$
$\ddot{f}(t_0)$ (s^{-3})	2.19$\times 10^{-22}$

The spectrum is modeled in the basis of a power law with super exponential cutoff, with parameters retrieved from (Nel & De Jager, 1995; De Jager et al., 2002). The spectral index for the power law is g=2.1 and the cutoff energy E_0 is set to 40 GeV. The cutoff is super exponential, with a value of b=2.0. The resulting spectrum is shown in Fig. 6.10. According to the value reported by EGRET, the total flux of the pulsar has been set to (1.28×10^{-6} ph cm^{-2}s^{-1}).

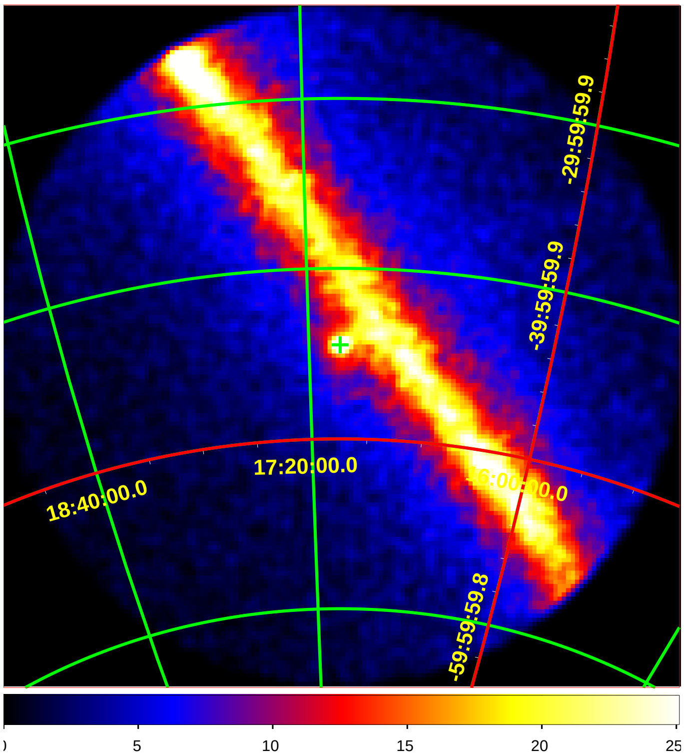

Figure 6.11: Sky map of the region within 20° around position of PSR B1706-44. The position of the radio pulsar is marked by a cross.

6.4.2 Spatial Analysis

The count map of PSR B1706-44 is displayed in Fig.6.11, that comprises a region of 20° around the position of the source. This pulsar corresponds to the source 3EG J1710-4439 in the Third EGRET Catalog (Hartman et al., 1999). A similar radius for the region to be analyzed is useful to better have an estimate of the behaviour of the contribution of the diffuse background around the source.
Likelihood analysis estimation of flux above 100 MeV is of $1.22\pm0.07\times10^{-6}$ ph cm^{-2}s^{-1}. This computed statistics for this source is $T_S^{1/2}$=31.3, corresponding to 31.3σ and confirming the spatial position with high confidence level.

6.4.3 Pulse profile

The steps followed in this example are the same as in the analysis of the Vela pulsar. However the determination of the pulsar properties has bigger uncertaines, because the

flux is much lower than the Vela flux, with a consequent smaller statistics.
The position of the pulsar PSR B1706-44 used for simulations is α_{2000}=257.2842803°, δ_{2000}=-44.48562°. The region selected for the temporal analysis is of 3 degrees as for the Vela pulsar. As remarked also for Vela pulsar, an energy-dependent radius is a better solution, because the Point Spread Function vary with energy of the incoming photon. In case of PSR B1706-44 the analysis show that selecting a region around pulsar smaller than 3° increase the significance of the periodicity test. Using photons above 100 MeV around 3° from the pulsar the chance probability is of the order of 10^{-7}, while cutting selecting photons above 100 MeV and around 1.5° the chance probability increase to about 10^{-19}. The periodicity test using this second analysis cut will be explained here with more detail.
In order to test periodicity I started with an approximated frequency of 9.76019 Hz and used the χ^2 test. This approximated value was chosen in order to check if the periodicity test works fine and returns the correct frequency of pulsar.
If the periodicity test is performed using the frequency derivatives the result is better, as displayed in Fig. 6.12, using a frequency scan of 0.5 ISF. Since frequencies are scanned at intervals of 0.5 IFS, i.e. 2×10^{-7} Hz, I assumed as error on the frequency estimate a value of 10^{-7} Hz. A value of 9.7601984$\pm$ (1×10^{-7})Hz is obtained. This test has been performed with 200 trial frequencies centered at the frequency found with the previous test. The statistics S is higher, S=115.556, corresponding to a chance probability p$\approx 7.5 \times 10^{-16}$. I then refined this value by a "zoom" in frequency around

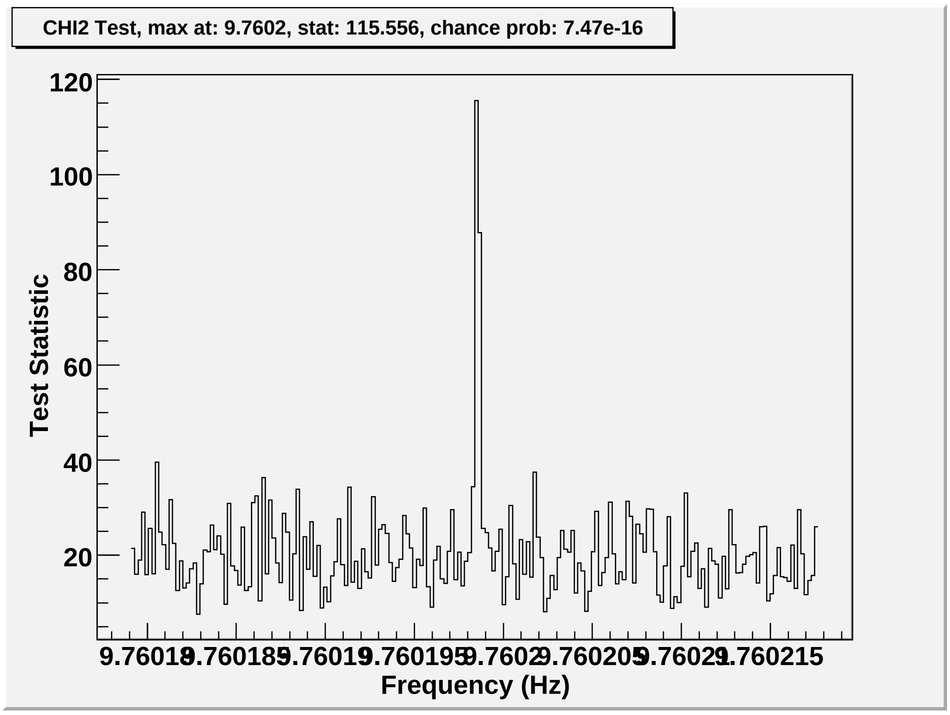

Figure 6.12: χ2 applied to PSR B1706-44 by taking into account the frequency first derivative.

the central peak, by choosing steps of 0.05 the frequency resolution centered on the previous value. Since the frequencies are scanned at intervals of 0.5 IFS, i.e. 2×10^{-8}

Hz, I assumed as error on the frequency estimate a value of 10^{-8} Hz. The result is remarkably better and the obtained frequency is displayed in Fig. 6.13. A value of $9.76019856 \pm (2 \times 10^{-8})$ Hz is obtained. This test has been performed with 200 trial frequencies centered at the frequency found with the previous test. The statistics S is higher , S=137.59, corresponding to a chance probability p$\simeq 5.3 \times 10^{-20}$. This means that the periodicity have been found with high confidence level. The identification with the pulsar PSR B1706-44 could then be confirmed. The dataset for PSR B1706-44 has

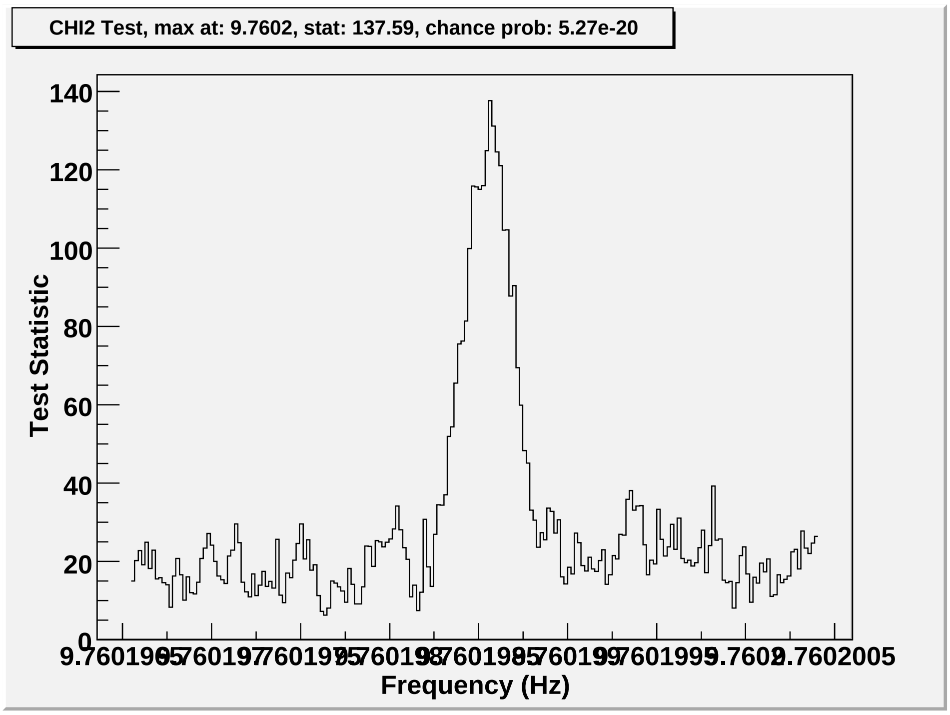

Figure 6.13: $\chi2$ applied to pulsar B1706-44 by taking into account the frequency first derivative and ”zooming” on the central frequency

been then used to build the lightcurve, using LAT SAE tool *gtpphase*. Using the cuts of energies above 100 MeV and a radius around 1.5° a sample of 1860 photons have been selected and the resulting lightcurve is shown in in Fig. 6.14. The case of PSR B1706-44 offer an opportunity to look at the number of photons at high energies. The original lightcurve is not phase dependent, then we expect that the shape of the lightcurve with energy is not dependent on the pulsar spectrum itself, but from the capability of the LAT to collect photons at high energies.

I examined 2 high-energy bands, obtained by selecting photons and displaying using the plotting features of a set of Python classes called *pyPulsar*, that will be presented in detail in the next Chapter. Since the PSF is energy-dependent, for photons above 5 GeV a selection radius of 1° has been applied. This results in 30 photons from 5 GeV to 10 GeV and 15 above 10 GeV. The lightcurves in these 2 energy bands are represented in Fig. 6.15 (5 Gev-10 GeV)and 6.16 (E> 10 GeV). Compared with 5 high-energy photons seen by EGRET above 10 GeV, this show how good can be LAT capabilities of detect high-energy γ-rays. In particular the lightcurve above 5 GeV agree with the lightcurve for photons above 5 GeV found with EGRET data in (Thompson et al., 2005).

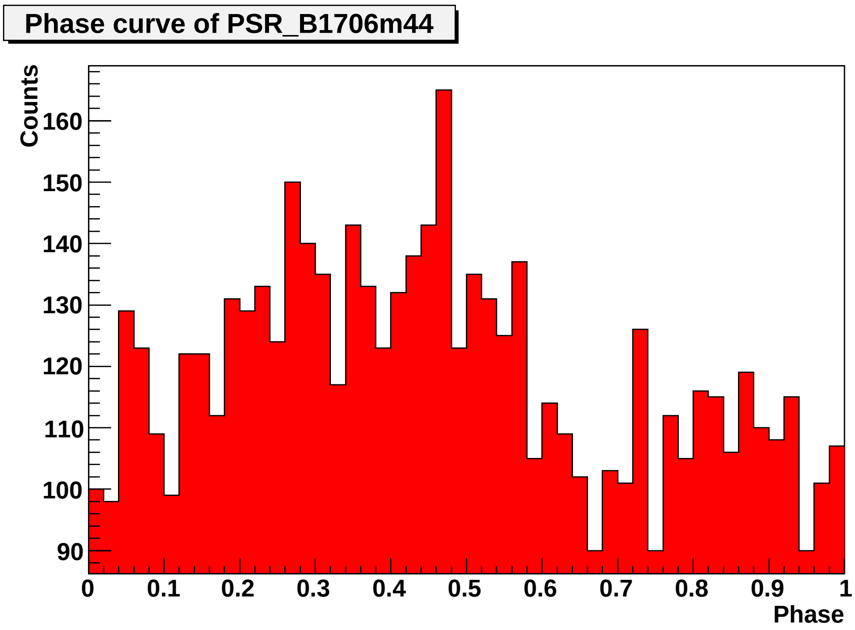

Figure 6.14: Reconstructed lightcurve of PSR B1706-44 with the analyzed data set (photons above 100 MeV and around 1.5° from the radio position of the pulsar).

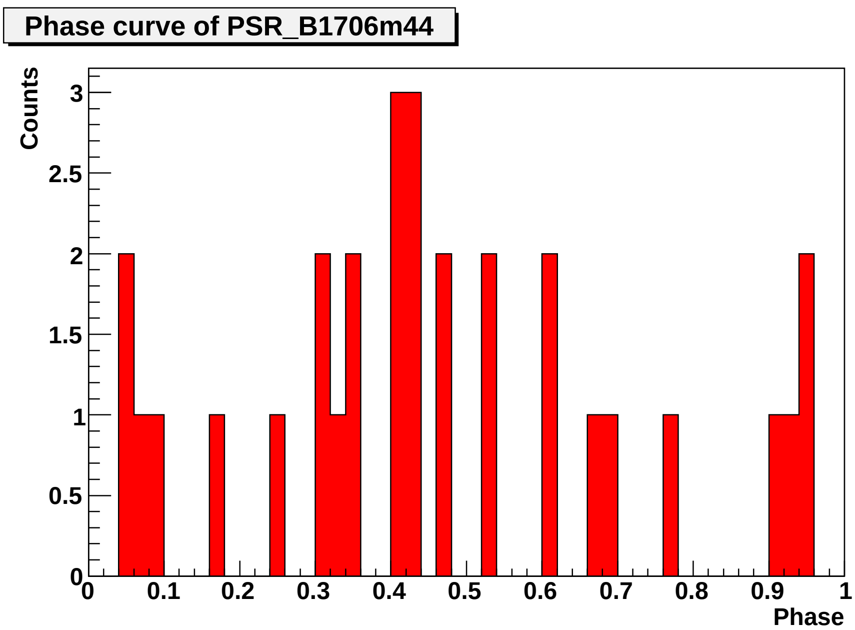

Figure 6.15: Reconstructed lightcurve of PSR B1706-44 with the analyzed data set within 1° from the radio pulsar and in the energy band 5 GeV - 10 GeV.

6.4.4 Spectral analysis

In this Section an example of spectral analysis is presented using both the maximum likelihood tool available in the LAT SAE and using XSpec package.

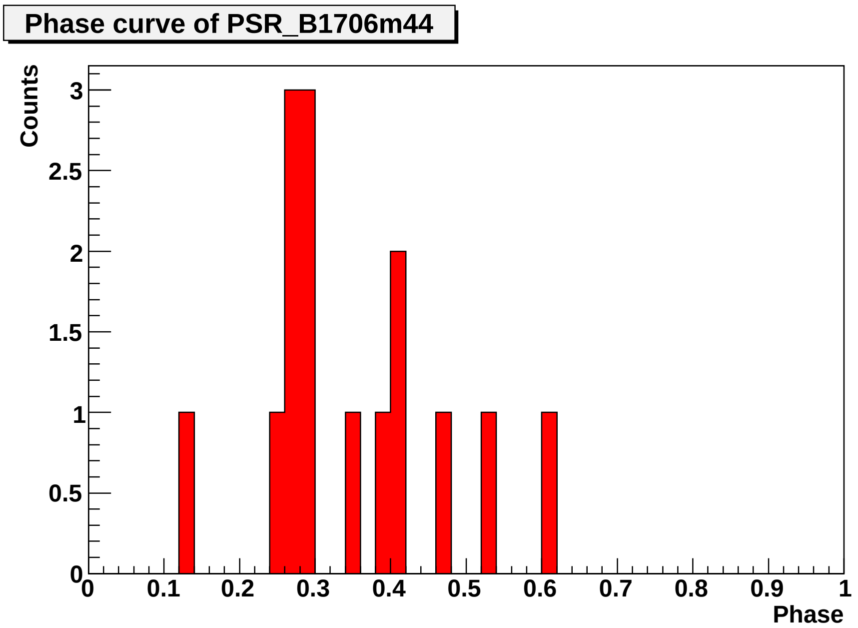

Figure 6.16: Reconstructed lightcurve of PSR B1706-44 with the analyzed data set within 1° from the radio pulsar and in the energy band above 10 GeV.

The spectral model used for maximizing the likelihood has been a simple power law, a broken power law and a power law with exponential cutoff as the original model described at the beginning of this Section. This last model has the goal to see if it is possible to reconstruct the spectral cutoff for this pulsar with 1 month of LAT observation.
The statistics is not sufficient for this study, while the spectrum appear to be better fit by a power law. The broken power law give similar results, providing two spectral indexes that coincide within the error and also in agreement with what has been found using a simple power law.
The results of maximum likelihood is displayed in Fig. 6.17, where the observed counts are compared with the sum of counts from the pulsar and the diffuse background on the sample of photons considered for likelihood analysis, i.e. about 20° around the pulsar.

I then used the power law model to retrieve the results. The maximum likelihood provide a spectral shape above 100 MeV as:

$$\frac{dN}{dE} = (6.0 \pm 0.1) \times 10^{-4} \times (E/100MeV)^{-2.29\pm0.04} \mathrm{ph\ cm^{-2}s^{-1}\ MeV^{-1}} \tag{6.20}$$

The maximum likelihood give a total flux of F(E>100MeV)=
$(1.23\pm0.07)\times10^{-6}$ ph cm^{-2}s^{-1}. The flux distribution obtained integrating the Eq. 6.20 over energy is displayed in Fig. 6.18. An analog spectral analysis has been performed also using XSpec in order to show how this standard tool can be used also with LAT data. In order to increase signal to noise ratio, I selected a region around 1.5° around the radio pulsar, resulting in a total of 1860 photons, since in the timing analysis this cut give an higher significance for periodicity testing, then it is reasonable that this cuts increase the S/N ratio.
The correspondent spectral PHA file and Response Matrix Function RMF files have

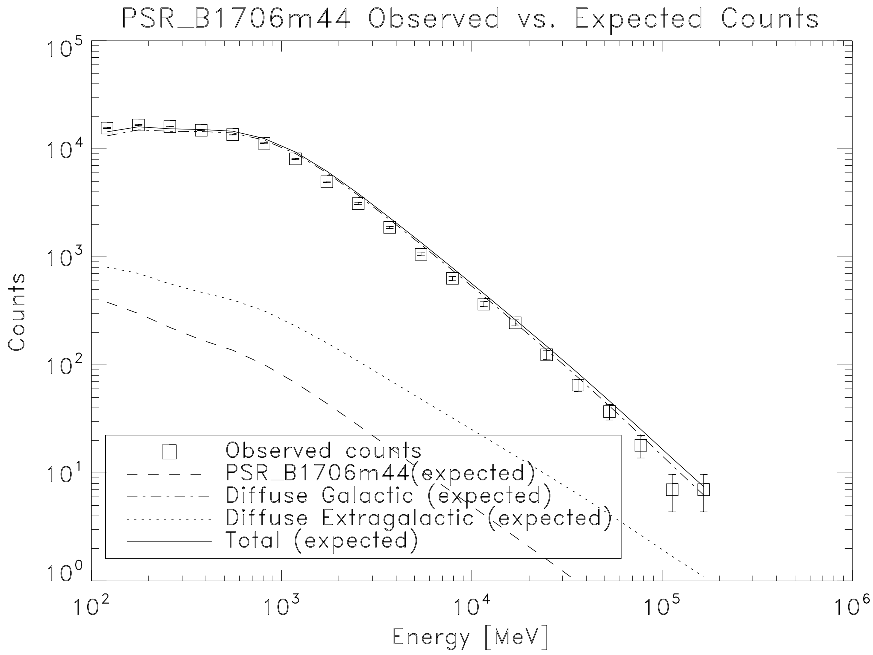

Figure 6.17: Energy distribution of observed counts from a region of 20° around PSR B1706-44 compared with the modeled counts using the maximum likelihood method.

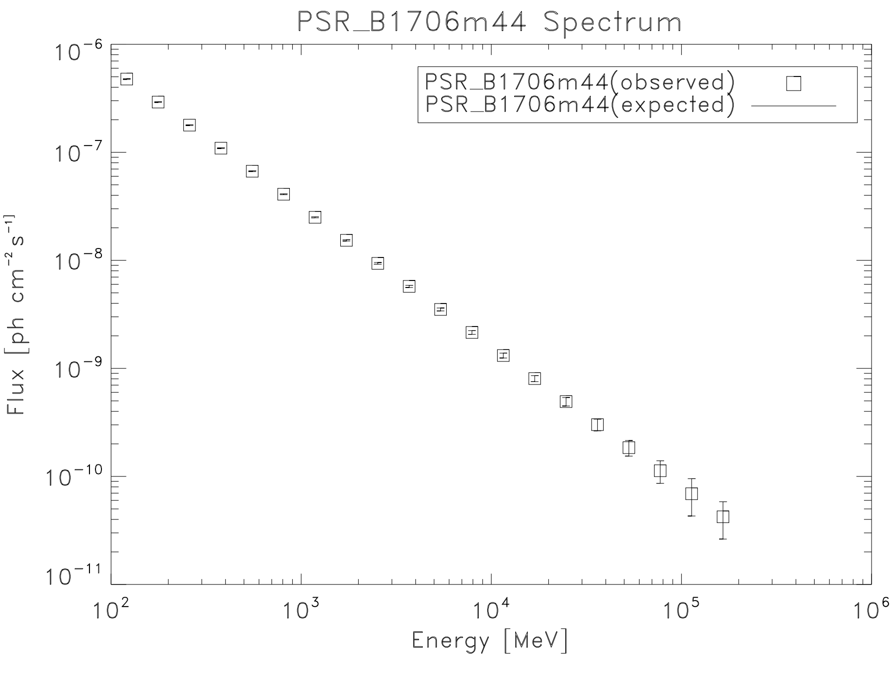

Figure 6.18: Integral flux of PSR B1706-44 compared with the spectrum model fit obtained using the maximum likelihood method.

been produced using LAT SAE tools and in the spectrum channel with counts less than 20 have been grouped together.

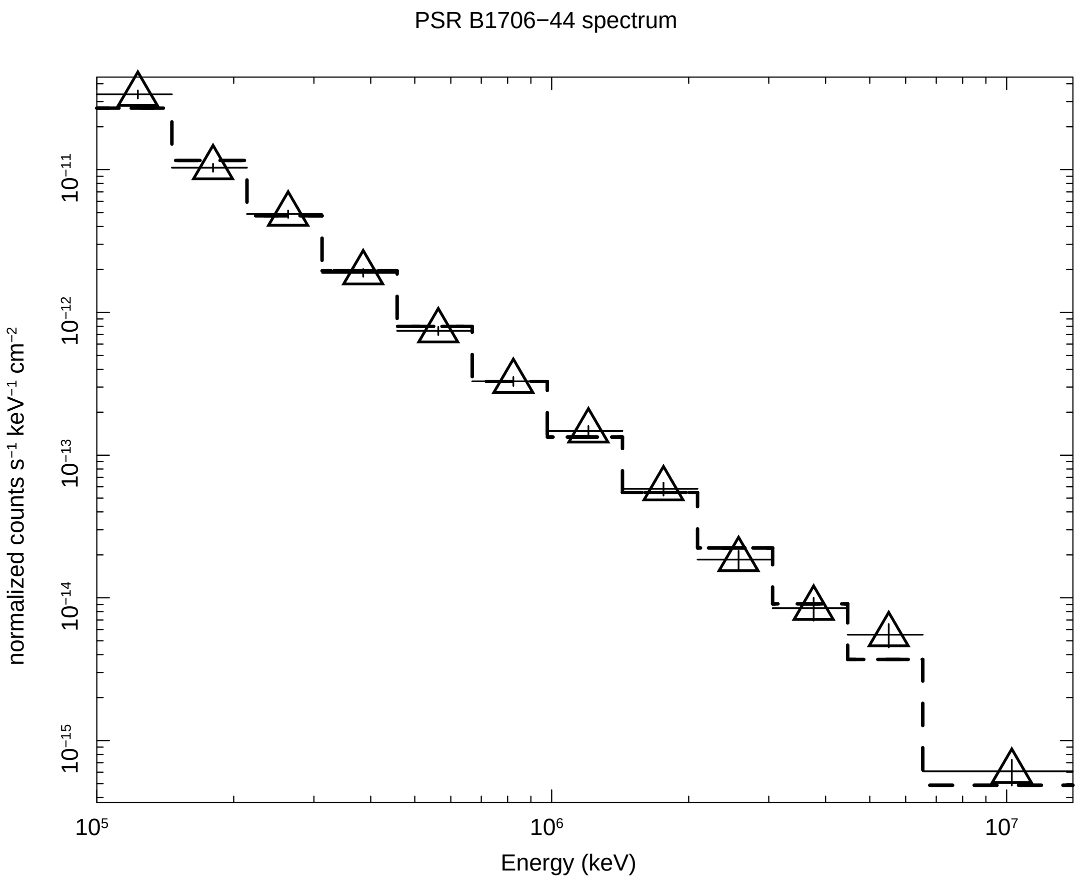

Figure 6.19: Differential spectrum of PSR B1706-44 compared with the spectrum model fit obtained using the maximum likelihood method. In the top paned the best-fit model spectrum (dashed line) is compared with data (triangles). In the bottom paned the contribution to the χ^2 of each energy bin is displayed. This spectrum has been obtained using XSpec v12.

The resulting spectrum has been fitted with a power law, giving a resulting spectral index g=-2.27±0.04. This seem to be a reasonable fit, since the χ^2 of the best-fit model provided by XSpec is of 1.3 for 10 degrees of freedom, meaning that this fit is good at a probability of 80%. The result of the fit is shown if Fig. 6.19, where the spectrum is compared with the model and with the contribution to the χ^2 in each energy bin.
Using this model it is possible to estimate the total fluix above 100 MeV, that results in an estimate of the flux of about 1.41×10^{-6} ph cm^{-2}s^{-1}, in agreement with the value found by likelihood analysis.

6.5 The faintest of EGRET pulsars: PSR B1951+32

I this Section I will show an example of analysis of PSR B1951+31, the faintest among the γ-ray pulsars discovered by EGRET, in order to show LAT data can be analyzed in case of sources with low counts. The purpose of this analysis is to show how LAT

analysis tools can be used to optimize cut in order to extract more information from the source.
The simulated dataset cover an 1 month simulated LAT observation in scanning mode and contain a model of the pulsar and the Galactic and Extragalactic diffuse emission.
PSR B1951+32 was discovered in 1988 in the radio synchrotron nebula CTB 80 as a radio pulsar with a period of 39.5 ms (Kulkarni et al., 1988). From radio observation it can be deduced that this pulsar has a characteristic age $\tau_c \approx 1.1 \times 10^5$ yr and an inferred surface magnetic field $B_S \approx 4.9 \times 10^{11}$G (Ramanamurthy et al., 1995). Located at a distance of about 1.3-3 kpc this pulsar appear to have rotation energy loss of about $\dot{E} \approx 3.7 \times 10^{36}$ergs^{-1} (Ramanamurthy et al., 1995). This pulsars have been also seen as pulsed X-ray source in EXOSAT data and ROSAT data (Oegelman & Buccheri, 1987; Safi-Harb et al., 1995). A γ-ray emission was claimed in the COS B data (Li et al., 1987) but contradicted after by analyzing the same data (D'Amico et al., 1987).
Using EGRET telescope this pulsar was studied and eventually the γ-ray emission was found in 1995 (Ramanamurthy et al., 1995) using data from May 1991 to July 1994 in nine EGRET viewing periods and aspect angle θ less than 20° [8]. Using EGRET data it was recognized that γ-ray lightcurve have two peaks loated approximatively at $\phi \approx 0.15$ and $\phi \approx 0.60$ with respect to the single pulse visible in radio (Fierro, 1995).
The spectrum measured was a power law with a spectral index of g=-1.74±0.11 and the total measured flux using likelihood of about (6.0±1.6)$\times 10^{-8}$ ph cm^{-2}s^{-1} above 300 MeV. Integrating the flux down to 100 MeV a value of (1.6±0.2)$\times 10^{-7}$ ph cm^{-2}s^{-1} was found.

6.5.1 Simulated dataset

The parameters used for the simulations are based on EGRET observations and have been implemented in *PulsarSpectrum* using the *PSRPhenom* model presented in Ch. 5.
The simulated source has been positioned at the location of the radio pulsar retrieved from ATNF catalog, at equatorial coordinates α_{2000}=298.24252° and δ_{2000}=+32.87793°.
The lightcurve has been produced on the basis of the EGRET lightcurve but it have been smoothed using a box car smoothing algorithm with a smoothing window of 2 bin, and then the number of bin have been increased using linear interpolation in order to obtain a bin width of about 10 μs, smaller than LAT deadtime, with a total of 4000 phase bins. The resulting lightcurve is shown in Fig. 6.20 compared with the original EGRET lightcurve.
The ephemerides used for the simulations have been obtained from (Fierro, 1995) but the epoch to which they are referred have been shifted to MJD 54840. The values of frequency and its derivative is f_0=25.29660916363, f_1=-3.74277$\times 10^{-12}$Hz s^{-1} and a null second derivative of frequency.
The spectrum have been modeled using a power law with superexponential cutoff as descrived in Ch. 5. The value of spectral parameters have been taken from (Nel & De Jager, 1995) observations and have been set to be g=-1.74 (spectral index), E_0=40 GeV (energy cutoff) and b=2.0 (exponential index). The total flux above 100 MeV has been set according to EGRET results to (1.6$\times 10^{-7}$ ph cm^{-2}s^{-1}). The simulated spectrum is

[8] I use here the definition of aspect angle as the angle between the z-axis of the telescope and the arrival direction of the photon in the telescope coordinate frame

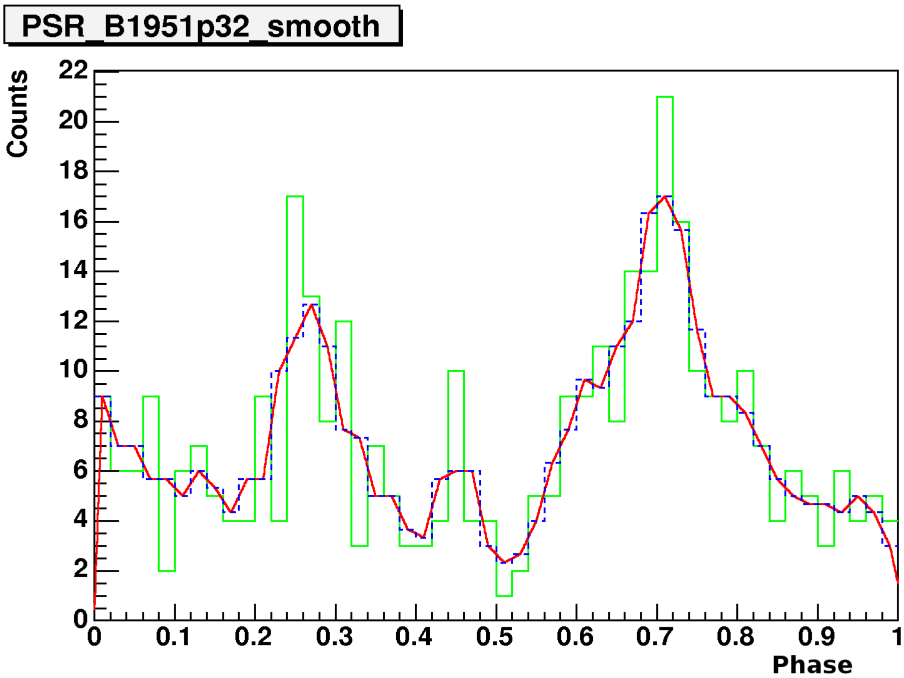

Figure 6.20: Simulated lightcurve for PSR B1951+32. The histogram represent the original EGRET data from (Fierro, 1995) where the lightcurve is binned in 50 phase bins. The dotted blue histogram is the smoothed lightcurve using boxcar algorithm, and the solid line is the resulting lightcurve of 4000 bins using after interpolating the dotted histogram.

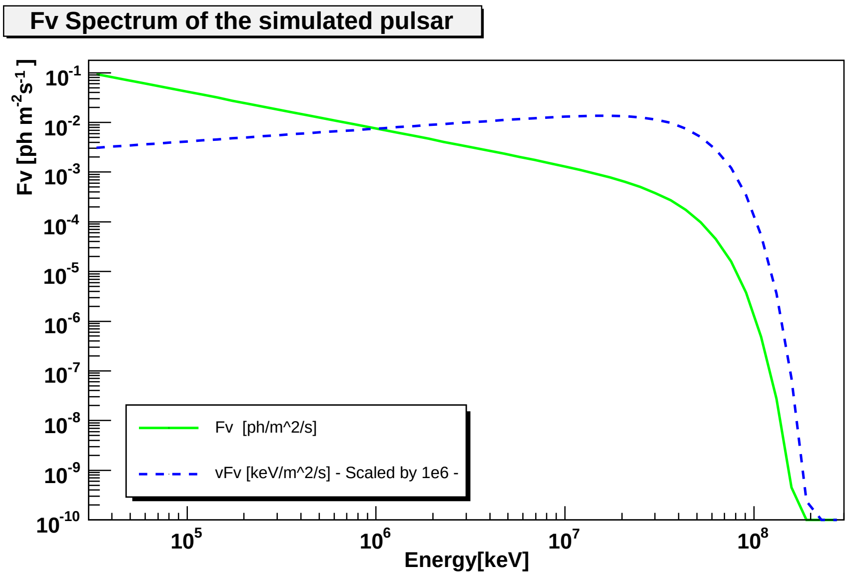

Figure 6.21: Simulated spectrum of PSR B1951+32 using a power law with exponential cutoff. The flux and νF_{ν} distributions are showed

.

presented in Fig. 6.21.

6.5.2 Spatial analysis

The analysis of the simulated dataset for PSR B1951+32 is complicated by the presence of the diffuse emission by the Galactic plane. The galactic coordinates of the source are l=68.77° and b=2.82°, then this pulsar is located almost on the Galactic plane where a huge emission is present.
Over a region of 6° around the position of the source, corresponding to about a couple of PSF at 100 MeV, the simulations show that photons coming from the pulsar are 285 out of 9018 total, corresponding to a S/N ratio of about 3. A map of the region around 20° from the pulsar is shown in Fig. 6.22. The photons have been binned at 0.25° and then the resulting map has been smoothd using Gaussian filter in order to better see the background structure. In this map the emission from the near Galactic plane is clearly visible.
The likelihood analysis of this pulsar give a resulting flux F(E>100MeV)= (0.9±0.2)

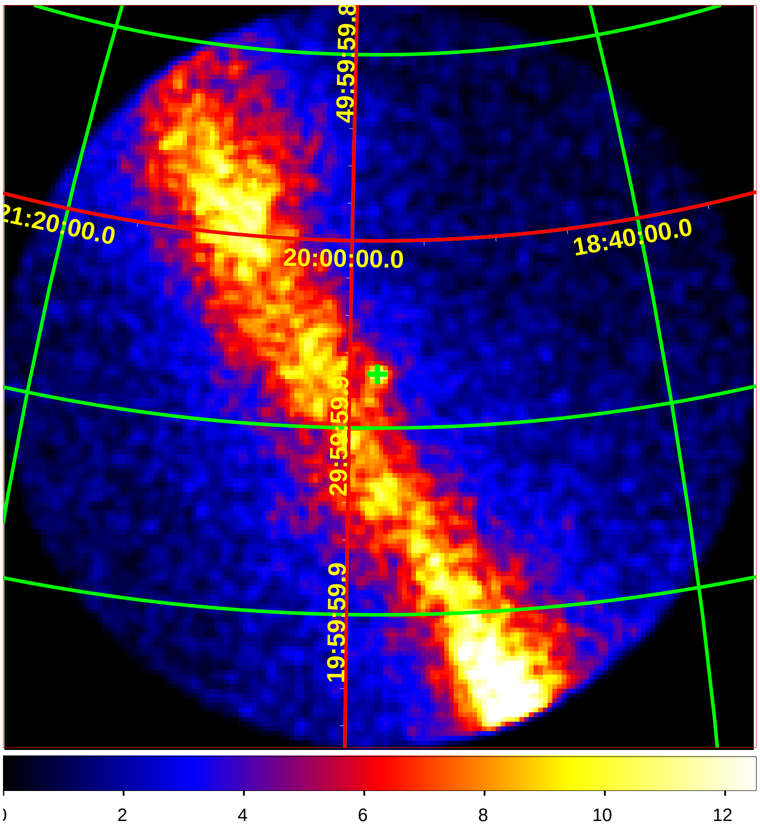

Figure 6.22: Map of the simulate photons in a region a round 20° from PSR B1951+32. A Gaussian smothing filter with a radius of 2° has been used to improve the perception of the structured background. The position of the radio pulsar is marked with a cross.

$\times 10^{-7}$ ph cm^{-2}s^{-1} and a TS$^{1/2}$ value of about 10, with a maximum at a position within 5' from the radio source.The spectrum used for maximizing the likelihood has been a power law and the result of the fit will be discussed below in the section devoted to spectral analysis.

6.5.3 Pulse profile

The diffuse emission near the source impose that the selection of the sky region around pulsar in order to reduce as much as possible contamination from background. The strategy with EGRET data was to apply an energy-dependent cut on the acceptance angle around the pulsar position, but for PSR B1951+32 an energy independent cut was adopted for the analysis.
Some different cuts on energy, acceptance angle r and also galactic coordinates l,b have been tried and then periodicity tests have been applied to the selected photons. I also checked a cut on aspect angle θ to select photons coming from 20° from the z-axis of the LAT but the resulting statistics was too poor for a good significativity of the periodicity test.
The best cut resulted by selecting photons around 3° from the radio pulsar position, for energies above 100 MeV and with two additional cuts on galactic coordinates. In order to reduce the contamination from Galactic diffuse emission, only photons with b greater than 1.5° and l greater than 66° have been selected. With these cuts, the χ^2

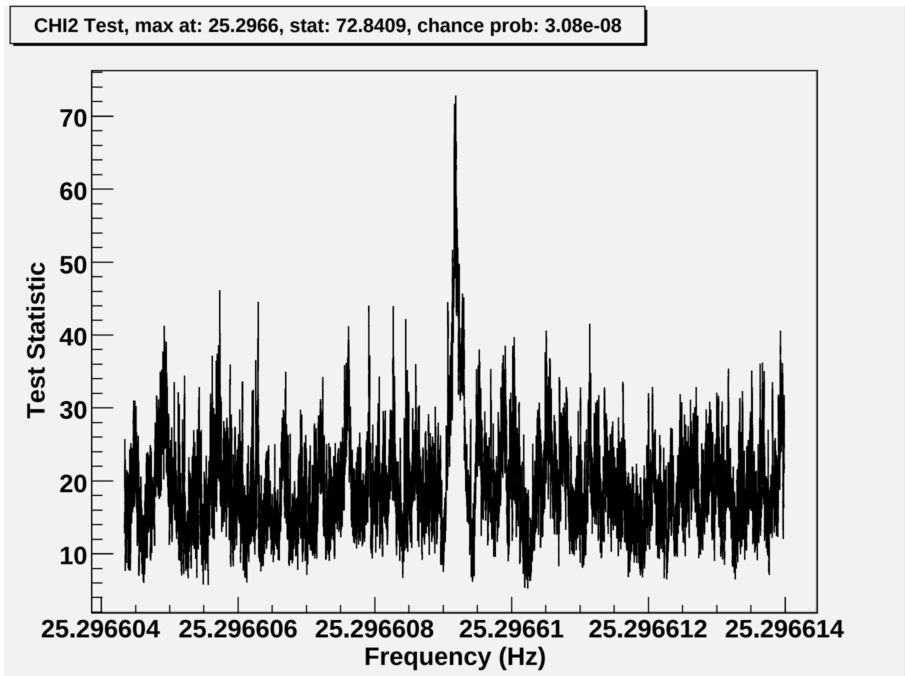

Figure 6.23: $\chi 2$ periodicity test applied to PSR B1951+32 and considering the phase shift due to frequency first derivative.

periodicity test was performed and gave a value of the statistic S_{χ^2}=72.8 for 49 degrees of freedom. This value correspond to a probability of pulsation occurring by chance at a level of about 3×10^{-8} for single trial. The frequency found is $25.2966092\pm1\times10^{-7}$ Hz at the epoch MJD 54844. The result of χ^2 periodity test is displayed in Fig. 6.23.
Also the H-test was performed giving a chance probability of 1.6×10^{-6}. Since three

other cuts have been tested, these chance probabilities must be multiplied by a factor 3.
The resulting phase curve obtained after selecting the photons using these cuts is displayed in Fig. 6.24, where a phase shift has been applied in order to have phase 0 corresponding to the radio pulse as in (Ramanamurthy et al., 1995).
6.23.

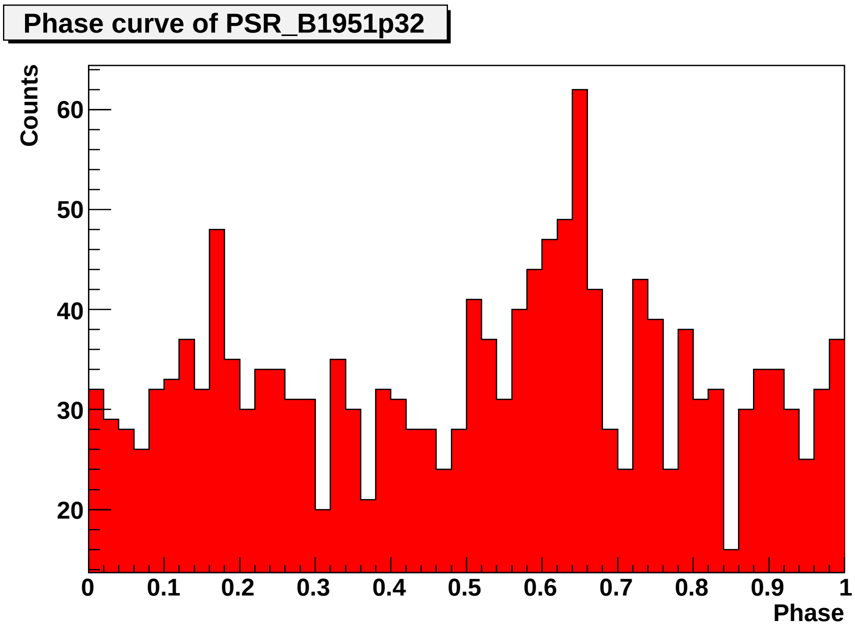

Figure 6.24: Lightcurve obtained by selecting the photons as described in the text and using 50 phase bins. The phase 0 has been set to be coincident with radio pulse.

6.5.4 Spectral analysis

The spectral analysis of this pulsar has been carried using mainly the maximum likelihood method. Three different spectral models have been used for this source, i.e. 1) a simple power law, 2) a broken power law and 3) a power law with superexponential cutoff in order to see if the spectral cutoff can be measured on the timescale of 1 month of LAT observation.
Good results have been obtained only in the case of power law, since the statistic was too poor to fit the spectrum with a broken power law or a super exponential cutoff.
The results of maximum likelihood is displayed in Fig. 6.25, where the observed counts are compared with the sum of counts from the pulsar and the diffuse background on the sample of photons considered for likelihood analysis, i.e. about 20° around the pulsar.
The maximum likelihood give a total flux of F(E>100MeV)=
$(0.9\pm0.2)\ \times10^{-7}$ ph cm^{-2}s^{-1} and a differential spectrum:

$$\frac{dN}{dE} = (3.33 \pm 0.02) \times 10^{-6} \times (E/100MeV)^{-1.82\pm0.07} \text{ph cm}^{-2}\text{s}^{-1}\ \text{MeV}^{-1} \qquad (6.21)$$

The flux distribution obtained integrating the Eq. 6.21 over energy is displayed in Fig. 6.26.

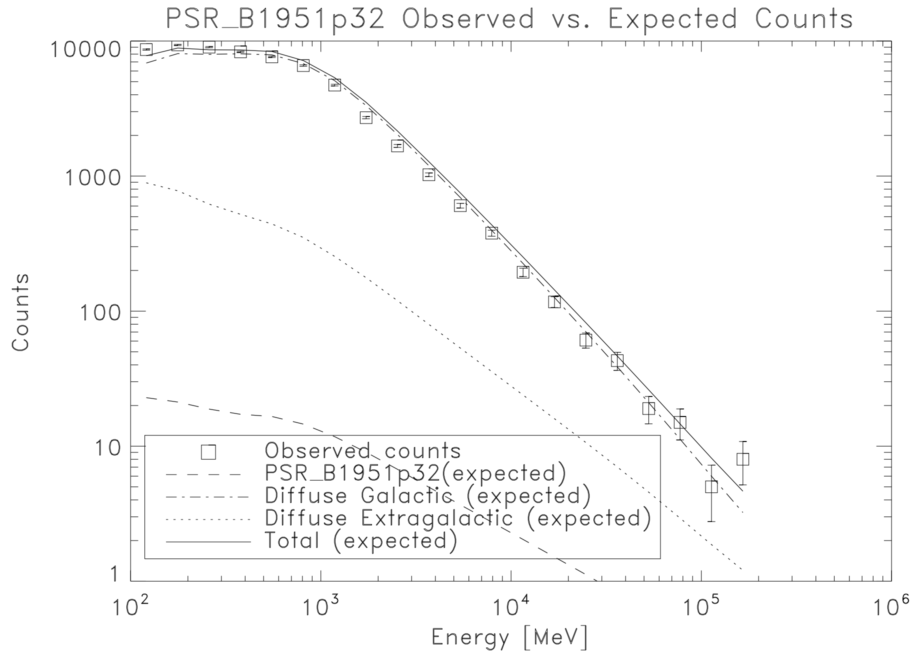

Figure 6.25: Energy distribution of observed counts from a region of 20° around PSR B1951+32 compared with the modeled counts using the maximum likelihood method.

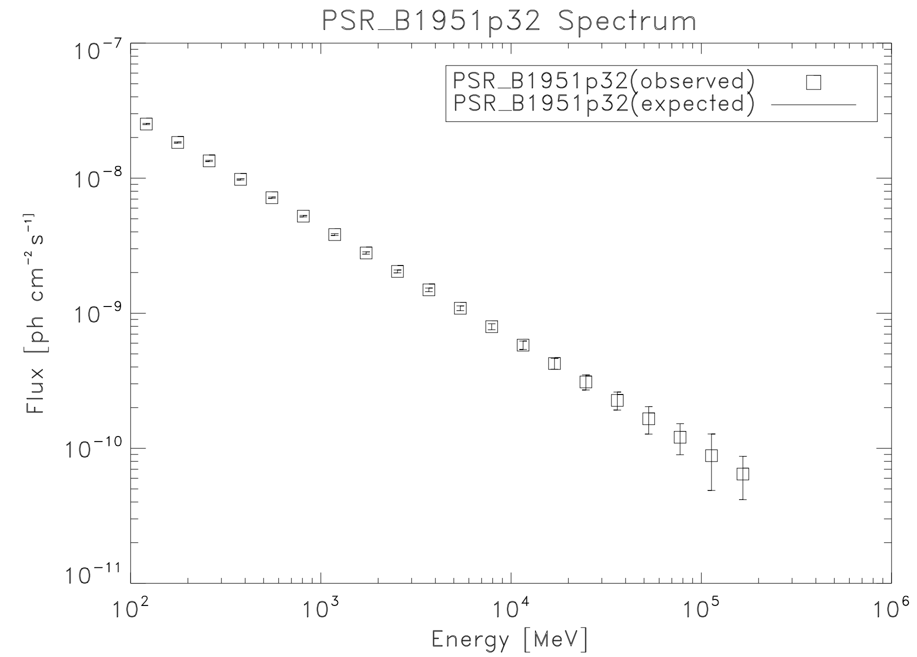

Figure 6.26: Flux of PSR B1951+32 compared with the spectrum model fit obtained using the maximum likelihood method.

6.6 Summary

Analysis of simulated LAT data is an important task for some reasons. First of all thanks to simulated data one can gain pratice with manipulation of high-level data that

will be distributed to the community. Second it is possible to face some possible problems and bugs in LAT analysis tools and notice them for corrections. The third aspect is the possibility to see what kind of analysis tools and techniques are needed for better extract information from data.
In this Chapter some examples of analysis of simulated data have been presented, using as analysis case smulated models of the EGRET pulsars. The example of Vela pulsar show how the periodicity can be tested in the ideal case of high number of photons and the basic steps to parform to analyze LAT data applied to it.
The example of PSR B1706-44 show a more complete analysis, where the temporal analysis show the lightcurve profile at some energies and the high statistic that can be achieved by the LAT at high energies. In particular spectral analysis has been performed using two parallel strategies and two different tools, i.e. maximum likelihood and XSpec analysis, that give results in agreement one with the other and with the original simulated model.
Finally an example of the analysis of PSR B1951+32 has been presented, as an analysis of faint pulsar where particular cuts on photons should be used to optimize the signal extraction, periodicity testing and spectral analysis. Apart from traditional cuts on energy and acceptance angle, also cuts on galactic position have been performed and they seem to work well to increase the significance of the detection of periodicity.
From the use of simulations, as I have presented, it can be draws some possible recommendations to improve the analysis tool. The analsis of this Chapter have shown that for example a good improvement could be the possibility to apply an energy-dependent cut as it was done for EGRET data. In the next Chapter a simple case of energy-dependent cut will be presented with the related improvement. Another possible upgrade could be the possibility to apply phase selection on the data, and this will play an important role for the phase-resolved analysis and spectroscopy. Presently this task can be made using the tool *fselect* that is part of the standard FTOOLS suite.
In this Chapter example of how simulated data can be applied to single source, while in the next Chapters there will be a discussion on analysis method that have been developed to perform analysis on large sample of data in order to automatic process large number of pulsars.

Chapter 7

Pulsar simulations for LAT Data Challenge 2

The preparation for the launch of a mission like GLAST is a very complex process. First there is construction, testing and integration phases of the LAT and GBM hardware, that have been accomplished.
In order to maximize the scientific output of this important space mission the GLAST collaboration must also be prepared to receive and analyze the anticipated data. Preparation of the ground support and analysis software has been carried out by the GLAST collaboration in parallel with the instruments construction. The testing and validation of the analysis software is a major task in this direction. In order to better test and study the LAT *Science Analysis Environment* (SAE), and to better study the LAT response and capabilities, the LAT collaboration has planned a series of *Data Challenges* (DCs).
The second Data Challenge (DC2) took place during 2006 and has been of fundamental importance for γ-ray pulsars studies. The LAT Collaboration chose the *PulsarSpectrum* simulator for the generation of the whole γ-ray pulsar population in the DC2.
In this Chapter the Data Challenges concepts are introduced and then the work of pulsar simulation for DC2 is shown.
The pulsar simulations prepared for DC2 served to provide a realistic pulsar population useful for testing analysis tools in SAE but also for deriving some first LAT capabilities for studying pulsars. An example of software developed for automatic analysis of LAT data applied to DC2 is presented in next Chapter together with some first conclusions on LAT ability to discover new γ-ray pulsars.

7.1 The LAT Data Challenges

The LAT Data Challenges (DCs) are intended to be milestones in the LAT software development, where LAT scientists have the possibility to exercise the LAT analysis tools on a simulated γ-ray sky. During Data Challenge the analysis tools designed for the LAT can be investigated and exercised, in order to see what kind of new functionalities can be included.
Data Challenges are an important innovation in the history of γ-ray missions. At EGRET times there was not enough computing power to create such detailed full sky

simulations as the ones prepared for the LAT, then the DCs experience has been a powerful tool for learning better how to analyze LAT data.
The original plans included a first Data Challenge (DC1) at the end of 2003, followed by a Data Challenge 2 (DC2) in mid 2006, concluding with a Data Challenge 3 planned for the beginning of 2007, just prior to launch. To create a most realistic situation, the source model used for the simulation (the so-called *DC truth*) are not revealed to the users until the end of the Data Challenge. The users then compare their analysis results (sources found, lightcurves, spectra, etc..) with the original model and check for mistakes in the analysis or for bugs in the analysis tools. During the Data Challenges web-based infrastructure have been created for archiving bugs to the analysis tools developers.
The DC1 started at the *DC1 Kickoff Meeting* (December 8-9 2003 at Stanford University) and ended in the *DC1 Closeout Meeting* held at the Stanford Linear Accelerator Center (February 12-13, 2004).
DC1 was designed for exercising the functionality of the analysis tools on a single simulated days of LAT observation. In the following a series of additional days were provided mainly for testing GRB analysis, for a total of 7 days of simulated data.
The sky model in the DC1 was not too detailed: it contained all the EGRET sources and a population of about 500 blazars and about 90 low-latitude objects and a series of Gamma Ray Bursts spread over the seven days of simulated observation in order to test alert algorithms for GRBs. No other variable point sources, e.g. pulsars or flaring blazars, were included. An image of the DC1 sky is displayed in Fig. 7.1.
The *South Atlantic Anomaly* (SAA) was not included nor were the Sun or the Moon. The initial DC1 dataset contained photons from one day-long observation, then another 6 days were added. The sources in these extra days were the same, except from the GRBs, since for these days new GRBs were included.
The goals of the DC2 were more ambitious, since the sky model contained many more

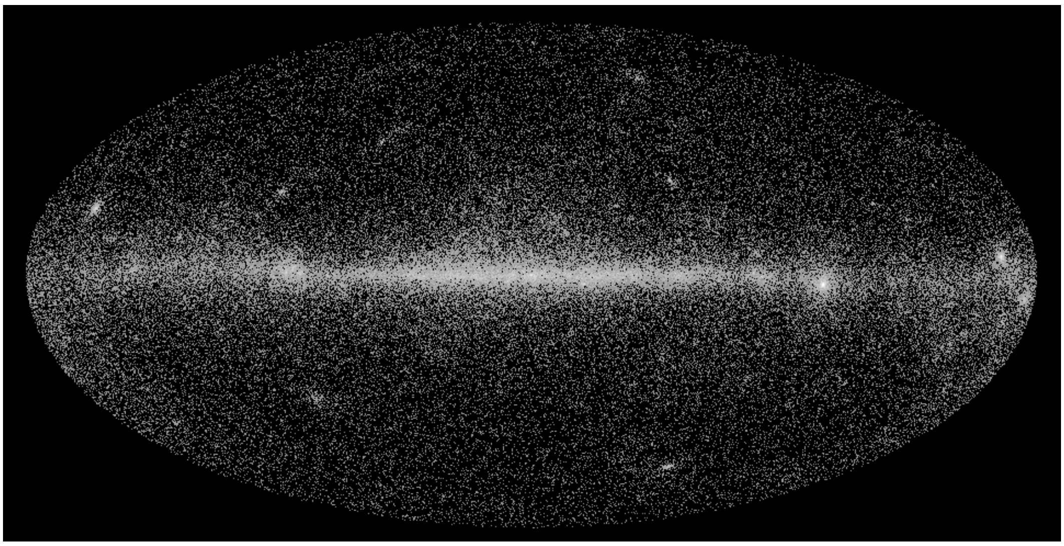

Figure 7.1: The simulated sky of the GLAST LAT DC1 (see *http://glast.phys.washington.edu/DC1/sources*)

sources than DC1, most of them with variable flux. The DC2 started with a *DC2 Kickoff Meeting* held at the Stanford Linear Accelerator Center (March 1-3, 2006) and ended with a *DC2 Closeout Meeting* held at NASA Goddard Space Flight Center (May 31-June 2, 2006). During DC2 LAT scientists analyzed simulated data coming from a 55 day long LAT observation.
The sky model was quite detailed and contained not only the DC1 sources but also many simulated γ-ray sources, e.g. thousands of blazars and hundreds of pulsars.
The original plans for the DC3 were to provide a simulation of 1 year of LAT observationsin order to offer the last test of LAT software on a large scale before launch.
The original plans for a single DC3 were changed to a set of *Service Challenges*, i.e. an ensemble of more focused simulations designed to study particular issues. The first Service Challenge runs took place at the beginning of October 2006 with a simulation of the DC2 sky model over a time scale of 1 year and a next have been started in March 2007.
In comparison with the DC1 and DC2 the users can access the simulation models just from the beginning instead of mantain them secret up to the end of the Service Challenge.

7.1.1 The DC2 sky model

The sky of Data Challenge 2 is much richer in new sources than DC1 sky model. A count map of the simulated photons of the DC2 is displayed in Fig.7.2.
The main component of the DC2 sky is the Galactic diffuse emission, that contained

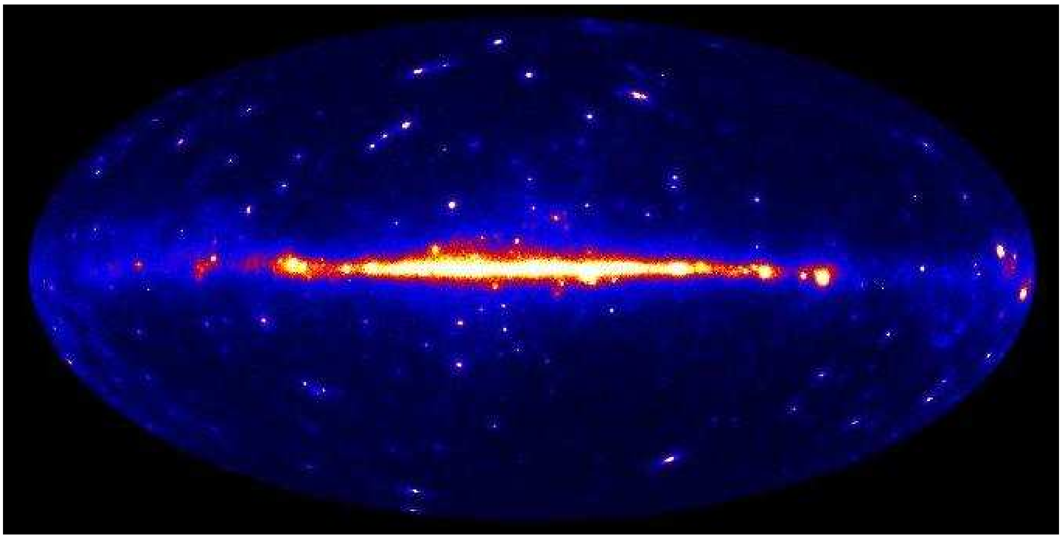

Figure 7.2: The simulated sky of the Data Challenge 2.

about 1.7×10^6 simulated photons. The model for the Milky Way diffuse emission was already tested in a previous simulation run and it is based on a GALPROP [1] simulation based on the gas distribution along the Galaxy.
The Galactic sources included in the DC2 sky consist of different classes, some already

[1]See $http://galprop.stanford.edu/web_galprop/galprop_home.html$ for details.

known as γ-ray emitters, while some other with an inferred γ-ray emission based on other criteria, e.g. observation at VHE γ-rays or coincidence with known sources in other wavelengths.
The main Galactic component is γ-ray pulsars, that provided a total of about 1.4×10^5 photons. The simulations of pulsars were made with the *PulsarSpectrum* simulator that have been described in Chap. 5. The details on the pulsars populations will be described more in detail in this Chapter.
A population of plerions was also added. Plerions are nebulae that surround most of pulsars and that are energized by the pulsar wind of outgoing particles. For three of them published data have been used for the derivation of spectrum (the Crab and the GeV J1809-2327 and GeV J1825-1310). Other 8 plerions were associated with simulated pulsars within 3EG unidentified sources and their fluxes were adjusted accordingly. Also 10 Supernova Remnants have been simulated, including 4 HESS sources.
Five X-Ray Binaries (XRBs) are also included, since their emission can be discovered also at GLAST energies. In particular the 2 microquasars LS I +61 303 and LS 5039, recently observed in VHE γ-ray respectively by MAGIC and H.E.S.S. (Albert et al., 2006; Aharonian et al., 2006).
A key target of the GLAST scientific program is the search of WIMP Dark Matter. A continuum emission centered at the Galactic center with flux above 100 MeV of 10^{-6}ph cm^{-2}s^{-1} has been included from π_0 decay. A line emission at 100 GeV due to neutralino decay into $\gamma\gamma$ with a branching ratio of 1% has also been included with a flux of 10^{-8}ph cm^{-2}s^{-1}.
A new interesting γ-ray source in the DC2 sky is the Moon, that is recognized to be a bright γ-ray source and provided about 60 photons per day. A broken power law has been used for simulations, since the spectrum is fairly soft at high energies and it is estimated to be 1.5 at energies below 200 MeV and 3.5 above. The Moon is intended to be useful for studying a tool for analysis of moving sources, that is not currently yet included in the LAT SAE.
The Sun was also included as a flaring source. The solar flare has been simulated using a broken powerlaw spectrum with indices Γ_1=1.43 and Γ_1=2.5 and the break occurring at 150 MeV. This flare have been modeled on the basis of the spectacular the June 11 1991 Solar Flare (Murphy et al., 1987).
The sources present in the 3^{rd} EGRET Catalog (Hartman et al., 1999) were also included, with exception of the ones that have been already simulated as a specific class of sources. For all of them a power law spectrum have been used.
The extragalactic component of the DC2 sky is made of different classes of sources. First there are 4 galaxy clusters, Coma, Oph, Perseus and Virgo, that are believed to be γ-ray emitters. Also 5 galaxies were included in the DC2 sky, among them the two Magellanic Clouds, and for them simulations were based on observational data.
An important component of the extragalactic γ-ray emission is made of blazars. About 1400 blazars were included as point sources and for about 200 of them a lightcurve was provided in order to simulate flares.
During the 55 days of the DC2 simulation a total of 132 Gamma Ray Burts were included, 64 of them triggered the GBM, while the others did not because of some effects, among other SAA passages or Earth occultation. For 9 GRBs afterglows were simulated with soft decay of brightness with time or with a steady flux with time.

The extragalactic diffuse component was also included and have been modeled as a power law with spectral power of 2.1, and the EBL attenuation have been simulated for extragalactic sources.

7.2 Pulsar Simulations for DC2

In the DC1 only the EGRET pulsars were included and they were inserted as steady sources, then all studies of the timing of these source were impossible and only become feasible in the DC2 also when a large population of realistic pulsars was included in the sky model. For the simulation of the whole population the *PulsarSpectrum* simulator was used.
The modeled pulsar population has been constrained to mimic a realistic sample and to allow users to perform some basic studies on LAT response for pulsars.
In order to simulate the large population of DC2 pulsars, the *Pulsar Simulation Suite* presented in Ch. 5 was also upgraded to standardize the data format.
Part of the sample of simulated pulsars was based on population synthesis code and Slot Gap emission models (Gonthier et al., 2004; Muslimov & Harding, 2003). The basic assumption of this model will be described in detail below.
Starting from this simulated population some assumption were made in order to generate the information required for DC2 simulations, e.g. the ephemerides.
Each pulsar was generated using a specific timing model, and corresponding entry for the DC2 *Pulsar Database* have been generated.
To test the LAT capabilities for discovering Geminga-like pulsars it was decided to not include the ephemerides of the complete DC2 population in the DC2 Pulsar Database. We will refer here to the pulsars with an entry in the DC2 Pulsar Database as *Radio-Loud* (RL) pulsars and the ones with missing ephemerides as *Radio-Quiet* (RQ). The characteristic of RL or RQ was computed by the population synthesis code combined with main radio surveys (Gonthier et al., 2004). For each generated pulsar a radio flux is computed and then compared to the sensitivity of the major current radio survey. If the radio flux is lower than this flux limit the pulsar is labeled as RQ and the corresponding ephemerides used to produce it is removed from the DC2 Pulsar Database and keep hidden from DC2 users. The other pulsars are labeled as RL and their ephemerides are included in the Pulsar Database.
The resulting population is 414 γ-ray pulsars, distributed over 4 main subgroups with different characteristics that will now be presented together with the details of the simulations.

7.3 The EGRET pulsars

A first component of the DC2 pulsars are the γ-ray pulsars presently known after the EGRET era; we will refer at these as *EGRET pulsars*. The aim of including these is to have a rough estimate of the difference between the LAT sensitivity and that of EGRET. Another use of these simulation is to study the possibility to use bright pulsars such as Vela or Crab for LAT calibrations. The six EGRET pulsars included are Vela pulsar (PSR B0833-45) (Kanbach et al., 1994), Crab pulsar (PSR B0531+21)

(Thompson & et al., 1993), Geminga (PSR J0633+1746) (Mayer-Hasselwander et al., 1994), PSR B1706-44(Thompson et al., 1992), PSR B1055-52 (Fierro et al., 1993) and PSR B1951+32(Ramanamurthy et al., 1995).
PSR 1509-58 (Ulmer et al., 1993) has been not included since the γ-ray emission from this pulsar falls below the lower LAT energy so the number of photons expected from this pulsar is negligible.
Also the other γ-ray low-confidence pulsars, i.e. PSR B1046-58, PSR B0656+14 and PSR J0218+4232 are not included in this sample of simulated data. The lightcurves

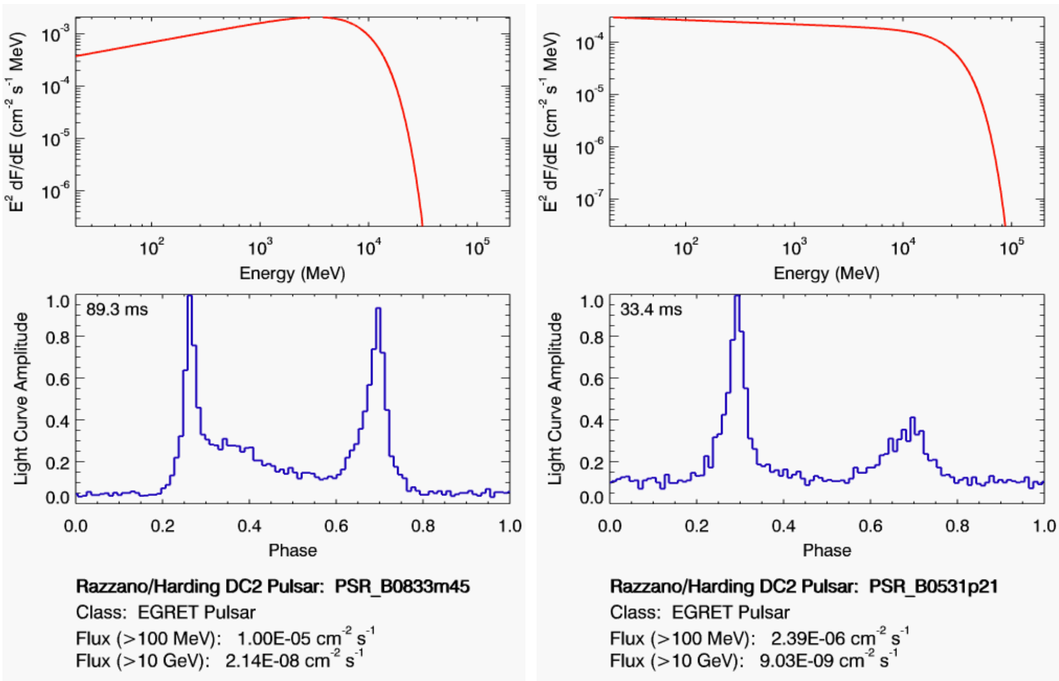

Figure 7.3: The simulation model of lightcurve and spectrum used for EGRET pulsars in DC2. Left: Vela pulsar. Right: Crab pulsar.

that have been used as *TimeProfile* for these pulsars come from EGRET data, as listed in Tab. 7.1. At this stage no refinement of the binning was applied, so the lightcurves of the faintest pulsars appear a little bit noisy because of statistical fluctuation due to the limited EGRET statistics. The simulation of the spectrum was performed using the phenomenological model *PSRPhenom* of *PulsarSpectrum*. The spectral parameters have been retrieved from (Nel & De Jager, 1995) and from (De Jager et al., 2002) as listed in Tab. 7.1. At this point no phase-dependent information was included; these were included in the *Service Challenge* simulations.
The Fig. 7.3, Fig.7.4 and Fig.7.5 show the original lightcurves and spectra used for the simulations.

7.4 Isolated pulsars with Slot Gap emission

A second important component of the DC2 pulsar simulations are a groups of isolated pulsars whose spectra and luminosities have been derived using the extended Slot Gap

Pulsar	Flux(ph/cm2/s)	g	E_0 (GeV)	b
PSR B0833-45 (Vela)	1×10^{-5}	1.62	8	1.7
PSR B0531+21 (Crab)	2.39×10^{-6}	2.08	30	2.0
PSR J0633+1746 (Geminga)	4.06×10^{-6}	1.42	5	2.2
PSR B1706-44	1.27×10^{-6}	2.1	40	2.0
PSR B1055-52	2.8×10^{-7}	1.8	20	2.0
PSR B1951+32	1.6×10^{-7}	1.74	40	2.0

Table 7.1: Parameters used for the simulation of EGRET pulsars in DC2. The meaning of the spectral parameters g,E_0 and b are explained in Ch.5. Spectral parameters are retrieved from (Nel & De Jager, 1995) and from (De Jager et al., 2002). All lightcurves data are from (Fierro, 1995).

emission (Muslimov & Harding, 2003).
This population has been created using the population synthesis code described in (Gonthier et al., 2004; Harding et al., 2004b), that is able to produce a realistic pulsar population starting from physical considerations compared to the observations .
Starting from an initial distribution of neutron stars, the software evolves them in the gravitational potential of the Milky Way and takes into account the magnetic field decay and the evolution of the spin with time.
The neutron stars are followed up to present time and their fluxes according to an emission scenario is computed. The model assumed for the radio beam is described in (Gonthier et al., 2004) and is basically a two-component model with a core and an extended cone. The emission geometry and view angle (that is extracted from an uniform random distribution) are used to determine a simple lightcurve.
According to pulsar period P, its first derivative $\dot{P}$ and the pulsar distance the radio and gamma flux is determined. The flux is then compared with the flux limit of some of the most sensitive radio surveys (e.g. Parkes or Arecibo) to determine if the radio emission is visible from Earth. If the pulsar radio emission is visible it is labeled as *Radio-Loud*, otherwise it is called *Radio-Quiet*. A total of 37 Radio Loud and 103 Radio Quiet isolated pulsars were synthesized by this code and their parameters have been used for DC2. The distribution of the 37 Radio-Loud DC2 pulsars in sky and in the $P-\dot{P}$ diagram is shown respectively in Fig. 7.6 and Fig. 7.7. The distribution of the 103 Radio-Quiet DC2 pulsars in sky and in the $P-\dot{P}$ diagram is shown in Fig. 7.8 and in Fig. 7.9. From all pulsars generated we decided to use only those with flux greater than 10^{-9} ph cm^{-2} s^{-1}. The birth rate of the neutron stars is assumed to be constant through the history of the Galaxy and the age of a pulsar is randomly selected from the present to 1 Gyr in the past.
According to (Gonthier et al., 2004) the birth periods are uniformly extracted in a range from 0 to 150 ms and the initial magnetic field is chosen according to a bimodal gaussian distribution with peaks at logB_0=12.75 and logB_0=13, while a time scale of 2.8 Myr is assumed for the magnetic field decay.
The initial kick velocity of the neutron stars has been random extracted from a bimodal distribution that peaks at 90 km/s and 500 km/s and the stars are then evolved in the gravitational potential up to the present age (Gonthier et al., 2004). The emission model is an extension of the basic Slot Gap Model proposed by Arons and Scharlemann

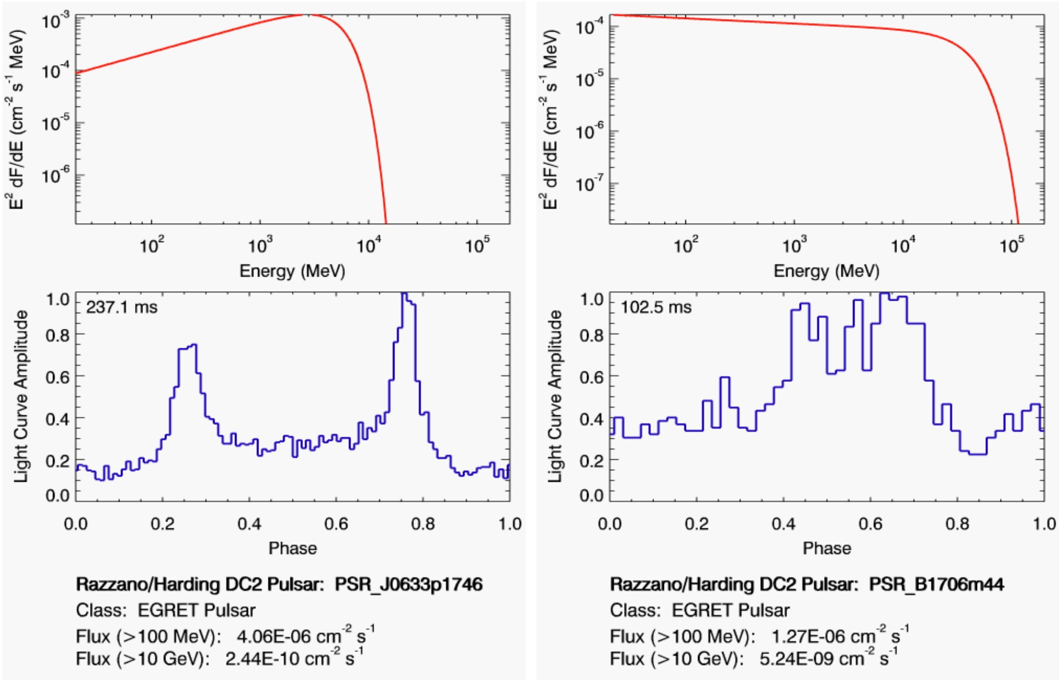

Figure 7.4: The simulation model of lightcurve and spectrum used for EGRET pulsars in DC2. Left: Geminga pulsar. Right: PSR B1706-44.

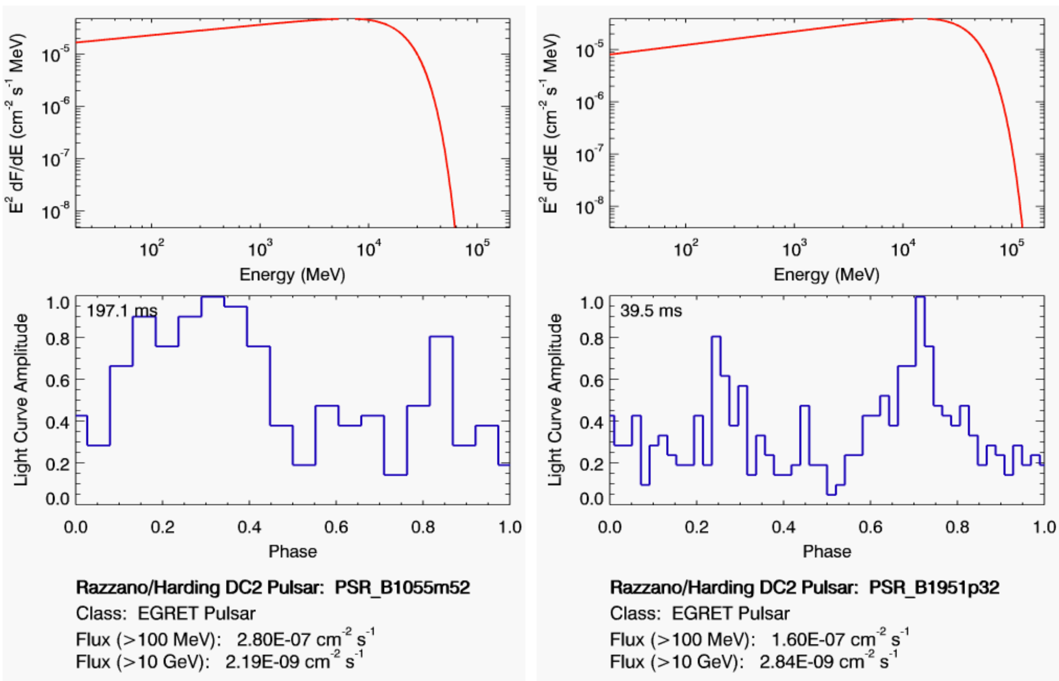

Figure 7.5: The simulation model of lightcurve and spectrum used for EGRET pulsars in DC2. Left: PSR B1055-52. Right: PSR B1951+32.

(Arons & Scharlemann, 1979; Arons, 1983). This model can be regarded as an extension

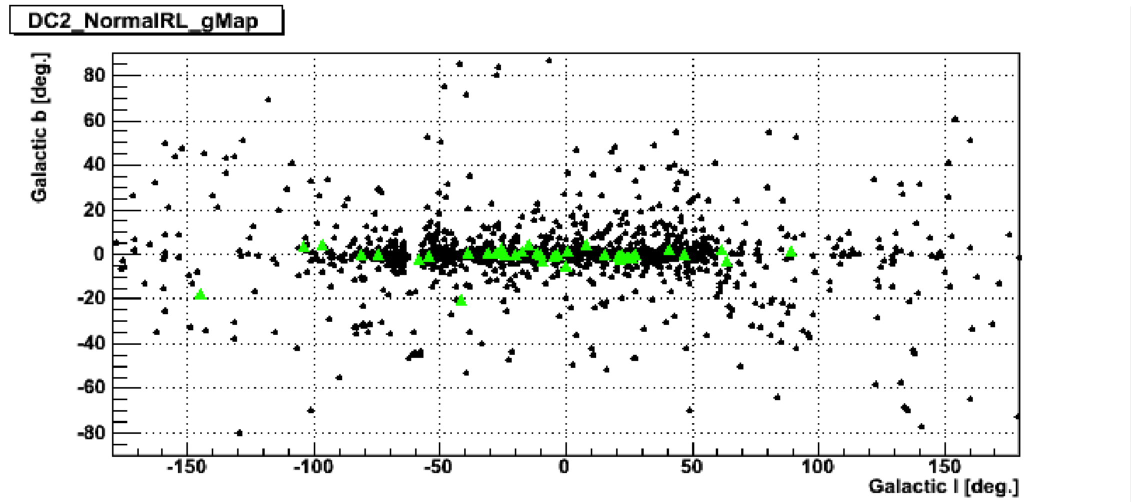

Figure 7.6: The distribution of the normal Radio Loud pulsars (triangles) in the sky. The black points represent the distribution of the radio pulsars of the ATNF catalog.

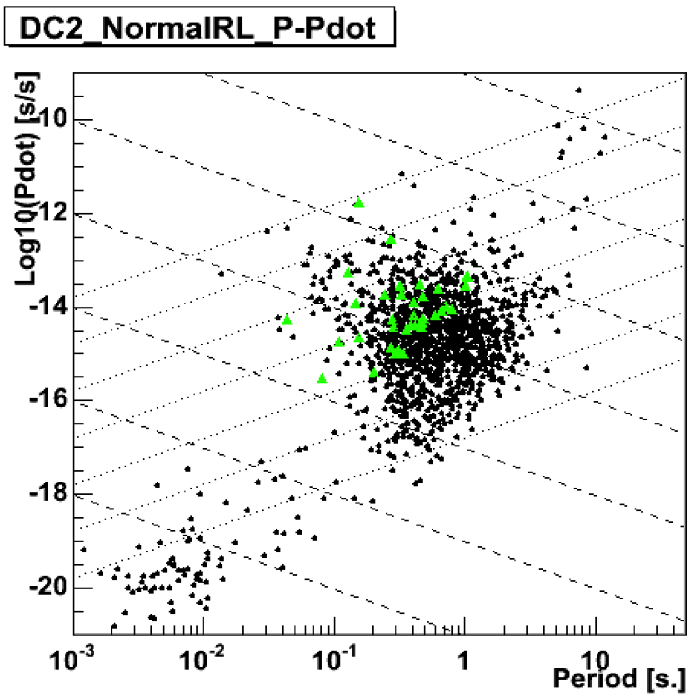

Figure 7.7: The distribution of the normal Radio Loud pulsars (triangles) in the $P-\dot{P}$ diagram. The black points represent the distribution of the radio pulsars of the ATNF catalog.

of the basic Polar Cap model created in order to overcome some problems, mainly the possibility to have broad peaks in the ligthcurves in γ-rays. The basic idea starts from the consideration that the plasma *Pair Formation Front* (PFF) altitude varies across the Polar Cap region. The PFF is the surface above which the electric field parallel to

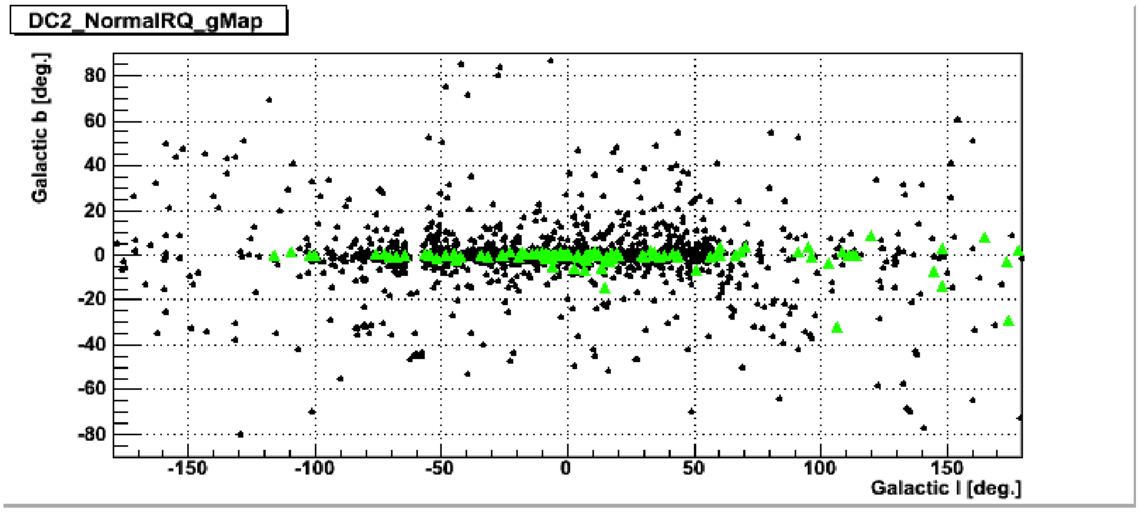

Figure 7.8: The distribution of the normal Radio Quiet pulsars (triangles) in the sky. The black points represent the distribution of the radio pulsars of the ATNF catalog.

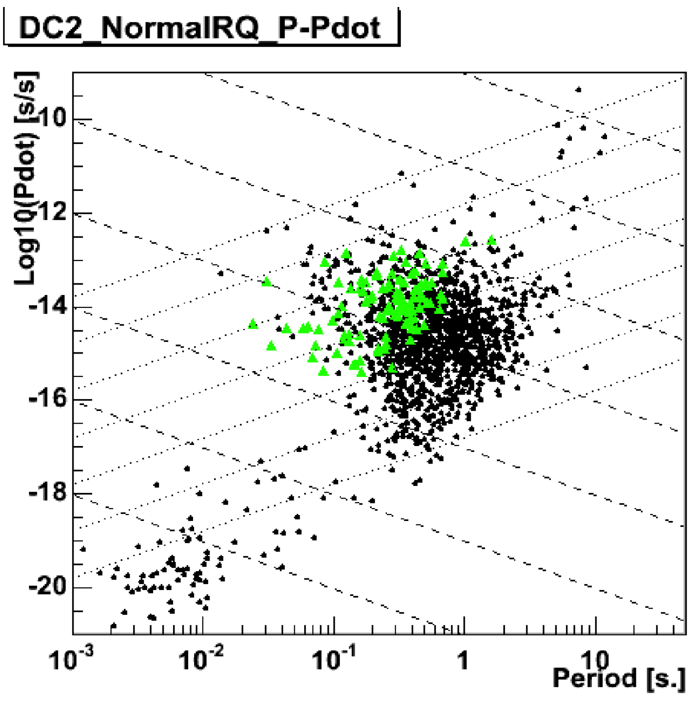

Figure 7.9: The distribution of the normal Radio Quiet pulsars (triangles) in the $P - \dot{P}$ diagram. The black points represent the distribution of the radio pulsars of the ATNF catalog.

magnetic lines is screened by the pairs produced by the electromagnetic cascade from primary accelerated electrons above the surface. It was recognized that PFF is located at increasing altitudes when the magnetic colatitude is near the last open field line (Arons & Scharlemann, 1979). The possibility of such a gap, called *Slot Gap*, was soon

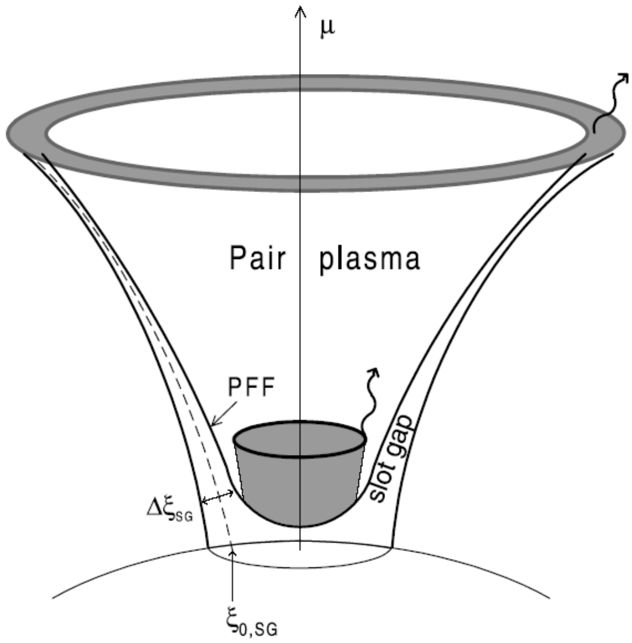

Figure 7.10: Schematic illustration of PC geometry, showing the outer boundary of the open field line region (where $E_{||}$=0) and the curved shape of the PFF, which asymptotically approaches the boundary at high altitude. The slot gap exists between the pair plasma, which results from the pair cascades above the PFF, and the outer boundary. A narrow beam of high-energy emission originates from the low-altitude cascade on field lines interior to the slot gap. A broader, hollow-cone beam originates from the high-altitude cascade above the interior edge of the slot gap. $\Delta\zeta_{SG}$ is the slot gap thickness (see text). From (Muslimov & Harding, 2003)

recognized as a possible acceleration site for charged particles and that the formation of the Slot Gap is unavoidable in any Polar Cap model with space-charge limited flow (Arons, 1983). The geometry of the Slot Gap is presented in Fig. 7.10.
A self consistent model of Slot Gap emission model has been developed including General Relativity (Harding & Muslimov, 1998) and screening by pairs (Harding & Muslimov, 2002) and their high-energy emission was investigated in (Muslimov & Harding, 2003). This last work has been used to produce the isolated Slot Gap pulsar parameters for DC2.
High-energy emission is efficient not only for large inclination angles and for the so-called "favorable" field lines, i.e. these that are curved toward the rotation axis, but also in many more cases (Arons, 1983).
The other important finding of this work is the calculation of the electric field parallel to the magnetic field, that is useful to locate the height of the PFF, at some stellar radii. The luminosity L_{prim} of the Slot Gap can be calculated from the distance d, the Slot Gap surface A_{SG} and the Goldreich-Julian current n_{GJ}:

$$\frac{L_{prim}}{\Omega_{SG}} = 2 \times 10^{34} \text{ erg s}^{-1} \text{ sr}^{-1} \, L_{SD}^{3/7} P_{0.1}^{5/7} \tag{7.1}$$

where L_{SD} is the spin-down luminosity, $P_{0.1}$ the pulsar period expressed in units of 0.1 s. and Ω_{SG} is the solid angle where the Slot Gap emission is emitted. Since the distance is known it is possible to calculate the γ-ray flux. The distribution of fluxes for these pulsars is shown in Fig. 7.11. In the model the primary electrons are accelerated by the

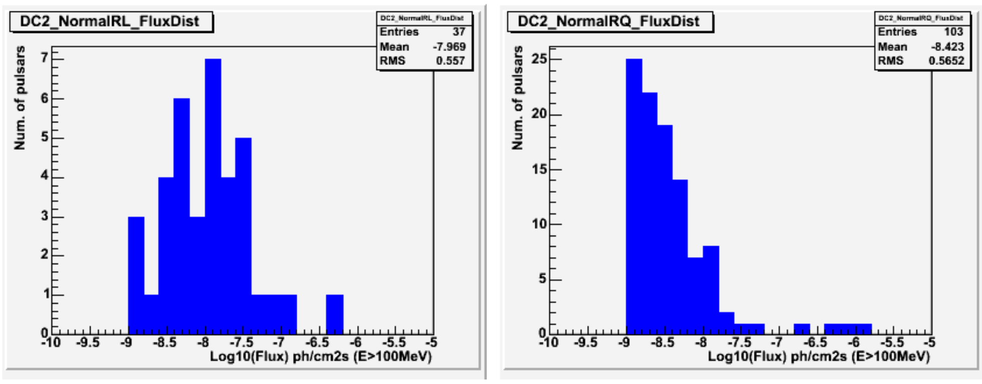

Figure 7.11: The distribution of fluxes of DC2 Radio Loud pulsars (left) and Radio Quiet pulsars (right).

electric field and emit curvature radiation. The γ-rays emitted can produce pairs that lead to an electromagnetic cascade. The Inverse Compron scattering of the pairs and primary electrons is neglected in this model. Also the photon splitting for high magnetic fields is neglected.
The spectral parameters can be evaluated from theory using the pair cascade evolution and of particular interest is the cutoff energy, that is determined by the γ-ray magnetic absorption in high magnetic fields. This energy, that in Ch. 5 has been designed with E_0, can be estimated to be:

$$E_0 \approx \; 2 \text{ GeV } P^{1/2} B_{12}^{-1} \left(\frac{r}{R}\right)^{7/2} \tag{7.2}$$

where B_{12} is the magnetic field expressed in units of $\times 10^{12}$G, R is the radius of the neutron star and r is the height of the PFF, usually few stellar radii. Since the Slot Gap emission model predicts a sharp cutoff above E_0 we decided to choose a cutoff index b uniformly extracted between 1.8 and 2.2 in order to mimic a cutoff sharper than the simple exponential. An exemplar from this groups is shown in Fig. 7.12, where ζ indicate the viewing angle and α is the inclination between magnetic moment and rotation axis. Since this model considers only the γ-ray emission from the Slot Gap hollow cone emission, there is no offpulse emission. In the basic Polar Cap theory the interpulse emission comes from the inner region of the hollow cone, from the center of Polar Cap. An extended treatment of the full geometry of the system is under development (Muslimov & Harding, 2003).

7.5 Millisecond pulsars

Another important component that was included in DC2 pulsar simulation are the millisecond pulsars (MSPs). A relatively large fraction of MSPs has been detected in

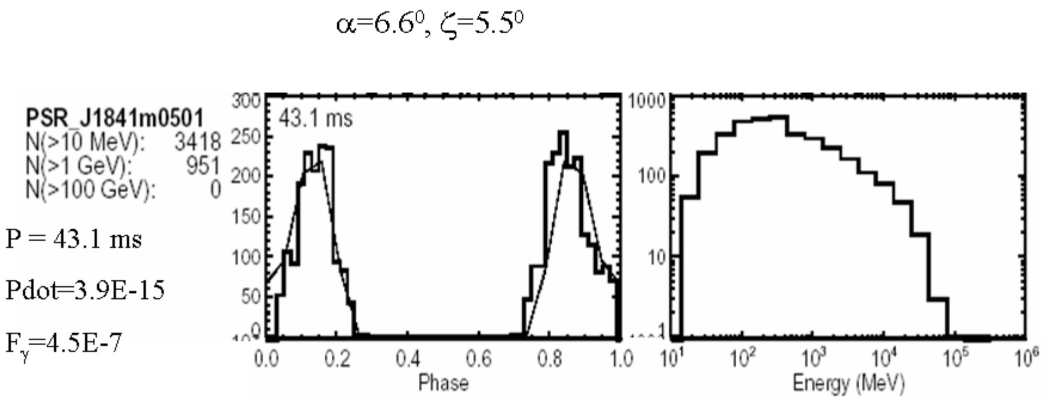

Figure 7.12: An example if a DC2 Slot Gap pulsar, called J1841-0501 according to the standard J2000 labeling. The parameters meaning are explained in the text.

X-rays, showing mainly an hard power-law spectrum at energies 01-30 keV, which must break or turn over at energies before about 1-100 MeV.
In fact γ-ray from PSR J0218+4232 have been detected with low confidence (Kuiper et al., 2000b). The spectrum of PSR J0218+4232 measured by EGRET is much softer, with a spectral index of 2.6, than the typical γ-ray pulsar with photon index 1.5-2, and it is not detected at energies above 1GeV. Altought it is 30 time closer, PSR J0437-4715 has not been detected by EGRET, altough its predicted flux is well above EGRET sensitivity, if a standard γ-ray spectrum is assumed.
MSPs then seems to show a different behaviour and since they are believed to emit γ-rays it is interesting to have an estimate on the number of MSPs that can be detected with GLAST. For the DC2 MSPs a population synthesis code developed by P.Gonthier et al. as been used as for the Slot Gap pulsars (Gonthier et al., 2004; Story et al., 2007). The emission model used to calculate the flux and the spectrum is based on work by Harding et al. (Harding et al., 2005) that assume a Polar Cap emission scenario in order to compute the high-energy emission from MSPs.
The resulting population contains 17 *Radio-Loud* (RL) MSPs, whose distributions are shown is Fig. 7.13and Fig. 7.14, and 212 *Radio-Quiet* (RQ) and Fig. 7.15 and Fig. 7.16. The synthesis code for generating the initial distribution of MSPs is based on some assumptions.
The initial distribution of MSPs period has been chosen to lie along the *spin-up* line corresponding to $P = 0.3B_8^{6/7}$, where B_8 is the magnetic field in units of 10^8 G. According to the model of Cordes et al. (Cordes & Chernoff, 1997) the magnetic field strength B is following the distribution:

$$n(B) = \frac{\sqrt{B_m}}{2B^{3/2}} \tag{7.3}$$

for $B > B_m \approx 2 \times 10^8 G$. According to the same work the distribution of initial kick velocity v is an exponential as:

$$n(v) = v^2 e^{-\frac{v^2}{2\sigma_v}}, \text{ with } \sigma_v \approx 52 \text{ km s}^{-1} \tag{7.4}$$

In the DC2 we simulate only MSPs on the Galactic potential, neglecting the MSPs in globular clusters, since they are too faint to allow a possible pulsed detection.

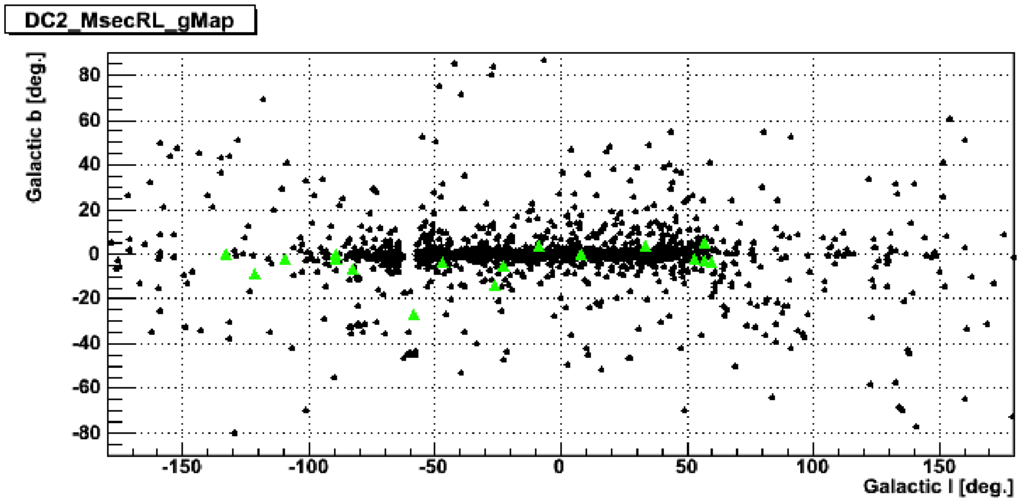

Figure 7.13: The distribution of the Millisecond Radio Loud pulsars (triangles) in the sky. The black points represent the distribution of the radio pulsars of the ATNF catalog.

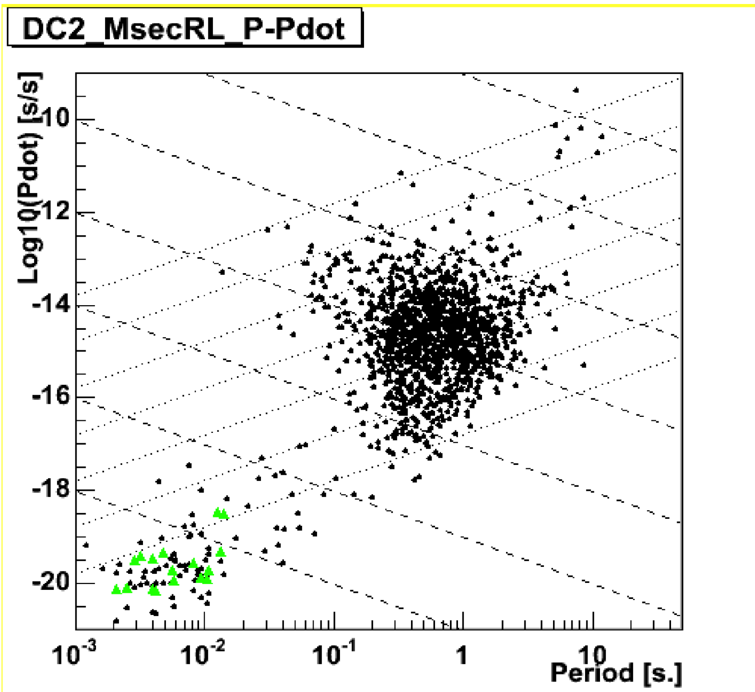

Figure 7.14: The distribution of the Millisecond Radio Loud pulsars (triangles) in the $P - \dot{P}$ diagram. The black points represent the distribution of the radio pulsars of the ATNF catalog.

The assumed emission model is based on a Polar Cap geometry and consider the emission from accelerated particles above Polar Cap. This model is based on three main assumptions: a space-charge limited flow, one-photon pair creation by curvaure radiation and Inverse Compton Scattering photons, and the screening of electric field by

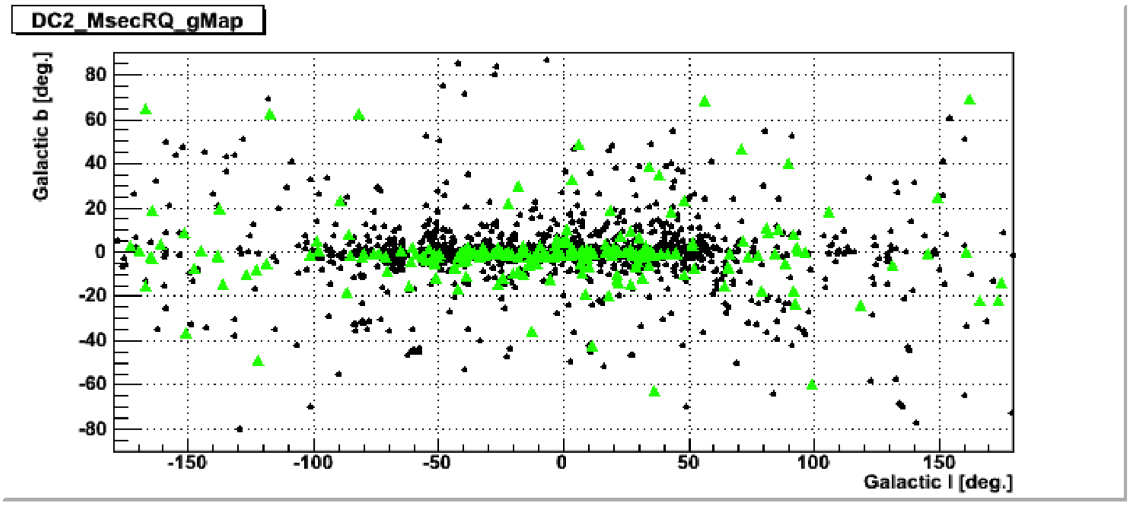

Figure 7.15: The distribution of the Millisecond Radio Quiet pulsars (triangles) in the sky. The black points represent the distribution of the radio pulsars of the ATNF catalog.

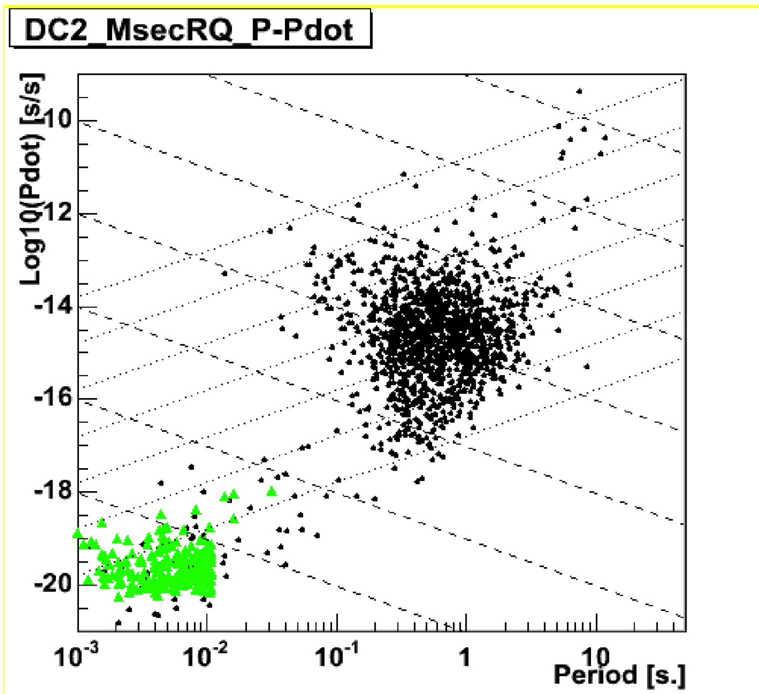

Figure 7.16: The distribution of the Millisecond Radio Quiet pulsars (triangles) in the $P - \dot{P}$ diagram. The black points represent the distribution of the radio pulsars of the ATNF catalog.

returning positrons. This model shows two main differences between γ-ray emission in MSPs compared with isolated pulsars.

In normal pulsars the multiplicity of the pairs produced above Polar Cap is high enough to screen the electric field and then reducing the acceleration region to small altitudes.

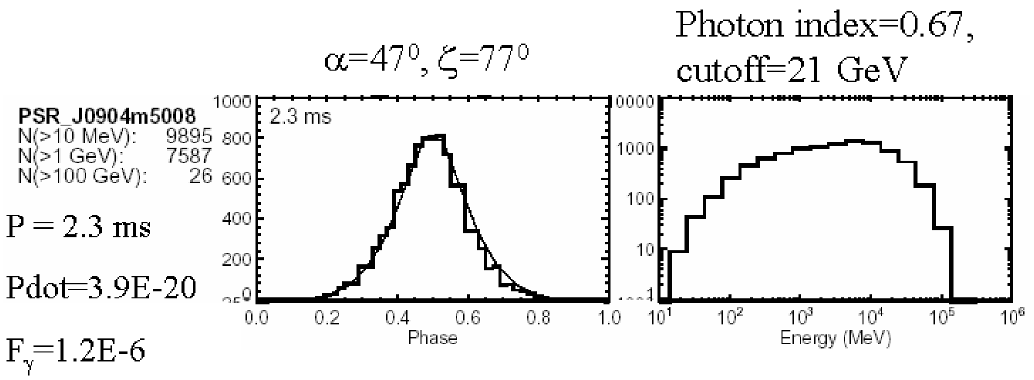

Figure 7.17: An example if a DC2 Millisecond pulsar called J0904-5008 according to the standard J2000 labeling. The parameters meaning are explained in the text.

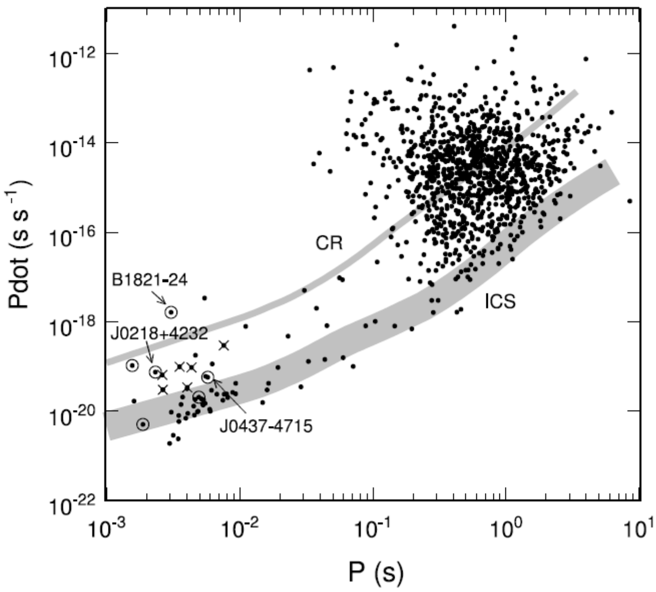

Figure 7.18: Plot of P vs. $\dot{P}$ for known radio pulsars in the ATNF catalog (*http : //www.atnf.csiro.au/research/pulsar/psrcat*) with measured period derivative. Superposed are the pair death lines for curvature radiation (CR) and inverse Compton-scattered (ICS) photons. The width of the death lines indicates the range of uncertainty due to unknown values of NS surface temperature, mass, radius, and moment of inertia. From (Harding et al., 2005)

Since MSPs lies below the dead-line for pair production by curvature radiation (Fig. 7.18), the pairs can be produced by photons created by Inverse Compton Scattering of the accelerated particles on thermal X-ray radiation. Hovewer the multiplicity of these pair is smaller, then the electric field cannot be screened efficiently, then the acceleration region extends to much higher altitudes. The particles can be then accelerated up to higher energies while radiating will become radiation-limited, since the energy gained is equal to the radiation losses. A second important difference is the much higher energy

of the pair production attenuation cutoff, due to lower magnetic field.
The calculation of accelerating electric field provide and estimate of the Lorenz factor of the primary electrons, which in turns emit a spectrum that can be written as:

$$N_{CR}(E) \propto P_{ms}^{-1/3} E_{MeV}^{-2/3}, \text{ for E>E}_{cr} \tag{7.5}$$

where P_{ms} is the pulsar period in ms. and E_{MeV} the energy expressed in MeV. E_{cr} is the cutoff energy that can be estimated as:

$$E_{cr} \approx 10 \text{ GeV } B_8^{3/4} P^{-5/4} \tag{7.6}$$

where B_8 is the magnetic field in units of 10^8 G and P is the pulsar period. From these two equations we derive the parameters g=2/3 and E_0 as in Eq. 7.6 for the phenomenological model in *PulsarSpectrum* as described in Ch. 5. Since the high-energy emission is radiation-limited we choose an exponential cutoff, i.e. b=1. The total

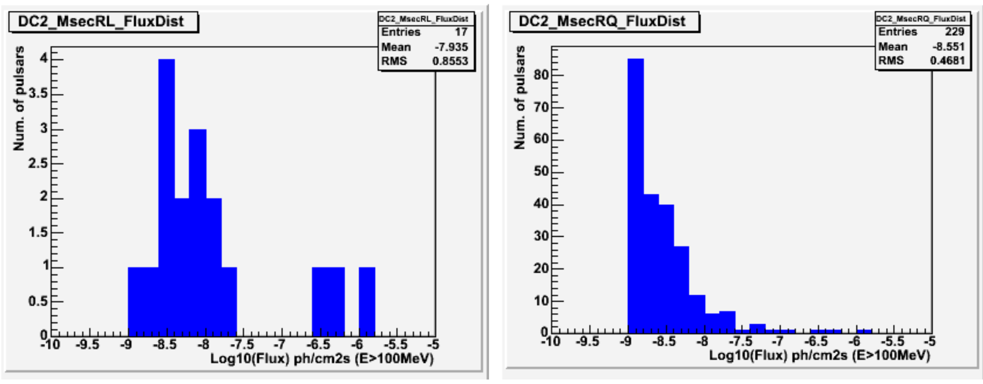

Figure 7.19: The distribution of fluxes of DC2 Millisecond Radio Loud pulsars (left) and Millisecond Radio Quiet pulsars (right).

flux can be evaluated by integrating the spectrum, obtaining:

$$F(E) \simeq 4 \times 10^{-8} B_{8,0} P_{ms}^{-7/3} E_{MeV} d_{kpc}^{-2} \text{ ph cm}^{-2}\text{s}^{-1}\text{MeV}^{-1}, \text{ E>E}_{cr} \tag{7.7}$$

where $B_{8,0}$ is the magnetic field in units of 10^8 G, E_{MeV} the energy expressed in MeV, $P_{0.1}$ the pulsar period expressed in units of 0.1 s., and d_{kpc} the pulsar distance expressed in kpc.
The distribution of the fluxes is presented in Fig. 7.19. From the initial distribution we decide to cutoff all MSPs with fluxes lower than 10^{-9} ph cm^{-2}s^{-1}, since they are too faint to be detected in a 55-days observation. An example of a synthetic MSP is shown in Fig. 7.17. The model predict also a number of Radio-Quiet MSP, in case of pulsars that evolve below the ICS pair-production dead line. This model consider also an Inverse Compton Scattering of electrons with thermal X-rays that is much smaller than curvature radiation emission and that can extend up to TeV energies. This flux is then too low to be easily detected by the Cherenkov telescopes and it is not of great importance for the GLAST LAT energy range.

7.6 3EG pulsars

Another interesting component of the DC2 pulsar population is made of a set of 39 real radio pulsars that lie within the error bars of EGRET, in particular of the Third EGRET Catalog (3EG)(Hartman et al., 1999). For these object the frequency and its derivatives are known, then simply an epoch has been chosen to be compatible with the date of the simulated observation window used in DC2.
This component has been inserted for two main reasons. First of all because most of the original unidentified 3EG sources have been splitted in two or more DC2 sources. In this case the relative flux of sources have been adjusted in order that the sum of the sources correspond to the flux of the original 3EG source. Additionally these pulsars have been inserted in order to allow users the possibility to study some real pulsars that could give some γ-raysignal. In order to compute a flux and the spectral parameters it

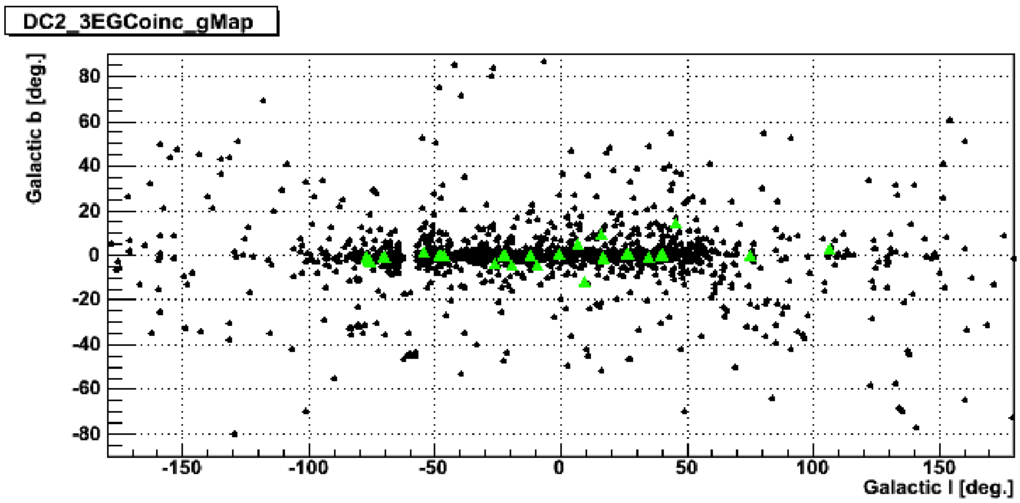

Figure 7.20: The distribution of the pulsars within 3EG error boxes (triangles) in the sky. The black points represent the distribution of the radio pulsars of the ATNF catalog.

is mandatory to choose a model. For this set of pulsars we decided to use the Slot Gap model, that has been presented in Sec. 7.4. In particular we select 39 radio pulsars that lies within EGRET sources, avoiding those that are too close in order to avoid confusion problems due to the small distances.
The spectrum has been simulated using the phenomenological model *PSRPhenom* of *PulsarSpectrum* using the Polar Cap cascade scenario (Gonthier et al., 2002; Harding & Daugherty, 1998), where the spectral index is estimated as:

$$g = 0.85 - 0.45 \log\left(\frac{P}{B_{12}}\right) \tag{7.8}$$

where B_{12} is the magnetic field expressed in units of 10^{12} G. The cutoff energy E_0 can be calculated from photon absorption in magnetic fields using numerical codes of electromagnetic cascade evolution. An estimated of this cutoff energy is provided by the equation:

$$E_0 \simeq \frac{10\mathrm{GeV}}{B_{12}} \tag{7.9}$$

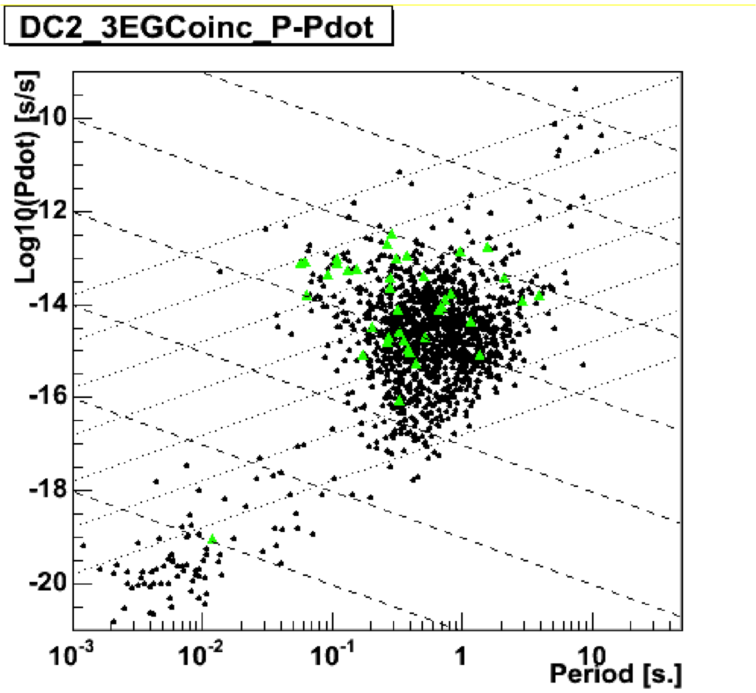

Figure 7.21: The distribution of the pulsars within 3EG error boxes (triangles) in the $P-\dot{P}$ diagram. The black points represent the distribution of the radio pulsars of the ATNF catalog.

where B_{12} is the magnetic field expressed in units of 10^{12} G. The resulting distribution of the 39 pulsars coincident with the 3EG sources is shown in Fig. 7.20 and Fig. 7.21, where the sky map and the $P-\dot{P}$ diagram is used in order to compare these pulsars with the ATNF catalog of radio pulsars [2]. The fluxes have been computed using the extended Slot Gap emission (Muslimov & Harding, 2003) and luminosity of equation 7.1. The lowest flux in this sample of pulsars is of about 1×10^{-8} ph cm^{-2}s^{-1}.

7.7 Summary

In this Chapter the pulsar simulations for LAT Data Challenge 2 have been presented. The pulsar popusation has been simulated using *PulsarSpectrum* and the *Pulsar Simulation Suite* described in Ch. 5.
The DC2 pulsars consisted in a set of pulsar sub-populations, for a total of about 400 pulsars. A component of real pulsars has been included, considering the currently known γ-ray pulsars and some radio-pulsars located within EGRET error boxes.

A component of simulated pulsars according to Slot Gap emission scenario has been also included, as well as a population of millisecond pulsars. The summary table of these pulsars is presented in Tab. 7.2. All these simulated pulsars have been useful for creating a realistic model of the potential γ-ray pulsar population. An additional component of *Radio-quiet* pulsars has been also included for testing blind search algorithms.A sky

[2] $http://www.atnf.csiro.au/research/pulsar/psrcat/$

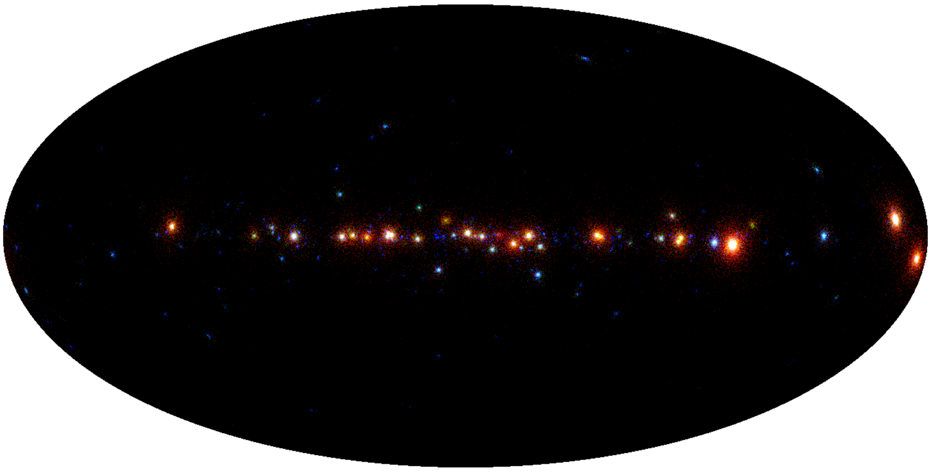

Figure 7.22: A sky map with all the DC2 simulated pulsars

Component	Number of pulsars
EGRET Pulsars	6
3EG Coincident	39
Normal Radio Loud	37
Normal Radio Quiet	103
Millisecond Radio Loud	17
Millisecond Radio Quiet	212

Table 7.2: Summary of the simulated pulsar populations in the DC2

map of all the DC2 pulsar can be seen in Fig. 7.22.
These simulated data have been used by the members of the collaboration for testing the pulsar analysis tools present in the LAT SAE and for deriving some first estimates of the LAT capabilities for studying pulsars. An analysis performed on these DC2 pulsars will be presented in next Chapter.

Chapter 8

Pulsar Analysis in Data Challenge 2

LAT Data Challenge 2 (DC2) has been an unique opportunity for LAT scientists to gain practice with a rich and highly-detailed γ-ray sky with thousands of fixed and variable sources.
The DC2 pulsar population described in previous Chapter acted as an useful tool for studying several aspects of pulsar analysis.
First of all the data generated for the DC2 were useful for testing and studying pulsar analysis tools currently present in the LAT SAE, with the possibility to exercise them in order to find possible bugs and suggest useful upgrades.
The DC2 data also helped as benchmark for new analysis techniques, as some analysis for detecting point sources or for finding pulsars using *blind searches* without knowing ephemerides of the pulsars.
Another very interesting opportunity was the possibility to use these simulated data to derive some first LAT capabilities for detection and study of γ-ray pulsars.
In this Chapter I will present the analysis, the tools and the techniques that I have developed for analyzing the Radio-Loud components of the DC2 pulsars. This analysis has been performed without looking before at the detail of the sky model, in order to be in a more realistic situation without knowing the *DC2 truth*, i.e. the input to the simulations.
During this analysis the blind searches techniques have not been explored, so the Radio-Quiet pulsars have been ignored during the analysis. However, during DC2 other members of the LAT Collaboration studied techniques for blind searches of pulsars (Atwood et al., 2006).

8.1 Automated Analysis Procedure for DC2 pulsars

Thanks to its sensitivity and effective area the GLAST Large Area Telescope is expected to detect many new γ-ray pulsars. As described in Ch. 4 the estimates on the number of detected pulsars varies depending on many parameters, as for example the lightcurve, the duty-cycle or the galactic position.
In addition a critical aspect in such estimates is the assumed emission scenarios. Since Polar Cap models and Outer Gap models show a different cutoff spectrum, the number of detected pulsars will differ significantly, as shown in several studies (Thompson, 2001; Gonthier et al., 2002; Romani & Yadigaroglu, 1995). The number of new discovered

pulsars has been found to range from some tens to some hundreds.
The increased statistics available with the LAT and the much powerful computing power presently available with respect to EGRET poses some interesting challenges in data analysis. In particular an automated processing system for detecting γ-ray pulsars can be developed. The DC2 was a perfect opportunity for designing a similar system and study its performances.
The basic idea of this automated analysis is to look for pulsars with a radio counterparts, using the ephemerides present in the pulsar Database that was released during DC2 in order to look for periodicity.
The automated procedure has been carried with two different situations. The first part of the analysis was devoted to the study of radio pulsars within a γ-ray source detected in the DC2 sky as point source, as for example using the the maximum likelihood. During the DC2 a LAT Catalog of source was released as it will be done after the first year of LAT data taking. This catalog contained all the point sources detected by the various algorithms developed for DC2 and the corresponding estimated position and flux.
The second analysis is a complete scan over all the radio pulsars present in the Database, in order to look if some of them, even though not detected as point sources, can be detected using the timing signature. This was the case of the PSR B1951+32, that was detected with EGRET by folding the γ-rays at the period of the radio pulsar (Ramanamurthy et al., 1995). The analysis can be summarized in the following steps:

8.1.1 Identification of the pulsars

This first step depends whether the radio pulsar have or not a counterpart in the LAT database. In the first case a search was performed in order to find all radio pulsars in the database close to a LAT Catalog source.
Otherwise a list of all radio pulsars in the database was prepared. In both cases a list of pulsar to analyze is provided and the selection of the region of the sky is started.

8.1.2 Selection of the Region of Interest

After a radio pulsar has been found a selection of the region around radio pulsar has been performed in order to maximize the number of photons from the source compared with the background photons. This region will be indicated as *Region Of Interest*(ROI). This task is not trivial since the LAT *Point Spread Function* depend on the energy: At 100 MeV it is about 3°, while it decreases to about 0.1° for energies above 10 GeV.
For EGRET an energy-dependent cut was adopted, since the radius of the Region of Interest (ROI) around the pulsar varied with energy. Such approach should be more efficient but at the DC2 time similar *PSF-dependent* selection were not implemented, then it was decided to apply two sets of cuts depending on energy:

- Radius of ROI fixed to 3° for energies above 100 MeV (*Selection A*);
- Radius of ROI fixed to 0.5° for energies above 1 GeV (*Selection B*);

The *Selection A* is more suitable for detecting pulsar that have a sharp cutoff and/or are fainter, since with this selection a major number of photons is considered. Conversely the *Selection B* is more suitable for pulsars that have a smoother cutoff (e.g. our simulated

MSPs) and/or are brighter. In this case such a selection lower the statistics but does not reduce too much the signal/background ratio.

The results of this trade off between angular resolution and statistics can be seen by

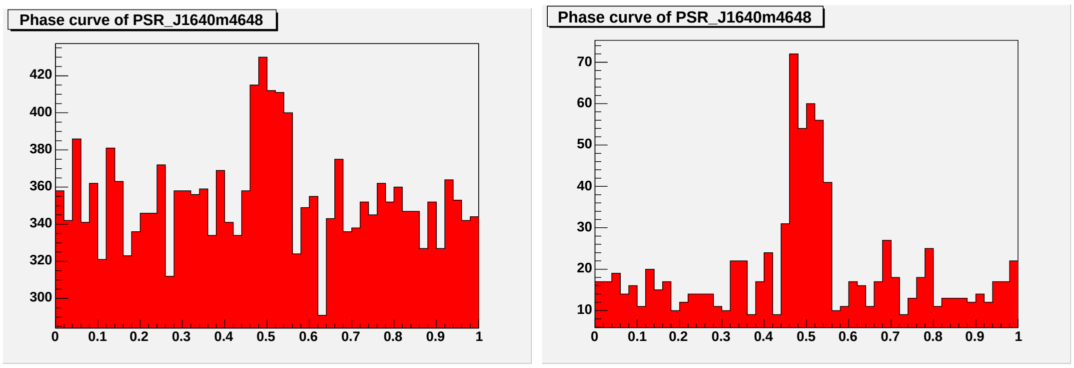

Figure 8.1: Example of DC2 pulsar J1640-4648, that can be detected with both Selection A and B. Left: Selection A (E>100 MeV and r<3°). Right: Selection B (E>1 GeV and r<0.5°).

looking at some examples of reconstructed lightcurves of DC2 pulsars with Selection A or Selection B. For each one of these examples the periodicity has been tested using χ^2-Test and the lightcurve has been built.

Fig. 8.1 show the case of the simulated PSR J1640-4648, a DC2 pulsar with a period of 0.17 s. and located almost on the Galactic plane (galactic latitude b=0.2°). The total flux above 100 MeV is about 10^{-7} ph cm^{-2}s^{-1} and the spectrum has a cutoff energy at about 10 GeV and a spectral index $g \simeq$-1.2. This spectral characteristics made this pulsar detectable with both selections A and B (even if Selection A has more background), and the lightcurve can be distinguished with both Selections.

Fig. 8.2 show the case of the simulated PSR J1741-2019, a DC2 pulsar with a period

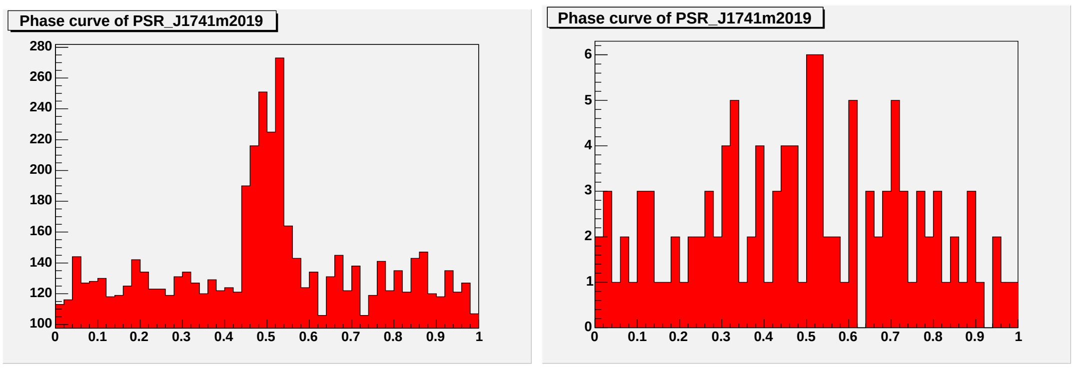

Figure 8.2: Example of DC2 pulsar J1741-2019, that can be detected with Selection A but not by Selection B. Left: Selection A (E>100 MeV and r<3°). Right: Selection B (E>1 GeV and r<0.5°).

of 3.9 s. and located at galactic latitude b=0.2°. The total flux above 100 MeV is about 2.4×10^{-7} ph cm^{-2}s^{-1} and the spectrum has a cutoff energy at about 1 GeV and

a spectral index $g \simeq$-1.1.
We can see that using Selection A the lightcurve is visible and the pulsar is also easily detectable, while with selection B the detection is not possible and the lightcurve it is not clearly visible. This is an example where the diffuse background can deteriorate the observation at high energies, especially for pulsar like this, whose spectrum has a cutoff at few GeV.
Fig. 8.3 show the case of the simulated PSR J1841-0501, a DC2 pulsar with a period

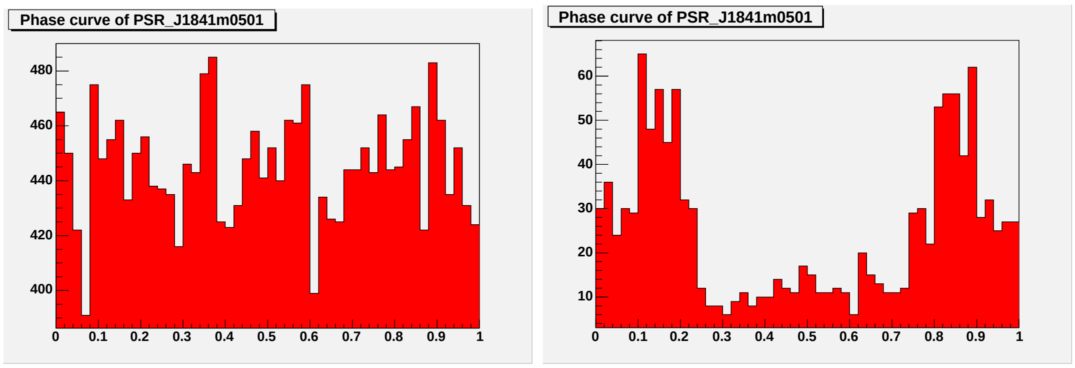

Figure 8.3: Example of DC2 pulsar J1841-0501, that can be detected with Selection B but not with Selection A. Left: Selection A (E>100 MeV and r<3°). Right: Selection B (E>1 GeV and r<0.5°).

of 0.04 s. and located at galactic latitude b=-0.14°. The total flux above 100 MeV is about 4.5×10^{-7} ph cm^{-2}s^{-1} and the spectrum has a cutoff energy at about 33 GeV and a spectral index $g \simeq$-1.48.
We can see that with Selection B the two-peaked lightcurve is clearly visible and the pulsar is also easily detectable, while with Selection A the detection is not possible and the lightcurve cannot be easily distinguished. This is mainly due to the fact that, because of the cutoff at high energy and the spectrum harder than the diffuse background, many high-energy photons are produced. Due to relatively low flux and the position (almost on the Galactic plane), at lower energies the diffuse background exceed the pulsar signal, then Selection A is not very efficient. Selection B select only high energies, where pulsar has more photons than background, then with Selection B the lightcurve is clearly visible.
These examples show how the diffuse background can deteriorate the observation at high energies, especially for pulsars that cut off at few GeV.
This situation is better visible for pulsars near the Galactic plane as most of the DC2 pulsars. For other galactic latitudes other selection cuts can be studied. Indeed this is a first example of a selection strategy that is important to study extensively in order to improve the possibility of detecting pulsars with the LAT.
Other cuts have been implemented by selecting the events by *class*, i.e. selecting those that converted in the front or in the back section of the LAT Tracker, but we ignored such property and select all photons, in order to maximize the statistics of photons.
The analysis has been performed using these two selection methods independently and then compare results at the end of the analysis chain. In this way the detections have been compared in order to see what pulsar has been detected with two cuts and which

pulsar appeared with only one particular cut.

8.1.3 Barycentric corrections

Once the region of the sky is selected, the barycentric corrections have been performed in order to convert the arrival time of the TT to arrival times to the Solar System Barycenter in TDB[1].
In order to do that, the position of the radio source has been used and the orbit file of the DC2, that contains the position of GLAST around Earth during the simulated DC2 period. The details of the barycentering procedure are explained in Ch. 5.

8.1.4 Periodicity Tests

After these preliminary steps performed for each pulsar the next step is the periodicity testing. This phase is critical since it permit to know if the γ-rays coming from the ROI are modulated at the same frequency of the radio source.
Not all radio pulsars have a γ-ray emission or it is too faint, then this test fails to reveal a source. In the DC2 data there is only this second possibility, since we included some pulsars with low fluxes as described in previous Chapter. This low fluxes serve to give an estimate of the lower detectable flux with the LAT.
The periodicity tests available in DC2 analysis are those presented in Ch. 2. For sake of simplicity we perform this first analysis using the χ^2-Test. In following analysis we also used the H-Test in order to reduce the dependence of the method upon the shape of the lightcurve, but in general the results are almost the same.

8.2 Pulsar Detection

For each analyzed pulsar a periodicity test has been performed using the correspondant ephemerides in the pulsar database and the *Chance Probability* P_c is found for every pulsar. This Chance Probability is described in Ch. 2 and means the probability that a non periodic source give by chace a value of the χ^2 statistic greater or equal to the value found in the data.
According to the literature the γ-ray pulsars detected in the EGRET era are 7 *High-Confidence* and three marginal or *Low-Confidence* detections as described in Ch. 4 (Thompson, 2001).
In order to have a kind of rough comparison with the pulsars detected using EGRET we fixed some limits in P_c and define three range of detection:

- *High-Confidence detection* when $P_c < 10^{-9}$, determined from the Chance Probability of PSR B1951+32, the faintest of the EGRET pulsars (Ramanamurthy et al., 1995);

- *Low-Confidence detection* when $10^{-9} < P_c < 2\times10^{-3}$, determined from the Chance Probability of PSR B0656+14 (Ramanamurthy et al., 1996);

[1]For definition of TT and TDB refer to Ch. 5

- *No detection* when $P_c > 2 \times 10^{-3}$;

According to these values each pulsar is classified and then the general properties of the detected pulsars are studied, as the distributions together with the lower flux and other important characteristics.

8.3 The *pyPulsar* Analysis Package

The implementation of the analysis procedure described in Sec. 8.1 has been developed using three main tools.
The first one is the LAT pulsar analysis tools present in the SAE, since one of the goal of this analysis is to test the possible use of these tools in an automatic approach.
The second tool used in this analysis is the *Python* scripting language [2] that has revealed to be very useful for managing long analysis because of it flexibility.
Automated analysis can also be carried out with several other scripting languages, as the classic *bash* or *tcsh* Linux shell. Instead of those Python language has been preferred since many operations are fairly simple, as the parsing operations on ASCII files. For this reasons the manipulation of long lists of output results from analysis is very simple. In particular Python has many extensions to the most common software package, including an extension to manage FITS files called *pyFits*[3] and an extension to the classes of the ROOT framework called pyROOT[4].
We collect these useful software in a collection of classes and scripts called *pyPulsar* that will be described in the following.
A basic scheme of *pyPulsar* is shown in Fig. 8.4. The basic component is a set of classes interfacing with the *Science Tools*. These classes, as for example *pyGtbary.py*, contain methods for setting parameters and running the correspondant tool in the SAE. All these classes are linked to a main class called *pyPulsar.py* that contains all the relevant parameters of each pulsar together with the methods to do specific operations on it (selection, barycentering, phase assignment, etc..). For each pulsar under analysis an object of *pyPulsar.py* class is created.
The *pyPulsar.py* class uses pyFits for managing I/O on FITS files and pyROOT for plotting output, as for example the lightcurve or the skymap relative to a specific pulsar under analysis.
Because *pyPulsar.py* is implemented and all the classes corresponding to the pulsar SAE tools are also available, the analysis can be carried on simply creating some scripts that perform in sequence the steps described in the previous Section. In particular the output files can be filtered in order to group the pulsars with same characteristics, e.g the *High-Confidence* pulsars.
All the procedure has been tested on a desktop computer and also using the SLAC computing farm[5]. In this second case two approach have been followed. A *serial* analysis, where all pulsars were analyzed in sequence, and a *parallel* analysis, where each single-pulsar analysis was sent to an independent batch jobs on the SLAC computing farm and then the final results were collected in a final report.

[2] $http://www.python.org$
[3] See: $http://www.stsci.edu/resources/software_hardware/pyfits$
[4] See $http://wlav.web.cern.ch/wlav/pyroot/$
[5] See $http://www.slac.stanford.edu/comp/unix/unix-hpc.html$

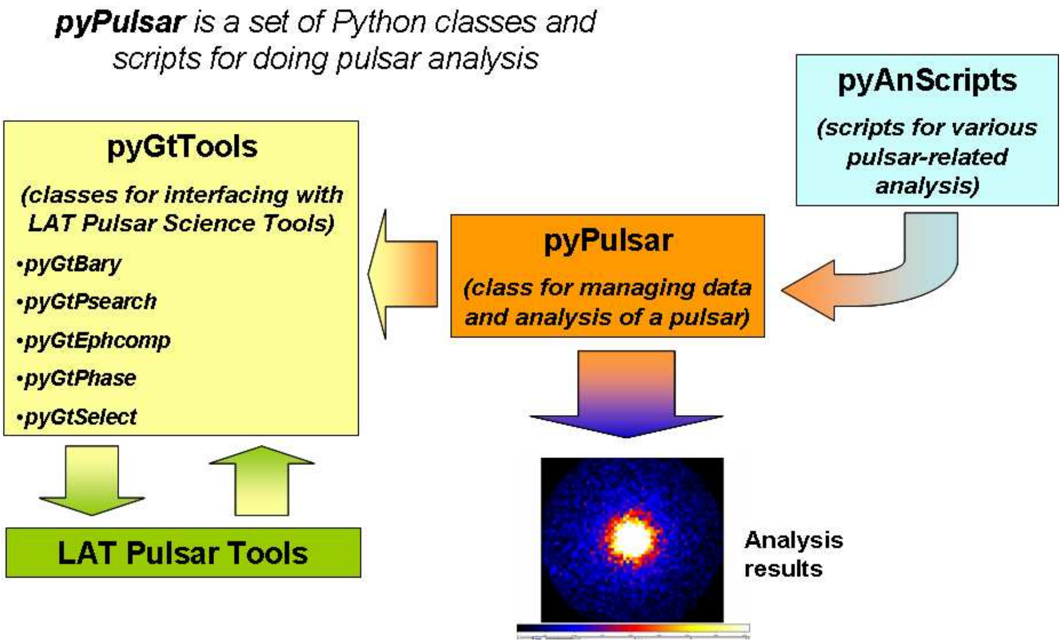

Figure 8.4: A scheme of the *pyPulsar* automated Python-based automated pulsar analysis

8.4 Analysis of pulsars detected as point sources

During the first part of the analysis we are interested to study the detection of pulsars that have been also detected as point sources using the source detection algorithms, e.g the *maximum likelihood*.
As a product of such algorithms is a source catalog called LAT Source Catalog that contains list of point sources detected and their properties, e.g. estimated position, flux, etc. This DC2 LAT Source Catalog is a prototype of the real LAT Catalog of the sources that will be detected during the mission.
This is an important situation, since the brightest pulsars will be hopefully the firsts to be detected by looking at the photons coming from the point source that lie nearby a known radio pulsar.

8.4.1 Finding the counterparts

In DC2 sky there was a set of radio pulsars that represent a realistic population of radio pulsars in the sky, some of them have a γ-ray detectable emission. In order to determine which γ-ray source can be detected as pulsar using the radio ephemerides the first step to perform is a search for coincidences between the LAT Source Catalog and the radio pulsars contained in the official pulsar database of DC2.
In order to do that a Python script has been created, that searched if a radio pulsar in the DC2 pulsar database was within the localization error box of a LAT Catalog source. In LAT Catalog a localization error box was associated to each source detected as a point source. In the LAT Catalog provided during the DC2 to each LAT source there was an associated localization error box, meaning the radius of 95% confidence

limit obtained using maximum likelihood. The error box depend on the energy band where the highest confidence detection occurred. Four energy bands with the associated localizarion errors were used: 1) 2.2° for 100 MeV <E<300 MeV; 2) 0.95° for 300 MeV <E<1 GeV; 3) 0.38° for 1 GeV <E<3 GeV, and 4) 0.17° for E> GeV. Using this method

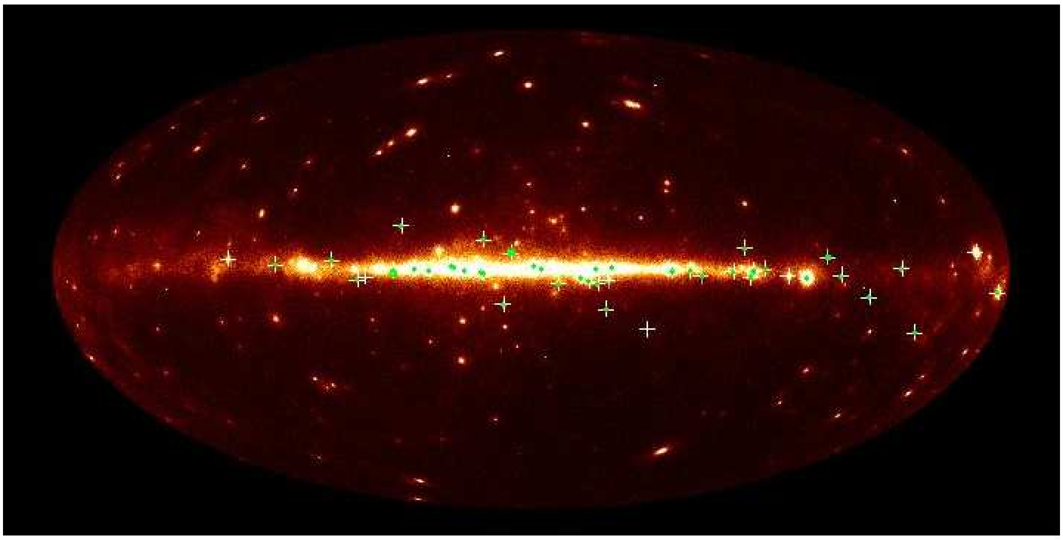

Figure 8.5: The coincidences between simulated radio pulsars in DC2 (crosses) and γ-ray point sources (circles) detected in the LAT Catalog

a sample of 49 radio pulsars were found to be concident to sources in the LAT Catalog as shown in Fig. 8.5. The ephemerides of these radio pulsars have been then used to apply periodicity test and look for pulsed emission.

8.4.2 Results

After running the automatic analysis procedure to these pulsars selecting photons above 100 MeV and with a radius of 3 degrees around radio pulsar positions, turned out that 22 pulsars were detected as high-confidence and 14 as low-confidence detections.
The spatial distribution of these pulsars is shown in Fig. 8.6 compared with pulsars in ATNF Catalog, where it can be seen that most of them lie on the Galactic Plane.

By looking at the P-$\dot{P}$ diagram of Fig. 8.7 some interesting information can be derived for the detected pulsars. Using the characteristic age and surface magnetic field estimated as in Chap. 3 we can see that the yougest pulsars detected are Vela and Crab, with ages of about 10^3 yr and magnetic fields that can be estimated as $B_S \approx 10^{11}$ G. This is not surprising since Vela and Crab are the brightest γ-ray pulsars in the sky so we expect to detect them easily.

Another interesting issue is the detection of 5 MSPs, four of them with high-confidence level. These MSPs appear to be older ($\tau_c \approx 10^8$ yr) and have low magnetic fields ($B_S < 10^9$ G). These characteristics are in agreement with the original values used for simulations, showing that at least an order-of-magnitude estimate on pulsar parameters can be done from this diagram. Pulsars with a γ-ray emission detected as a point sources allow the possibility to study the flux distribution, where the flux is the one estimated

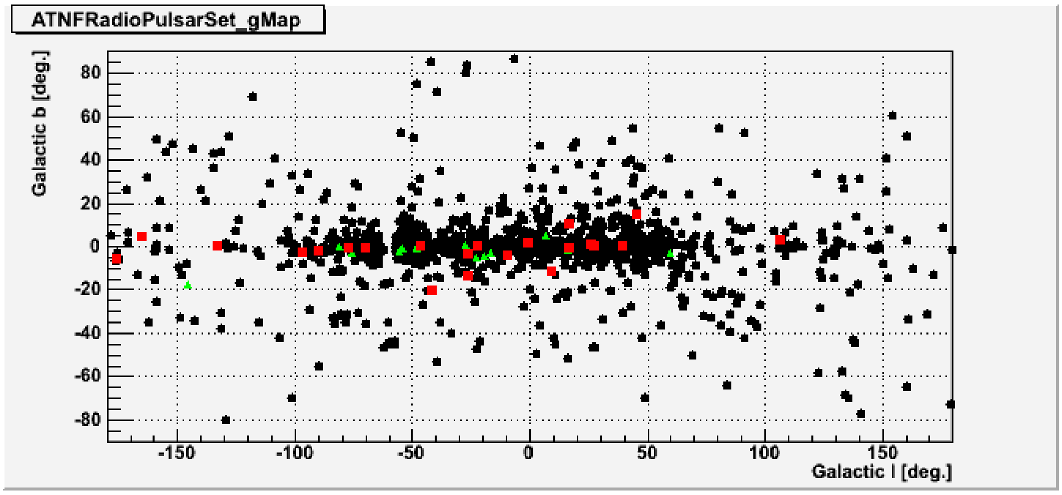

Figure 8.6: Skymap showing the pulsars detected in the DC2 LAT Catalog with High-Confidence (squares) and Low-Confidence (triangles). The pulsars present in the ATNF Catalog (May 2006) are also shown for comparison.

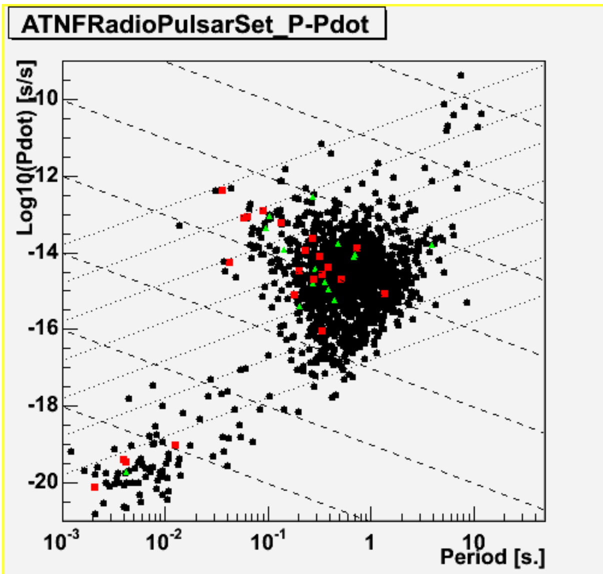

Figure 8.7: The P-$\dot{P}$ Diagram for pulsars detected in the DC2 LAT Catalog with High-Confidence (squares) and Low-Confidence (triangles).The pulsars present in the ATNF Catalog (May 2006) are also shown for comparison.

using maximum likelihood algorithm.
The flux distribution is presented in Fig. 8.8. From such a distribution we can see that in the DC2 observing time the lowest detected flux is of the order of log(F)≈-7.5 for high-confidence detections and log(F)≈-8 for low-confidence detections. Of course these have to be considered as crude estimates, but at the same time they provide a good way to determine an estimate on the flux limit for pulsed emission.
With a similar strategy it important to build a log(N)-log(S) diagram, that show a

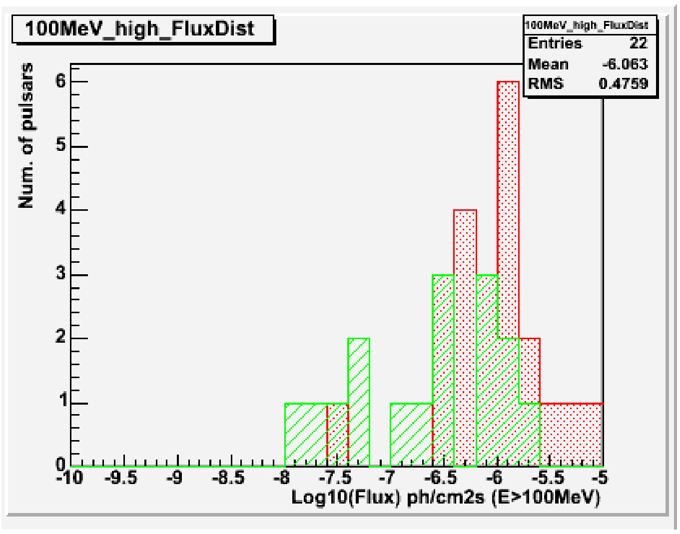

Figure 8.8: Flu distribution for pulsars detected in the DC2 LAT Catalog with High-Confidence (dot-shaded) and Low-Confidence (line-shaded)

change of slope that we can interpret as due to the LAT sensitivity. In the Fig. 8.9 this cumulative distribution has been obtained collecting the information of all pulsars detected both High-Confidence detection and Low-Confidence detection.

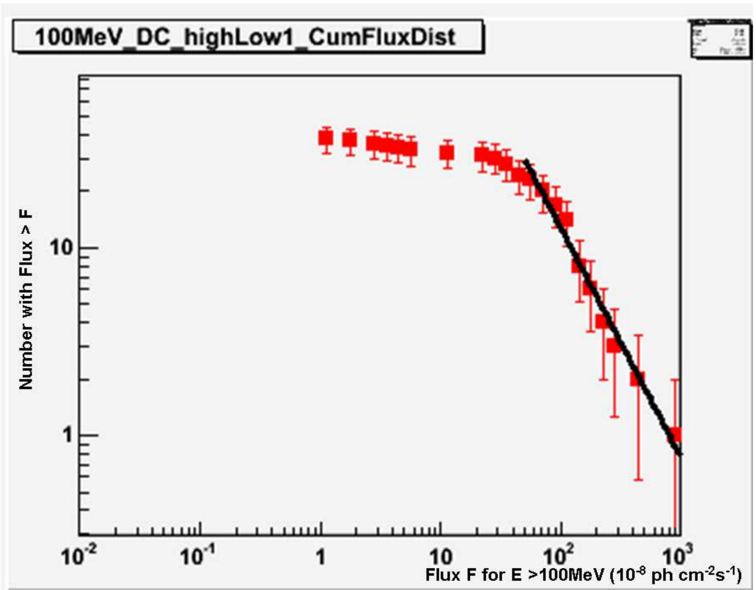

Figure 8.9: The logN-logS distribution for pulsars detected in the DC2 LAT Catalog with both High Confidence and Low-Confidence detections. The change of slope is visible, that can be interpreted as due to the limit of the LAT sensitivity.

8.5 Beyond the LAT Source Catalog

The study of periodicity of sources detected from Maximum Likelihood Analysis is of particular importance for estimating the fluxes that LAT can reach for pulsed emission. Using the simple Chi-Square periodicity test it has been shown that fluxes as low as 10^{-8} ph cm^{-2}s^{-1} could be detected in about 55 days. The information about timing

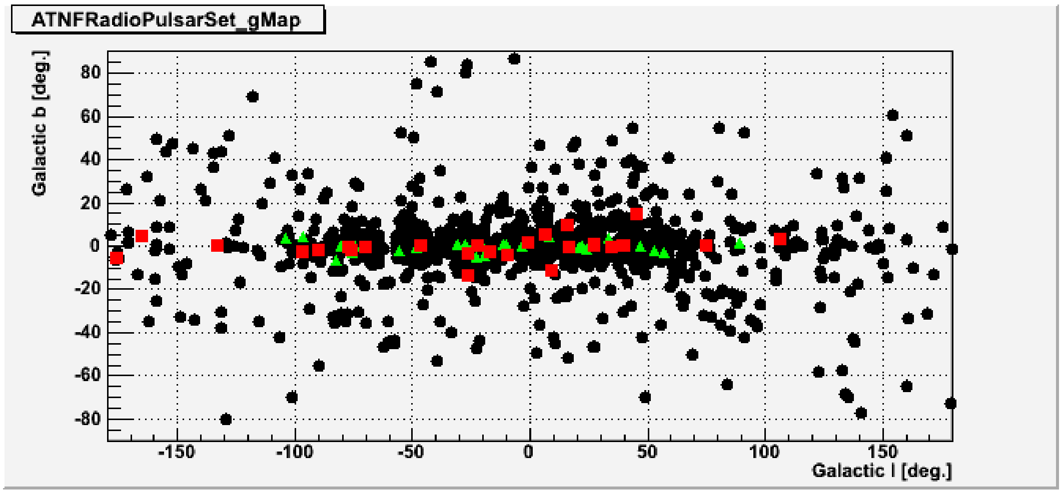

Figure 8.10: Skymap showing the pulsars detected from the scan of the whole LAT DC2 database. In this case the selected photons have energies greater than 100 MeV and are within 3° from the radio source. High-Confidence pulsars are indicated by squares and Low-Confidence pulsars by triangles. The pulsars present in the ATNF Catalog (May 2006) are also shown for comparison.

that is available from the database of the radio pulsars simulated for DC2 provide the possibility to see if some radio pulsar is also emitting γ-rays, by looking at the periodicity of the photons coming from a region within the radio source position. With a similar approach the periodicity is searched even if there is no clear evidence for γ-ray point source emission.
Historically this approach has been successfully during the EGRET era, since the γ-ray emission from PSR B1951+32 has been discovered by looking if photons coming from the region around the radio pulsar were periodic. Using periodicity testing techniques it has been found that PSR B1951+32 was also a γ-ray pulsar (Ramanamurthy et al., 1995). In this second part of the analysis a scan is performed on the whole sample of pulsars in the DC2 pulsar database and for each radio pulsar a cut is performed around radio pulsar and periodicity is tested. For DC2 the pulsar database contain 98 radio pulsars, while the real LAT pulsar database will contain several hundreds of radio pulsars according to the LAT timing program that is going to be established. As a comparison we should remember that during the CGRO mission the pulsar database of monitored pulsars contained about 500 pulsars.
The scan over the DC2 pulsar database has been repeated with two different sets of energy and angular selections as explained in the beginning of this Chapter.
A first analysis has been performed by selecting photons above 100 MeV and within a radius of 3° around the radio counterpart (*Selection A*). The second analysis has been

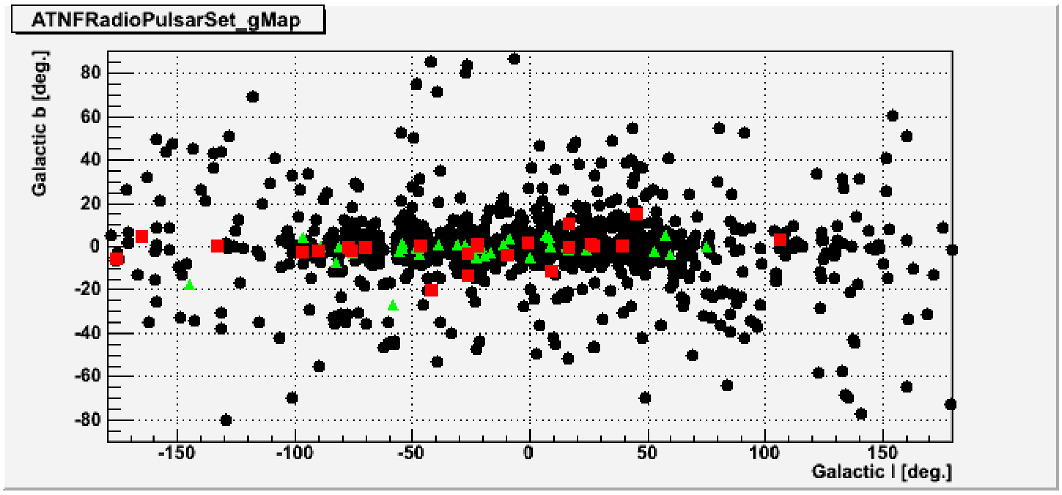

Figure 8.11: Skymap showing the pulsars detected from the scan of the whole LAT DC2 database. In this case the selected photons have energies greater than 1 GeV and are within 1° from the radio source. High-Confidence pulsars are indicated by squares and Low-Confidence pulsars by triangles. The pulsars present in the ATNF Catalog (May 2006) are also shown for comparison.

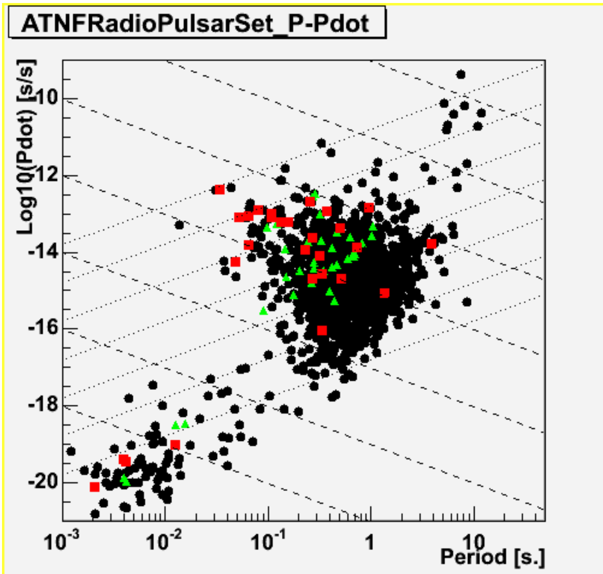

Figure 8.12: The P-$\dot{P}$ Diagram for pulsars detected from the scan of the DC2 pulsar database.In this case the selected photons have energies greater than 100 MeV and are within 3° from the radio source. High Confidence detections are indicated by squares and Low-Confidence pulsars by Triangles

performed selecting photons above 1 GeV and within a radius of 1° (*Selection B*).
The skymaps of the detected pulsars using these two cuts are shown in Fig. 8.10 and Fig. 8.11.
The application of the first selection lead to 29 High-Confidence detections and 26

Low-Confidence detections, while the selection of photons above 1 GeV lead to 25 High-Confidence detections and 34 Low-Confidence detections.
The difference between the number of pulsar detected using the two selection methods depends from the spectrum of pulsars and from a selection effect due to flux. Selecting photons above 1 GeV few photons are considered then only the brightest pulsars should be detectable.
At the same time for E greater than 1 GeV the MSP are favoured since their spectrum is harder than pure Slot Gap pulsars presented in previous Chapter. In this way there is a major number of photons above 1 GeV where the PSF is better and then the signal to background is increased.
This can also be seen by looking at the P-$\dot{P}$ diagram for these two cases as shown in Fig. 8.12 and Fig. 8.13 with a comparison the pulsars in ATNF catalog.
This is also confimed by looking at the P-$\dot{P}$ diagram. Pulsars detected using photons above 1 GeV show that there is a greater number of MSP detected with respect to the MSP detected selecting photons above 100 MeV. At the same time the fainter pulsars that were detected above 100 MeV disappear when analyzed using photons above 1 GeV because of the lower statistics.

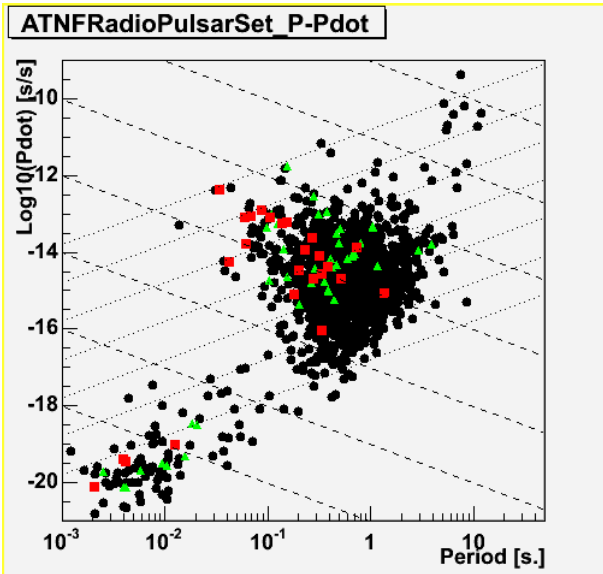

Figure 8.13: The P-$\dot{P}$ Diagram for pulsars detected from the scan of the DC2 pulsar database.In this case the selected photons have energies greater than 1 GeV and are within 1° from the radio source. High Confidence detections are indicated by squares and Low-Confidence pulsars by Triangles

8.6 Comparing the results

Using the information of the two selections it is interesting to merge the results in order to obtain a more general summary of detectable pulsars. The partial and total results are shown in Table 8.1.

Using these data it is possible to see that a total of 32 High-Confidence detections

	Selection A	Selection B	Merged	1 year extrapolation
No Detections	42	38	14	34
Low-Confidence	26	34	51	125
High-Confidence	29	25	32	78

Table 8.1: Summary of pulsar analysis from scanning the whole DC2 pulsar database. The extrapolation of 1 year has been also computed

could be expected using both these two selection methods. Since the number of High-Confidence detection derived looking only at the LAT Catalog of point sources is 22 we can expect that the direct testing of periodicity directly looking at the pulsar database coult be a good technique for discovering new pulsars.
A rough estimate could be obtained by simply extrapolating the number of pulsars detections to 1 year. The number of expected detection scales as the ratio of the root squares of the observing time, since the exposure is almost uniform for such long observation times.
In this way it is possible to estimate that the number of High-Confidence detections is of about 78 and 125 Low-Confidence detections for 1 year of LAT observation in scanning mode. This is in agreement with the estimates found is some studies like (Gonthier et al., 2002). This is to be entirely expected, since most of the DC2 pulsar simulations are based on a very similar model. Indeed this result turns out to be very helpful to test consistency for simulation chain.

8.7 Perspectives for an optimized analysis

The results shown here are useful for presenting possible strategy for an automated processing of pulsar data using LAT data. Of course there are a lot of major issues that can be refined in order to improve the performances of this algorithm.
A first improvement comes from the use of multiple statistical tests for periodicity search. For example after DC2 also the Z^2_n and H-test presented in Chap. 2 have been included. In this way also a comparison can be made among the different detection strategy.
In this analysis it has also became clear that the selection on energy and radius around the radio pulsar position is important for discovering new pulsars. In order to discover what kind of selection in energy and angle is optimal an upgrade to this procedure has been developed. A scan over different couples of energy and radii of the ROI is performed, in order to understand which cut minimize the Chance Probability.
This solution is much complex since includes much more trials over minimum energy and radius but it should be possible to finally implement using a parallel computing farm. Another interesting possibility is to use an energy-dependent cuts as done for EGRET data.

8.8 Summary

In this Chapter an analysis of the DC2 pulsars has been presented. This analysis had two main goals.

The first is to show that the SAE pulsar tools can be interfaced and run automatically using an opportune infrastructre based in scripting language. In this case the Python scripting language is being used but similar approach using other scripts, e.g. bash shell, have been developed. Python has the main advantage to be much more flexible, then many operations can be much simplified.
The idea of this analysis is not to be focused on single sources, since almost all pulsars comes from simulations and does not correspond to reality. For example the great part of them is at simulated location in the sky. However, useful information that can be obtained from such an analysis is the LAT capability to study the general population of the detected pulsars, without taking care of the single sources. With this approach very useful information can be obtained, e.g. the minimum detectable flux and the estimated number of detection in 1 year.
As it has been shown in this Chapter this *Population point-of-view* can be very useful and effective and thanks to the computing resources presently available is very simple to implement an automatic system of analysis like the one presented here.
In this way the enourmous discovery potential of the LAT for pulsars could be gratly enhanced.

Chapter 9

Polar Cap or Outer Gap: what can GLAST say?

GLAST is expected to increase our knowledge about pulsar physics by investigating γ-ray emission.According to current data and to LAT performances it is possible to give estimates on its capabilities for studying pulsars and discover new ones.
Simulations are an optimal way to know how the instrument behaves and how well it can reconstruct the photon distribution in time, energy and space from a specific sources.
In previous chapters pulsar simulations developed for GLAST have been described. These include the *PulsarSpectrum* simulator as well as simulation models that are suitable for studying LAT performances and for testing LAT pulsar analysis tools.
Here I will show how simulations can be used for studying a specific problem regarding pulsar physics at high-energies. One of the most interesting topic that GLAST will investigate is the capability to constrain emission models and in particular to distinguish between the two main emission scenarios, the Polar Cap and Outer Gap emission model.
In order to do this study the *PulsarSpectrum* simulator has been used and particular simulations have been created in order to implement two of the current theoretical models for pulsar emission.
These simulations have been very useful to give a more accurate answer to the question wheter GLAST will be able to distinguish what emission model is involved in high-energy emission for a particular pulsar. Not only the effective capability has been shown, but also some estimate on the required observation time for distinguish between these models have been calculatd.
In order to restrict the space of free parametesr for such a study, I assumed to study the case of Vela pulsar for two main reasons. First it is the better model since it is the pulsar with better statistics in term of photons. Second, because of it brightness, it will be the first pulsar to have enough statistics to allow a good constraint on the theoretical models. Similar study can be performed for other pulsars, but Vela is the best candidate for showing if GLAST will be able to distinguish between Polar Cap and Outer Gap.

9.1 Background

The current models for γ-ray emission from pulsars are divided in two main classes, as described in Ch. 4. These two models are based on different places where emission take

place.
Polar Cap models are based on the assumption that high-energy γ-ray emission take place within a few stellar radii of the neutron star in the vicinity of the neutron star polar caps.(Sturrock, 1971; Ruderman & Sutherland, 1975; Harding, 1981).
In Outer Gap models the emission comes from charged particles that are accelerated in regions at large distance from the neutron star at high altitudes in the magnetosphere, in vacuum gaps formed within a charge-separated plasma (Cheng et al., 1986a; Romani & Yadigaroglu, 1995; Romani, 1996).
A key point is that these models cannot be distinguished using EGRET data but they provided very different predictions for γ-ray emission in the LAT energy range, so GLAST is expected to discriminate between models.
There are at least three main item where Polar Cap models and Outer Gap models make different predictions (Harding, 2001).
As described in Ch. 4 the models can be distinguished by looking at high-energy cutoff, at luminosities and at population statistics. The easiest and more direct way is the first one, that will be discussed in this work.
Polar Cap models predict a sharp spectral cutoff due to pair production in high magnetic fields, while Outer Gap predict softer exponential spectral cutoff since emitting particles are radiation-limited, i.e the rate of energy gain by acceleration is the same that the energy loss by emission.
Thanks to its high effective area and high energy resolution LAT will provide enough statistics in the multi-GeV energy range to provide the possibility to distinguish among the two spectral cutoffs.
Two examples of models among Polar Cap and Outer Gap scenario have been selected and used for this study. Altough presently many variations exists in the two categories, we chose these because they contain the basic features of the high-energy cutoff. At the end of the Chapter we will discuss how other most recent models change with respect to these here but we will see that the basic features of the cutoff - super exponential for Polar Cap and exponential for Outer Gap - are mantained also in most recent models.
The study of the cutoff for distinguishing models is a definitive LAT capability to distinguish an exponential cutoff from a super exponential cutoff.
The Polar Cap model that we decided to use for simulation is the one presented by Daugherty and Harding in 1996 (Daugherty & Harding, 1996). The assumptions are:
First of all 1) emission is assumed to be initiated by accelerated electrons above the polar caps that enclose all open magnetic field lines. 2) primary electrons emit curvature radiation on curved magnetic field lines and 3) the process of direct 1-γ pair conversion in magnetic field and synchrotron radiation from the produced pairs initiate an electromagnetic cascade (Meszaros, 1992).
These first three assumptions are common to the original Polar Cap scheme proposed by Sturrock (Sturrock, 1971). The model used in this study also assumed 4)small inclination angle but not necessary aligned or quasi-aligned rotator.
Finally 5) the acceleration of the primary electrons take place over an extended distance above Polar Cap. This assumption has been introduced in order to avoid what has been called the *observability problem*. A reduced acceleration distance produced γ-rays that have energies too small to be in agreement with what is observed for γ-ray pulsars. The acceleration region extend up to few stellar radii above neutron star. Among the various

parameterization used in (Daugherty & Harding, 1996) we choose the set of parameters that they labeled with the letter D, since this is the one that better match observations. The chosen Outer Gap model is the one presented by Romani in 1996 (Romani, 1996) that extended a previous work (Romani & Yadigaroglu, 1995) where γ-ray emission beaming was presented and also statistics on population of Radio Loud and Radio Quiet were presented.
Since this model had difficulties in producing spectral index variation with phase as observed for Vela and Crab the model was extended and further study on the outer magnetosphere was presented.
This model investigate with more detail the physics at the gap and the radiation mechanisms that play a dominant role, i.e. the importance ot synchrotron radiation.
The loss of energy by radiation is then balanced by the acceleration that take place in the gap then the resulting spectrum is radiation-limited and the γ-ray spectrum is expected to show an exponential cutoff.
Both models make predictions on the variation of spectrum with phase but for our purpose we are interested in the total flux since we want to have an estimate on the LAT capability of distinguish between them and the timescales where this can be achieved.
In order to do this we prepares a simulated model of Vela pulsar using as input the phase-averaged spectra for Polar Cap model and Outer Gap model. Then we fold them into the LAT response function in order to have a set of detected photons that will be used for the analysis.

9.2 Simulations and Data Analysis

We chose to study GLAST LAT observation of the Vela pulsar, since it is the brightest among γ-ray pulsars, thus it will provide in shorter observation time a number of photons big enough to study the High-Energy cutoff.
The simulations that we prepared have been created using *PulsarSpectrum* , that has been described in detail in Ch. 5 (Razzano, 2007).
Once the model for Vela has been created photons are then extracted according to source flux and they are folded through the LAT Instrument Response Functions using *Observation Simulator* (gtobssim), a fast MC simulator of the LAT included in the SAE (See Ch. 2).
Two simulation model for Vela have been prepared: a) a Polar Cap model based on the model of Daugherty and Harding (Daugherty & Harding, 1996) and b) an Outer Gap model based on work of Romani (Romani, 1996). For our purposes we are interested in studying the phase-averaged total spectrum of Vela pulsar. We assumed a lightcurve based on EGRET data (Kanbach et al., 1994).
The resulting spectra build using Polar Cap model[1] of (Daugherty & Harding, 1996) is displayed in Fig. 9.1.
The resulting spectrum built using Outer Gap model[2] of (Romani, 1996) is displayed in Fig. 9.2. No additional normalization have been applied to the histogram used for

[1] I would like to thank Alice K. Harding for kindly providing me the data relative to Polar Cap model in (Daugherty & Harding, 1996)

[2] I would like to thank Roger W. Romani for kindly providing me the data relative to the Outer Gap model in (Romani, 1996).

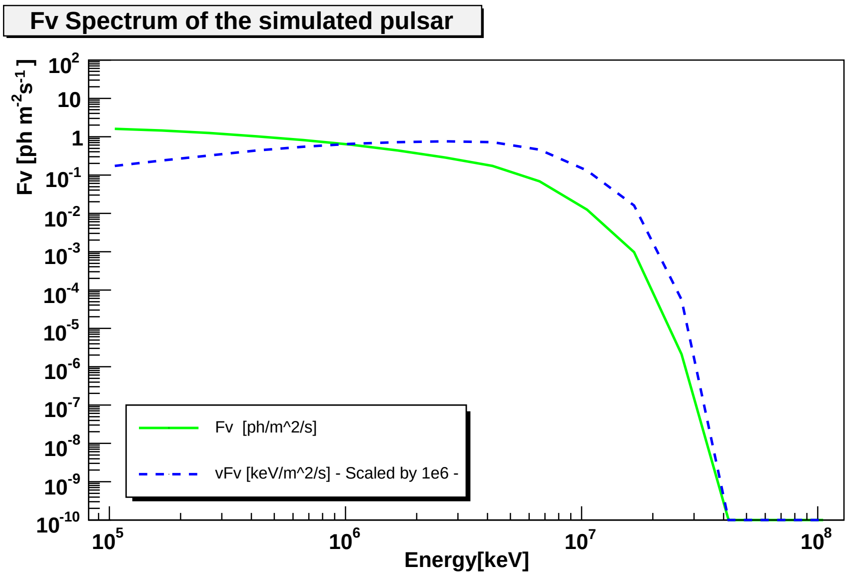

Figure 9.1: Spectrum of simulated Vela pulsar using phase-averaged total flux in Polar Cap scenario from (Daugherty & Harding, 1996).

the model. A period of 89 ms and a period first derivative of 10^{-15} s/s has been assigned

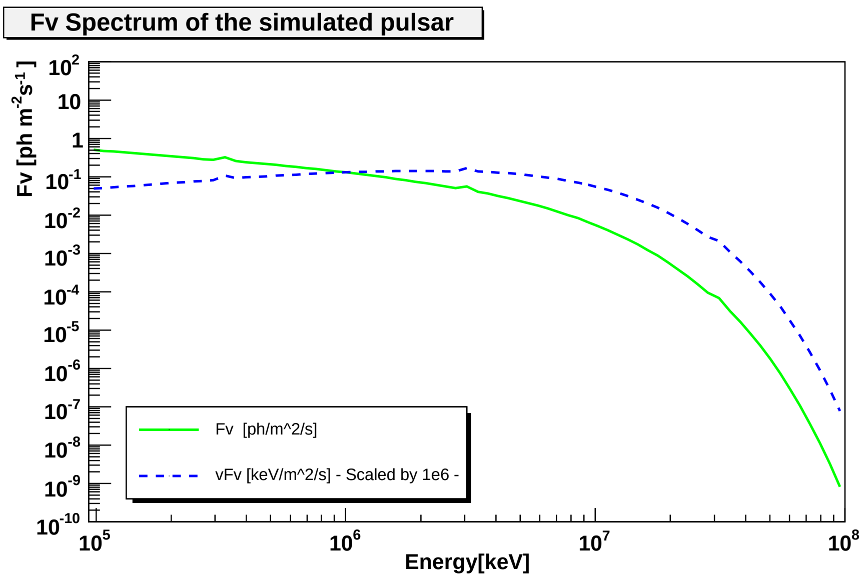

Figure 9.2: Spectrum of simulated Vela pulsar using phase-averaged total flux in Outer Gap scenario from (Romani, 1996). The three small spikes in the spectral curve are due to numerical approximation.

to the simulated Vela. Vela pulsar has a $\dot{P}$ of 1.2×10^{-13}s/s, but since we are interested to spectrum this will make no difference. Since we are interested in spectral study, we can relax the details of the timing simulation then we choose a period and period first derivative not too much precise.

An important aspect of the simulation has been the position of Vela pulsar in the sky. The location is important for detailed simulation since the view angle of observation of the LAT depends on the position of the source in the sky. Instead of doing two separate simulations, we decide to displace a little the simulated Vela from the real position in the sky, placing both simulated sources at simmetric position with respect to the original position of Vela. The simulated model of Vela with Polar Cap spectrum, that we will refer hereafter as *VelaPC*, has been placed at (α_{PC}=127.17°, δ_{PC}=-43.56°). The other simulated pulsar, that we will call *VelaOG*, has been placed at (α_{OG}=136.61°, δ_{OG}=-43.16°).
The simulation of the observation has been chosen to be using the LAT in scanning mode, that will be the normal operational mode of GLAST. We choose a rocking angle of 30°, that is very similar to the angle that will be established for the orbital mode of the satellite.
A complete simulation of 1 year of observation has been performed and the resulting high-level data stored as FITS files have been used for extracting data also for shorter observation times.
Vela pulsar is very bright object then we study the possibility to include the background and its influence. The diffuse γ-ray background can be modeled using two components: a Galactic diffuse component and an Extragalactic diffuse component. The Galactic diffuse emission is mainly due to interaction between cosmic rays and interstellar medium and has a distribution concentrated in the Galactic plane. The extragalactic component has a quite isotropic distribution and probably it is mainly due to the emission of faint unresolved extragalactic blazars.
We used simulations to study the number of photons detected by the LAT around the position of the simulated sources and we used it to estimated the Signal to Noise ratio. The Galactic diffuse emission intensity has been simulated using an emission model developed by the LAT Collaboration and based on GALPROP (Strong & Moskalenko, 1998; Strong et al., 2004). The spectrum of the galactic diffuse background is fairly complex since it is the result of several processes, including pion decay, bremsstrahlung and Compton scattering. The simulation uses intensities maps at 17 energies ($\sim$ factor of 2 from 10 MeV to about 655 GeV), that are generated by GALPROP considering pion decay, Inverse Compton scattering and Bremsstrahlung. The total flux between 10 MeV and about 655 GeV is of about 10.58 ph m^{-2} s^{-1}.
The extragalactic diffuse emission has been modeled as a power-law with spectral index of 2.1 and a total flux of F_{extr}=10.7 $ph\ m^{-2}s^{-1}$ between 20 MeV and 200 GeV.
We can write the signal to noise ratio is function of the observation time t_{obs}:

$$\frac{S}{N}(t_{obs}) = \frac{st_{obs}}{\sqrt{b_{gal}\Delta\Omega t_{obs} + b_{extr}\Delta\Omega t_{obs} + st_{obs}}} \tag{9.1}$$

Where s is the rate of photons from Vela, b_{gal} is the rate of photons per solid angle of the Galactic diffuse emission, b_{extr} is the rate of detected photons per solid angle of the extragalactic diffuse emission. Since we selected photons coming from a region within 3° from the simulated sources, $\Delta\Omega$ is the correspondant the solid angle of the selected sky region.
Since diffuse emission would have been different at the two locations of pulsar VelaPC and VelaOG, we used simulations to evaluate how many background photons are in

t_{obs}(days)	N_{gal}	N_{extr}	b_{bg_tot}	N_{VelaPC}	S/N
1	60	5	65	411	18.84
7	420	35	455	2957	50.62
30	1800	150	1950	15425	117.02
90	5400	450	5850	39280	184.90
180	10800	900	11700	75578	255.83
365	21900	1825	23725	152983	363.93

Table 9.1: Evaluation of Signal to Noise ratio for Vela Polar Cap. The background photon number N_{gal},N_{extr} and their total N_{gal} are evaluated on the basis of a single-day background simulation. The number of photons from the source comes directly from the simulation.

t_{obs}(days)	N_{gal}	N_{extr}	b_{bg_tot}	N_{VelaPC}	S/N
1	56	5	61	456	20.05
7	392	35	427	3200	53.13
30	1680	150	1830	16249	120.85
90	5040	450	5490	41017	190.20
180	10080	900	10980	79453	264.21
365	20440	1825	22265	160854	375.89

Table 9.2: Evaluation of Signal to Noise ratio for Vela Outer Gap. The background photon number N_{gal},N_{extr} and their total N_{gal} are evaluated on the basis of a single-day background simulation. The number of photons from the source comes directly from the simulation.

these region. We compute background for one day. Since GLAST orbital period, this means that in one day there is about 15 orbits, that guarantee an uniform exposure over the entire sky, then a simulation of 1 day give an good average of detected photons from the background.

We evaluate the signal to noise ratio for different observation timescales and the results are reported in Tab. 9.1 and for Outer Gap in Tab. 9.2.

The various signal to noise ratios for both models are also displayed in Fig. 9.3. It is clear that already for 1 day the signal to noise ratio is about 20 and it is increasing with time, so we assume that we can neglect the background in our simulations.

We then prooceed to simulated only VelaPC and VelaOG for 1 year of simulated LAT observation with GLAST orbiting in scanning mode.

In order to evaluate the capability to measure spectrum of simulated sources with time the original 1-year simulation has been divided into smaller pieces, in order to obtain smaller observations, with respective lengths of 1 day, 1 week, 1 month, 3 months, 6 months and the original 1 year long observation.

The selection of region of the sky is very important since with real data it is important to reduce diffuse emission and pollution from other sources. Since LAT *Point Spread Function* (PSF) is energy-dependent, it should be very useful to apply an energy-dependent selection on the acceptance angle.

Since Vela is very bright we found that an energy-independent acceptance radius can be also used. The LAT PSF at 100 MeV is little more than 3° and then we choose a selection angle of exactly 3°, that means that all photons within this angular distance

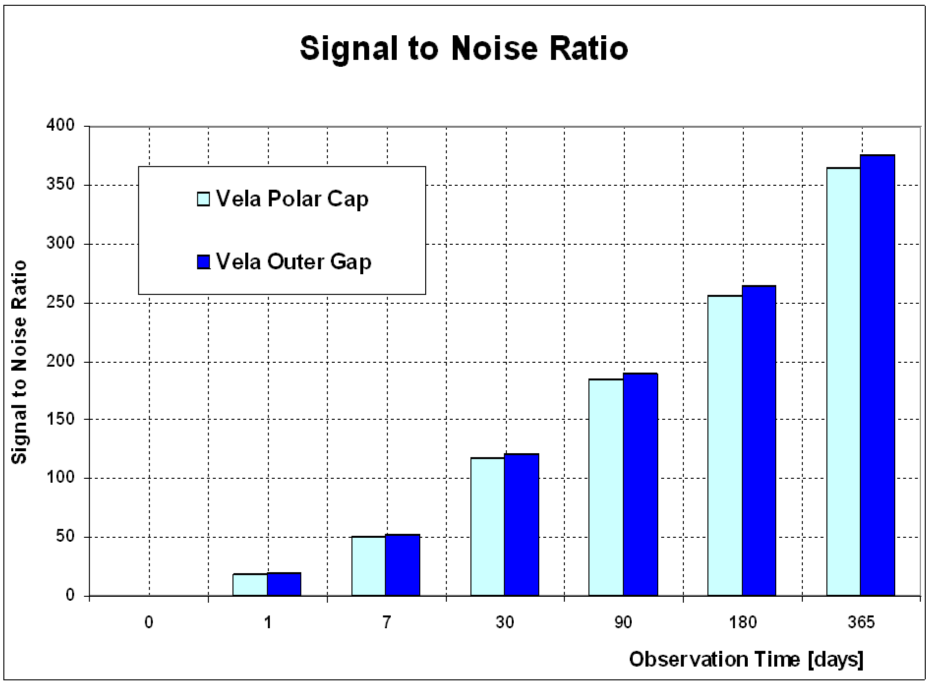

Figure 9.3: Signal to noise for both Vela Polar Cap and Vela Outer Gap for different observation times t_{obs} with LAT operating in scanning mode.

from the location where the simulation source is places are accepted.
The spectra have been then constructed and analyzed using XSpec v12[3], and the total spectrum have been divided in 15 or 20 energy bins equally logarithmically spaced.
In order to study the spectra with XSpec we adopt a model spectrum composed by a power law with exponential or super-exponential cutoff respectively for Polar Cap or Outer Gap Vela. Since the super-exponential cutoff is not implemented in the basic version of XSpec, we develop a simple spectral component with these characteristics and implement as user-defined model in XSpec.

9.3 Results

In order to do spectral analysis the spectral data have been binned in 15 bin equally spaced between 100 MeV and 300 GeV. We analyzed data on timescales of 1 day, 1 week, 1 month, 3 months, 6 months and 1 year. Fig. 9.4 and Fig. 9.5 show the reconstructed spectrum using the procedure described before. The normalization in the plots have been computed using XSpec, that consider the exposure and also the response matrix of the instrument. An important observation timescale is the full simulation of 1 year, whose result is displayed in Fig. 9.6 In order to establish how the difference between models varies with energy we decided to plot the theoretical difference between the fluxes for the two models and compare with the reconstructed spectra. We introduce

[3]XSpec's Home Page at $http://heasarc.gsfc.nasa.gov/docs/xanadu/xspec/$

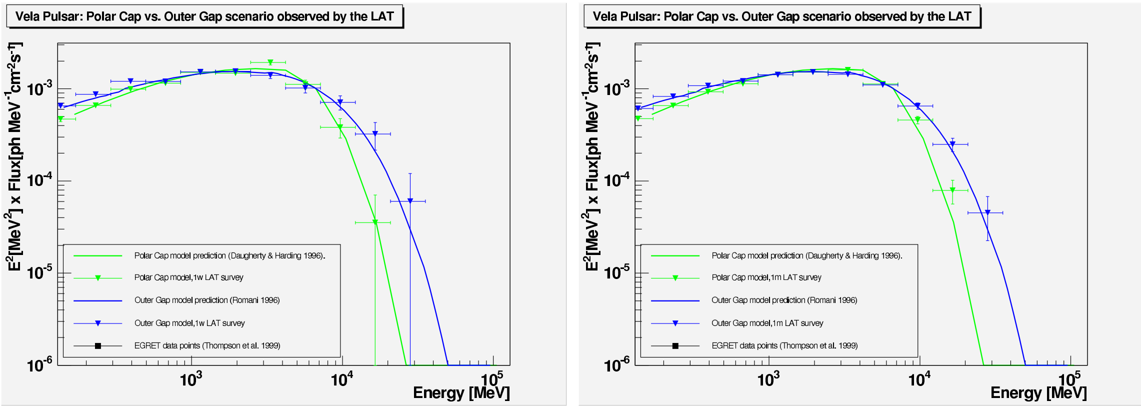

Figure 9.4: Reconstructed spectra of Vela Pulsar for Polar Cap model (light green) and Outer Gap model (dark blue). The lines represent the theoretical model, and the points the reconstructed spectrum. Left: Observation of 1 week in scanning mode. Right: Observation of 1 month in scanning mode.

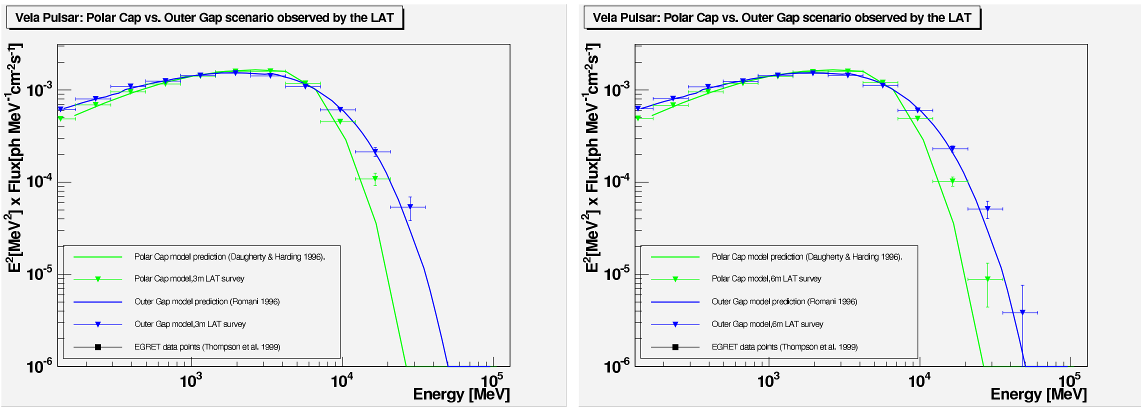

Figure 9.5: Reconstructed spectra of Vela Pulsar for Polar Cap model (light green) and Outer Gap model (dark blue). The lines represent the theoretical model, and the points the reconstructed spectrum. Left: Observation of 3 months in scanning mode. Right: Observation of 6 months in scanning mode.

the quantitity F_{PC} defined as:

$$F_{PC} = E^2 \frac{dN}{dEdtdS} \tag{9.2}$$

that indicate the square of the energy times the differential photon flux in ph cm^{-2} s^{-1} for Polar Cap Vela. This correspond to write the $\nu log F_\nu$ useing the energy and represent the output flux per unit of logarithmic energy. For Outer Gap we define in a similar way F_{OG}.
The quantity $D_{OG-PC} = |F_{OG}$-$F_{PC}|$ can be used to show where the specrta of the two models show the higher difference or distance.
These plots are useful to show where the maximum difference is, that could give a good hint to show which energy band select to better look for checking one or the other model. Fig. 9.7 The error of the quantity D_{OG-PC} depends on both uncertanty on δF_{PC} and

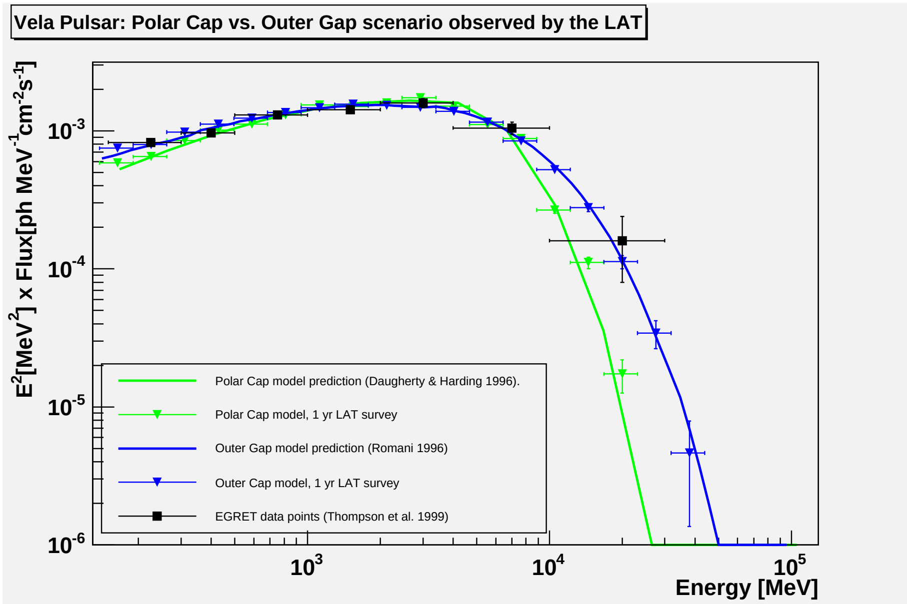

Figure 9.6: Reconstructed spectra of Vela Pulsar for Polar Cap model (light green) and Outer Gap model (dark blue) for an observation time of 1 year. The lines represent the theoretical model, and the points the reconstructed spectrum. The black square points represent the EGRET data.

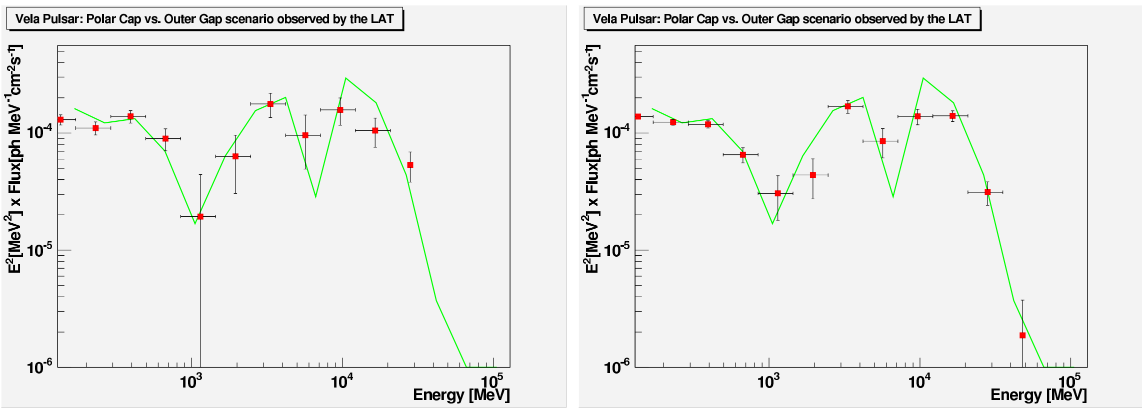

Figure 9.7: The quantity D_{OG-PC} defined in the text that show how the difference between spectra vary with energy. The line show the theoretical prediction and the points represent reconstructed spectra from LAT simulations.Left: Observation of 3 months in scanning mode. Right: Observation of 1 year in scanning mode.

δF_{OG}. Since these errors are independent, the error on the difference have been computed by summing them in quadrature. The error $\delta D_{OG-PC} = \sqrt{\delta F_{PC}^2 + \delta F_{OG}^2}$. In this way the errors shown for points in Fig. 9.7 have been computed. It is possible to see that the maximum of the theoretical difference is about at 10 GeV, then this is to be considered a good energy band, but before it has to be established the weight of the errors on this evaluation.

The value of D_{OG-PC} can be used also for comparing theoretical predictions and simu-

lations in order to give where is the better energy band to choose in order to maximize the relative error in D_{OG-PC}. At lower energy the flux estimate has lower uncertanty but the difference itself is also very small. Viceversa at higher energies the difference will become more evident but the uncertanty increase due to lower statistics. Thanks to the quantity D_{OG-PC} is it possible to estimate what is the best energy band to have the relative error lower.
We computed and plot the difference in term of δD_{OG-PC} and we labeled this as difference between models expressed in terms of sigmas from the mean.
The quantity σ_{OG-PC} is then defined as:

$$\sigma_{OG-PC} = \frac{D_{OG-PC}}{\delta D_{OG-PC}} = \frac{|F_{OG} - F_{PC}|}{\sqrt{\delta F_{PC}^2 + \delta F_{OG}^2}} \tag{9.3}$$

Fig. 9.8 and Fig. 9.9 show the quantity σ_{OG-PC} for different time scales, respectively

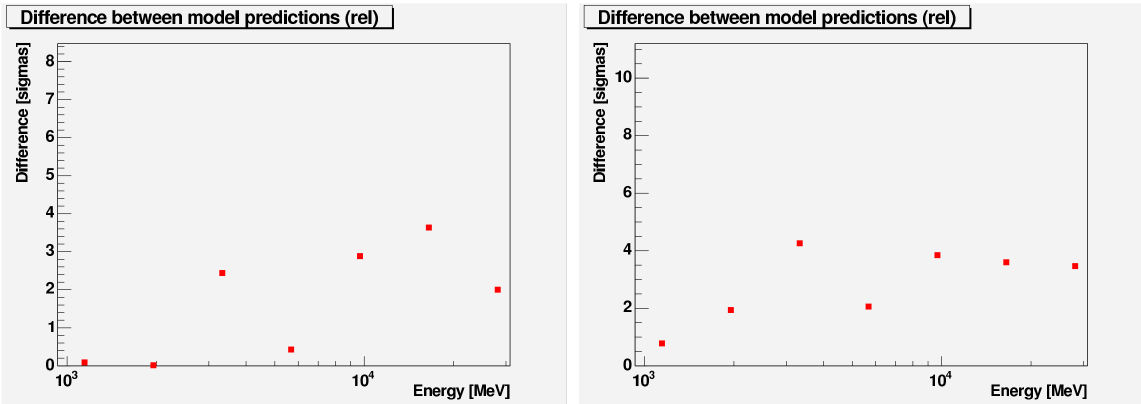

Figure 9.8: Difference D_{OG-PC} vs. energy evaluated in terms of sigma as explained in the text. Left: Observation of 1 month in scanning mode. Right: Observation of 3 months in scanning mode.

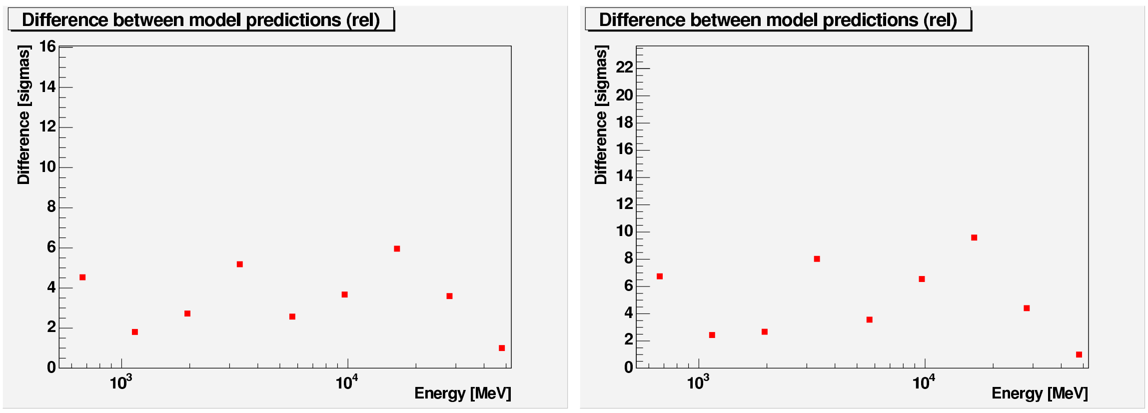

Figure 9.9: Difference D_{OG-PC} vs. energy evaluated in terms of sigma as explained in the text. Left: Observation of 6 months in scanning mode. Right: Observation of 1 year in scanning mode.

of 1 month, 3 months, 6 months and 1 year.
There is a peak at about 3 GeV, in agreement with the Fig. 9.6, since at these ebergie the Polar Cap model exceeds the Outer Gap model. Altough at this energy the difference reach 8 sigma, we decided to neglect it since this bump does not appear to be a definite feature that distinguish Polar Cap from Outer Gap model. For example a small change in the power law at these energies could change this bump, while the high-energy cutoff appear to be a features that strongly characterize the Polar Cap emission from Outer Gap emission.
We are interested in studying high-energy cutoff and it is clearly visible that above 10 GeV σ_{OG-PC} increase up to the energy band centered in 9.6 GeV and then begin to decrease. This behaviour is in agreement with our evaluation that at higher energies the uncertanties in flux estimated become larger because of lower statistics. This lower statistics impact in the decrease if the denominator of the Eq. 9.3 then after about 10 GeV we expect that the difference between models begin to decrease. From these calculations in turns out that the best energy range where to look for maximum difference between model prediction is about 10 GeV.
The results of plots in Fig. 9.8 and Fig. 9.9 can be summarized together with plots for lower observation times of 1 day and 1 week as in Fig. 9.10.
From this plot it can be seen that at lower energy (1.1 GeV and 5.5 GeV) the value of

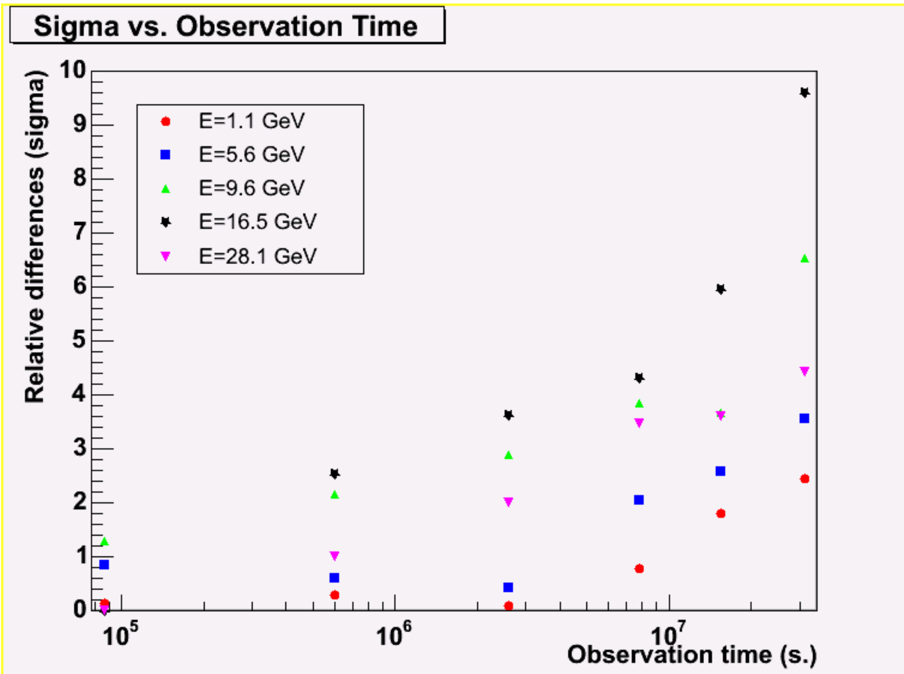

Figure 9.10: Behaviour of σ_{OG-PC} with observation time. Some relevant energies are indicated with different markers.

σ_{OG-PC} is steady increasing but is always lower than 3, while the two enegies wher is is increasingly better is 9.6 GeV and 16.5 GeV, where is is greater than 7σ for one year of observation.
As we expected at higher energies the value of σ_{OG-PC} increase not too much with time, since the error bars on the flux are larger.

9.4 Discussion of the results

The LAT capabilities to distinguish between Polar Cap and Outer Gap model by looking at the high-energy cutoff is one of the most important item for better understanding physics of γ-ray emission in pulsars.
This enhanced capaility of studying spectra comes from the wider energy band of the LAT, that will allow the observation at energies above 30 GeV, a range that was not accessible to EGRET telescope. The higher effective area of the LAT will help to have much more photon statistics and then to measure with smaller errors fluxes at GeV energies.
A comparison between EGRET data and LAT simulated observation for 1 year has been presented in Fig. 9.6. The greater LAT energy range is clearly visible as well as the smaller error bars at few GeV that are expected to be very important to constrain one or the other model.
Results presented in previous Section show that it is possible to look for greater difference between models by lookng at some particular energy band. The behaviour of D_{OG-PC} is useful to see where the difference is greater, but we need to know what are the errors in flux estimates to correctly say what is the optimal energy band.
In order to do that simulations are very important to estimate what are the errors on flux. These are affected by energy resolution and by number of detected photons, then a knowledge of LAT Response Function is critical.
We decided to use as quantity to discriminate between models the σ_{OG-PC}, that is the reciprocal of the relative error. It give the difference between model expressed in terms of flux uncertanty, that we identified as *sigmas*.
It appear that the optimal range where to look for finding higher differences between model predictions is 10-16 GeV, since the maximum of the σ_{OG-PC} occurr for E=9.6 GeV and E=16.5 GeV. Above this energy statistics is very low and then σ_{OG-PC} become lower.
For observation time of the order of 1 year in scanning mode the discrimination between models is of 6σ for E=9.6 GeV and about 9.6σ for E=16.5 GeV.
From Fig. 9.10 it is possible to have a rough estimate on the smaller time required to have a distinction of 3σ and 5σ.
If the energy band selected is around 16.5 GeV we have that the minimum time $t_{3\sigma} \simeq$13 days to achieve a 3σ difference and $t_{5\sigma} \simeq$4 months for achieve a 5σ difference. These values are of course rough estimates and are dependent on the fact that these calculations have been made using simulations of LAT in scanning mode. LAT pointed observations will lead to similar estimates on shorter time scales.
The estimates and calculations made in this Section are based on some assumptions that must be considered in order to discuss also the possible limitation and extension to this work.
Regarding simulations, we decide to not simulate the dependence on the spectrum from the phase. Altough original theoretical models predict also phase-dependent spectra, our simulations have been built without considering them, since the main goal was to study the total flux witouth doing phase-resolved spectroscopy.
In the first Section an argument has been presented to show that the flux of background have been neglected for this study. The study of signal to noise ratio show clearly that for Vela it is always very high, so that the photons that contribute to the spectrum are

very few. Since no significant unpulsed component for Vela has been detected, such a background would have been removed without many problems.
This argument against simulation of background is valid as far as we consider Vela. For other pulsars fainter than it more detailed study should be considered and the influence of the spectrum of background must be taken into account.
The analysis procedure considered for extracting spectrum of Vela has been very simple and for example no energy-dependent cut have been performed. Since LAT Point Spread Function is dependent on energy, a similar energy-dependent cut (as was used for EGRET) could have contributed to select the better reconstructed photons. In particular no additional cuts on instrumental variables have been done, and the standard Instrument Response Function have been used.
However with such assumptions and limitations some initial estimated have been provided together that the confirm that LAT will be able to distinguish between models. We selected basic Polar Cap and Outer Gap models.
Many advanced and refinement in Outer Gap models have been introduced to explain the TeV emission, e.g. model of (Romani, 1996), but the spectrum at GeV energies does not differ to much from the model considered here. In particular there are more recent estension to Polar Cap, e.g. the Slot Gap models (Muslimov & Harding, 2003). The Slot Gap model produces emission from both low altitude cascade, the spectra for which have a super-exponential cutoff (Muslimov & Harding, 2003), and from electrons accelerating at high altitudes, whose spectra are simple exponential, similar to the Outer Gap expected cutoff (Muslimov & Harding, 2004). This kind of study can then also be useful to distinguish betwen inner and outer magnetospheric emission.

9.5 Summary

In this Chapter a study of the LAT cabability to constrain pulsar emission models by looking at the high-energy cutoff have been presented. In order to use the better data today available we decide to simulate Vela pulsar, since because its brightness it is the most studied and better modeled.
Appropriate simulation models have been prepared for this goal and the *PulsarSpectrum* simulator has been used with the *PSRShape* model presented in Ch. 5.
Using the distribution of detected γ-rays it has been shown that LAT will be able to distinguish between the super exponential cutoff predicted by the Polar Cap models and the exponential cutoff of the Outer Gap models.
Using simulated observation of the LAT in scanning mode, an estimate of the better energy band where to look at have been studied, by finding that the energy of about 10 GeV is where the difference between the two models is higher.
Using the same simulations it has been derived a time scale for having enouggh statistics to discriminated between these models, and it has been shown that a difference between the theoretical prediction at a level of 3σ can be achieved in 13 days.

Conclusions

In this thesis I have presented the work for my Ph.D. project, that focuses on the simulation of γ-ray pulsar emissions for the GLAST mission, scheduled for launch at the end of 2007.
The GLAST Large Area Telescope (LAT) will be a powerful instrument for studying γ-ray pulsars, and we expect many important discoveries because of the optimal detection performances of this new-generation γ-ray telescope.
GLAST will have sensitivity and angular and energy resolutions better than its predecessor EGRET and will study in more details the already-known classes of sources. Additionally we expect that it will discover many new sources in the γ-ray sky.
The optimal detection performances of GLAST are a direct consequence of the new detection technology employed for designing the instrument subsystem, the Calorimeter, the Tracker and the AntiCoincidence Detector. A detailed description of the LAT has been given in Chapter 2. LAT is a pair conversion telescope, that allow the incoming γ-rays to convert in an electron-positron pair whose energy and direction can be measured to find the energy and direction of the primary γ-ray.
In particular the silicon microstrip Tracker has many advantages compared to previous tracking detectors, e.g. high detection efficiency, high spatial resolution and no consumables. The segmentation of the Calorimeter will add the capability to image the electromagnetic shower produced by the electron-positron pair and will also improve the event recontruction and background rejection. The segmented Anticoincidence Detector will help reduce the self-veto problem for high-energy photons. This will further increase efficiency and effective area at energies above 10 GeV.
The optimal detection performances of the LAT will provide higher statistics in order to study γ-ray pulsars and explore its emission at energies above 10 GeV.
Pulsars are not the only target of the LAT. From past missions we know that the γ-ray Universe is incredibly dynamic and rich in sources.

Since pulsars are source emitting in various energy window it is important to know how their appear at wavelengths other than γ-rays. In Chapter 3 I give a brief review of the basic properties of, and model for pulsars as Neutron Stars and their characteristic emission in radio, optical and X-rays.
Presently only seven γ-ray pulsars have been detected but we expect that LAT will substantially increase this sample and our knowledge in this field, as it has been discussed in Chapter 4. The high timing accuracy will permit study of pulsar lightcurves with increased time resolution, in order to reveal temporal substructure in the lightcurve. The study of pulsar specral cutoff of pulsars will be possible thanks to the wide spectral range and high energy resolution of the LAT at high energies, greater than few GeV. As

discussed in more detail in Chapter 9 this will help to constrain the two main emission scenarios, the Polar Cap and Outer Gap models.
Another very exciting possibility of the LAT will be the discovery of many new γ-ray pulsars. As discussed in Chapter 4 this number ranges from some tens to some hundreds of new pulsars.
Another interesting possibility is the discovery of new γ-ray pulsars, radio-loud or even radio-quiet like Geminga. Altough in this thesis the blind searches have been not described in detail, the LAT Collaboration has made also efforts in developing and improving such techniques.
In order to better understand the science capabilities of the LAT for pulsars it is important to have simulated data that are as realistic as possible.
The *PulsarSpectrum* simulator has been created and developed in this project in order to provide GLAST members with a complete tool for simulating detailed timing model and spectral distribution of γ-rays.
As discussed in Chapter 5 *PulsarSpectrum* is based on two main simulation models, a phenomenological model that produces a spectrum obtained from an analytical expression, and a more flexible model that can simulate any arbitrary phase-energy photon distribution.
The photons that are extracted from the source model are then processed and corrected in order to consider several effects, mainly 1) barycentric effects due to GLAST motion and relativistic corrections; 2) period change with time; 3) timing noise and 4) orbital motion for simulated binary pulsars.
During this project I also improved them and I found that they permit to obtain high-detailed simulations that match very close the observed features of γ-ray pulsars observed by EGRET.
PulsarSpectrum has been also used for testing the pulsar analysis tools of the LAT Standard Analysis Environment, in order to find for possible bugs and to study the feasibility of possible improvements of the analysis tools. In order to show how *PulsarSpectrum* can be used to simulate γ-raypulsars and how LAT simulated data can be simulated I proposed some simple analysis cases in Chapter 6. This also helped show how *PulsarSpectrum* can be used for testing analysis tools, developing analysis techniques and gaining pratice with LAT data. Three of the EGRET pulsars - Vela, PSR B1706-44 and PSR B1951+32 - have been simulated and analyzed as examples.
The *PulsarSpectrum* simulator has been used by the GLAST LAT Collaboration for simulating the pulsars in the Data Challenge 2 (DC2), as explained in Chapter 7. Since the simulation of the whole pulsar population in DC2 has been under the responsibility of *PulsarSpectrum* simulator, I developed and extended *PulsarSpectrum* with a set of macros and programs of the *Pulsar Simulation Suite* , that made possible the simulation of hundreds of pulsars at the same time. These tools were very useful for generating the final catalog of simulated pulsars for the DC2 skymodel.
The DC2 offered a first possibity to have a realistic full sky simulation of the γ-ray sky, LAT scientists had the possibility to work on it and develop new analysis techniques and test LAT Analysis Tools. In particular, for pulsar analysis I developed a suite of scripts called *pyPulsar* for automated analysis of large samples of pulsars, discussed n Chapter 8. This program have been successfully applied to LAT DC2 data, demonstrating the feasibility of an automated, script-based analysis tool for γ-ray pulsars. This analysis

highlighted some general LAT capabilities for studying pulsar population, when the theoretical model is folded with a detailed description of the LAT response function as in the DC2.
One of the most interesting fields where LAT data are expected to be particularly useful is the study of high-energy spectral cutoffs in order to put constraints on the emission scenario. The Chapter 9 is devoted to such a study, where two sample simulations for Polar Cap and Outer Gap models for Vela pulsar are introduced and LAT ability to distinguish between them is presented. In this Chapter I show that LAT will be able to discriminate over a timescale of few of week of observation in scanning mode, but shorter observation times are required for pointed observation.
The *PulsarSpectrum* simulator that has been used successfully for Data Challenge 2 is also presently in use for the next full sky simulation runs called Service Challenges, that are also a testbench for studying the data production and calibration before and after launch.
The work presented in this thesis has been developed to provide a basic simulator for pulsars that has been expanded to reach a high degree of detail. This results in a wide use of *PulsarSpectrum* by the LAT Collaboration for several activities, in particular testing of analysis tools and development of new analysis techniques. In the period preceding launch it is being also used to obtain some general information on the LAT science capabilities for pulsar detection.
Most of the simulation and analysis work developed in this thesis have been proved useful to the LAT Collaboration for studying and developing detection and analysis strategy in order to better organize the high discovery potential of the LAT for γ-ray pulsar science.
Most of the instruments developed here can be easily adapted to study mode focused analysis strategies: this work is ongoing in collaboration with other members of the LAT Collaboration in order to insure high-detail simulations of pulsars for the period before the launch of the Gamma Ray Large Area Space Telescope.

Acknowledgements

During this Ph.D. I had the luck and priviledge to participate to a project such as GLAST, working with people that strongly contributed in these last years to my scientific formation. To write acknoledgements is very difficult, because I have many people to thank and I would like to express my own gratitude to each one in the appropriate way. I know this is impossible, but I will try to do my best.
My first thanks go my advisor, Ronaldo Bellazzini, who strongly encouraged me from the beginning to work on gamma-ray pulsars, a field of activity that was a kind of new in his team. He stronly supported the results coming out of this work, and gave me a continuous feedback during the development of my research. I would like to express my gratitude also to the people of the GLAST team in Pisa, who received me as an undergraduate student and continued supporting me sharing the adventure of an experiment like the Large Area Telescope. I would like to thank all members of the group, Gloria Spandre, Nicola Omodei, Luca Latronico, Alessandro Brez, Luca Baldini, Melissa Pesce-Rollins, Michael Kuss, Carmelo Sgró, Giovanna Senatore, Johan Bregeon, Massimo Minuti, Dario Grasso, Marco Maria Massai, Franco Angelini, Adele Saredo Parodi, Michele Pinchera and Sandro Bianucci. A special thanks also to Prof. Steven Shore, for the interesting discussions about several topics in Astrophysics, and for the almost infinite energy in giving me as a referee useful suggestions to improve the quality of this thesis.
During the last three years I shared work and ideas with a lot of people of the GLAST italian collaboration. The list of GLAST italian fellows is very long, so I would like to thank few of them: Francesco Longo, Patrizia Caraveo, Riccardo Rando, Omar Tibolla, Aldo Morselli, Gino Tosti and Andrea Caliandro. Working in a project as GLAST gave me the opportunity to work with people spread all around the planet but as they were right at the next door. I would like to express my gratitude to my colleagues William Atwood, James Chiang, Toby Burnett, Seth Digel, Richard Dubois, Masaharu Hirayama, Julie McEnery, James Peachey, Luis Reyes, Steve Ritz, Tracy Usher. I'm also grateful also to members of the LAT Science Group on Pulsar/PWN/SNR, in particular Alice Harding, David Thompson, Gottfried Kanbach, Roger Romani and David Smith, that encouraged my work within the group, providing a lot of useful suggestions for improving quality of simulations.
I would like to express twice my gratitude both to David Thompson and Alice Harding, that kindly accepted to be my referees for this thesis and read carefully every part of it proposing very useful comments and suggestions. They both are pioneers in this research field, and this thesis largely benefits from the results of their past and present work in High-Energy Astrophysics.
Out of the strange and crazy world of Physics, I had the luck of sharing the beautiful

student's life with a lot of friends in Pisa. I would like to thank them all, in particular my fellows at *Pisa-Mensa*, for the almost endless series of meals and walks around the city during summer nights. This friendship has growth in these years and new friends come in, someone I need to thank twice, and *someone* even more. I can't forget to thank my friends of the choir of the University, for sharing with me the amusements of singing together in every place at every time. A credit also to my colleagues of the Ph.D. Course in Physics, that shared with me these three years of intense work.
Finally I would like to address my special thanks to my family and in particular to my parents. They supported me and encouraged me to follow the stars but always having an eye to the earth. To them go my heartfelt *Grazie*.

Bibliography

Aharonian, F., Akhperjanian, A. G., Aye, K.-M., Bazer-Bachi, A. R., Beilicke, M., Benbow, W., Berge, D., Berghaus, P., Bernlöhr, K., Bolz, O., Boisson, C., Borgmeier, C., Breitling, F., Brown, A. M., Bussons Gordo, J., Chadwick, P. M., Chitnis, V. R., Chounet, L.-M., Cornils, R., Costamante, L., Degrange, B., Djannati-Ataï, A., O'C. Drury, L., Ergin, T., Espigat, P., Feinstein, F., Fleury, P., Fontaine, G., Funk, S., Gallant, Y., Giebels, B., Gillessen, S., Goret, P., Guy, J., Hadjichristidis, C., Hauser, M., Heinzelmann, G., Henri, G., Hermann, G., Hinton, J. A., Hofmann, W., Holleran, M., Horns, D., De Jager, O. C., Jung, I., Khélifi, B., Komin, N., Konopelko, A., Latham, I. J., Le Gallou, R., Lemoine, M., Lemière, A., Leroy, N., Lohse, T., Marcowith, A., Masterson, C., McComb, T. J. L., de Naurois, M., Nolan, S. J., Noutsos, A., Orford, K. J., Osborne, J. L., Ouchrif, M., Panter, M., Pelletier, G., Pita, S., Pohl, M., Pühlhofer, G., Punch, M., Raubenheimer, B. C., Raue, M., Raux, J., Rayner, S. M., Redondo, I., Reimer, A., Reimer, O., Ripken, J., Rivoal, M., Rob, L., Rolland, L., Rowell, G., Sahakian, V., Saugé, L., Schlenker, S., Schlickeiser, R., Schuster, C., Schwanke, U., Siewert, M., Sol, H., Steenkamp, R., Stegmann, C., Tavernet, J.-P., Théoret, C. G., Tluczykont, M., van der Walt, D. J., Vasileiadis, G., Vincent, P., Visser, B., Völk, H. J., & Wagner, S. J. 2004, A&A, 425, L13

Aharonian, F., Akhperjanian, A. G., Bazer-Bachi, A. R., Beilicke, M., Benbow, W., Berge, D., Bernlöhr, K., Boisson, C., Bolz, O., Borrel, V., Braun, I., Brown, A. M., Bühler, R., Büsching, I., Carrigan, S., Chadwick, P. M., Chounet, L.-M., Cornils, R., Costamante, L., Degrange, B., Dickinson, H. J., Djannati-Ataï, A., O'C. Drury, L., Dubus, G., Egberts, K., Emmanoulopoulos, D., Espigat, P., Feinstein, F., Ferrero, E., Fiasson, A., Fontaine, G., Funk, S., Funk, S., Füßling, M., Gallant, Y. A., Giebels, B., Glicenstein, J. F., Goret, P., Hadjichristidis, C., Hauser, D., Hauser, M., Heinzelmann, G., Henri, G., Hermann, G., Hinton, J. A., Hoffmann, A., Hofmann, W., Holleran, M., Horns, D., Jacholkowska, A., De Jager, O. C., Kendziorra, E., Khélifi, B., Komin, N., Konopelko, A., Kosack, K., Latham, I. J., Le Gallou, R., Lemière, A., Lemoine-Goumard, M., Lohse, T., Martin, J. M., Martineau-Huynh, O., Marcowith, A., Masterson, C., Maurin, G., McComb, T. J. L., Moulin, E., de Naurois, M., Nedbal, D., Nolan, S. J., Noutsos, A., Orford, K. J., Osborne, J. L., Ouchrif, M., Panter, M., Pelletier, G., Pita, S., Pühlhofer, G., Punch, M., Raubenheimer, B. C., Raue, M., Rayner, S. M., Reimer, A., Reimer, O., Ripken, J., Rob, L., Rolland, L., Rowell, G., Sahakian, V., Santangelo, A., Saugé, L., Schlenker, S., Schlickeiser, R., Schröder, R., Schwanke, U., Schwarzburg, S., Shalchi, A., Sol, H., Spangler, D., Spanier, F., Steenkamp, R., Stegmann, C., Superina, G., Tavernet, J.-P., Terrier, R., Tluczykont, M., van Eldik, C., Vasileiadis, G., Venter, C., Vincent, P., Völk, H. J., Wagner, S. J., & Ward, M. 2006, A&A, 460, 743

Albert, J., Aliu, E., Anderhub, H., Antoranz, P., Armada, A., Asensio, M., Baixeras, C., Barrio, J. A., Bartelt, M., Bartko, H., Bastieri, D., Bavikadi, S. R., Bednarek, W., Berger, K., Bigongiari, C., Biland, A., Bisesi, E., Bock, R. K., Bordas, P., Bosch-Ramon, V., Bretz, T., Britvitch, I., Camara, M., Carmona, E., Chilingarian, A., Ciprini, S., Coarasa, J. A., Commichau, S., Contreras, J. L., Cortina, J., Curtef, V., Danielyan, V., Dazzi, F., De Angelis, A., de los Reyes, R., De Lotto, B., Domingo-Santamaría, E., Dorner, D., Doro, M., Errando, M., Fagiolini, M., Ferenc, D., Fernández, E., Firpo, R., Flix, J., Fonseca, M. V., Font, L., Fuchs, M., Galante, N., Garczarczyk, M., Gaug, M., Giller, M., Goebel, F., Hakobyan, D., Hayashida, M., Hengstebeck, T., Höhne, D., Hose, J., Hsu, C. C., Isar, P. G., Jacon, P., Kalekin, O., Kosyra, R., Kranich, D., Laatiaoui, M., Laille, A., Lenisa, T., Liebing, P., Lindfors, E., Lombardi, S., Longo, F., López, J., López, M., Lorenz, E., Lucarelli, F., Majumdar, P., Maneva, G., Mannheim, K., Mansutti, O., Mariotti, M., Martínez, M., Mase, K., Mazin, D., Merck, C., Meucci, M., Meyer, M., Miranda, J. M., Mirzoyan, R., Mizobuchi, S., Moralejo, A., Nilsson, K., Oña-Wilhelmi, E., Orduña, R., Otte, N., Oya, I., Paneque, D., Paoletti, R., Paredes, J. M., Pasanen, M., Pascoli, D., Pauss, F., Pavel, N., Pegna, R., Persic, M., Peruzzo, L., Piccioli, A., Poller, M., Pooley, G., Prandini, E., Raymers, A., Rhode, W., Ribó, M., Rico, J., Riegel, B., Rissi, M., Robert, A., Romero, G. E., Rügamer, S., Saggion, A., Sánchez, A., Sartori, P., Scalzotto, V., Scapin, V., Schmitt, R., Schweizer, T., Shayduk, M., Shinozaki, K., Shore, S. N., Sidro, N., Sillanpää, A., Sobczynska, D., Stamerra, A., Stark, L. S., Takalo, L., Temnikov, P., Tescaro, D., Teshima, M., Tonello, N., Torres, A., Torres, D. F., Turini, N., Vankov, H., Vitale, V., Wagner, R. M., Wibig, T., Wittek, W., Zanin, R., & Zapatero, J. 2006, Science, 312, 1771

Amelino-Camelia, G., Ellis, J., Mavromatos, N. E., Nanopoulos, D. V., & Sarkar, S. 1998, Nature, 393, 763

Arons, J. 1983, ApJ, 266, 215

Arons, J. & Scharlemann, E. T. 1979, ApJ, 231, 854

Arzoumanian, Z., Nice, D. J., Taylor, J. H., & Thorsett, S. E. 1994, ApJ, 422, 671

Atwood, W. & et al. 2008, ApJ in prep.

Atwood, W. B., Ziegler, M., Johnson, R. P., & Baughman, B. M. 2006, ApJL, 652, L49

Baade, W. & Zwicky, F. 1934, Proceedings of the National Academy of Science, 20, 254

Band, D. L., Digel, S. W., GLAST LAT Instrument Team, & GLAST Science Support Center Team. 2005, in American Astronomical Society Meeting 207, Vol. 37, 1199

Barbiellini, G., Celotti, A., Ghirlanda, G., Longo, F., Piro, L., & Tavani, M. 2004, MNRAS, 350, L5

Baring, M. G. 2004, Adv. Space Res., 33, 552

Becker, W. & Truemper, J. 1997, A&A, 326, 682

Bednarek, W. & Bartosik, M. 2004, in ESA Special Publication,Proceedings of the 5^{th} INTEGRAL Workshop, Vol. 552, Proceedings of the 5^{th} INTEGRAL Workshop, ed. V. Schoenfelder, G. Lichti, & C. Winkler, 449

Bellazzini, R. et al. 2003, Nucl. Instrum. Meth., A512, 136

Bertsch, D. L., Brazier, K. T. S., Fichtel, C. E., Hartman, R. C., Hunter, S. D., Kanbach, G., Kniffen, D. A., Kwok, P. W., Lin, Y. C., & Mattox, J. R. 1992, Nature, 357, 306

Beskin, G. M., Neizvestnyi, S. I., Pimonov, A. A., Plakhotnichenko, V. L., & Shvartsman, V. F. 1983, Soviet Astron. Lett., 9, 148

Bignami, G. F., Caraveo, P. A., & Lamb, R. C. 1982, in Bulletin of the American Astronomical Society, Vol. 14, Bulletin of the American Astronomical Society, 869

Brazier, K. T. S., Kanbach, G., Carraminana, A., Guichard, J., & Merck, M. 1996, MNRAS, 281, 1033

Browning, R., Ramsden, D., & Wright, P. J. 1971, Nature, 232, 99

Buccheri, R., Bennett, K., Bignami, G. F., Bloemen, J. B. G. M., Boriakoff, V., Caraveo, P. A., Hermsen, W., Kanbach, G., Manchester, R. N., Masnou, J. L., Mayer-Hasselwander, H. A., Ozel, M. E., Paul, J. A., Sacco, B., Scarsi, L., & Strong, A. W. 1983, A&A, 128, 245

Cheng, K. S. 2004, Adv. Space Res., 33, 561

Cheng, K. S., Ho, C., & Ruderman, M. 1986a, ApJ, 300, 500

—. 1986b, ApJ, 300, 522

Cocke, W. J., Disney, M. J., & Taylor, D. J. 1969, Nature, 221, 525

Cordes, J. M. 1980, ApJ, 237, 216

Cordes, J. M. & Chernoff, D. F. 1997, ApJ, 482, 971

Cordes, J. M. & Downs, G. S. 1985, ApJS, 59, 343

D'Amico, N., Bennett, K., Clear, J., Buccheri, R., & Sacco, B. 1987, IAU Circular, 4507, 2

Daugherty, J. K. & Harding, A. K. 1982, ApJ, 252, 337

—. 1994, BAAS, 26, 1442

—. 1996, A&AS., 120, C107

De Jager, O. C. & Harding, A. K. 1992, ApJ, 396, 161

De Jager, O. C., Harding, A. K., Michelson, P. F., Nel, H. I., Nolan, P. L., Sreekumar, P., & Thompson, D. J. 1996, ApJ, 457, 253

De Jager, O. C., Oña-Wilhelmi, E., Konopelko, A., Fonseca, F., & Lopez-Moya, M. 2002, African Skies, 7, 21

De Jager, O. C., Raubenheimer, B. C., & Swanepoel, J. W. H. 1989, A&A, 221, 180

Dermer, C. D., Schlickeiser, R., & Mastichiadis, A. 1992, A&A, 256, L27

Diehl, R. 1988, Space Science Reviews, 49, 85

Digel, S. & Myers, J. D. 2001, NASA STI/Recon Technical Report N, 1, 1

Duncan, R. C. & Thompson, C. 1992, ApJL, 392, L9

Ellis, J., Ferstl, A., Olive, K. A., & Santoso, Y. 2003a, Phys. Rev. D, 67, 123502

Ellis, J., Olive, K. A., & Santoso, Y. 2003b, Astroparticle Phys., 18, 395

Fichtel, C. E., Gehrels, N., & Norris, J. P. 1994, Computer

Fichtel, C. E., Hartman, R. C., Kniffen, D. A., Thompson, D. J., Ogelman, H., Ozel, M. E., Tumer, T., & Bignami, G. F. 1975, ApJ, 198, 163

Fierro, J. M. 1995, Ph.D. Thesis

Fierro, J. M., Bertsch, D. L., Brazier, K. T. S., Chiang, J., D'Amico, N., Fichtel, C. E., Hartman, R. C., Hunter, S. D., Johnston, S., Kanbach, G., Kaspi, V. M., Kniffen, D. A., Lin, Y. C., Lyne, A. G., Manchester, R. N., Mattox, J. R., Mayer-Hasselwander, H. A., Michelson, P. F., von Montigny, C., Nolan, P. L., Schneid, E., & Thompson, D. J. 1993, ApJL, 413, L27

Fishman, G. J., Meegan, C. A., Wilson, R. B., Parnell, T. A., Paciesas, W. S., Pendleton, G. N., Hudson, H. S., Matteson, J. L., Peterson, L. E., Cline, T. L., Teegarden, B. J., & Schaefer, B. E. 1989, in Bulletin of the American Astronomical Society, 860

Forman, M. A., Ramaty, R., & Zweibel, E. G. 1986, in Physics of the Sun. Volume 2, 249–289

Fritz, G., Henry, R. C., Meekins, J. F., Chubb, T. A., & Friedman, H. 1969, Science, 164, 709

Gehrels, N., Macomb, D. J., Bertsch, D. L., Thompson, D. J., & Hartman, R. C. 2000, Nature, 404, 363

Gehrels, N. & Michelson, P. 1999, Astroparticle Phys., 11, 277

Ghirlanda, G., Ghisellini, G., Lazzati, D., & Firmani, C. 2004, ApJL, 613, L13

Gold, T. 1968, Nature, 218, 731

Goldberg, H. 1983, Physical Review Letters, 50, 1419

Goldreich, P. & Julian, W. H. 1969, ApJ, 157, 869

Gonthier, P. L., Ouellette, M. S., Berrier, J., O'Brien, S., & Harding, A. K. 2002, ApJ, 565, 482

Gonthier, P. L., Van Guilder, R., & Harding, A. K. 2004, ApJ, 604, 775

Gotthelf, E. V., Halpern, J. P., & Dodson, R. 2002, ApJL, 567, L125

Grenier, I. A. 2002, APS Meeting Abstracts, 2004

Grenier, I. A. 2003, in Texas in Tuscany. XXI Symposium on Relativistic Astrophysics, 397–404

Halpern, J. P. & Holt, S. S. 1992, Nature, 357, 222

Harding, A. K. 1981, ApJ, 245, 267

Harding, A. K. 2001, in American Institute of Physics Conference Series, 115

Harding, A. K. & Daugherty, J. K. 1998, Advances in Space Research, 21, 251

Harding, A. K., Gonthier, P. L., Grenier, I. A., & Perrot, C. A. 2004a, Adv. Space Res., 33, 571

—. 2004b, Adv. Space Res., 33, 571

Harding, A. K. & Muslimov, A. G. 1998, ApJ, 508, 328

—. 2002, ApJ, 568, 862

Harding, A. K., Usov, V. V., & Muslimov, A. G. 2005, ApJ, 622, 531

Hartman, R. C., Bertsch, D. L., Bloom, S. D., Chen, A. W., Deines-Jones, P., Esposito, J. A., Fichtel, C. E., Friedlander, D. P., Hunter, S. D., McDonald, L. M., Sreekumar, P., Thompson, D. J., Jones, B. B., Lin, Y. C., Michelson, P. F., Nolan, P. L., Tompkins, W. F., Kanbach, G., Mayer-Hasselwander, H. A., Mücke, A., Pohl, M., Reimer, O., Kniffen, D. A., Schneid, E. J., von Montigny, C., Mukherjee, R., & Dingus, B. L. 1999, ApJS, 123, 79

Hartman, R. C., Bertsch, D. L., Fichtel, C. E., Hunter, S. D., Kanbach, G., Kniffen, D. A., Kwok, P. W., Lin, Y. C., Mattox, J. R., Mayer-Hasselwander, H. A., Michelson, P. F., von Montigny, C., Nel, H. I., Nolan, P. L., Pinkau, K., Rothermel, H., Schneid, E., Sommer, M., Sreekumar, P., & Thompson, D. J. 1992, ApJL, 385, L1

Hewish, A., Bell, S. J., Pilkington, J. D., Scott, P. F., & Collins, R. A. 1968, Nature, 217, 709

Higgs, L. A., Landecker, T. L., & Roger, R. S. 1977, Astron. J., 82, 718

Hulse, R. A. & Taylor, J. H. 1975, ApJL, 195, L51

Jackson, J. D. 1962, Classical Electrodynamics (Classical Electrodynamics, New York: Wiley, 1962)

Johnson, R. P. & GLAST LAT Collaboration. 2005, in Bulletin of the American Astronomical Society, 1198

Johnson, W. N., Grove, J. E., Phlips, B. F., Ampe, J., Singh, S., & Ponslet, E. 2000, in Bulletin of the American Astronomical Society, 1263

Johnson, W. N., Kurfess, J. D., Purcell, W. R., Matz, S. M., Ulmer, M. P., Strickman, M. S., Murphy, R. J., Grabelsky, D. A., Kinzer, R. L., Share, G. H., Cameron, R. A., Kroeger, R. A., Maisack, M., Jung, G. V., Jensen, C. M., Clayton, D. D., Leising, M. D., Grove, J. E., & Dyer, C. S. 1993, A&AS., 97, 21

Kanbach, G., Arzoumanian, Z., Bertsch, D. L., Brazier, K. T. S., Chiang, J., Fichtel, C. E., Fierro, J. M., Hartman, R. C., Hunter, S. D., Kniffen, D. A., Lin, Y. C., Mattox, J. R., Mayer-Hasselwander, H. A., Michelson, P. F., von Montigny, C., Nel, H. I., Nice, D., Nolan, P. L., Pinkau, K., Rothermel, H., Schneid, E., Sommer, M., Sreekumar, P., Taylor, J. H., & Thompson, D. J. 1994, A&A, 289, 855

Kaspi, V. M. 2004, in Soft Γ Repeaters and Anomalous X-ray Pulsars: Together Forever, ed. F. Camilo & B. M. Gaensler, IAU Symposium 218, 231

Kaspi, V. M., Lackey, J. R., Mattox, J., Manchester, R. N., Bailes, M., & Pace, R. 2000, ApJ, 528, 445

Klebesadel, R. W., Strong, I. B., & Olson, R. A. 1973, in Bulletin of the American Astronomical Society, Vol. 5, Bulletin of the American Astronomical Society, 322

Kniffen, D. A., Hartman, R. C., Thompson, D. J., Bignami, G. K., Fichtel, C. E., Tumer, T., & Ogelman, H. 1974, Nature, 251, 397

Krolik, J. H. 1999, in IAU Symposium, Vol. 194, Activity in Galaxies and Related Phenomena, ed. Y. Terzian, E. Khachikian, & D. Weedman, 453

Kuiper, L., Hermsen, W., Verbunt, F., Thompson, D. J., Stairs, I. H., Lyne, A. G., Strickman, M. S., & Cusumano, G. 2000a, A&A, 359, 615

—. 2000b, A&A, 359, 615

Kulkarni, S. R., Clifton, T. C., Backer, D. C., Foster, R. S., & Fruchter, A. S. 1988, Nature, 331, 50

Kuz'min, A. D. & Losovskii, B. Y. 1997, Astronomy Lett., 23, 283

Leahy, D. A., Darbro, W., Elsner, R. F., Weisskopf, M. C., Kahn, S., Sutherland, P. G., & Grindlay, J. E. 1983, ApJ, 266, 160

Li, J. D., Li, T. P., Ma, Y. Q., & Wu, M. 1987, IAU Circular, 4492, 2

Lin, Y. C., Bertsch, D. L., Chiang, J., Fichtel, C. E., Hartman, R. C., Hunter, S. D., Kanbach, G., Kniffen, D. A., Kwok, P. W., Mattox, J. R., Mayer-Hasselwander, H. A., Michelson, P. F., von Montigny, C., Nolan, P. L., Pinkau, K., Schneid, E., Sreekumar, P., & Thompson, D. J. 1992, ApJL, 401, L61

Lorimer, D. R. & Kramer, M. 2004, Handbook of Pulsar Astronomy (Cambridge University Press)

Lyne, A. G. & Graham-Smith, F. 1990, Pulsar astronomy (Cambridge University Press)

Maeda, Y., Baganoff, F. K., Feigelson, E. D., Morris, M., Bautz, M. W., Brandt, W. N., Burrows, D. N., Doty, J. P., Garmire, G. P., Pravdo, S. H., Ricker, G. R., & Townsley, L. K. 2002, ApJ, 570, 671

Mandzhavidze, N. & Ramaty, R. 1992a, ApJL, 396, L111

—. 1992b, ApJ, 389, 739

Mannheim, K. & Biermann, P. L. 1992, A&A, 253, L21

Maraschi, L., Ghisellini, G., & Celotti, A. 1992, ApJL, 397, L5

Mattox, J. R., Bertsch, D. L., Chiang, J., Dingus, B. L., Digel, S. W., Eposito, J. A., Fierro, J. M., Hartman, R. C., Hunter, S. D., Kanbach, G., Kniffen, D. A., Lin, Y. C., Macomb, D. J., Mayer-Hasselwander, H. A., Michelson, P. F., von Montigny, C., Mukherjee, R., Nolan, P. L., Ramanamurthy, P. V., Schneid, E., Sreekumar, P., Thompson, D. J., & Willis, T. D. 1996, ApJ, 461, 396

Mayer-Hasselwander, H. A., Bertsch, D. L., Brazier, K. T. S., Chiang, J., Fichtel, C. E., Fierro, J. M., Hartman, R. C., Hunter, S. D., Kanbach, G., Kwok, P. W., Kniffen, D. A., Lin, Y. C., Mattox, J. R., Michelson, P. F., Nolan, P. L., Pinkau, K., Rothermel, H., Schneid, E. J., Sommer, M., Sreekumar, P., Thompson, D. J., & von Montigny, C. 1994, ApJ, 421, 276

Mayer-Hasselwander, H. A., Bertsch, D. L., Dingus, B. L., Eckart, A., Esposito, J. A., Genzel, R., Hartman, R. C., Hunter, S. D., Kanbach, G., Kniffen, D. A., Lin, Y. C., Michelson, P. F., Muecke, A., von Montigny, C., Mukherjee, R., Nolan, P. L., Pohl, M., Reimer, O., Schneid, E. J., Sreekumar, P., & Thompson, D. J. 1998, A&A, 335, 161

Mayer-Hasselwander, H. A., Kanbach, G., Bennett, K., Lichti, G. G., Bignami, G. F., Caraveo, P. A., Buccheri, R., Lebrun, F., Masnou, J. L., & Hermsen, W. 1982, A&A, 105, 164

Meegan, C. A. e. a. 2000, GLAST Burst Monitor Proposal, Vol. 1

Meszaros, P. 1992, High-energy radiation from magnetized neutron stars (University of Chicago Press)

Michel, F. C. & Li, H. 1999, Physics Reports, 318, 227

Michelson, P. F. a. a. 2000, LAT Flight Investigation, Vol. 1

Moiseev, A. A., Hartman, R. C., Ormes, J. F., Thompson, D. J., Amato, M. J., Johnson, T. E., Segal, K. N., & Sheppard, D. A. 2007, Astroparticle Phys., 27, 339

Morselli, A. 2002a, Surveys in High Energy Physics, 16, 255

Morselli, A. 2002b, in Frascati Physics Series, Vol. 24, 363–380

Murphy, R. J., Dermer, C. D., & Ramaty, R. 1987, ApJS, 63, 721

Muslimov, A. G. & Harding, A. K. 2003, ApJ, 588, 430

—. 2004, ApJ, 606, 1143

Nel, H. I. & De Jager, O. C. 1995, Astrophys. & Space Sci., 230, 299

Nolan, P. L., Arzoumanian, Z., Bertsch, D. L., Chiang, J., Fichtel, C. E., Fierro, J. M., Hartman, R. C., Hunter, S. D., Kanbach, G., Kniffen, D. A., Kwok, P. W., Lin, Y. C., Mattox, J. R., Mayer-Hasselwander, H. A., Michelson, P. F., von Montigny, C., Nel, H. I., Nice, D., Pinkau, K., Rothermel, H., Schneid, E., Sommer, M., Sreekumar, P., Taylor, J. H., & Thompson, D. J. 1993, ApJ, 409, 697

Nolan, P. L., Fierro, J. M., Lin, Y. C., Michelson, P. F., Bertsch, D. L., Dingus, B. L., Esposito, J. A., Fichtel, C. E., Hartman, R. C., Hunter, S. D., von Montigny, C., Mukherjee, R., Ramanamurthy, P. V., Thompson, D. J., Kniffen, D. A., Schneid, E., Kanbach, G., Mayer-Hasselwander, H. A., & Merck, M. 1996, A&AS., 120, C61

Oegelman, H. & Buccheri, R. 1987, A&A, 186, L17

Oezel, M. E. & Thompson, D. J. 1996, ApJ, 463, 105

Omodei, N., Cohen-Tanugi, J., & Longo, F. 2004, in AIP Conf. Proc. 727: Gamma-Ray Bursts: 30 Years of Discovery, 681–683

Pacini, F. 1967, Nature, 216, 567

Padovani, P. 1997, in Very High Energy Phenomena in the Universe; Moriond Workshop, ed. Y. Giraud-Heraud & J. Tran Thanh van, 7

Percival, J. W., Biggs, J. D., Dolan, J. F., Robinson, E. L., Taylor, M. J., Bless, R. C., Elliot, J. L., Nelson, M. J., Ramseyer, T. F., van Citters, G. W., & Zhang, E. 1993, ApJ, 407, 276

Ramanamurthy, P. V., Bertsch, D. L., Dingus, B. L., Esposito, J. A., Fierro, J. M., Fichtel, C. E., Hunter, S. D., Kanbach, G., Kniffen, D. A., Lin, Y. C., Lyne, A. G., Mattox, J. R., Mayer-Hasselwander, H. A., Merck, M., Michelson, P. F., von Montigny, C., Mukherjee, R., Nolan, P. L., & Thompson, D. J. 1995, ApJL, 447, L109

Ramanamurthy, P. V., Fichtel, C. E., Kniffen, D. A., Sreekumar, P., & Thompson, D. J. 1996, ApJ, 458, 755

Ramaty, R. & Murphy, R. J. 1987, Space Science Reviews, 45, 213

Razzano, M. 2007, Astrophys. & Space Sci., 157

Romani, R. W. 1996, ApJ, 470, 469

Romani, R. W. & Yadigaroglu, I.-A. 1995, ApJ, 438, 314

Ruderman, M. A. & Sutherland, P. G. 1975, ApJ, 196, 51

Ryan, J. M. & Lee, M. A. 1991, ApJ, 368, 316

Safi-Harb, S., Ogelman, H., & Finley, J. P. 1995, ApJ, 439, 722

Schoenfelder, V. 2001, The universe in gamma rays (Springer-Verlag Berlin Heidelberg)

Seidelmann, P. K. 1992, Explanatory Supplement to the Astronomical Almanac (University Science Books)

Seiradakis, J. H. & Wielebinski, R. 2004, Astron. & Astrophys. Rev., 12, 239

Shapiro, S. L. & Teukolsky, S. A. 1983, Black holes, white dwarfs, and neutron stars: The physics of compact objects (Wiley-Interscience New York)

Sreekumar, P., Bertsch, D. L., Dingus, B. L., Esposito, J. A., Fichtel, C. E., Hartman, R. C., Hunter, S. D., Kanbach, G., Kniffen, D. A., Lin, Y. C., Mayer-Hasselwander, H. A., Michelson, P. F., von Montigny, C., Muecke, A., Mukherjee, R., Nolan, P. L., Pohl, M., Reimer, O., Schneid, E., Stacy, J. G., Stecker, F. W., Thompson, D. J., & Willis, T. D. 1998, ApJ, 494, 523

Stairs, I. H. 2004, Science, 304, 547

Stecker, F. W. & Salamon, M. H. 1996a, Physical Review Letters, 76, 3878

—. 1996b, ApJ, 464, 600

Story, S. A., Gonthier, P. L., & Harding, A. K. 2007, ApJ

Strong, A. W. & Moskalenko, I. V. 1998, ApJ, 509, 212

Strong, A. W., Moskalenko, I. V., & Reimer, O. 2004, ApJ, 613, 962

Sturner, S. J. & Dermer, C. D. 1994, ApJL, 420, L79

Sturrock, P. A. 1971, ApJ, 164, 529

Swanenburg, B. N., Hermsen, W., Bennett, K., Bignami, G. F., Caraveo, P., Kanbach, G., Mayer-Hasselwander, H. A., Masnou, J. L., Paul, J. A., & Sacco, B. 1978, Nature, 275, 298

Tavani, M., Barbiellini, G., Argan, A., Basset, M., Boffelli, F., Bulgarelli, A., Caraveo, P., Chen, A., Costa, E., De Paris, G., Del Monte, E., Di Cocco, G., Donnarumma, I., Feroci, M., Fiorini, M., Foggetta, L., Froysland, T., Frutti, M., Fuschino, F., Galli, M., Gianotti, F., Giuliani, A., Labanti, C., Lapshov, I., Lazzarotto, F., Liello, F., Lipari, P., Longo, F., Marisaldi, M., Mastropietro, M., Mattaini, E., Mauri, F., Mereghetti, S., Morelli, E., Morselli, A., Pacciani, L., Pellizzoni, A., Perotti, F., Picozza, P., Pittori, C., Pontoni, C., Porrovecchio, G., Prest, M., Pucella, G., Rapisarda, M., Rossi, E., Rubini, A., Soffitta, P., Traci, A., Trifoglio, M., Trois, A., Vallazza, E., Vercellone, S., Zambra, A., & Zanello, D. 2006, in Proceedings of the SPIE, Vol. 6266, Space Telescopes and Instrumentation II: Ultraviolet to Gamma Ray, ed. M. J. L. Turner & G. Hasinger

Thompson, D. J. 2001, in High Energy Gamma-Ray Astronomy, International Symposium, American Institute of Physics Conference Series, 103

Thompson, D. J. 2003, astro-ph/0312272

Thompson, D. J., Arzoumanian, Z., Bertsch, D. L., Brazier, K. T. S., D'Amico, N., Fichtel, C. E., Fierro, J. M., Hartman, R. C., Hunter, S. D., & Johnston, S. 1992, Nature, 359, 615

Thompson, D. J., Bertsch, D. L., & O'Neal, Jr., R. H. 2005, ApJS, 157, 324

Thompson, D. J. & et al. 1993, in Isolated Pulsars, ed. K. A. van Riper, R. I. Epstein, & C. Ho, 230

Thompson, D. J., Fichtel, C. E., Kniffen, D. A., & Ogelman, H. B. 1975, ApJL, 200, L79

Truemper, J., Pietsch, W., Reppin, C., Voges, W., Staubert, R., & Kendziorra, E. 1978, ApJL, 219, L105

Ulmer, M. P., Matz, S. M., Wilson, R. B., Finger, M. J., Hagedon, K. S., Grabelsky, D. A., Grove, J. E., Johnson, W. N., Kinzer, R. L., Kurfess, J. D., Purcell, W. R., Strickman, M. S., Kaspi, V. M., Johnston, S., Manchester, R. N., Lyne, A. G., & D'Amico, N. 1993, ApJ, 417, 738

Wallace, P. T., Peterson, B. A., Murdin, P. G., Danziger, I. J., Manchester, R. N., Lyne, A. G., Goss, W. M., Smith, F. G., Disney, M. J., Hartley, K. F., Jones, D. H. P., & Wellgate, G. W. 1977, Nature, 266, 692

Weinberg, S. 1983, Physical Review Letters, 50, 387

Zhang, B. & Harding, A. K. 2000, ApJ, 532, 1150